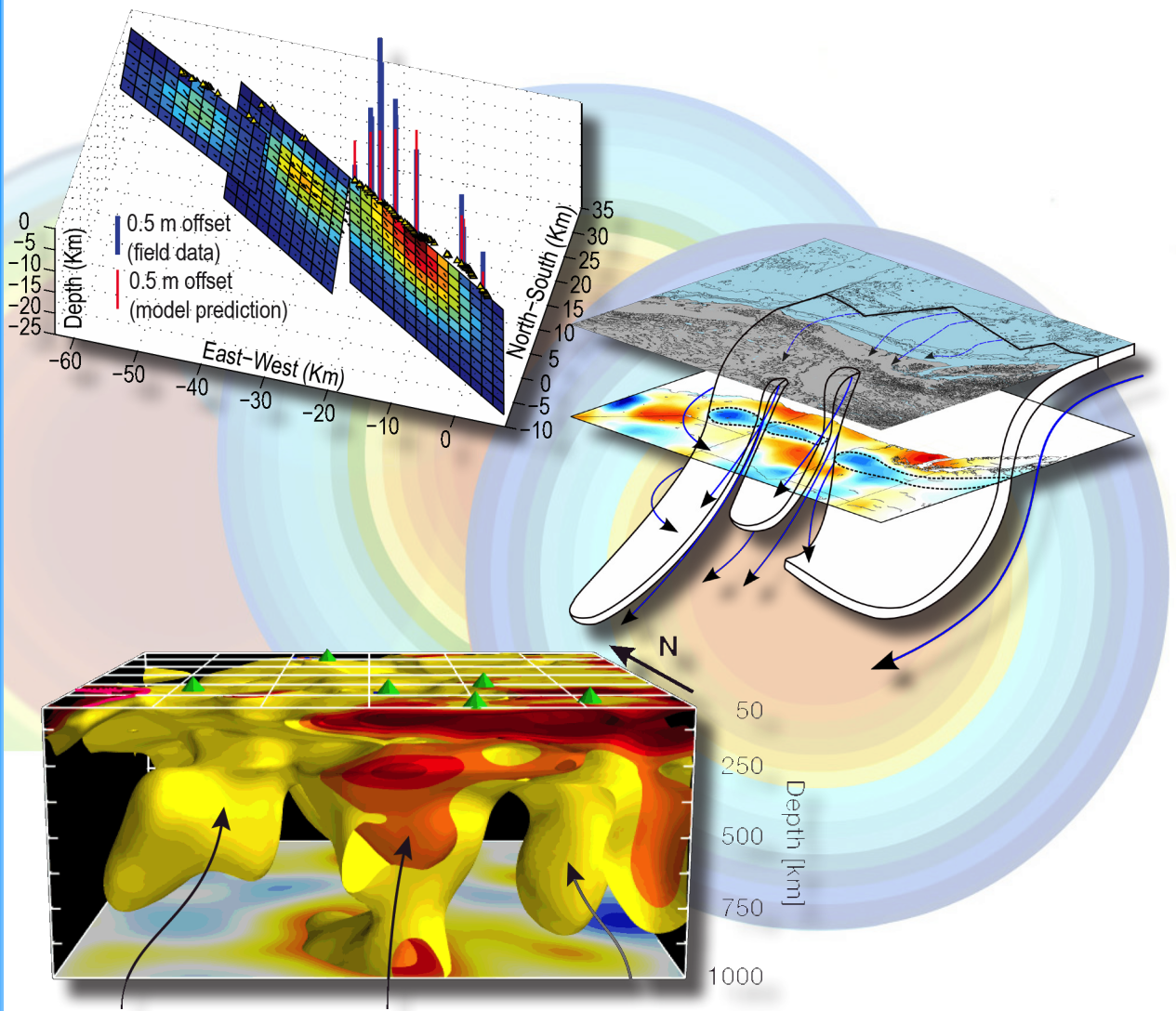


University of California
Berkeley

Seismological Laboratory



Annual Report

July 2012–June 2013

Berkeley Seismological Laboratory

Annual Report
July 2012—June 2013



Contents

Director's Report	1
Highlights	1
BSL Personnel News	2
Facilities review	3
Acknowledgements	4
Research Studies	7
<i>Mineral Physics</i>	
1 <i>Ab Initio</i> Calculations of Elastic Constants of Plagioclase Feldspars	8
2 Laboratory Studies of Crystalline FeSi to 47 GPa and 2800 K	10
<i>Earth Structure</i>	
3 Shear Wave Velocity Model of the Eastern North America Upper Mantle Using Full Waveform Tomography	12
4 Slab fragments in the western U.S.	14
5 Mantle Flow Geometry Through the Segmented Juan de Fuca Plate	16
6 Seismic Constraints on a Double-Layered Asymmetric Whole-Mantle Plume Beneath Hawaii	18
7 New Oceanic Mantle Structures Revealed by Global Full-Waveform Inversion	20
8 Variable Seismic Anisotropy Across the African LLSVP Southern Margin	22
9 The Application of the Local Slant-Stack Filters (LSSF) for High Resolution Upper Mantle Discontinuity Imaging	24
10 Probabilistic Downscaling of Full Waveform Smooth Tomographic Models: Separating Intrinsic and Apparent Anisotropy	26
11 Mapping Embedded Low-velocity Zones in Permafrost Using Full-wavefield Inversion of Multichannel Surface Waves	28
<i>Rheology and Fault Mechanics</i>	
12 Probing Deep Rheology Across the Eastern Margin of the Tibetan Plateau: Constraints from the 2008 M_w 7.9 Wenchuan Earthquake	31
13 Viscoelastic Postseismic Deformation Following the 2011 M_w 9.0 Tohoku Earthquake	32
14 Ambient Seismic Noise Monitoring for Stress-Induced Changes in the Geysers Geothermal Field, California	34
15 Automated Measurement of P- and S-Wave Differential Times for Imaging Spatial Distributions of the V_p/V_s Ratio with a Moving-Window Cross-Correlation Technique	36
16 Inferring a Maximum <i>A Posteriori</i> Probability Model from Geodetic Data	38
17 Exploring Landslide and Granular Mechanics from Geodetically Derived Surface Flow Kinematics	40
18 Geodetic Tracking and Characterization of Precipitation Triggered Slow Moving Landslide Displacements in the Eastern San Francisco Bay Hills, California, USA	42
19 Repeating Earthquake Slip Evolution Along 200 km of the Central San Andreas Fault	44
20 Variability of Fault Slip Behaviors along the San Andreas Fault in the San Juan Bautista Region, Inferred from Characteristically Repeating Earthquake	46
21 Seismic Quiescence Following Large Magnitude Earthquakes	48
22 Laboratory Investigations into Micromechanical Mechanisms Controlling the Onset of Stick-slip Instabilities	50
<i>Seismic Source</i>	
23 Source Characterization of Underground Explosions from Combined Moment Tensor and First Motion Analysis	52
24 Moment Tensor Inversion of Seismic Events Associated with the Sinkhole at Napoleonville Salt Dome, Louisiana	54

25	Full Moment Tensor Solutions Constrained using First Motion Polarities for Seismicity at the Geysers Geothermal Field, California	56
<i>Enhancements to Observational Systems</i>		
26	TremorScope: Imaging the Deep Workings of the San Andreas Fault	58
27	Near Real-Time Infragravity Noise Removal for the Monterey Ocean Bottom Broadband (MOBB) Station	60
28	Potential Applications Using a Smartphone Network	62
29	ShakeAlert: A Unified EEW System for California	64
30	Optimal Seismic Network Density for Earthquake Early Warning: A Case Study from California	66
31	Designing a Network-Based Earthquake Early Warning System for California: ElarmS-2	68
32	G-larmS—Integrating Real-Time GPS into Earthquake Early Warning I: Implementation	70
33	G-larmS—Integrating Real-Time GPS into Earthquake Early Warning II: Testing	72
34	Application of Seismic Array Processing to Earthquake Early Warning	74
Broadening Engagement		77
1	Earthquake Research Affiliates Program	78
2	Engaging the Public	80
3	Science and Society	84
Operations		87
1	Berkeley Digital Seismic Network	89
2	California Integrated Seismic Network	99
3	Northern Hayward Fault Network	104
4	Parkfield Borehole Network (HRSN)	113
5	Bay Area Regional Deformation Network	123
6	Data Acquisition and Quality Control	129
7	Northern California Earthquake Monitoring	137
8	Northern California Earthquake Data Center	145
Glossary of Common Acronyms		157
Appendix I: Publications, Presentations, Awards and Panels		159
Appendix II: Seminar Speakers		169
BSL Organizational Chart		171

Chapter 1

Director's Report

Highlights

It is a great pleasure to present this year's Berkeley Seismological Laboratory (BSL) Annual Report. It is exhilarating to be reminded of the wide range of BSL activities, as captured in these pages. The BSL today fosters both an active solid Earth research program and a cutting-edge geophysical observing facility. Spanning both of these realms, BSL provides an environment in which the extramural research program is strengthened and broadened by the facility, and the facility continues to push the boundaries of terrestrial observations in response to research needs. In addition, the BSL continues to reach out and connect with the consumers of our data and our science. These include students, the public, and private or public sector institutions with a need and desire for an improved understanding of solid Earth processes. The contributions to this report are divided along these three lines. The research accomplishments are covered in Chapter 2, outreach efforts to broaden engagement are in Chapter 3, and progress in the development of our facilities is contained in Chapter 4. But first, I would like to highlight some of this year's activities.

Chapter 2 of the report contains 34 research summaries highlighting ongoing projects. In this year's report we have encouraged the submission of contributions from a broader spectrum of the BSL's 18 affiliated faculty and their students. The topics the summaries report on fall into five broad categories:

1. The mineral physics section includes experimental and numerical experiments on the properties of minerals found in the Earth's crust and beyond, to the cores of Mars and Mercury.
2. The Earth structure section includes new models of North America. Some focus on the old geologic and tectonic structures that underlie the eastern US. Others describe investigations of the actively deforming western US, including flow through the segmented Juan de Fuca plate. Other Earth structure studies model mantle flow beneath the oceans, including upwelling hotspots and anisotropy at the base of the mantle; and the structure of permafrost zones. Finally, this section also describes the development of new imaging techniques.
3. The rheology and fault mechanics section includes studies of lithospheric rheology based on the deformation induced by large earthquakes; studies of temporal changes in active geothermal regions; monitoring and modeling of landslide processes; and the detection of temporal changes in fault zone properties.
4. In the seismic source section, new techniques to characterize underground explosions are developed along with a study of the seismic characteristics of a sinkhole. Earthquake sources in the Geysers geothermal region are also investigated.
5. The final group of research papers focuses on efforts to enhance our observational systems. This includes the installation of a borehole plus surface instrument network to study tremor on the San Andreas Fault; a signal enhancement technology for OBS stations; and the ongoing development of a smartphone-based seismic network. Significant effort to design and build an earthquake early warning system is also covered in this section with papers on both seismic and GPS-based techniques; the design of optimal networks; the use of arrays to track large earthquakes; and a summary describing California's demonstration warning system.

Many of these research efforts are stimulated and inspired by our facilities. These include our geophysical networks that continuously collect a variety of data from across northern California, and the data center (<http://www.ncedc.org/>) that delivers the data to researchers around the world and within the BSL. More information about these networks and their development can be found in the Facilities Review below. Here I would like to note some key developments this year.

Our instrumentation along the San Andreas Fault in central California continues to play a key role in studies of earthquake fault processes conducted by researchers around the world. Data from the High Resolution Seismic Network (HRSN) located near Parkfield, California is highly used placing this network at the center of faulting studies. A high-profile Nature paper links laboratory results of fault healing to naturally occurring microearthquakes using data from the HRSN (*McLaskey et al.*, 2012). Other research efforts, both national and international, continue to rely on HRSN data for a variety of investigations including finite source modeling and scaling (BSL), tracking of repeating events (US Geological Survey, BSL), understanding the relationship between nonvolcanic tremor and low frequency earthquakes (ETH Zurich), ETAS forecasting and prediction modeling of recurrent earthquakes (Japan), and testing of forecasts/predictions with ongoing repeating microearthquakes (BSL, ETH Zurich). In response to the scientific opportunities presented along this section of the San Andreas Fault we are also expanding our network in the region with the development of "Tremorscope". This is a combined borehole and surface station network currently under construction by the BSL just south of the HRSN designed to focus in on the low amplitude seismic tremor that has been detected along the fault by the HRSN. This year the surface stations were completed and we anticipate drilling the borehole stations in the coming year.

Following the upgrade of our Bay Area Regional Deformation Network (BARD) last year, we have also made substantial progress in our real-time processing of these continuous high-accuracy GPS stations. For several years the data have been processed automatically to produce "daily time series". This is a procedure in which the one sample per second data

are combined with other information to provide a single average position for the day. This allows tracking of plate movement and other slow surface deformation caused by a variety of processes including land-use subsidence, landslides and aquifer inflation and deflation. The data are now also being processed much more rapidly in order to provide real-time information about earthquakes. Firstly, "Earthquake Rapid Response" processing is triggered by moderate and large earthquakes. One to two minutes of data are first accumulated following the earthquake. They are then processed to provide high accuracy position changes which can be used in a non-linear inversion for the size, orientation and distribution of slip on the active fault plane. This information, available within about five minutes, can then be used to improve the quality of ShakeMaps generated for the event. Secondly, inclusion of GPS data in the Earthquake Early Warning system is well underway. This processing proceeds even more rapidly so that information about large earthquakes can be extracted within seconds. The development of the G-larmS module that uses GPS data and complements the ElarmS seismic-based alerts is well underway and is expected to become operational next year.

This year's report includes a new chapter on "broadening engagement". This reflects the increase in activities at the BSL to reach out and engage with a broad spectrum of society interested in the data products and research efforts at the lab. With the addition of our new External Relations Officer, Dr Jennifer Strauss, to the BSL staff in November 2012, the lab has been able to increase the efforts of the Earthquake Research Affiliates (ERA) Program (<http://earthquakes.berkeley.edu/ERA/>). This program focuses on engaging public and private institutions with an interest in the development of new earthquake information products and research. Current members include the Bay Area Regional Transit (BART) District, Google, San Francisco's Department of Emergency Management, the UC Berkeley Police Department, and Deutsche Telekom's Silicon Valley Innovation Center. BART now uses our earthquake early warning feed to slow and stop trains automatically during earthquakes, while Deutsche Telekom is working with us on the development of smartphone seismic networks. The other groups are primarily interested in making use of earthquake early warning feeds and are currently in the process of identifying how they would make use of the feed. The BSL is also now better represented within the emergency response community as Strauss participates in conferences and exercises, including this year's Golden Guardian exercise that focused on a major earthquake in Northern California.

BSL's other efforts to broaden engagement are focused on the public. During this year the BSL developed a new webpage that is more focused on information for the public, while still providing information about BSL activities for the research community. The pages are now available at the URL <http://earthquakes.berkeley.edu>, which is hopefully easier for the public to remember than our <http://seismo.berkeley.edu> URL (which remains active). The front page shows a realtime map of earthquakes in California and zooms to the most recent significant earthquake reported. In addition, the BSL has a iOS (iPhone/iPad) app called MyQuake that delivers realtime earth-

quake information to users as well, and also provides information about past earthquakes in an effort to inform the public about the likely impact of future events. MyQuake is available for free at the iTunes store. Additional activities include public lectures, CalDay activities, tours, new displays at the BSL, a new art exhibit based on the real-time seismic data feed from the lab called Bloom, and new "Science on a Sphere" exhibits being developed in collaboration with the Lawrence Hall of Science.

Finally, during this year the BSL has been participating in the development of new Legislation in California relating to the development of a public earthquake early warning system. The legislation, know as Senate Bill 135, was introduced by Senator Alex Padilla in January 2013. Several members of the BSL participated in press conferences, in briefings for legislators, and in Senate and Assembly hearings on the legislation since its introduction. The bill passed the California Senate on May 28th, 2013, the Assembly on September 12th, 2013 and was signed into law by Governor Jerry Brown on September 24th, 2013. In addition to calling for a public state-wide warning system and naming the University of California as one of the participants, this is the first legislation in California that requires the state to play a role in monitoring earthquake activity. There is still much work to be done, however, as the legislation provides no funding. Instead, it calls on the Governor's Office of Emergency Services to develop plans for a system and to identify sources of funding. The BSL will continue to contribute to this development. More next year.

BSL Personnel News

Three new PhD graduate students joined the lab during the 2012/13 academic year: Meng Cai, Avinash Nayak, and Katie Wooddell. Also, two Postdoctoral Fellows joined: Ronni Grapenthin and Lingsen Meng. Five PhD student graduated, their names and thesis titles were: Holly Brown, "Evaluating and Improving the ElarmS Earthquake Early Warning Algorithm"; Sanne Cottaar, "Heterogeneity and Flow in the Deep Earth"; Rob Porritt, "Tracing the Farallon plate through seismic imaging with USArray"; Amanda Thomas, "Fact or Friction: Inferring Rheology from Nonvolcanic Tremor and Low-Frequency Earthquakes on the Deep San Andreas Fault"; and Kelly Wisemann, "The Far Reach of Megathrust Earthquakes: Evolution of Stress, Deformation and Seismicity Following the 2004 Sumatra-Andaman Rupture".

The BSL also continued to provide a range of research projects for undergraduate students. This year's cohort consisted of Rohan Agarwal, Cora Bernard, Voon Hui Lai, Kimberly Lin, Robert Martin-Short, Irene Munafo, and Michael Tran.

As usual, a stream of visitors spent varying amounts of time at the lab. These included Jamie Barron, Pierre Clouzet, Frances Leiva, Florian Rickers, and Sergi Ventosa visiting Barbara Romanowicz's group; Alistair Boyce, Ahyi Kim, and Seung-Hoon Yoo visiting Doug Dreger's group, and Simona Colombelli, William B. Hawley, and Robert Martin-Short visiting my group. One of our former graduate students, Aurelie Guilhem, returned to work with several members of the lab. Finally, Tea Godoladze spent a year at the lab on a Fulbright Fellowship.

During the year we also gained several new members of staff. Sarah Snyder and Nicole Crisosto joined the engineering staff, although Nicole departed towards the end of the year. Jennifer Strauss also joined as our new External Relations Officer. Aaron Enright who was on the engineering staff for several years departed, as did Huaiyu Yuan who was working as a researcher.

Facilities review

The Berkeley Seismological Laboratory (BSL) is an Organized Research Unit (ORU) on the UC Berkeley campus. Its mission is unique in that, in addition to research and education in seismology, geophysics, and earthquake-related science, it is responsible for providing real-time earthquake information. This information is required by the UC Berkeley constituency, various local and state government and private organizations including emergency response, and is consumed by the general public. The BSL is therefore both a research center and a facility/data resource, which sets it apart from most other ORUs. A major component of our activities is focused on developing and maintaining several regional observational networks, and participating, along with other agencies, in various aspects of the collection, analysis, archival, and distribution of data pertaining to earthquakes, while maintaining a vigorous research program on earthquake processes and Earth structure. In addition, the BSL staff spends considerable time on public relations activities, including tours, talks to public groups, response to public inquiries about earthquakes, and an informational web presence.

UC Berkeley installed the first seismograph in the Western Hemisphere at Mount Hamilton (MHC) in 1887. Since then, it has played a leading role in the operation of state-of-the-art seismic instruments and in the development of advanced methods for seismic data analysis and interpretation. Notably, the installation, starting in 1927, of Wood-Anderson seismographs at four locations in Northern California (BKS, ARC, MIN, and MHC) allowed the accurate determination of local earthquake magnitude from which a unique historical catalog of regional earthquakes has been maintained to this day, providing crucial input to earthquake probability studies.

Over the years, the Berkeley Seismographic Stations (BSS), as the BSL was then called, continued to drive technological improvements. The first centrally telemetered network using phone lines in an active seismic region was installed by BSS in 1960. The BSS was the first institution in California to operate a 3-component “broadband” system (1963). It played a major role in the early characterization of earthquake sources using “moment tensors” and source-time functions. The BSS also made important contributions to the early definitions of detection/discrimination of underground nuclear tests and, jointly with UCB Engineering, to earthquake hazards work.

Starting in 1986, the BSS acquired four state-of-the-art broadband instruments (STS-1), while simultaneously developing PC-based digital telemetry. These two developments laid the groundwork for the modern networks we operate today. As telecommunication and computer technologies made rapid progress, in parallel with broadband instrument development, paper record reading was abandoned in favor of automated

analysis of digital data. One paper-based helicorder does remain operational, primarily for the press and visitors to view.

Today, the BSLs networks can be divided into three groups of instrumentation that are deployed at a total of ~70 sites across central and northern California. The instrumentation types predominantly consist of broadband plus strong motion seismic, borehole seismic, and GPS equipment, and are often co-located when appropriate. Data from all instrumentation streams continuously into the BSLs real-time monitoring system providing for earthquake warnings, notification and characterization. It is also delivered to the archive where it can be accessed immediately by researchers from around the world for scientific study.

The Berkeley Digital Seismic Network (BDSN) is our regional seismic network of about 40 sites where both broadband and strong motion seismic instrumentation is installed. This network is the backbone of the BSLs operations, feeding the necessary data for real-time estimation of location, size and rupture parameters for earthquakes in central and northern California. This network has been steadily growing since the 1990s and consists of very high quality, low noise sites making the data ideal for a range of research efforts. The array can be used to study local or global earthquake sources, and provides data for investigation of 3D crustal structure in California and its effects on regional waveform propagation, which in turn affect the intensity of ground shaking in larger earthquakes. Recent additions to the network include an ocean bottom seismometer in the Monterey Bay (MOBB) providing real-time data via an undersea cable (operated in collaboration with MBARI), and also the Tremorscope stations along the Cholame section of the San Andreas Fault just south of Parkfield, CA.

The real-time data is also Berkeley’s contribution to the California Integrated Seismic Network (CISN), which is a federation of networks that jointly provide all real-time earthquake information in the state. Since 1996, the BSL and the USGS in Menlo Park have closely cooperated to provide the joint earthquake notification program for Northern California. This program capitalizes on the complementary capabilities of the networks operated by each institution to provide rapid and reliable information on the location, size and other relevant source parameters of regional earthquakes. The real-time earthquake information is made available through the BSLs website (<http://earthquakes.berkeley.edu>).

The BSLs borehole networks represent the second grouping of instrumentation. The High Resolution Seismic Network (HRSN) was installed in 1987 and now consists of 12 operating sites. Additional borehole sites will soon be added as part of the Tremorscope project. These instruments have led to wide-ranging research into earthquake processes due to their high sensitivity, low noise, and proximity to micro-earthquakes, clusters and tremor sources along the highly studied Parkfield section of the San Andreas Fault. In the Bay Area, the Hayward Fault Network also includes 15 borehole instruments that have been installed progressively since the 1990s. Again, the goal of this network is to collect high signal-to-noise data for micro-earthquakes along the Hayward Fault to gain insight into the physics that govern fault rupture and its nucleation.

The third instrumentation type is GPS. The BSL operates the Bay Area Regional Deformation (BARD) Network consisting of 32 primary sites, 18 collocated with BDSN seismometers. All sites record with a 1 Hz sample rate and telemeter the data to BSL in real-time. Continuous GPS data track the motion of the tectonic plates and allows us to assess the strain buildup along faults as well as its release either through creeping episodes or through earthquakes. The application of GPS data feeds to real-time earthquake information is also a relatively new development. Very rapid processing now generates displacement waveforms that in turn support the development of improved real-time earthquake analysis methods for significant earthquakes.

The BSL's IT group is active in the development of new software for the collection, archival and real-time analysis of the various geophysical data streams that we collect. In 2009, the new AQMS seismic network software package was rolled out following a multi-year development effort by the BSL in collaboration with other CISN partners. This software provides all the real-time processing components needed by regional seismic networks and is now being rolled-out across the US. The development of real-time GPS processing software is a current area of focus for the lab along with development and implementation of earthquake early warning algorithms that can process the data quickly enough to provide alerts to people a few seconds to tens of seconds before shaking is felt.

Archival and distribution of data from the BSL and other regional geophysical networks is performed at the Northern California Earthquake Data Center (NCEDC), operated at the BSL in collaboration with USGS Menlo Park. The data reside on a mass-storage device (current holdings ~70 Tb), and are accessible online (<http://www.ncedc.org>). In addition to BSL network data, data from the USGS Northern California Seismic Network (NCSN), and other northern California networks, are archived and distributed through the NCEDC. The NCEDC also maintains, archives and distributes various earthquake catalogs.

Finally, the field engineering team is responsible for maintaining our existing ~70 geophysical observatories across Northern California, and designing and installing new sites. Of particular note is the completion in 2011 of the ARRA-funded upgrades. These urgently needed equipment upgrades replaced aging dataloggers at almost all BSL observatories providing for more robust and more rapid transmission of data from the sites to the BSL real-time system. The group is now focused on the design and installation of the new Tremorscope borehole and surface stations just south of Parkfield along the Cholame section of the San Andreas Fault, and on upgrading the HRSN.

All of these operations are supported by an operations and research staff of 9, an IT staff of 7, an engineering staff of 3, and an administrative support group largely shared with the Department of Earth and Planetary Science consisting of 7. In addition, there are currently 6 Postdoctoral Scholars and 15 PhD graduate students associated with the lab, along with 18 affiliated faculty.

Core University funding to our ORU provides salary support for one staff scientist (shared by three researchers), one IT

staff member, one engineer, our operations manager, and two administrative assistants, and represents about one fifth of the total infrastructure support budget. The remaining support comes from extramural grants and contracts, primarily from the USGS, DOE, NSF, and the State of California, through its Office of Emergency Services (CalOES). Currently, grants from the Gordon and Betty Moore Foundation contribute significantly to our operations as do the contributions from the members of our Earthquake Research Affiliates (ERA) Program. Additional extramural research funding to BSL affiliated faculty and staff conducting earthquake science more than doubles the total annual budget.

Acknowledgements

I would like to thank our technical and administrative staff, scientists and students for their efforts throughout the year and their contributions to this annual report. In particular I would like to thank our affiliated faculty, whose research groups are contributing to this report for the first time: Professors Steven Glaser, Raymond Jeanloz, Burkhard Militzer and Rudy Wenk. Individual contributions to activities and report preparation are mentioned in the corresponding sections, except for the appendix sections, which were prepared by Clay Miller.

The BSL Advisory Committee plays an important role providing feedback and guidance on BSL activities and priorities. The committee members are Prof. Steven Glaser (Chair – Civil and Environmental Engineering, UC Berkeley), Prof. Josh Bloom (Astronomy, UC Berkeley), Dr. Thomas Brocher (US Geological Survey), Prof. Michael Manga (Earth and Planetary Science, UC Berkeley), Prof. John Vidale (University of Washington). In particular I would like to thank them for their participation in the Advisory Meeting in June 2013 and the thoughtful preparation of the report that followed.

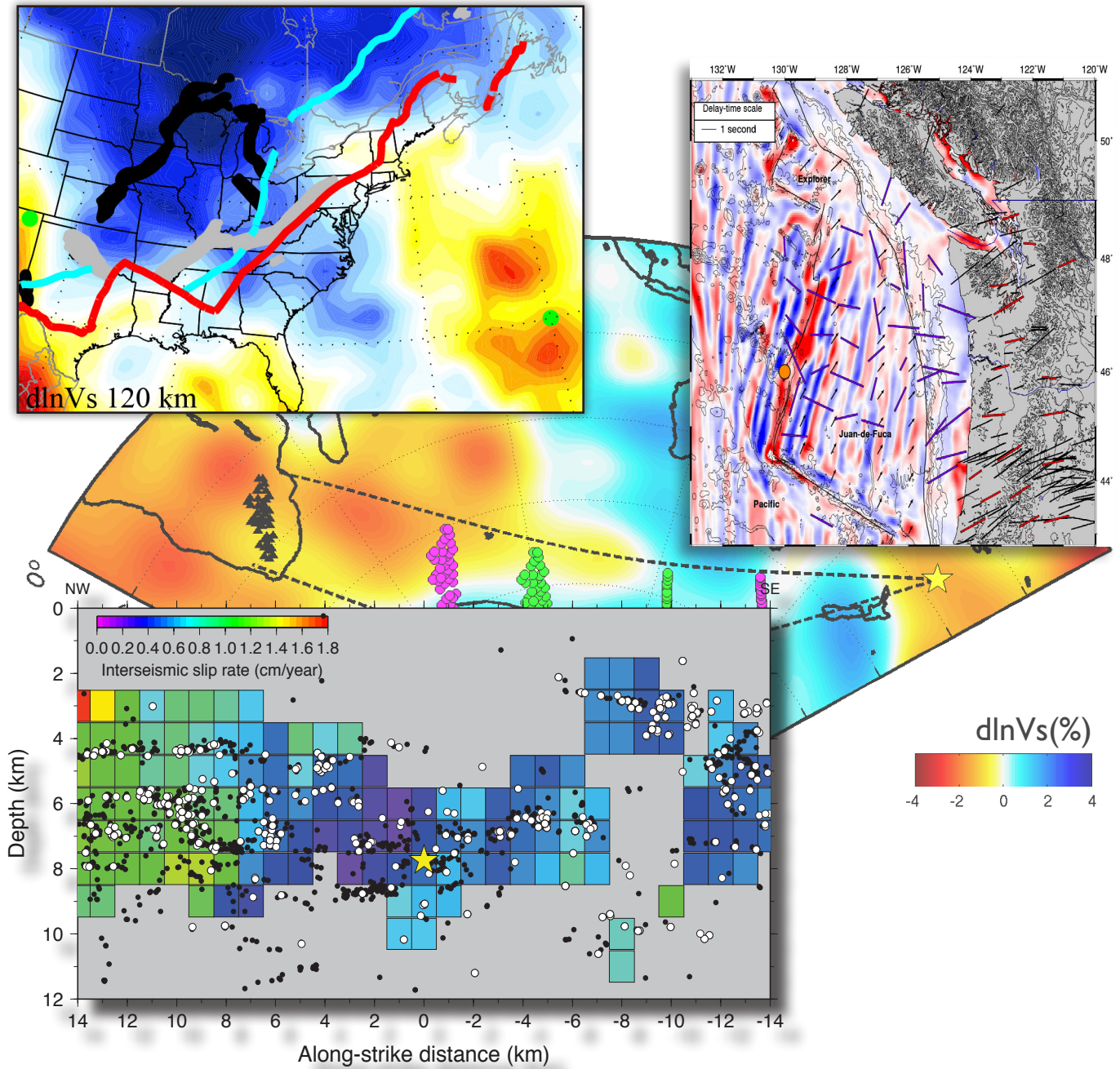
I also wish to especially thank the individuals who have regularly contributed to the smooth operation of the BSL facilities: Mario Aranha, Nicole Cristosto, Doug Dreger, Aaron Enright, John Friday, Peggy Hellweg, Ivan Henson, Ingrid Johanson, Clay Miller, Josh Miller, Pete Lombard, Bob Nadeau, Doug Neuhauser, Charley Paffenbarger, Jennifer Strauss, Sarah Snyder, Jennifer Taggart, Taka'aki Taira, Stephen Thompson, Bob Uhrhammer, and Stephane Zuzlewski, and, in the administrative office, Marion Banks, Matt Carli, Judith Coyote, Clarissa Foreman, Dawn Geddes, Raluca Iordache, and Gretchen von-Duering.

I am particularly grateful to Clay Miller, Jennifer Taggart and Peggy Hellweg for their help in putting together this annual report and bringing it to completion.

The Annual Reports of the Berkeley Seismological Laboratory are available on the web at http://earthquakes.berkeley.edu/annual_report.

Chapter 2

Research Studies



1 *Ab Initio* Calculations of Elastic Constants of Plagioclase Feldspars

Pamela Kaercher, Burkhard Militzer, Hans-Rudolf Wenk

Introduction

Plagioclase feldspars are one of the most important rock-forming minerals, comprising roughly 40% of the Earth's crust. Their elastic properties are essential for interpreting seismic data to determine the structure and deformation history of the Earth's crust, especially the seismically anisotropic lower crust. This anisotropy has been largely attributed to preferred orientation of plagioclase and orientation patterns have been investigated with advanced methods (e.g., *Ji and Mainprice, 1988, Seront et al., 1993*) including work at Berkeley (e.g., *Xie et al., 2003, Feinberg et al., 2006, Gómez-Barreiro et al., 2007*). However, to relate crystal orientation patterns to macroscopic seismic anisotropy, we need the elastic properties of plagioclase single crystals, which are not completely known.

Nearly all of the existing elastic constants for plagioclases (e.g., *Alexandrov and Ryzhova, 1962, Ryzhova, 1964*) were measured in highly twinned polycrystals, generating monoclinic symmetry for the truly triclinic plagioclase crystals. Only recently, *Brown et al. (2006)* measured velocities on untwinned albite and retrieved all 21 elastic constants to fully describe triclinic symmetry.

We have performed *ab initio* calculations using density functional theory to calculate elastic constants for albite $\text{NaAlSi}_3\text{O}_8$ (An0), andesine/laboradorite $\text{NaCaAl}_3\text{Si}_5\text{O}_{16}$ (An50), and anorthite $\text{CaAl}_2\text{Si}_2\text{O}_8$ (An100) in order to assess and improve upon the precision of existing elastic constants.

Method

We calculated the elastic constants of An0, An50, and An100 with density functional theory using the local density approximation within the Vienna *Ab-initio* Simulation Package (VASP). We used the finite strain approach with the experimentally-determined density (e.g., *Militzer et al., 2011*) and calculated elastic constants (C_{ijkl}) with Hooke's Law.

The lattice vectors of the unit cells ($\vec{a}, \vec{b}, \vec{c}$) $\equiv \vec{A}$ were strained by $\vec{A}' = (\vec{I} + \vec{\epsilon}_i)\vec{A}$, where \vec{I} is the identity matrix, and $\vec{\epsilon}_i$ is the strain matrix, where the three diagonal ($i = 1, 2, 3$) and three off-diagonal ($i = 4, 5, 6$) strain tensors are defined similarly to

$$\vec{\epsilon}_1 = \begin{pmatrix} \delta & 0 & 0 \\ 0 & 0 & 0 \\ 0 & 0 & 0 \end{pmatrix} \quad \text{and} \quad \vec{\epsilon}_4 = \begin{pmatrix} 0 & 0 & 0 \\ 0 & 0 & \delta/2 \\ 0 & \delta/2 & 0 \end{pmatrix},$$

with $\delta = \pm 0.005$, to define new lattice vectors ($\vec{a}', \vec{b}', \vec{c}'$) $\equiv \vec{A}'$.

We estimate total errors in elastic constants to be $< \pm 2$ GPa based on comparison of differences between C_{ij} and C_{ji} values and observations of the effect of different values of δ on elastic constants.

Results and Discussion

Most of our computed elastic constants for An0 are higher than those of *Ryzhova (1964)* and lower than those of *Brown et al. (2006)*, but tend to be closer to those of *Brown et al. (Figure*

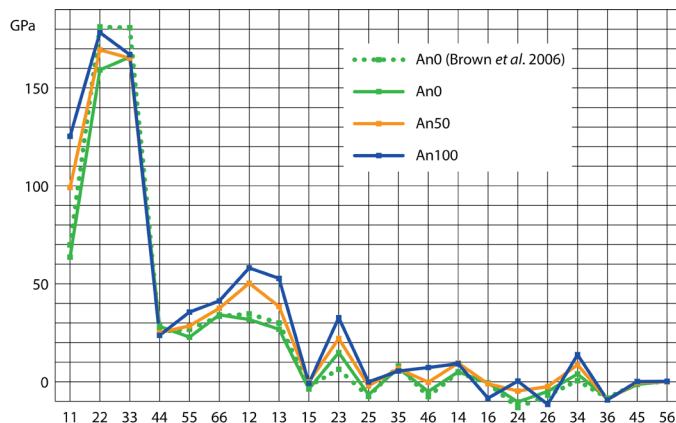


Figure 2.1.1: Comparison of measured An0 (*Brown et al., 2006*) and computed An0, An50, and An100 elastic constants in gigapascals (GPa). The horizontal axis shows subscripts for elastic constants in Voigt notation.

2.1.1). Our calculated An50 elastic constants are comparable to those of both *Alexandrov and Ryzhova (1962)* and *Ryzhova (1964)*.

Elastic properties and mineral density may be used to calculate wave velocities in different directions through a single crystal. *P*-wave and *S*-wave velocity maps (Figure 2.1.2) show seismic anisotropy generally decreases as An0 \rightarrow An100, likely due to changes in bond lengths as Al substitutes in for Si, which in turn cause tetrahedra (with oxygen at the four corners and either Al or Si in the center cation position) to rotate. Specifically, *P*-wave velocity anisotropy (A_p) for our calculated An0, An50, and An100 is 39%, 26%, and 28%, respectively, where $A_p = \frac{V_{max} - V_{min}}{V_{max}} \times 100\%$. In comparison, other deep crustal minerals such as olivine and hornblende are 22% and 28%, respectively.

Elastic constants may also be combined with the orientation distribution of a polycrystal to model seismic anisotropy for a rock with preferred orientation. The relationship between preferred orientation and seismic velocities has been studied in a number of natural aggregates with high plagioclase content (e.g., *Wenk et al., 1986, Ji and Mainprice, 1988*), which found that *P*-wave anisotropy in plagioclase amounts to 2-15% depending on the fabric, suggesting that an accurate and complete set of C_{ij} s for the plagioclase series is important for calculating seismic velocities through the lower mantle.

Summary

The 21 elastic constants were calculated for An0, An50, and An100 using DFT. Results for An0 and An50 agree well with experimental results. In addition we calculated C_{ij} s for An100, and results can be extrapolated for the entire plagioclase family. These C_{ij} s can be applied to model anisotropy of plagioclase-containing rocks, and are particularly useful to improving velocity calculations through the lower crust.

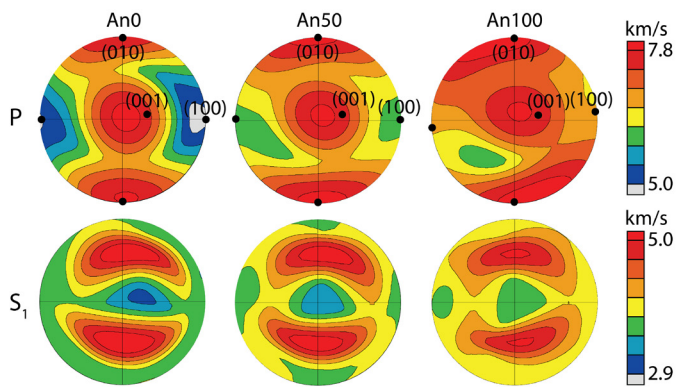


Figure 2.1.2: Velocity surface maps calculated from densities and the elastic constants calculated for An0, An50, and An100. The top row shows are P-wave velocities, and the bottom row shows fastest S-wave velocities. These are equal area projections.

Acknowledgements

P. Kaercher is grateful to Siegfried Matthies and Roman Vasin for help with this work. We also thank the Carnegie/Department of Energy Alliance Center (CDAC) for financial support.

References

- Alexandrov, K.S., Ryzhova, T.V., Elastic properties of rock-forming minerals: III feldspars, *Bull. Acad. Sci. USSR Geol. Ser.* 10, 129-131., 1962.
- Brown, J.M., Abramson, E.H., Angel, R.J., Triclinic elastic constants for low albite, *Physics and Chemistry of Minerals* 33, 256-265, 2006.
- Feinberg J., Wenk H.-R., Scott G.R., Renne P.R., Preferred orientation and anisotropy of seismic and magnetic properties in gabbro-norites from the Bushveld layered intrusion, *Tectonophysics*, 420, 345-356, 2006.
- Gómez-Barreiro, J., Lenardelli, I., Wenk, H.-R., Dresen, G., Rybacki, E., Ren, Y., Tomé, C.N., Preferred orientation of anorthite deformed experimentally in Newtonian creep. *EPSL* 264(1), 188-207, 2007.
- Ji, S., Mainprice, D., Natural deformation fabrics of plagioclase: implications for slip systems and seismic anisotropy. *Tectonophysics* 147, 145-163, 1988.
- Militzer, B., Wenk, H.-R., Stackhouse, S., Stixrude, L., First-principles calculation of the elastic moduli of sheet silicates and their application to shale anisotropy, *American Mineralogist*, 96, 125-137, 2011.
- Ryzhova, T.V., Elastic properties of plagioclase, *Bull. Acad. Sci. USSR Geol. Ser.* 7, 633-635, 1964.
- Seront, B., Mainprice, D., Christensen, N.I., A determination of the three-dimensional seismic properties of anorthosite: comparison between values calculated from the petrofabric and direct laboratory measurements, *J. Geophys. Res.* 98, 2209-2221, 1993.
- Wenk, H.-R., Bunge, H.J., Jansen, E., Pannetier, J., Preferred orientation of plagioclase – neutron diffraction and U-stage data, *Tectonophysics* 126, 271-284, 1986.
- Xie, Y., Wenk, H.-R., Matthies, S., Plagioclase preferred orientation by TOF neutron diffraction and SEM-EBSD, *Tectonophysics* 370, 269-286, 2003.

2 Laboratory Studies of Crystalline FeSi to 47 GPa and 2800 K

Zack Geballe and Raymond Jeanloz

Introduction

Equations of state, melting curves, mixing relations and solid-solid phase boundaries in iron and its alloys are the key equilibrium properties needed for modeling the constitution and evolution of planetary cores. Silicon is one element that is likely to be alloyed with iron in the cores of rocky planets; it is abundant in the rocks found on the surfaces of Mercury, Venus, Earth and Mars (*de Pater and Lissauer, 2010*), and in the laboratory it is known to alloy with liquid iron at high pressures (*Sanloup and Fei, 2004*) or at low oxygen fugacity (*McCoy et al., 1999*).¹

Recently, the cubic ϵ -phase of FeSi was found to transform to another cubic phase, B2, at 24 GPa and high temperature (*Dobson et al., 2002*)—conditions that exist in the cores of Mars and Mercury. Yet several properties of the ϵ to B2 phase transition remain uncertain, including the location of the phase boundary in pressure-temperature space, and the entropy difference between the two phases.

Here we present X-ray diffraction data of hot, dense FeSi. First, we show that it remains solid up to at least 2350 ± 200 K at 23 GPa and 2770 ± 200 K at 47 GPa, which means that addition of silicon does not cause a large amount of melting point depression (the melting temperature of pure iron ranges from 2300 ± 100 K to 2700 ± 150 K between 20 and 50 GPa). Second, the ϵ to B2 crystal-crystal phase transition occurs at 30 ± 2 GPa at all temperatures from 1200 K to 2300 K. It results in a 5% density increase, which may cause an increase in the miscibility of silicon in iron at $P > 30$ GPa, with potential implications for the cores of small rocky planets such as Mars and Mercury.

Experimental Method

Stoichiometric FeSi was synthesized and given to us by Ravhi S. Kumar. It was ground to a fine powder and loaded into diamond anvil cells with rhenium gaskets. The samples were surrounded with an argon or neon pressure transmitting medium. High-pressure samples were laser-heated at GeoSoilEnviroCARS (GSECARS) end-station ID-D, and simultaneous emission spectra and X-ray diffraction images were collected (*Prakapenka et al. 2008*).

Details of temperature and pressure measurements and of their uncertainties will be presented in an upcoming publication.

Results and Discussion

The solid-solid phase transition from the low pressure ϵ phase to the high pressure B2 phase of FeSi occurs at 30 ± 2 GPa, the weighted average of the transition pressures detected in a neon pressure medium (31.2 ± 1.7 GPa) and in an argon medium (28 ± 1.9 GPa) (Figure 2.2.1). We detected no temperature dependence

1. Much of this report is quoted from a manuscript submitted to American Mineralogist: paper #4612R

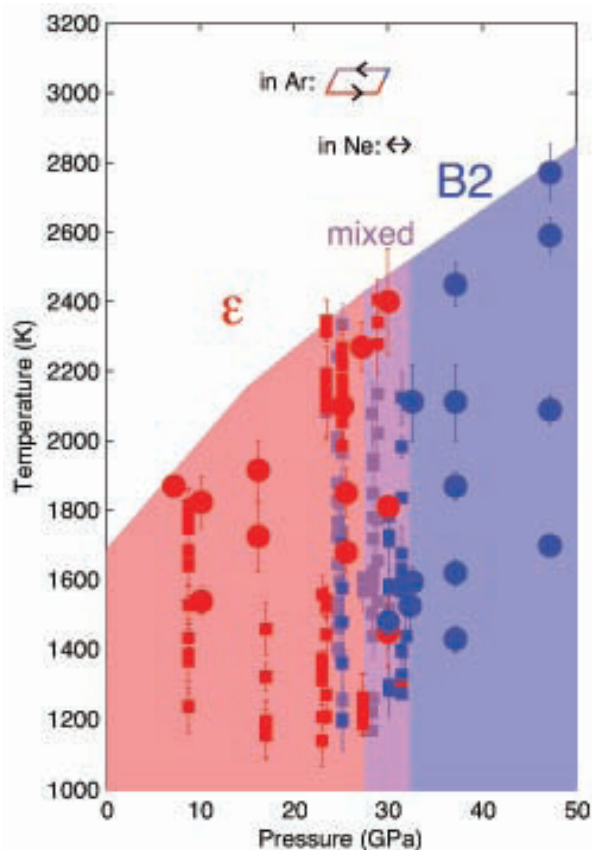


Figure 2.2.1: The ϵ -B2 phase transition of FeSi occurs at 30 ± 2 GPa, with no detectable temperature dependence between 1000 and 2400 K. Data using an argon pressure medium are represented by squares. Red symbols represent ϵ -FeSi, blue represents B2-FeSi, and purple indicates that a mixture of the two phases is seen in the diffraction data. Overlapping squares of various colors results from the hysteresis of the phase transition, revealed by reversing the transition multiple times. The phase boundary and hysteresis are summarized by the loop between 23 and 30 GPa, shown at the top of the figure. Data using a neon medium are represented by circles and summarized by the double-headed arrow from 30 to 32.3 GPa that indicates no observed hysteresis within our pressure intervals. Temperature uncertainties are indicated at each data point, whereas the typical pressure uncertainty is estimated to be 1.2 GPa.

of the ϵ -B2 transition in either pressure medium, despite controlling the temperature at 1200 ± 100 K for tens of seconds before increasing laser power: either the sample started transforming immediately upon heating to 1200 K, or it did not transform until pressure was increased. The ϵ -B2 transition was reversed multiple times in each pressure medium. Examples of the X-ray diffraction spectra that evidence the transition are shown in Figure 2.2.2. To constrain the hysteresis of the phase transition, we reversed the transition four times in a cell containing the neon pressure medium, and twice in a cell containing the argon medium. The reversals in neon showed no evidence of hysteresis once they were laser-heated, but rather bracket the

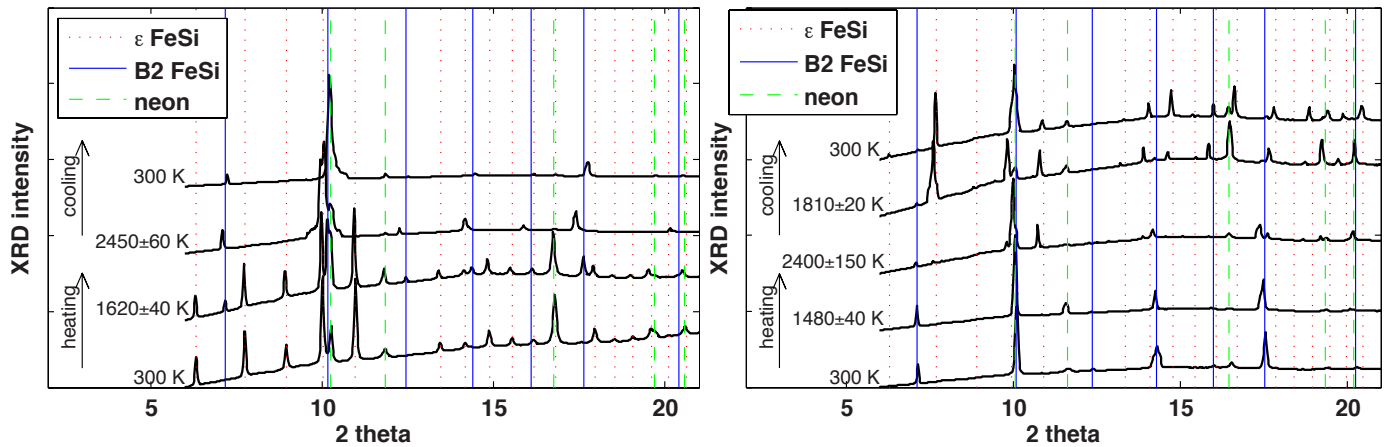


Figure 2.2.2: Diffraction pattern examples show a transition from the ϵ to the B2 phase of FeSi at 37 GPa (left) and the reverse transition, from B2 to ϵ at 30 GPa (right). Black curves show integrated powder diffraction data during the two heating/cooling cycles. Temperatures measured by spectroradiometry are shown to the left of diffraction patterns. Red dotted lines mark diffraction peak positions of FeSi lattice planes at 37 GPa or 30 GPa, while blue solid lines mark positions of B2-FeSi lattice planes and green dashed lines mark positions of neon lattice planes. Deviations of high-temperature diffraction peaks from theoretical peak positions are mostly due to thermal expansion of sample and pressure medium..

transition to between 30 and 32.3 GPa. The reversals in argon, on the other hand, show hysteresis—upon laser-heating, the B2 phase is created at 32 GPa, transformed into the phase at 23 GPa on decompression, and transformed back into the B2 phase at 30 GPa upon re-compression.

X-ray diffraction patterns of samples at room temperature provide data to constrain the P-V equation of state of both phases of FeSi and show that density increases by 5% during the phase transition at 30 GPa, which may have implications for the cores of Mercury ($P_{\text{core}} \sim 10$ to 40 GPa) and/or Mars ($P_{\text{core}} \sim 24$ to 40 GPa) if silicon is an abundant alloying element. Qualitatively, the miscibility of silicon in crystalline iron may increase at ~ 30 GPa due to the increase in the effective hard sphere radius of silicon in the FeSi lattice as its coordination changes from 7-fold (ϵ -phase) to 8-fold (in the B2 structure), thereby improving the similarity of the radii of silicon and iron. Specifically, the immiscibility gap documented between iron-rich and iron-poor iron-silicon alloys at < 50 mol% Si may be reduced at pressures above 30 GPa.

Acknowledgements

We thank Ravhi Kumar for the sample material, Laura Robin Benedetti for help designing the study, and Sergey Tkachev and Vitali Prakapenka for help loading the samples. We acknowledge the support of GeoSoilEnviroCARS, which is supported by the NSF- Earth Sciences (EAR-1128799), and the DOE, Geosciences (DE-FG02-94ER14466). Use of the Advanced Photon Source, an Office of Science User Facility operated for the U.S. DOE Office of Science by Argonne National Laboratory, was supported by the U.S. DOE under Contract No. DE-AC02-06CH11357. Support for Z. M. Geballe was provided in part by an NSF Graduate Fellowship.

References

de Pater, I. and Lissauer, J. J., *Planetary Sciences*, 2nd ed. (Cambridge University Press, New York), 2010.

Dobson, D. P., Vocadlo, L. and I. G. Wood, A new high-pressure phase of FeSi: *American Mineralogist*, v. 87, p. 784–787, 2002.

McCoy, T. J., Dickinson, T. L., and Lofgren, G. E., Partial melting of the Indarch (EH4) meteorite: A textural, chemical, and phase relations view of melting and melt migration: *Meteoritics and Planetary Science*, v. 746, p. 735–746, 1999.

Prakapenka, V. B., Kubo, A., Kuznetsov, A., Laskin, A., Shkurikhin, O., Dera, P., Rivers, M. L., and Sutton, S. R., Advanced flat top laser heating system for high pressure research at GSECARS: application to the melting behavior of germanium. *High Pressure Research*, v. 28, p. 225–235, 2008.

Sanloup, C., and Fei, Y., Closure of the Fe-S-Si liquid miscibility gap at high pressure: *Physics of the Earth and Planetary Interiors*, v. 147, p. 57–65, 2004.

3 Shear Wave Velocity Model of the Eastern North America Upper Mantle Using Full Waveform Tomography

Huaiyu Yuan, Scott French, Paul Cupillard and Barbara Romanowicz

Summary

The EarthScope Transportable Array (TA) deployment has provided dense array coverage across the continental US and with it, the opportunity for high resolution 3D seismic velocity imaging of both the lithosphere and asthenosphere in the continent. Building upon our previous work, we present a new 3D isotropic and radially anisotropic shear wave model of the North American (NA) lithospheric mantle, using full waveform tomography and shorter-period (40 s) waveform data. Our model exhibits pronounced spatial correlation between major tectonic localities of the eastern NA continent, as evidenced in the geology, and seismic anomalies. This suggests recurring episodes of tectonic events are not only well exposed at the surface, but also leave persistent scars in the continental lithosphere mantle, marked by isotropic and radially anisotropic velocity anomalies that reach as deep as 100-150 km. In eastern North America, our tomographic images distinguish the fast velocity cratonic NA from the deep rooted large volume high velocity blocks which are east of the continent rift margin, and extend 200-300 km offshore into the Atlantic Ocean. In between is a prominent narrow band of low velocities that roughly follows the south and eastern Laurentia rift margin and extends into New England. The lithosphere associated with this low velocity band is thinned likely due to combined effects of repeated rifting processes along the rift margin and northward extension of the Bermuda low-velocity channel across the New England region. Deep rooted high velocity blocks east of the Laurentia margin are proposed to represent the Proterozoic Gondwanian terranes of pan-African affinity, which were captured during the Rodina formation but left behind during the opening of the Atlantic Ocean.

Full waveform inversion

We present a new high-resolution 3D tomographic model of shear velocity in the cratonic North American mantle (Figure 2.3.1), developed using long-period full waveform inversion. The new inversion shares many of the methodological features of our previous continental scale time-domain 3D waveform tomographic inversions for isotropic and radially anisotropic structure (Yuan *et al.*, 2011). We largely mirror the processing performed in the global SEM (spectral element method)-based hybrid modeling approach (Lekic and Romanowicz, 2011), except the global SEM synthetic code is replaced by RegSEM (Cupillard *et al.*, 2012).

Tomographic Results

The cratonic root has been affected by the recurring episodes of tectonism, however its eastern margin seems largely intact

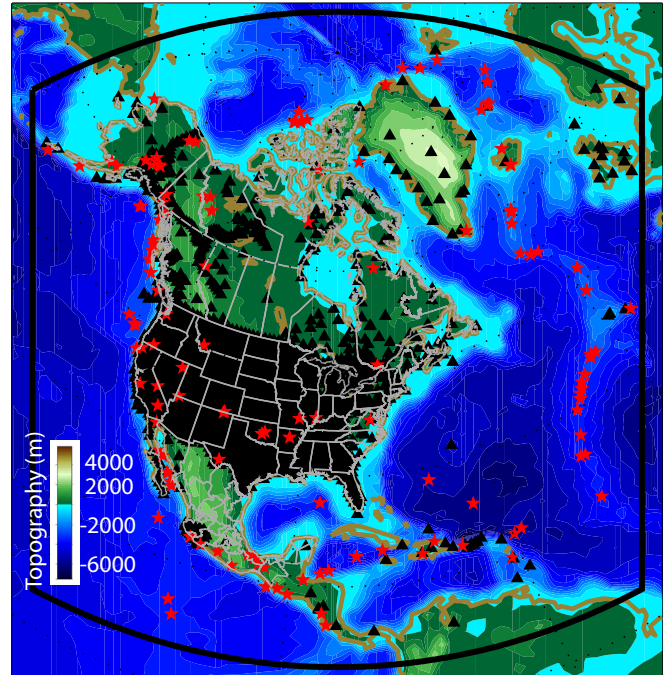


Figure 2.3.1: Source and station distribution for the new North American inversion. The black triangles show the seismic stations and the red stars show 136 local events in addition to our global and NA regional/teleseismic dataset. The thick black line indicates the model boundaries used for RegSEM forward modeling. The background shows the topography

west of the Grenville deformation front. The Archean lithosphere may have extended further outboard of the Proterozoic Grenville deformation front, as indicated by a high velocity Archean-like structure that extruded beyond the deformation front. Across the continental margin, thinning of the lithosphere is evident in our new tomographic images as well as discontinuity-sensitive receiver functions (Rychert *et al.*, 2007) and local Rayleigh wave dispersion inversion (Li *et al.*, 2003). A thinning process is likely further facilitated in New England by the passage of the Bermuda low velocity channel, which connects to the Bermuda hotspot in the Atlantic Ocean, and extends farther east in to the Atlantic Ocean.

Our new tomographic image reveals deeply rooted Gondwanian blocks that were captured during the North American/African collision that closed the Iapetus Ocean, but stayed behind when the present Atlantic Ocean was formed (*e.g.*, Nance and Murphy, 1994). These exotic terranes are clearly separated from the Laurentia core along the east continent margin, and extend greatly outboard into the Atlantic Ocean, reaching out to the oldest Atlantic oceanic crust. The presence of large segments of fossil continents off cratonic margins is thus not uncommon,

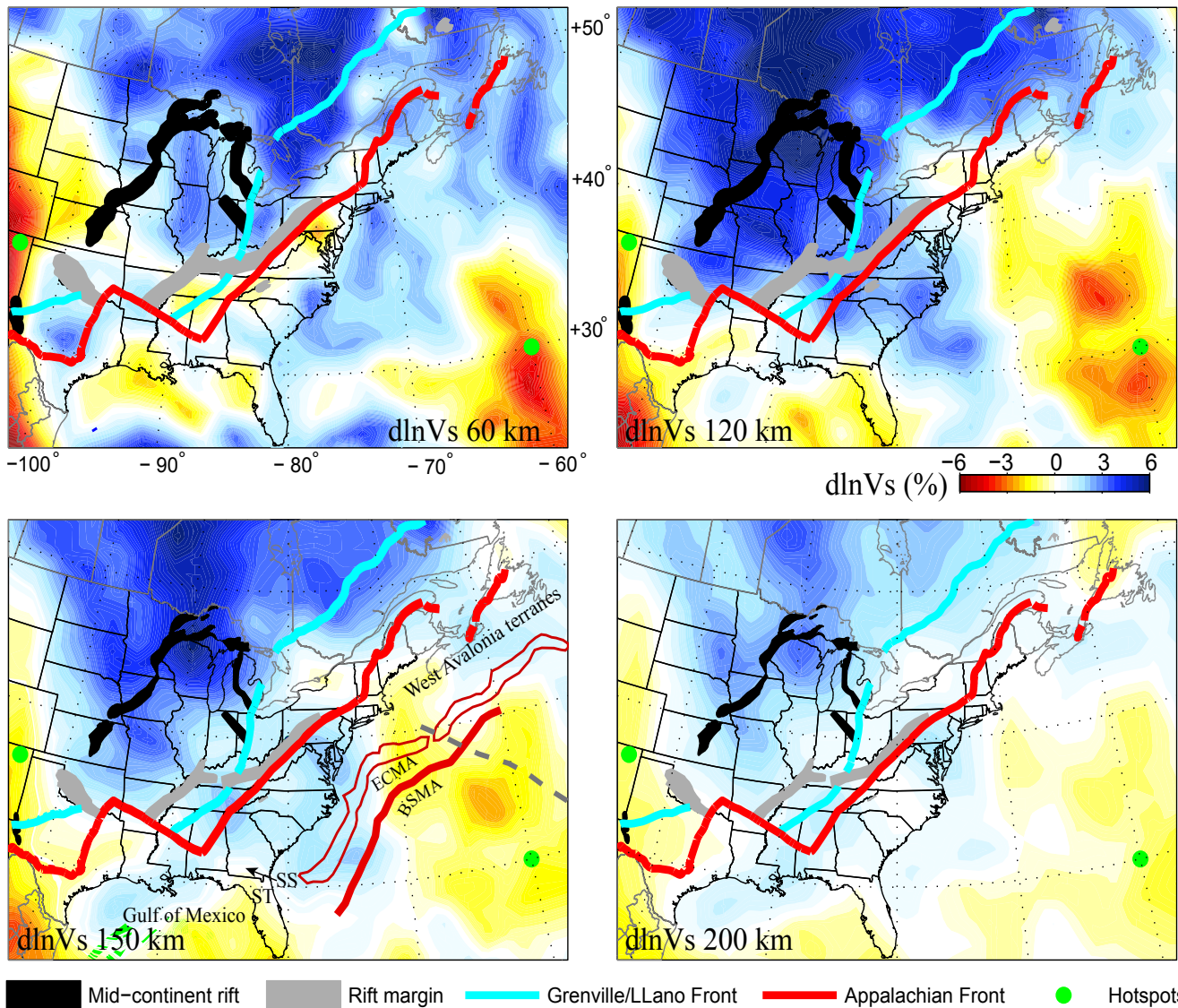


Figure 2.3.2: 3D isotropic Vs and radial anisotropy structure in eastern North America. The depth of each map is indicated. The Grenville/Llano deformation front is coded in cyan and continental rift margin in red. Green dots are hotspot locations; the Bermuda hotspot is near the lower right corner. The top four subpanels are for isotropic Vs; the bottom two are for radial anisotropy, ξ . Note the eastern edge of the high velocity craton closely follows the eastern continental rift margin (red line).

and may suggest greater roles in the global crustal-growth models (e.g., Griffin *et al.*, 2011).

References

- Griffin, W.L., Begg, G.C., Dunn, D., O'Reilly, S.Y., Natapov, L.M., Karlstrom, K., Archean lithospheric mantle beneath Arkansas: Continental growth by microcontinent accretion, *Geological Society of America Bulletin* 123, 1763-1775, 2011.
- Li, A., Forsyth, D.W., Fischer, K.M., Shear velocity structure and azimuthal anisotropy beneath eastern North America from Rayleigh wave inversion, *J. Geophys. Res.* 108, 24 PP, 2003.
- Nance, R.D., Murphy, J.B., Contrasting basement isotopic signatures and the palinspastic restoration of peripheral orogens: Example from the Neoproterozoic Avalonian-Cadomian belt, *Geology*, 22, 617-620, 1994.
- Rychert, C.A., Rondenay, S., Fischer, K.M., P-to-S and S-to-P imaging of a sharp lithosphere-asthenosphere boundary beneath eastern North America, *J. Geophys. Res.* 112, B08314, 2007.

- Yuan, H., Romanowicz, B., Fischer, K.M., Abt, D., 3-D shear wave radially and azimuthally anisotropic velocity model of the North American upper mantle, *Geophys. J. Int.* 184, 1237-1260, 2011.

4 Slab fragments in the western U.S.

Robert Porritt and Richard Allen

Introduction

The USArray deployment has provided new details of the seismic wave-speed structure of the western United States. The western U.S. is generally characterized as a low wave-speed region in global models (e.g. *Lekic and Romanowicz, 2011*) with relatively thin (~ 70 km) lithosphere (e.g. *Levander and Miller, 2012*). This relatively unusual geologic context is ideally suited for asthenospheric mantle imaging with teleseismic travel times as the background 1D model is simple and only a small proportion of the travel time delays can be accounted for by the lithosphere. Within this low velocity region, there exist several isolated high velocity bodies, which have been interpreted as either lithospheric delaminations (e.g. *Zandt et al., 2004; West et al., 2009; Frassetto et al., 2011; Darold and Humphreys, 2013*), or slab fragments (e.g. *Obrebski et al., 2010; Schmandt and Humphreys, 2011; Pikser et al., 2012; Wang et al., 2013*). In this contribution we explore the argument between delaminations or slab fragments as seen by our compressional wave-speed model, DNA13-P.

Imaging

We employ the multi-channel cross correlation method (*VanDecar and Crosson, 1990*) to measure relative P wave arrival times for 76,322 station and event pairs within the 0.4-0.8 Hz band during the USArray deployment. The station coverage extends across the entire United States and events are chosen to be between 30 and 80 degrees epicentral distance from the station providing ample path coverage to fully image the western portion while avoiding waveform complications. The sensitivity matrix of the delays is populated using finite frequency kernels (*Dahlen et al., 2000; Hung et al., 2000*) and then solved for compressional wave-speed variations with a least squares iterative solver (*Dahlen et al., 2000; Hung et al., 2000*). We also solve for station corrections representing the vertically averaged lithosphere structure under a given station where crossing ray coverage is poor. The full model is available for download at the IRIS Earth Model Collaboration website (<http://www.iris.edu/dms/products/emc/>).

Discussion

Figure 2.4.1 provides a broad view of the wave-speed structure of the U.S. The eastward dipping plane illustrates three main features: (1) the high velocity anomalies in the western U.S. are short lateral wavelength features, (2) the high velocity body in the eastern U.S. is continuous, and (3) the Isabella Anomaly is the only shallow high velocity anomaly south of the Gorda plate. Based on paleoseismic evidence, the Juan de Fuca-Gorda system is well characterized as a subduction zone, but the limited depth extent of the high wave-speed body is inconsistent with ongoing subduction for the past 150+ Ma.

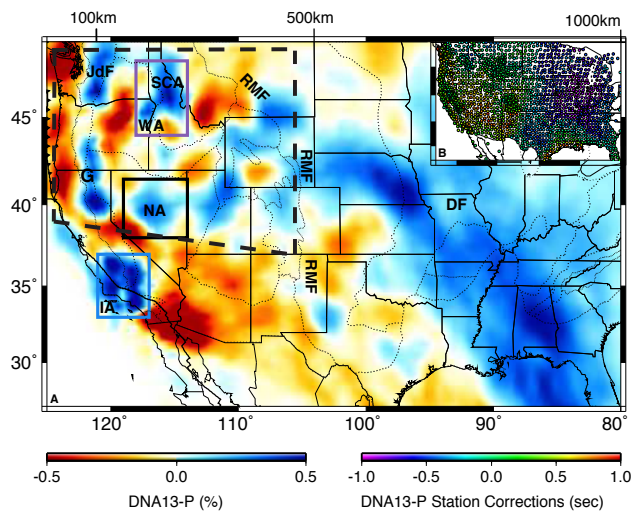


Figure 2.4.1: (A) An east-dipping plane through DNA13-P. Color scale gives relative compressional wave-speed (left color-bar). Purple, black, and blue boxes respectively outline the Siletzia Curtain Anomaly and Wallowa Anomaly, Nevada Anomaly, and Isabella Anomaly. The scale across the top edge of the map displays the depth of the tomography slice. Dotted lines mark the US physiographic boundaries (*Fenneman and Johnson, 1946*). Bold dashed outline displays the area considered in the calculation of expected western U.S. slab. (B) Inset map displays the station data used in the inversion and are color-coded according to station correction terms of DNA13-P (right color-bar). Abbreviations are given for the Juan de Fuca plate (JdF), Gorda plate (G), Isabella Anomaly (IA), Siletzia Curtain Anomaly (SCA), Wallowa Anomaly (WA), Nevada Anomaly (NA), Rocky Mountain Front (RMF), and Deep Farallon (DF).

However, the uplift of the modern Rocky Mountains and the distributed mantle high velocity anomalies suggest the slab was flat for a significant period of the subduction history. When we compare the expected amount of slab material from the coast to the Rocky Mountain Front (Figure 2.4.1, dashed box) against the observed amount of slab material, we find that $\sim 80\%$ of the expected material is observed as high velocity anomalies. If these anomalies are actually lower continental lithosphere in origin, it becomes unclear where the Farallon plate is currently.

Continental plate delamination has also been proposed due to observations of anomalous shear wave splitting (*West et al., 2009*), topography (*Saleeby and Foster, 2004*), and receiver function imaging (*Zandt et al., 2004*). However the regional anisotropy pattern identified in *West et al. (2009)* as due to vertical flow can also be readily reproduced by flow around the Gorda slab edge and the North American craton (*Yuan and Romanowicz, 2010*). Additionally, the topographic expression and receiver function images for the Isabella Anomaly are identical to those found in the Cascadia Subduction Zone (*Bostock et al., 2002*). Therefore, the primary pieces of evidence for delamination do not provide a unique fingerprint of the process.



Figure 2.4.2: Schematic representation of high velocity anomalies of the western U.S. The Monterey Microplate labeled here is also referenced as the Isabella Anomaly. All of the labeled blue bodies are interpreted here to be ocean lithosphere.

Conclusion

Ambiguous evidence prevents determining if high wave-speed anomalies in the upper mantle are drips or remnant slabs when considered as individual geologic objects. When the western U.S. is considered as a whole, the theory that continental lithosphere drips are the source for all of these anomalies becomes unreasonable. Conversely, an oceanic lithosphere origin, such as the western Farallon slab, provides a viable source of high wave-speed material. Indeed, if the observed high-wave-speed anomalies are not interpreted as remnant slabs, we must identify where the Farallon slab went. Relatively young oceanic lithosphere has less rheological contrast to typical asthenosphere and is more readily able to founder in the upper mantle, rather than sink into the lower mantle (Pikser *et al.*, 2012). With time, the eastward progression of the Farallon ridge toward North America provided younger and younger oceanic lithosphere into the subduction zone (Atwater and Stock, 1998). While the evidence does not show conclusively that these features must all be slabs, the slab hypothesis is consistent with the observations and follows naturally from the 150+ Ma subduction history. Therefore, analysis of high velocity anomalies in the western U.S., and elsewhere, must start with the hypothesis of an oceanic lithosphere origin before a delamination hypothesis should be invoked.

Acknowledgements

We would like to thank the UC-Berkeley regional imaging group (Cheng Cheng, Qingkai Kong, and William Hawley) for discussion of this work. We would also like to thank Jenny Taing for assistance in measuring arrival times. We thank IRIS and Earthscope for the USArray dataset. This work was funded by National Science Foundation grants EAR-0643077 and EAR-0745934.

References

- Atwater, T., and Stock, J.M., Pacific-North America plate tectonics of the Neogene southwestern United States – an update, *Int. Geol. Rev.*, v. 40, p. 375-402, 1998
- Bostock, M.G., Hyndman, R.D., Rondenay, S.J., and Peacock S.M., An inverted continental Moho and the serpentinization of the forearc mantle, *Nature.*, v. 417, p. 536-538, 2002
- Dahlen, F. A., Hung, S.-H. and Nolet, G., Fréchet kernels for finite-frequency traveltimes—I. Theory, *Geophysical Journal International*, 141: 157–174. doi: 10.1046/j.1365-246X.2000.00070.x, 2000.
- Darold, A., and Humphreys, E., Upper mantle seismic structure beneath the Pacific Northwest: A plume-triggered delamination origin for the Columbia River flood basalt eruptions: *Earth Planet. Sci. Lett.*, v. 365, p. 232-242, 2013.
- Fenneman, N.M., and Johnson, D. W., Physiographic divisions of the conterminous U. S.: *USGS Water Resources*, 1946
- Frassetto, A.M., Zandt, G., Gilbert, H., Owens, T.J., and Jones, C.H., Structure of the Sierra Nevada from receiver functions and implications for lithospheric foundering: *Geosphere*, v. 7, no. 4, p. 898-921, 2011.
- Hung, S.-H., Dahlen, F.A. and Nolet, G., Fréchet kernels for finite-frequency traveltimes—II. Examples, *Geophysical Journal International*, 141: 175–203. doi: 10.1046/j.1365-246X.2000.00072.x, 2000.
- Lekic, V. and B. Romanowicz, Inferring upper-mantle structure by full waveform tomography with the spectral element method, *Geophys. J. Int.* 185(2), 799-831, 2011.
- Levander, A., and Miller, M.S., Evolutionary aspects of lithosphere discontinuity structure in the western U.S., *Geochem., Geophys., and Geosys.*, v. 13, Q0AK07, doi:10.1029/2012GC004056, 2012.
- Obrebski, M., Allen, R.M., Xue, M., and Hung, S-H., Slab-plume interaction beneath the Pacific Northwest: *Geophys. Res. Lett.*, v. 37, L14305, doi:10.1029/2010GL043489, 2010.
- Pikser, J.E., Forsyth, D.W., and Hirth, G., Along-strike translation of a fossil slab: *Earth Planet. Sci. Lett.*, v. 331–332, p. 315-321, 2012.
- Saleeby, J. and Foster, Z., Topographic response to mantle lithosphere removal in the southern Sierra Nevada region, *California Geology*, V. 32; no. 3; p. 245-248; doi: 10.1130/G19958.1, 2004.
- Schmandt, B., and Humphreys, E., Seismically imaged relict slab from the 55 Ma Siletzia accretion to northwest United States, *Geology*, v. 39, no. 2, p. 175–178, 2011.
- Wang, Y., Forsyth, D.W., Rau, C.J., Carriero, N., Schmandt, B., Gaherty, J., and Savage, B., Fossil Slabs Attached to Unsubducted Fragments of the Farallon Plate, *Proc. Natl. Acad. Sci. U.S.A.*, v. 110, no. 14, p. 5342-5346, 2013.
- West, J.D., Fouch, M.J., Roth, J.B., and Elkins-Tanton, L.T., Vertical mantle flow associated with a lithospheric drip beneath the Great Basin, *Nature Geosci.*, v. 2, p. 439–444, 2009.
- Yuan, H. and Romanowicz, B., Depth dependent azimuthal anisotropy in the western US upper mantle, *Earth Planet Sci. Lett.*, v. 300, p. 385-394, 2010.
- Zandt, G., Gilbert, H., Owens, T.J., Ducea, M., Saleeby, J., and Jones, C.H., Active foundering of a continental arc root beneath the southern Sierra Nevada in California, *Nature*, v. 431, p. 41–46, 2004.

5 Mantle Flow Geometry Through the Segmented Juan de Fuca Plate

Robert Martin-Short, Richard M Allen

Introduction

The Juan de Fuca slab is a remnant of the ancient Farallon plate, which has been subducting beneath the North American continent over the past 150 million years (Eakin *et al.*, 2010). Complete subduction of parts of this giant plate has split it into several sections. The northern unit is bounded to the south by the Mendocino Triple Junction (MTJ) and to the north by the Queen Charlotte Triple Junction off Vancouver Island (Porritt, 2013). This unit is divided into the Gorda, Juan de Fuca and Explorer slabs, which descend along the Cascadia subduction zone.

This subduction zone features some unusual characteristics, the most notable of which include a lack of earthquake activity below a depth of 100km (Porritt, 2013), a lack of slab material below 400km and the possibility of segmentation. Various models of slab-mantle interaction have been proposed to explain such observations, but more data is required to constrain these ideas.

This article presents the shear wave splitting measurements determined at 27 onshore seismometers situated along the subduction zone and 43 offshore instruments deployed across the Juan de Fuca plate. These measurements are used to infer the direction and extent of athenospheric anisotropy and thus to determine mantle flow geometry in the region. This study assumes the existence of a type-A olivine crystal fabric, meaning that the anisotropy should be parallel to flow.

Method

This study analyzed waveform data from 27 onshore Transportable Array (TA) instruments and 57 ocean bottom seismometers deployed as part of the Cascadia Initiative between 2010 and 2012. Shear wave splitting observations were obtained for all of the TA instruments and 43 of the OBS devices.

Measurements of fast axis (φ) and delay time (δt) were carried out using the *Splitlab* software package (Wustefeld *et al.*, 2008). Teleseismic events of magnitudes greater than 5.75 and with epicentral distances of 85-130° were utilized, and each event was bandpass filtered between 0.02 and 0.3Hz.

The observations were rated 'good', 'fair' or 'poor' according to the criteria of Wustefeld and Bokelmann (2007). Average values of φ and δt for each instrument were then determined by stacking the error matrices resulting from a grid-search for the best parameter values from each observation followed by a determination of the global minimum.

In order to obtain useful results from the OBS data the orientations at which these devices settled on the seabed were calculated (Frassetto *et al.*, 2013). The splitting fast axis orientations were then determined relative to each station using the un-rotated seismograms and then rotated by the angle provided by Frassetto *et al.* (2013).

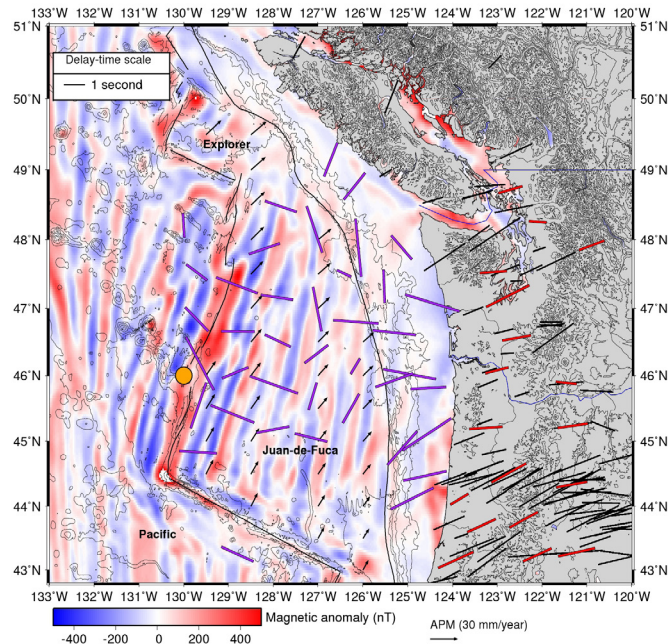


Figure 2.5.1. Map of the study region showing the oceanic crust magnetic anomaly pattern (Maus *et al.*, 2009) in addition to all available splitting results for the area. The onshore red splits are clearly trench-perpendicular, while the offshore results are sub-perpendicular to the magnetic striping pattern within about 2° of the ridge axis, but then appear to be affected by the presence of the subduction zone. There is also some indication of a superposition of ridge perpendicular and radial splitting close to Cobb Hotspot, whose rough position is shown by the orange mark.

Results

Figure 2.5.1 shows the stacked results from this study plotted alongside measurements provided by previous investigations. The TA stations have a mean fast direction of N57.4°E and a mean splitting time of 1.39 seconds. The pattern produced by the offshore splitting measurements is more complicated. Splitting times are generally higher than for the TA stations, with a mean delay time of 1.81 seconds and a standard deviation of 0.52 seconds. Stations within 100km of the ridge generally produce fast axes that are perpendicular to this structure. The splitting patterns seen at offshore stations closer to the trench and accretionary prism are not uniformly trench perpendicular (as they are onshore). Instead, the splitting fast axes are rotated roughly trench parallel between 47°N and 49°N but rapidly switch back to trench-perpendicular below 47°N. The offshore splitting pattern west of Oregon is consistent with the onshore observations, while farther north in Washington the trench-perpendicular onshore splits are juxtaposed against the trench-parallel offshore splits. Onshore and offshore splits once again become consistent north of the Canadian border.

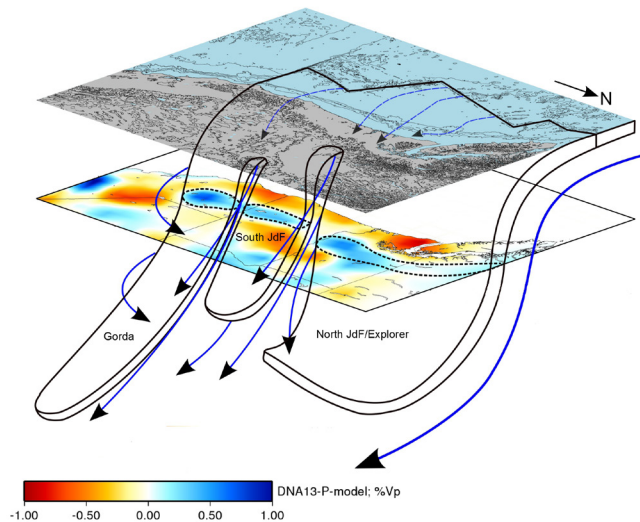


Figure 2.5.2: Cartoon summarising this study's interpretations in terms of mantle flow beneath and around the subducting Gorda, Juan de Fuca and Explorer plates. The tomography shows a depth slice through the DNA13-P wave model at 200km. The slab is segmented into at least three sections, with a third possible gap separating the Northern Juan de Fuca and Explorer sections. The tomography indicates that the slab beneath Oregon is particularly short, while the Gorda segment extends to at least 600km (Porrirt *et al.*, 2013). Splitting results from this study indicate that eastwards flow west of the trench is initially ridge-parallel, but is then channelled through the Oregon slab gap. To the south, the cartoon shows toroidal flow around the edge of the Gorda slab as described by Eakin *et al.*, (2010). The slab poses an insufficient barrier to mantle flow to prevent eastwards motion beneath its base, as shown.

Discussion and interpretations

The lack of variation in the splitting parameters with event backazimuth and the uniformity of the onshore pattern suggests the presence of a single layer of anisotropy. The main source of the signal is interpreted to be the upper mantle, which is the only source thick enough to produce delay times of over 1 second. Figures 2.5.1 and 2.5.2 suggest that flow is ridge-perpendicular east of 128°W, as is consistent with the outwards movement of asthenospheric material.

The splitting pattern beyond 150km of the ridge is interpreted as being a result of asthenosphere flow responding to the presence of the subducting slab. With the exception of the trench-parallel results, splits west of the margin are seen to reduce in delay time towards the trench and rotate sub-parallel to the direction of plate motion. The reduction in delay times is interpreted as a result of the increasing misalignment of asthenospheric and lithospheric anisotropy, as predicted by Nishimura and Forsyth (1989).

The offshore measurements provide an indication of funnelled asthenospheric flow into the gap within the elongate high velocity anomaly shown in Figure 2.5.2. This anomaly is interpreted to be the result of the subducting slab (Porrirt, 2013), implying that the relatively lower velocities beneath northern Oregon indicate a 'slab gap'. This may be a tear in the subduct-

ing lithosphere which allows for unimpeded eastwards flow of material.

The general pattern of trench perpendicular splitting seen in this study lends further support to the well established interpretation of a thick layer of mantle material entrained beneath the subducting slab. The slab appears provide an insufficient barrier to mantle flow to cause the trench parallel splitting pattern seen at other subduction zones (Eakin *et al.*, 2010).

Acknowledgements

This study benefited from discussions with Brent Evers, Caroline Eakin, Robert Porrirt and Cheng Cheng. The figures were created using the Generic Mapping Tools.

References

- Eakin, CM, Obrebski, M, Allen, RM, Boyarko, DC, Brudzinski, MR and Porrirt, R, 'Seismic anisotropy beneath Cascadia and the Mendocino triple junction: Interaction of the subducting slab with mantle flow', *Earth and Planetary Science Letters*, vol 297, pp. 627-632, 2010.
- Frassetto, A, Adinolfi, A and Woodward, B, 'Cascadia Amphibious Ocean Bottom Seismograph Horizontal Component Orientations', Seismic experiment report, OBSIP Management Office, Incorporated Research Institutions for Seismology (IRIS), 2013.
- Maus, S, Barckhausen, U, Berkenbosch, H, Bournas, N, Brozena, J, Childers, V, Dostaler, F, Fairhead, J, Finn, C, von Frese, R and others, 'EMAG2: A 2--arc min resolution Earth Magnetic Anomaly Grid compiled from satellite, airborne, and marine magnetic measurements', *Geochemistry, Geophysics, Geosystems*, vol 10, 2009.
- Nishimura, CE and Forsyth, DW, 'The anisotropic structure of the upper mantle in the Pacific', *Geophysical Journal International*, vol 96, pp. 203-229, 1989.
- Porrirt, RW, 'Tracing the Farallon plate through seismic imaging with USArray', PhD Thesis, University of California Berkeley, 2013.
- Wustefeld, A, Bokelmann, G, Zaroli, C and Barruol, G, 'SplitLab: A shear-wave splitting environment in Matlab', *Computers & Geosciences*, vol 34, pp. 515-528, 2008.
- Wustefeld, A and Bokelmann, G, 'Null detection in shear-wave splitting measurements', *Bulletin of the Seismological Society of America*, vol 97, pp. 1204-1211, 2007.

6 Seismic Constraints on a Double-Layered Asymmetric Whole-Mantle Plume Beneath Hawaii

Cheng Cheng, Richard M Allen, Rob W Porritt and Maxim Ballmer

Introduction

The Hawaii hotspot and the associated chain of islands have been long regarded as a case example of a deep-rooted mantle plume and a region thought to be an ideal place for studying intraplate hotspots located above a deep-rooted mantle plume. There is an ongoing debate, however, about the origin of the hotspot volcanism reservoir, in particular when examining the depth and direction from which any plume originates. Geochemistry observations of the region indicate the Hawaiian Plume contains 15-20% mafic lithologies such as eclogites, and they also show there is a conspicuous asymmetry in the mafic composition of different parts of the island. Based on volcano lava measurements, the island is divided into two parts: LOA and KEA, and there is more pyroxenite in the source of the LOA-volcanoes. In this work we address the question: is Pacific Plate rejuvenation occurring under the islands, and if it is, how wide and how deep is the region where the plume modifies the lithosphere? To answer these questions, we need to use geophysical, geochemical and seismological information.

Data and Method

The Hawaiian Plume-Lithosphere Undersea Melt Experiment (PLUME) included a large network of four-component broadband ocean bottom seismometers (OBSs) occupying more than 70 sites and having an overall aperture of more than 1000 kilometers. We selected ~750 S-wave relative arrival times (including direct S and SKS phases) on the SV component via multi-channel cross correlation. Of these, we selected 75 events distributed in as wide a range of back azimuth directions as possible (Figure 2.6.1), restricting the data to events with epicentral distances greater than 30 degrees and magnitudes greater than 5.5. The relative delays we obtain are inverted with a tomographic technique that uses finite-frequency sensitivity kernels that account for the frequency dependent width of the region to which body waves are sensitive and also accounts for wave front healing effects. Our tomographic method uses paraxial kernel theory to calculate the Born approximation forward-scattering sensitivity kernels for teleseismic arrival times. The surface-wave data we use here comes from two different sources. The first is ambient noise cross-correlation measurements in the period band of 10 to 25 sec. The second source is surface wave phase velocity measurements obtained using a two-plane wave tomography method in the period band of 25 to 100 sec. Following *Obrebski et al. (2011)* we create a joint matrix of body wave relative travel time anomalies and surface wave phase velocity anomalies to use in a joint inversion.

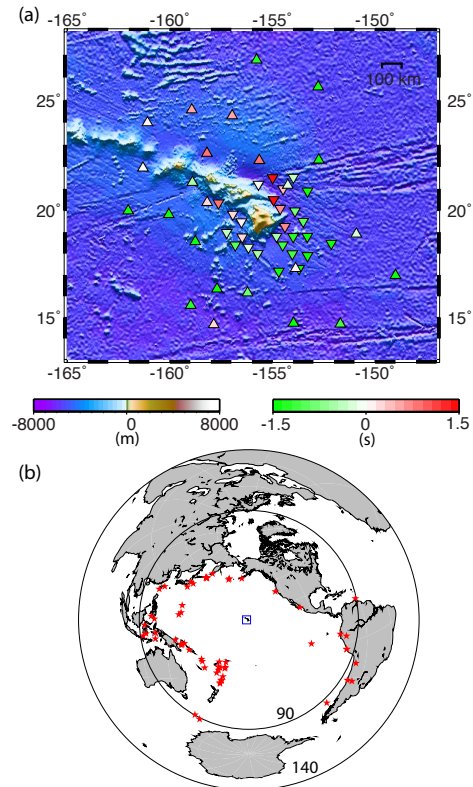


Figure 2.6.1. Map of the study area. (a) Study area showing seismometer locations (triangles) where stations deployed in the first year are indicated by inverted triangles and those deployed in the second year are marked by triangles. The station colors indicate the mean body-wave delays (measured at 0.04–0.1 Hz). Only stations that successfully recorded data are shown. These locations are juxtaposed on the topography and bathymetry of the region. (b) Map of earthquakes (red stars) used in this study and our study location (blue box). Black circles are 90° and 140° from the study region.

Imaging Results

We create two models, named as follows: HW13-SV based on inversion of SV body wave constraints only, and HW13-SVJ resulting from joint inversion of the body- and surface-waves. Figure 2.6.2 shows vertical cross-sections through the main features of the models, comparing HW13-SV and HW13-SVJ structures. The improvement our new model provides is a higher resolution within the upper mantle that results from our inclusion of surface wave data in the inversion. In addition to the shallow low-velocity layer observed immediately below the oceanic lithosphere, we also observe a second layer at the depth of about ~250–400 km (see cross-section in Figure 2.6.2b)

In the vertical cross-section perpendicular to the plate motion, the model shows an apparent asymmetry in the low velocity structure of this second layer. Larger volumes of low velocity

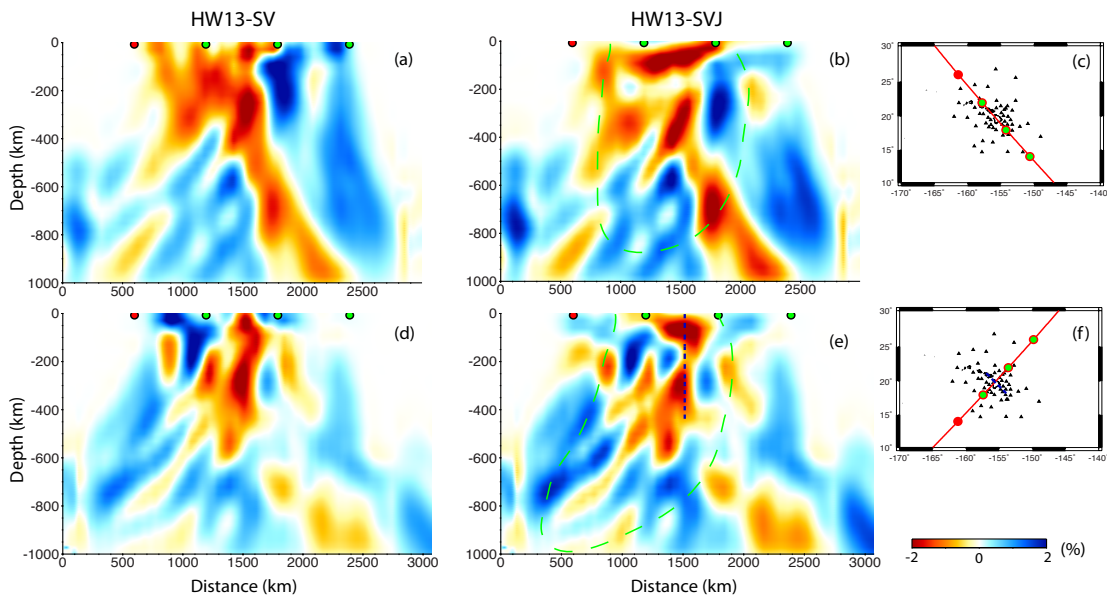


Figure 2.6.2: Vertical cross-sections through the HW13 models. Images (a-b) are cross-sections parallel to the Pacific plate motion, whereas images (d-e) are cross-sections perpendicular to the plate motion. (c, f) maps indicate the locations of the cross-sections and the distribution of stations. Results (a) and (d) are from the body-wave-only inversion (HW13-SV), (b) and (e) are from the joint ambient noise, surface wave and body wave inversion (HW13-SVJ). The dashed green contours on (b) and (e) encompass areas with good ray coverage. The dash blue line on (e) and (f) indicates the separation of the Loa (left) and Kea(right) volcano trends.

material are observed on the northwest side of the island chain (Figure 2.6.2e). Finally, good resolution is obtained through the crust and lithosphere by the joint ambient noise and earthquake surface wave data. We conduct checkerboard resolution tests using boxes with alternating high and low-velocity and of different sizes to identify what resolution our models can provide. The inclusion of the surface-wave dataset provides improved resolution in the upper ~ 200 km. The tests results show that the horizontal resolution is about 150 km in the upper 100 km, about 300km in the upper mantle and transition zone, and 500km in the lower mantle. The resulting structure also correlates well with previous surface-wave only tomographic models (Laske *et al.*, 2011).

Discussion

Though seismic imaging in the past has been considered inconclusive with regard to whether a lower-mantle plume source exists, our imaging results are similar to Wolfe *et al.* (2009)'s result in the lower mantle. Both results reveal low velocities within the mantle transition zone and in the topmost lower mantle, suggesting there is a deep source region for the Hawaiian plume.

Differing from the classic plume model, which has a vertical conduit feeding a thin pancake structure beneath the lithosphere, our model shows two layers of low velocity in the upper mantle. One layer is at <150 km depth, and the second is in the ~ 200 to 400 km depth range, thus forming a non-traditional double layered plume. Our model structure is consistent with a geodynamic model in which a plume composed of peridotite (85%) and chemically dense eclogite (15%) generates a neutrally buoyant layer at a depth of 260 to 410 km from which a fractionated upwelling rises further to feed a shallow pancake

(Ballmer *et al.*, 2013). When peridotitic material from the lower mantle crosses the 410-km discontinuity, its density decreases. However, the density of eclogite does not. The combination of the negative chemical buoyancy when eclogite is present with the positive thermal buoyancy will control the ascent motion of a plume rich in eclogite. This dense material tends to accumulate at the 410km depth, forming a deep eclogitic pool (DEP), which would produce a velocity structure consistent with the second low velocity layer in our tomographic model. Another important feature of our model is the asymmetric low velocity zone that trends perpendicular to the plate motion direction in the DEP depth range (Figure 2.6.2e). The low velocity structure beneath the southwest side of the island chain (left side of the dashed blue line in Figure 2.6.2e) is larger and wider than the structure on the northeast side (right side of the dashed blue line in Figure 2.6.2e). The lateral velocity variations observed, if indicative of lateral temperature variations, may reconcile geochemical evidence in Hawaii that imply a larger influence from pyroxenite-derived lavas along the southwest Loa trend compared to the northeast Kea trend.

References

- Obrebski, M., R.M. Allen, F. Pollitz, and S.-H. Hung, Lithosphere-asthenosphere interaction beneath the western United States from the joint inversion of body-wave traveltimes and surface-wave phase velocities, *Geophys. J. Int.* 185, 1003-1021, doi:10.1111/j.1365-246X.2011.04990.x, 2011.
- Ballmer, M., Ito, G., Wolfe, C., Solomon, S., Double-layering of a thermochemical Hawaiian plume in the upper mantle. Submitted.

7 New Oceanic Mantle Structures Revealed by Global Full-Waveform Inversion

Scott French, Vedran Lekic, Barbara Romanowicz

Introduction

The SEMum2 model (French *et al.*, in review) was derived using full long-period (60-400s) waveform inversion based on the spectral element method (SEM; e.g. Komatitsch and Vilotte, 1998). Much like its predecessor SEMum (Lekic and Romanowicz, 2011a), SEMum2 exhibits stronger lateral heterogeneity – particularly low velocities in the upper 250km – than previous generations of global models based purely on asymptotic theories (Lekic and Romanowicz, 2011b), while still confirming the robust long-wavelength structure present in the latter models. In addition to recovering more realistic amplitudes of heterogeneity, the oceanic upper mantle and transition zone in SEMum2 show a more continuous fast signature of subducted slabs with depth, as well as coherent conduit-like low-velocity anomalies extending to the lower mantle, most prominent beneath the South Pacific superswell and Hawaii. Further, SEMum2 exhibits a pattern of low-velocity anomalies in the oceanic upper mantle not clearly imaged in previous generations of global models: finger-like low-velocity bands aligned with absolute plate motion (Kreemer, 2009) between 200 and 350km depth. Here, we first briefly introduce SEMum2, focusing on model construction, and devote the remaining sections to discussion of these low-velocity finger (LVF) structures.

SEMum2: Model construction

SEMum2 represents an update to the SEMum model of Lekic and Romanowicz (2011a), incorporating a new crustal implementation and a change in parameterization that allows for higher resolution images of mantle structure. Both models employ a “hybrid” waveform inversion technique, where wavefield forward modeling is performed “exactly” using the SEM and combined with sensitivity kernels from non-linear asymptotic coupling theory (Li and Romanowicz, 1995). Though approximate, NACT kernels are computationally light and easily recalculated as the mantle model evolves, and further accommodate finite-frequency effects in the great-circle plane as well as multiple forward scattering. Each iteration of the hybrid approach represents a 3x reduction in cost over adjoint techniques (e.g. Tromp *et al.*, 2005), while also allowing for a quickly converging Newton-like inversion scheme, reducing the total number of iterations required.

To further reduce cost, we use a smooth crustal model with a minimum Moho depth of 30km, otherwise approximately honoring Crust2.0 Moho topography (Bassin *et al.*, 2000). The model is calibrated to match the seismic response of Earth’s crust, as seen through surface-wave dispersion, by introducing radial anisotropy – necessary to match the response of a realistically-layered model at long periods (Backus, 1962). By prolonging the SEM time step, the smooth crust reduces the cost of simulation an additional 3x over direct use of Crust2.0. While

SEMum also employed a smooth crustal model, its uniform 60km thickness could potentially complicate interpretation of oceanic upper-most mantle structure – thus motivating the now shallower, variable Moho topography. Details of the calibration procedure have also been improved (French *et al.*, in review).

Following the introduction of the new crustal model, we performed two additional inversion iterations starting from SEMum. Next, we refined the V_s mantle-model mesh from 4° to 2° node spacing and performed one further iteration. This change in parameterization allowed for a relaxation of a priori smoothness constraints on model structure, which was further justified by resolution analysis (French *et al.*, in review). While SEMum2 model structure appears sharper than SEMum at all depths and has evolved somewhat above 60km, the two models remain strikingly similar, validating a posteriori the approach taken in developing SEMum.

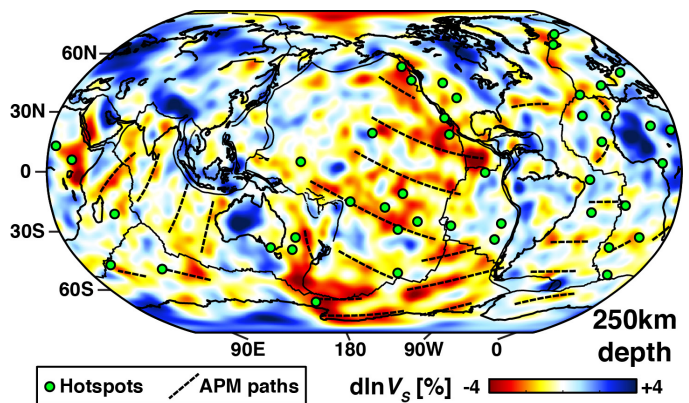


Figure 2.7.1: V_s anomaly structure at 250km depth in SEMum2, where low-velocity finger structures are immediately apparent. Dashed lines correspond to APM streamlines of Kreemer (2009).

Oceanic low-velocity structure

Clustering analysis (e.g. Lekic and Romanowicz, 2011b) of SEMum2 oceanic upper-mantle structure between 30 and 350km depth reveals a class of features characterized by lower-than-average V_s in the 200-350km depth range and a band like morphology in map view. These features are easily seen in SEMum2 at 250km depth (Figure 2.7.1) as elongate finger-like anomalies of significantly reduced V_s (3-4%), separated by regions of slightly elevated V_s . These features are most prominent in the central and eastern Pacific but are also present beneath other oceans (Indian, Western Antarctic, and North and South Atlantic, etc...). Intriguingly, as shown in Figure 2.7.1, these low-velocity fingers (LVFs) in the oceanic upper mantle preferentially align with the direction of present-day absolute plate motion (Kreemer, 2009).

In the Pacific, these APM-parallel LVFs exhibit an approx-

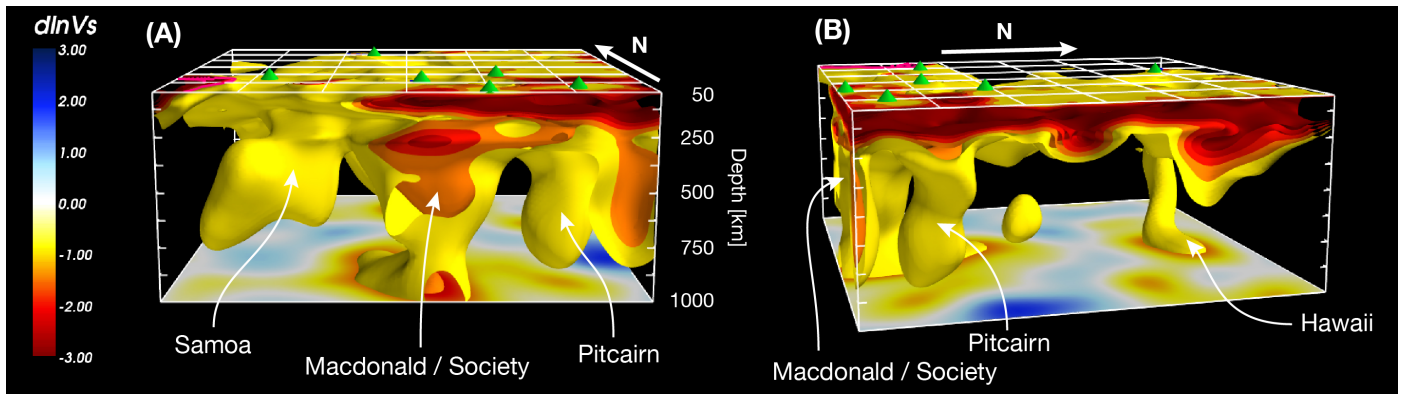


Figure 2.7.2: A 3D rendering of a 60°x60° portion of the central Pacific to 1000km depth. Min/max isocontour levels: -3 to -1%. Panel: (A) View from the South; (B) View from the East-South-East. Approximate correspondence between conduit-like anomalies and overlying hotspots (green cones; Steinberger, 2000) also noted.

imate 2000km periodicity, and their presence correlates with enhanced low velocity anomalies in the overlying classical oceanic low-velocity zone (LVZ). Intriguingly, in an analysis of the geoid using directional wavelets, Hayn et al. (2012) discovered a large-scale pattern of undulations matching both the ~2000km wavelength and APM alignment of the LVFs in the central and eastern Pacific – thereby providing independent geophysical evidence confirming their presence. In order to frame the LVFs in the context of surrounding mantle structure, in Figure 2.7.2 we present a 3D rendering of a 60°x60° portion of the central Pacific to 1000km depth. We see in SEMum2 a progressive transition from structure dominated by the classical oceanic LVZ at shallow depths (<200km), to that dominated by the LVFs (200-350km), to quasi-vertical conduit-like low-velocity anomalies (>300-400km) extending to the lower mantle that are spatially correlated with known hotspots or hotspot regions.

Morphology of the LVFs and their apparent interactions with the conduit-like anomalies below suggest channeling of buoyant upwellings into the asthenosphere – perhaps similar to laboratory experiments in viscous fingering (Snyder and Tait, 1998). Alternatively, their periodicity may be consistent with APM-aligned secondary convection similar to that suggested by Richter and Parsons (1975). Taken together, the observed interactions between the LVFs, the LVZ above, and the quasi-vertical conduit-like anomalies below evoke an interplay between a range of geodynamic phenomena that is both pervasive in the oceanic mantle and has not before been imaged at these scales.

Acknowledgements

This work was supported by the National Science Foundation (EAR-0738284). SF acknowledges support from the NSF Graduate Research Fellowship Program. SEM computations were performed at the National Energy Research Scientific Computing Center (supported by the DOE Office of Science, Contract No. DE-AC02-05CH11231).

References

- Backus, G. E., Long-wave elastic anisotropy produced by horizontal layering, *J. geophys. Res.*, 67, 4427-4440, 1962.
 Bassin, C. G. L., Laske, G., and Masters, G., The current limits of

resolution for surface-wave tomography in North America, *EOS, Trans. Am. geophys. Un.*, 81, 2000.

Hayn, M., Panet, I., Diament, M., Holschneider, M., Manda, M., and Davaille, A., Wavelet-based directional analysis of the gravity field: evidence for large-scale undulations, *Geophys. J. Int.*, 189, 1430-1456, 2012.

Komatitsch, D. and Vilotte, J.-P., The spectral element method: An efficient tool to simulate the seismic response of 2D and 3D geological structures, *Bull. Seism. Soc. Am.*, 88, 368-392, 1998.

Kreemer, C., Absolute plate motions constrained by shear wave splitting orientations with implication for hot spot motions and mantle flow, *J. geophys. Res.*, 116, B10405, 2009.

Lekic, V. and Romanowicz, B., Inferring upper-mantle structure by full waveform tomography with the spectral element method, *Geophys. J. Int.*, 185, 799-831, 2011a.

Lekic, V. and Romanowicz, B., Tectonic regionalization without a priori information: A cluster analysis of upper mantle tomography, *Earth Planet. Sci. Lett.*, 308, 151-160, 2011b.

Li, X. D. and Romanowicz, B., Comparison of global waveform inversions with and without considering cross-branch mode coupling, *Geophys. J. Int.*, 121, 695-709, 1995.

Richter, F. M. and Parsons, B., On the Interaction of Two Scales of Convection in the Mantle, *J. geophys. Res.*, 80, 2529-2541, 1975.

Snyder, D. and Tait, S., A flow-front instability in viscous gravity currents, *J. Fluid Mech.* 369, 1-21, 1998.

Steinberger, B., Plumes in a convecting mantle: Models and observations for individual hotspots, *J. geophys. Res.*, 105, 11,127-11,152, 2000.

Tromp, J., Tape, C., and Liu, Q., Seismic tomography, adjoint methods, time reversal, and banana-doughnut kernels, *Geophys. J. Int.*, 160, 195-216, 2005.

8 Variable Seismic Anisotropy Across the African LLSVP Southern Margin

Sanne Cottaar, Barbara Romanowicz

Introduction

Seismic anisotropy, *i.e.* the variation of seismic wave speed with propagation direction, provides information on material flow and therefore the dynamics in the earth's interior. Seismic anisotropy appears to be strong in the upper mantle and in the lowermost mantle (the D''), where strains related to horizontal flow in the large scale mantle convection system tend to be large.

Here we show evidence for strong seismic anisotropy in the D'' using waveforms of shear waves diffracted along the core-mantle boundary. The seismic anisotropy appears strong to the south of the African Large Low Shear Velocity Province (LLSVP). The anisotropy rotates or weakens towards the LLSVP boundary, and there is no apparent anisotropy inside the LLSVP.

Data and Methods

In this study, we use shear diffracted phases from a deep event near the Fiji islands (~ 621 km, M_w 6.2, 09/04/1997, Figure 2.8.1) towards stations in southern Africa at distances of $> 120^\circ$. Diffracted phases at these distances become polarized along the SH component due to the coupling of the SV component with the outer core. *To et al.* (2005) first pointed out the anomalously strong SV arrivals, which result in elliptical particle motions (Figure 2.8.2). These arrivals result from the splitting of the SH component due to the presence of anisotropy.

We measure the shear-wave splitting with the rotation-correlation method in SplitLab (*Wuestefeld et al.* 2010). The stations at smaller azimuths show a mean fast axis of -46° (defined to be positive away from the T component towards the R component) and a mean splitting time of 1.0 second.

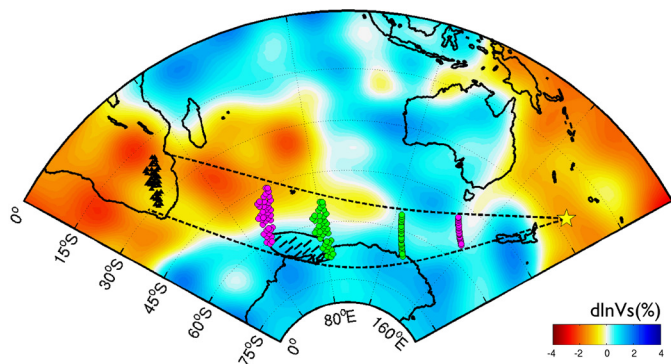


Figure 2.8.1: Coverage map of Sdiff phases from a deep Fijian earthquake (Sept. 4th 1997) observed on the Kaapvaal array in southern Africa. Magenta dots mark the entry and exit points to D'' and the green dots bound the diffracted parts of the paths. We interpret the apparent anisotropy to be where the phases turn upwards in the D'' indicated by the striped patch. The background model is SAW24B16 (*Megnin and Romanowicz, 2000*) at 2800 km depth.

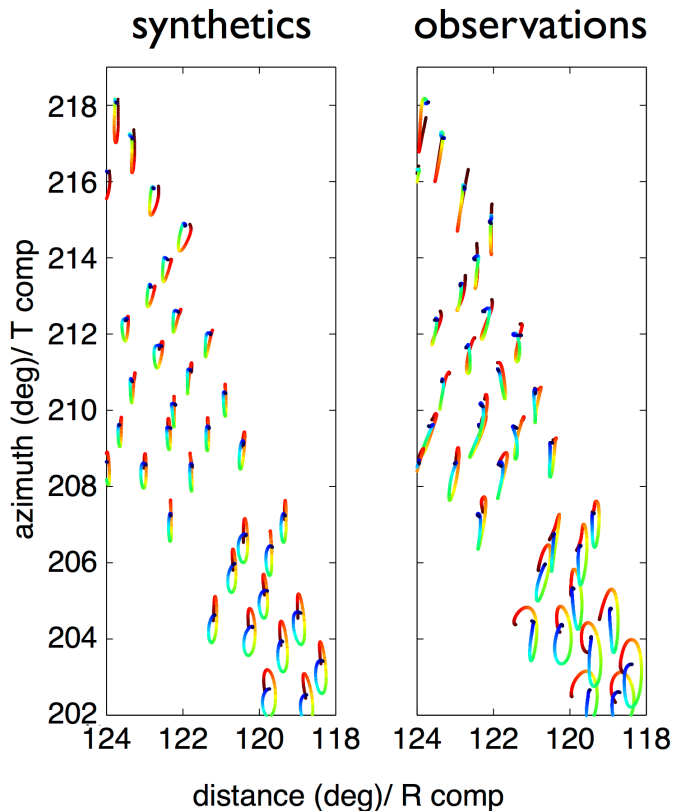


Figure 2.8.2: Particle motions for the horizontal velocity components. Waveforms are filtered between 10 and 30 seconds. Time runs from blue to red over 30 seconds. On the right are the observed particle motions at stations of the Kaapvaal array. Most striking are the elliptical particle motions at smaller azimuths. On the left are synthetic particle motions that capture most of the main features of the data (see Results subsection).

The splitting in Sdiff results from the presence of anisotropy in the upward leg of the path after the diffracted part of the path. We separately measure the splitting in the SKS and SKKS phases to exclude an origin of the splitting in the upper mantle. There is little and very scattered splitting in these phases for this event. Other studies of upper mantle anisotropy beneath the Kaapvaal array (*e.g., Adam and Lebedev, 2012*) show different trends than the shear-diffracted waveforms would suggest here.

We forward model full waveforms for anisotropic models in the D'' using the 'sandwiched' Coupled Spectral Element Method ('sandwiched'-CSEM, *Capdeville et al. 2003*). This method couples the spectral element solution for an anisotropic 3D velocity model in the lowermost 370 km of the mantle to a 1D normal mode solution in the rest of the mantle and the outer core. It is computationally advantageous to apply this method for different models in the lowermost mantle for a single event, as the normal mode computation only needs to be done once. The background model is SAW24B16 (*Megnin and Romanowicz, 2000*) saturated at +1% outside and -2.75% inside the LLSVP.

The saturated model captures the delay in travel time with increasing azimuth (which is apparent in the change in color in particle motions in the second panel of Figure 2.8.2). We define the anisotropy to be in the plane orthogonal to the direction of propagation, as this relates to the apparent anisotropy seen in the waveforms, but we acknowledge that this only represents part of the actual anisotropic elastic tensor. With full waveform modeling we test the sensitivity to fast direction, strength of anisotropy and radial and lateral extent of the anisotropy (Cottaar and Romanowicz, 2013). Here we only present the best model.

Results

The preferred model has a fast axis direction as measured in the data, and 8% of velocity contrast between the fast and slow axis. The anisotropy is constrained to the lowermost 150 km, although there is a strong trade-off between the vertical extent and the strength of anisotropy. Laterally, the anisotropy is constrained to the fast region (with isotropic velocity perturbations over 0.5%). The synthetic waveforms for this model are shown in Figure 2.8.2.

The synthetic waveforms capture the ellipticity of the particle motions at smaller azimuths. They do not capture the increase in amplitude at these azimuths. The amplitudes of the waveforms are higher than predictions for PREM. The synthetics show a decrease in amplitude and a postcursor due to multi-pathing around the LLSVP boundary. The postcursor in the synthetics is less delayed than in the observations (To *et al.*, 2005), resulting in elliptical particle motions. The amplitudes within the LLSVP, at the higher azimuths, are larger due to the slow velocities. The SHdiff arrivals are rotated slightly out-of-plane due to refractions at the LLSVP boundary. The rotations are opposite for the synthetics and observations, though. Capturing the exact multi-pathing and refraction behavior requires corrections to the boundary shape, which is beyond the scope of this study.

Conclusion

We found evidence for the presence of strong anisotropy to the south of the African LLSVP margin by using shear diffracted phases at large distances. We can constrain the part of the elastic tensor that causes the splitting in the waveforms, *i.e.* in the plane orthogonal to the direction of propagation. Most strikingly, the anisotropy weakens towards the LLSVP boundary, and appears absent within.

This study adds an additional location where the presence of strong complex anisotropy appears to correlate with fast velocities and possibly with the presence of slab remnants. Additionally, the presence of textured postperovskite could explain strong anisotropy, as its single crystals have stronger azimuthal anisotropy than in perovskite. The LLSVP margin might be acting as a mechanical boundary that rotates the present fabric (Figure 2.8.3). Within the LLSVP, convection is either too weak or small-scaled, or the material's intrinsic anisotropy is too weak to observe using diffracted waves.

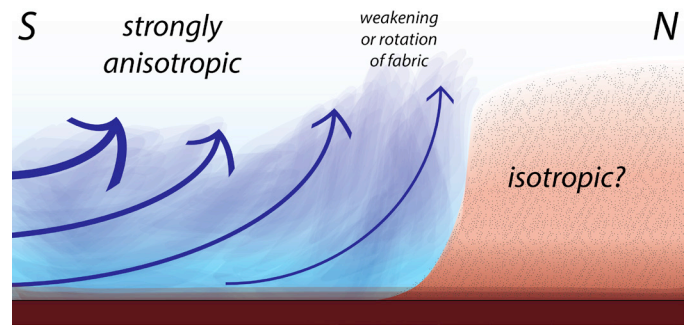


Figure 2.8.3: Cartoon cross-section from south to north through the edge of the African LLSVP with possible flow outside the LLSVP as suggested by the observed anisotropy.

Acknowledgements

The data for this project came from IRIS (www.iris.edu). We thank Yann Capdeville for providing the CSEM code which produced the synthetic data in this study. Shear wave measurements are done with help of the SplitLab Matlab package (www.gm.univ-montp2.fr/splitting/). This work was supported by NSF/CSEDI grant 1067513 and ERC grant 'WAVETOMO'.

References

- Adam, J. and Lebedev, S., Azimuthal anisotropy beneath southern Africa from very broad-band surface-wave dispersion measurements, *Geophys. J. Int.*, 191(1), 155–174, 2012
- Capdeville, Y., To, A., and Romanowicz, B., Coupling spectral elements and modes in a spherical Earth: an extension to the 'sandwich' case, *Geophys. J. Int.*, 154(1), 44–57, 2003.
- Cottaar S. and B. Romanowicz, Observations of changing anisotropy across the southern margin of the African LLSVP, *Geophys. J. Int.*, in revision, 2013.
- Megnin, C. and Romanowicz, B., The three-dimensional shear velocity structure of the mantle from the inversion of body, surface and higher-mode waveforms, *Geophys. J. Int.*, 143(3), 709–728, 2000.
- To, A., Romanowicz, B., Capdeville, Y., and Takeuchi, N., 3D effects of sharp boundaries at the borders of the African and Pacific Superplumes: Observation and modeling, *Earth Plan. Sci. Lett.*, 233(1-2), 1447–1460, 2005.
- Wuestefeld, A., Bokelmann, G., Zaroli, C., and Barruol, G., Split-Lab: A shear-wave splitting environment in Matlab, *Comput. Geosci.*, 34(5), 515–528, 2008.

9 The Application of the Local Slant-Stack Filters (LSSF) for High Resolution Upper Mantle Discontinuity Imaging

Zhao Zheng, Sergi Ventosa and Barbara Romanowicz

Introduction

Several discontinuities (primarily the 410-km and the 660-km) are present in the Earth's upper mantle. Their existence and characteristics provide important constraints on the temperature, composition and dynamics of the mantle. To image these discontinuities on global and regional scales, one effective tool is the SS precursors (e.g. *Shearer*, 1991). They are the underside reflections at the mantle discontinuities (Figure 2.9.1). One major advantage of the SS precursors, compared to the other data types such as receiver functions and triplications, is that they are sensitive to the structure at the midpoint of reflection, and therefore provides good coverage for the vast oceanic areas.

Despite the advantage, there are a few challenges that limit the resolution of the discontinuity images obtained from SS precursor studies. First of all, the precursors are weak in amplitude (typically 5-10% of the SS main phase), often at or below noise level. Stacking therefore is necessary. In practice, common-midpoint (CMP) stacking over rather large geographic bins (radius of 10° or 5°) has been common (for a review, see *Deuss*, 2009), which limits the resolution. Secondly, the SS precursors suffer from interference from other seismic phases, such as the post-cursors of S_{diff} (or S at shorter distances) and the precursors to ScSScS. To avoid this issue, common practice has been to limit the epicentral distance of data selection to the “safe ranges,” for example, 95-115° and 140-145°, although theoretically speaking the entire range of 80-160° is usable. This has reduced the amount of available data by a significant fraction and may have degraded the sampling density and led to loss of resolution.

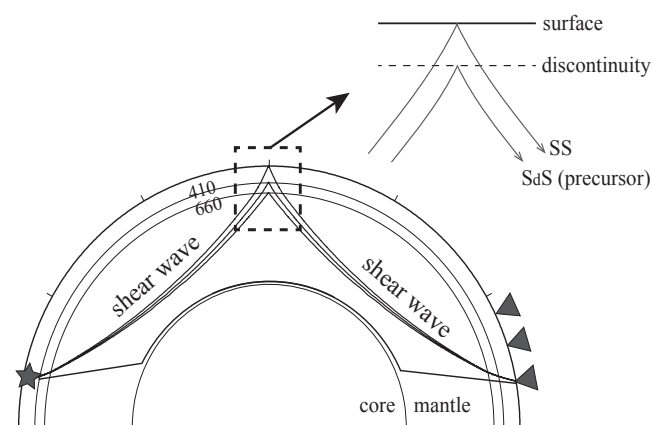


Figure 2.9.1. The ray paths of SS and its precursors. The SS precursors are reflected shear waves off the bottom side of the discontinuities in the Earth's upper mantle.

In recent years, the deployment of the much denser USArray (station spacing ~70 km) has provided unprecedented opportunities for higher resolution imaging. To overcome the above-mentioned limitations of SS precursors, here we propose

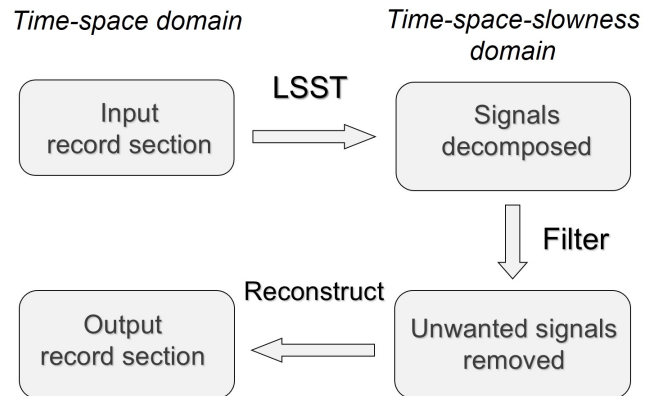


Figure 2.9.2. Workflow of the local slant-stack transform and filtering.

the local slant-stack filter (LSSF) method. In this report, we first introduce the method, then present examples of application to USArray data.

The Local Slant-Stack Filters

Slant stacking is commonly used in seismic signal processing. It aims to detect the slowness(es) of coherent signal(s) present in a given record section by maximizing the stacked amplitude (or other measures of energy). The stacked amplitude plot is also known as a “vespagram.” The local slant-stack filters (LSSF) are based on the localized slant stack transform (LSST. *Ottolini*, 1983; *Harlan et al.*, 1984; *Bohlen et al.*, 2004; *Shlivinski et al.*, 2005). It loops over all the traces in the entire record section, and conducts one slant stacking in the vicinity of each trace. The input record section is thus transformed from the time-space domain to the time-space-slowness domain. Filters are then applied in the latter domain to extract or mask out a coherent signal(s) that has a desired slowness and appears at a specified time and spatial location. For example, in the case of this study, the SS precursors have slownesses that is very close to that of the SS (difference $< \pm 0.5$ s/deg predicted for PREM), while the interfering phases (S_{diff} postcursors and ScSScS precursors) have distinctively different slownesses (difference > 2 s/deg). A filter can therefore be designed to preserve the SS slowness range and mask out the unwanted ones. Random noise has low coherence and can be easily removed. After the filtering, the record section is converted back to the time-space domain through a reconstruction process. The workflow of LSSF is summarized in Figure 2.9.2.

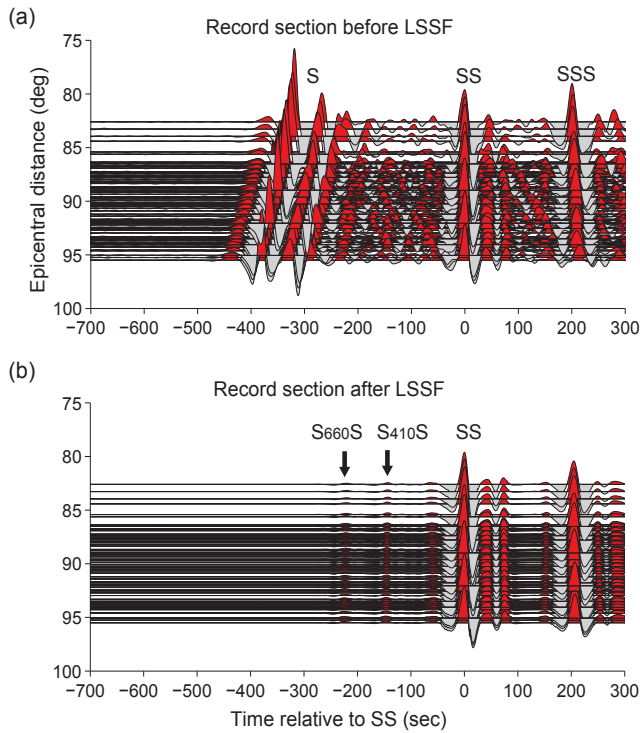


Figure 2.9.3. Record sections of an M_w 7.8 earthquake in Fiji recorded at the USArray, (a) before and (b) after the LSSF filtering.

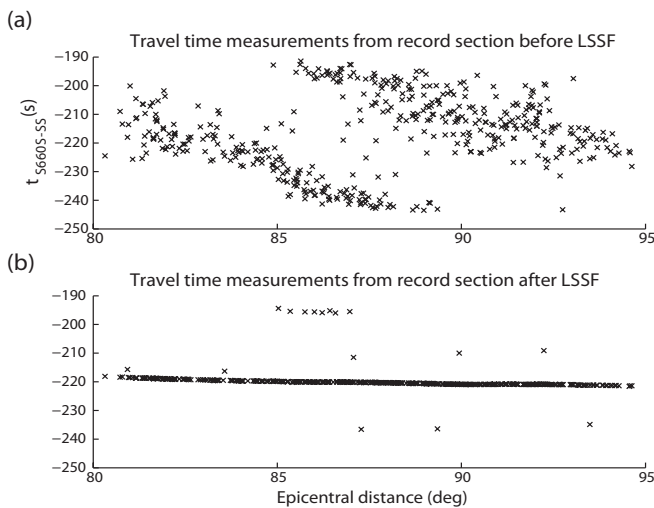


Figure 2.9.4. Differential (S_{660S} -SS) travel times measured by cross correlation, from (a) the record section before and (b) after the LSSF filtering. Each cross represents the measurements from one trace.

Application to the USArray Data

Figure 2.9.3(a) shows the record section from an M_w 7.8 earthquake recorded at the USArray. Considering the epicentral distance range, it would have been rejected by conventional SS precursor studies. The SS main phase is clear, however the precursors are not visible due to the strong noise following the S arrival. A vespagram analysis (not shown here due to page limit) indicates the primary content of the noise has a slowness

close to that of S, likely to be postcursors of S ($SdsS$ and/or $SsdS$, i.e. the shear wave bouncing once between a discontinuity d and the surface, either beneath the source or beneath the receiver). LSSF filters are then applied to the record section. Only the signals that are within the slowness range of ± 1 s/deg and that are spatially coherent over a radius of 1.5° are preserved. The filtered record section is shown in Figure 2.9.3(b). The noise is significantly reduced, and the S_{410S} and S_{660S} precursors can now be clearly identified. Their arrival times are in good agreements with the theoretical predictions, confirming the phase identification.

To quantify the improvement of the record section, Figure 2.9.4 compares the travel times of the S_{660S} precursor measured from the record section before and after the LSSF. Before the filtering, the travel time measurements are much more scattered, and the slope of the trend is in agreement with the slowness of S, indicating the measurements are biased by the postcursors of S. After the filtering, the measurements are much more coherent, and have the correct travel time and slowness.

Conclusions

LSSF has proven to be a powerful tool for cleaning up SS precursor record sections and bringing out the weak yet coherent precursor signals. Measurements (for travel time as well as amplitude) can now be done on each trace in the record section, and stacking over large geographic bins is not a necessity any more. Potentially, this will greatly improve the resolution of resultant mantle discontinuity images. The cleaned record sections can be used as input for mature array imaging techniques such as migration.

Acknowledgements

Data were downloaded via IRIS DMC. This study was funded by NSF EAR #0738284. ZZ presented this work at the 2013 SSA conference and the trip was partially supported by the UC Berkeley Student Travel Grant.

References

- Bohlen, T., S. Kugler, G. Klein, & F. Theilen, 1.5D inversion of lateral variation of scholte-wave dispersion, *Geophysics*, 69, 330–344, 2004.
- Deuss, A., Global observations of mantle discontinuities using SS and PP precursors, *Surv. Geophys.* 30, 301–326, 2009.
- Harlan, W. S., J. F. Claerbout, & F. Rocca, Signal/noise separation and velocity estimation: *Geophysics*, 49, 1869–1880, 1984.
- Ottolini, R., Signal/noise separation in dip space, *Stanford Exploration Project-37*, 143–149, 1983.
- Shearer, P.M., Constraints on upper mantle discontinuities from observations of long-period reflected and converted phases, *J. Geophys. Res.*, 96, 18147–18182, 1991.
- Shlivinski, A., E. Heyman & A. Boag, A pulsed beam summation formulation for short pulse radiation based on windowed Radon transform (WRT) frames: *IEEE Transactions on Antennas and Propagation*, 53, 3030–3048, 2005.

10 Probabilistic Downscaling of Full Waveform Smooth Tomographic Models: Separating Intrinsic and Apparent Anisotropy

Thomas Bodin, Yann Capdeville, and Barbara Romanowicz

Introduction

The global seismology group at the Berkeley Seismological Laboratory (BSL) has a long history of expertise in the development and application of global imaging using full waveform inversion, leading to several generations of global anisotropic 3D models of the Earth's mantle (e.g., *Li and Romanowicz*, 1996; 2002; *Gung et al.*, 2003; *Panning & Romanowicz*, 2004). In recent years, advances in numerical methods such as the spectral element method (SEM), and increasing computational power, have allowed us to model more accurately the entire seismic wavefield. At the BSL, *Lekic and Romanowicz* (2011) and *French et al.* (2012) recently constructed the first global upper mantle models developed using the spectral element method. However, the heavy computations involved remain a challenge, and the fitted waveforms need to be low pass filtered, which results in an inability to map features smaller than half the shortest wavelength, such as sharp discontinuities.

In this way, the tomographic images can be seen only as a smooth representation of the true Earth. However, they are not merely a simple spatial average of the true model, but rather an effective, apparent, or equivalent model that provides a similar 'long-wave' data fit. For example, it is well known that an isotropic medium with strong gradients will be seen by a long period wave as a smooth anisotropic medium.

Therefore, the observed anisotropy in tomographic models is a combination of intrinsic anisotropy produced by flow-induced lattice-preferred orientation (LPO) of minerals, and apparent anisotropy resulting from the incapacity of mapping discontinuities associated with layering. Interpretations of observed anisotropy (e.g., in terms of mantle flow) therefore require the separation of its intrinsic and apparent components.

The Elastic Homogenization

The relations that link elastic properties of a rapidly varying medium to elastic properties of the effective medium as seen by long waves are the subject of current research (*Guillot et al.*, 2010; *Capdeville et al.*, 2010a,b; *Capdeville & Marigo*, 2013). These homogenization laws have been recently used by tomographers to reduce computational costs when modeling propagation of long waves in a complex medium. That is, given a complex elastic medium, and given a minimum period for the wave equation, a smooth homogeneous equivalent medium can be constructed. The computation of the forward problem (solving the elastic wave equation) can be done in this smooth model, which drastically releases the meshing constraint and reduces the computational cost.

A simple example of homogenization (upscaling) is shown in Figure 2.10.1. Here, only residuals between a reference model (light blue) and a 'real' model (black) are homogenized. This is necessary because, although tomographic models are smoothly

parameterized, they are computed relative to a reference model that contains discontinuities (e.g., at 410 km) (*Capdeville et al.*, 2013).

The Inverse Homogenization

In the 1D case, *Capdeville et al.* (GJI, 2013) recently showed that a tomographic model which results from the inversion of low pass filtered waveforms is a homogenized model, *i.e.*, the same as the model computed by upscaling the true model.

Here we propose a method for the inverse homogenization, or downscaling of smooth tomographic models. The goal is to constrain a discontinuous realistic Earth model, given its observed smooth equivalent. Of course, the solution to the problem is by essence non-unique, *i.e.*, a smooth homogenized effective model is equivalent to a large number of inhomogeneous models with discontinuities. We therefore tackle the problem probabilistically and carry out a stochastic method to sample the ensemble of layered models equivalent to a given tomographic profile. We use a transdimensional formulation where the number of layers is variable (*Bodin et al.*, 2012a,b). Furthermore, each layer may be either isotropic (1 parameter) or intrinsically anisotropic (2 parameters). The parsimonious character of the Bayesian inversion gives preference to models with the least number of parameters (*i.e.*, least number of layers, and maximum number of isotropic layers).

The homogenized model shown in Figure 2.10.1 was downscaled, and results are shown in Figure 2.10.2. This method enables us to distinguish between intrinsic and apparent anisotropy in tomographic models, as layers with intrinsic anisotropy are only present when required by the data.

Acknowledgements

The authors wish to acknowledge support from the Miller Institute for Basic Research at the University of California, Berkeley. We also acknowledge support by the France-Berkeley fund (FBF), a partnership between the government of France and the University of California, at Berkeley

References

- Bodin, T., Sambridge, M., Rawlinson, N., and Arroucau, P., Transdimensional tomography with unknown data noise, *Geophysical Journal International*, 2012.
- Bodin, T., Sambridge, M., Tkalcic, H., Arroucau, P., Gallagher, K., and Rawlinson, N., Transdimensional inversion of receiver functions and surface wave dispersion, *J. Geophys. Res.*, 117, B02301, 2012.
- Capdeville, Y. and Marigo, J., A non-periodic two scale asymptotic method to take account of rough topographies for 2-d elastic wave propagation, *Geophysical Journal International*, 192(1), 163–189, 2013.
- Capdeville, Y., Guillot, L., and Marigo, J., 1-d non-periodic homogenization for the seismic wave equation, *Geophysical Journal International*, 181(2), 897–910, 2010.

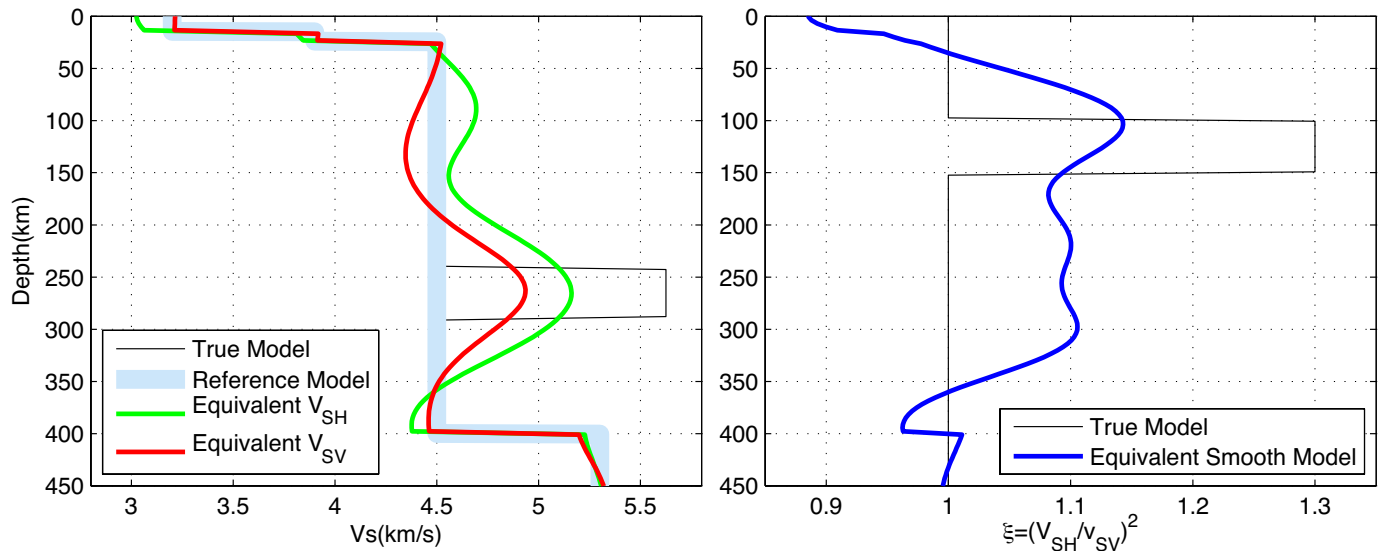


Figure 2.10.1: A true model (black) is defined as the sum of a reference model (light blue) and two anomalous layers. The first layer (100-150 km) contains intrinsic anisotropy (right panel) but does not present changes in the voigt Vs average (left panel). The second layer (250-300 km) is a simple isotropic velocity anomaly. The “residual model” is homogenized. The green (V_{sh}), red (V_{sv}), and blue (ξ) curves represent the smooth equivalent. Note how the two major discontinuities in Vs (250 km and 300 km) are mapped into artificial anisotropy.

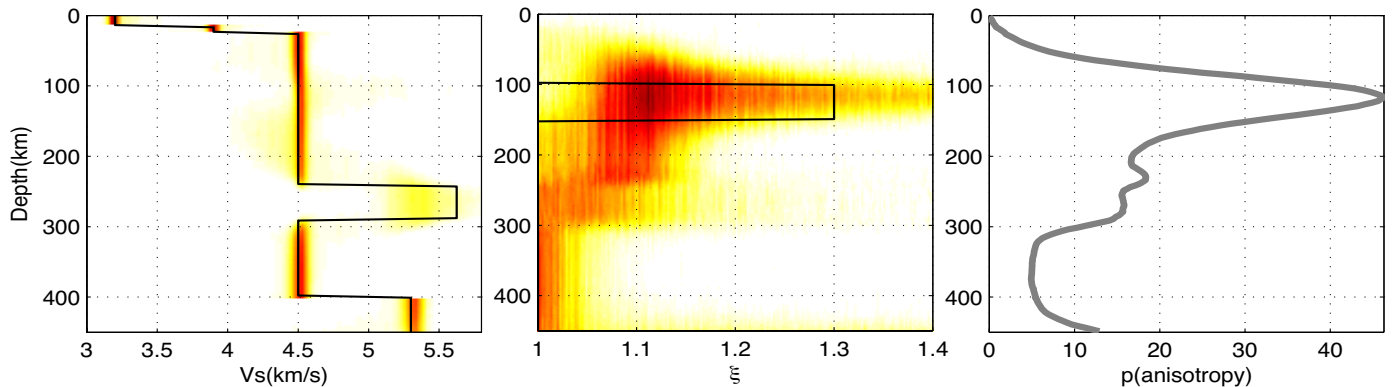


Figure 2.10.2: Probabilistic downscaling of the smooth model in Figure 2.10.1. Left: distribution showing the ensemble solution (true model is in Black). Middle: same thing for parameter ξ representing the intrinsic radial anisotropy. Right: probability (%) of having an anisotropic layer.

Capdeville, Y., Guillot, L., and Marigo, J., 2-d non-periodic homogenization to upscale elastic media for p-sv waves, *Geophysical Journal International*, 182(2), 903–922, 2010.

Capdeville, Y., Stutzmann, E., Wang, N., Montagner, J.P., Residual homogenization for seismic forward and inverse problems in layered media, 2013.

French, S., Lekic, V., and Romanowicz, B., Spectral-element global waveform tomography: A second-generation upper-mantle model, *AGU Fall Meeting*, 2012.

Guillot, L., Capdeville, Y., and Marigo, J., 2-d non-periodic homogenization of the elastic wave equation: Sh case, *Geophysical Journal International*, 182(3), 1438–1454., 2010.

Lekic, V. and Romanowicz, B., Inferring upper-mantle structure by full waveform tomography with the spectral element method, *Geophysical Journal International*, 185(2), 799–831, 2011.

Li, X. and Romanowicz, B., Global mantle shear velocity model developed using nonlinear asymptotic coupling theory, *Journal of geophysical research*, 101(B10), 22245–22, 1996.

Gung, Y., Panning, M., Romanowicz, B., et al., Global anisotropy and the thickness of continents, *Nature*, 422(6933), 707–711, 2003.

Panning, M. and Romanowicz, B., Inferences on flow at the base

of earth’s mantle based on seismic anisotropy, *Science*, 303(5656), 351–353, 2004.

11 Mapping Embedded Low-velocity Zones in Permafrost Using Full-wavefield Inversion of Multichannel Surface Waves

Shan Dou, Jonathan Ajo-Franklin (LBNL), Douglas Dreger

Introduction

Permafrost (soils and rocks that stay at or below 0°C for at least two consecutive years) is an important and yet challenging target for seismic imaging techniques. The challenge lies in the fact that seismic velocities in permafrost are primarily controlled by ice content rather than lithology. A variety of factors, including thermal, chemical, and hydrological cryo-alteration introduce large variations in ice content, a process which yields concomitant sharp contrasts in seismic properties. Because simple layering with normal velocity gradients (increasing velocities with depth) seldom exists in permafrost, body wave refraction imaging is often unable to effectively delineate the velocity structure, particularly in the near-surface where modern thermal processes interface with permafrost structure.

In contrast, surface wave methods do not require abrupt velocity (or impedance) contrasts or normal velocity gradients and thus are amenable for mapping irregular velocity structure in permafrost. However, irregular velocity variations often lead to dominant higher and leaky modes; thus conventional surface-wave inversion methods are inapplicable despite the sensitivity of the technique.

In this study, we apply an unconventional inversion method that uses the complete signal content of the wavefield. Because of the advantages of the full-wavefield method, we are able to infer embedded low-velocity zones from inversely dispersive field data acquired from our permafrost study site at Barrow, Alaska. The low-velocity zones may correspond to embedded cryopegs (hypersaline unfrozen zones), in which ground remains unfrozen or only partially frozen under sub-zero temperatures due to the freezing-point depression effect of salt. The high salt content could have originated from repeated regression and transgression of the Arctic Ocean around 100–350 million years ago (Thurston *et al.*, 1987). Because of the available access to liquid water in cryopegs, cold-adapted microorganisms could maintain their metabolisms under permafrost conditions. The presence of extensive cryopegs at our study site, now confirmed by exploratory sampling, may indicate additional soil carbon degradation occurring in the deep permafrost.

Background

The study site is located within the Barrow Environmental Observatory (BEO) in Alaska (Figure 2.11.1b). The entire area is underlain by continuous permafrost to depths of more than 300 m (Jorgenson *et al.*, 2008).

As part of the Next-Generation Ecosystem Experiments (NGEE-Arctic) project initiated by the U.S. Department of Energy (DOE), we acquired multichannel surface-wave data at the BEO study site during the period of May 11–14, 2012. The field data acquired at the BEO site exhibit inversely dispersive trends

(*i.e.* phase velocities increase with increasing frequencies) in both the space-time ($x-t$) and frequency-velocity ($f-v$) domains. This suggests that low frequency waves (which penetrate deeper into the ground because of the long wavelength) propagate with slower velocities, and hence the field site is likely to have embedded low-velocity zones/layers.

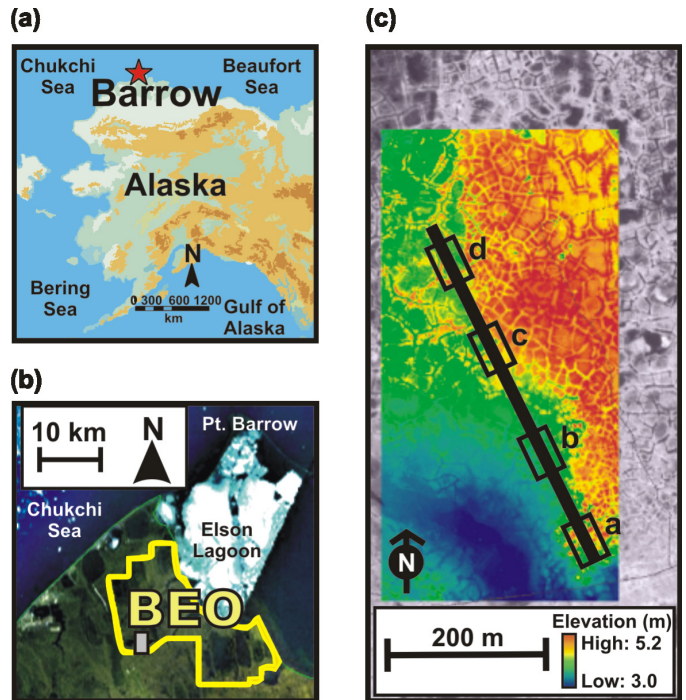


Figure 2.11.1. Site maps: (a) Location of Barrow area, Alaska (red star). (b) The location of the Barrow Environmental Observatory (BEO: yellow outline). The grey box indicates the NGEE-Arctic geophysics site. (c) The 475-meter-long seismic survey line. The black boxes (a, b, c, and d) denote the spatial locations that this study is focused on.

Methods

Conventional surface-wave inversions mostly use kinematic information (in the form of dispersion curves) carried by the wavefield. However, when applied to inversely dispersive media, the energy distribution (including the effect of higher modes, leaky modes, and the data acquisition and processing procedure), in addition to the kinematic information, becomes crucial for surface-wave inversion.

We use a non-linear full-wavefield method as an alternative to exploit the complete signal content of surface waves. Instead of fitting dispersion curves, the entire dispersion spectrum is used to construct the objective function. The nonlinear inverse problem can be framed as an optimization procedure which involves searching for optimal models that minimize the objective function. Because the objective function usually has multiple

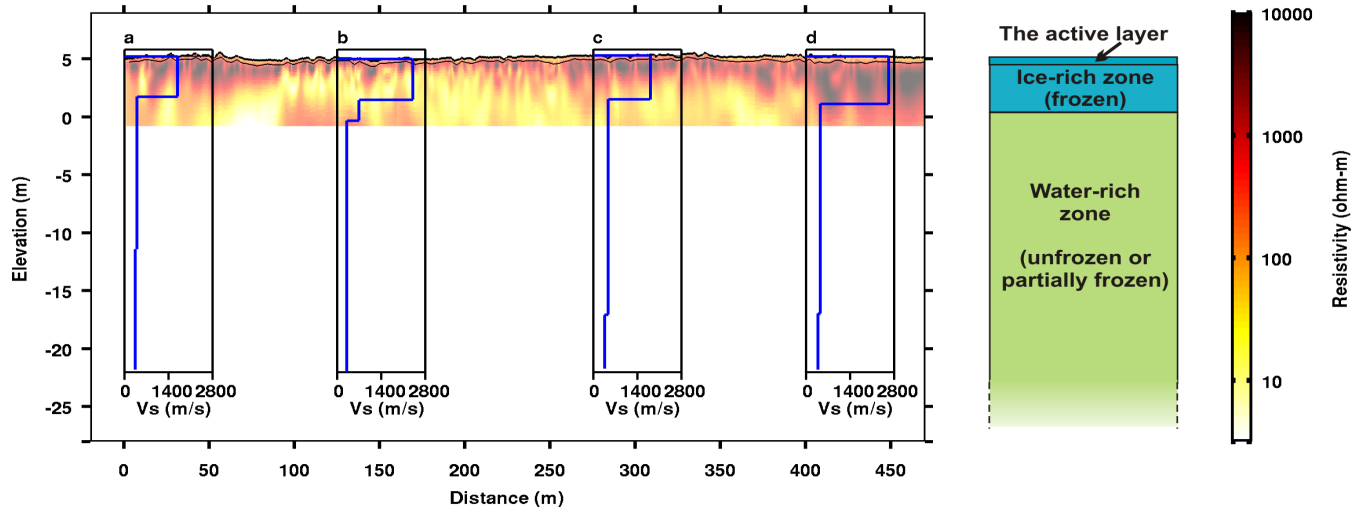


Figure 2.11.2: Comparison of shear-wave velocity profiles and the electrical resistivity tomography (ERT) results (Hubbard *et al.*, 2012). Shear-wave velocity (V_s) profiles (a), (b), (c), and (d) correspond to locations shown as section a, b, c, and d in Figure 1c. The schematic on the right shows the conceptual model with embedded water-rich zones.

local minima and rugged topography, many commonly-used algorithms that require derivative information are unsuitable. Instead, we adopt derivative-free approaches that only require values, rather than the derivative information, of the objective function. The optimization approach is a hybrid global/local technique which uses a global direct search method to find an approximate optimum solution and a local direct search method (Nelder-Mead) to refine the result.

Results

We apply the full-wavefield inversion method to the field data. The resultant models reveal pronounced low shear-velocity zones ($\sim 300\text{--}680\text{ m/s}$) underlying the thin high shear-velocity top-layer ($\sim 1700\text{--}2400\text{ m/s}$ with thickness ranges around 3.5–4 m). Despite the limited depth penetration of the field data, our inversion indicates these low-velocity zones should extend up to $\sim 25\text{ m}$ below the surface.

We also compare the seismic velocity models with collocated electrical resistivity tomography (ERT) profiles (Hubbard *et al.*, 2012) (Figure 2.11.2). Although the boundaries between high- and low-velocity do not match the boundaries between high- and low-resistivity in an exact way, the first-order layering structures between the two are in good agreement. The consistent results from two different geophysical methods suggest the reliability of the seismic models. These low seismic-velocity (and low electrical resistivity) zones may be constituted of sediments that are unfrozen or only partially frozen.

Acknowledgements

This study was sponsored by the Office of Biological and Environmental Research within the U.S. Department of Energy's Office of Science as part of the Next Generation Ecosystem Experiment (NGEE-Arctic).

References

- Hubbard, S.S., C. Gangodagemage, B. Dafflon, H. Wainwright, J. Peterson, A. Gusmeroli, C. Ulrich, Y. Wu, C. Wilson, J. Rowland, C. Tweedie, and S. D. Wulschleger, Quantifying and relating land-surface and subsurface variability in permafrost environments using LiDAR and surface geophysical datasets: *Hydrogeology Journal*, 21, 149-169, 2012.
- Jorgenson, M. T., K. Yoshikawa, M. Kanveskiy, Y. L. Shur, V. Romanovsky, S. Marchenko, G. Grosse, J. Brown, and B. Jones, Permafrost characteristics of Alaska: Institute of Northern Engineering, University of Alaska, Fairbanks, 2008.
- Thurston, D.K., and L.A. Theiss, Geologic report for the Chukchi Sea planning area, Alaska: U.S. Department of the Interior, Minerals Management Service, Alaska OCS Region, 1987.

12 Probing Deep Rheology Across the Eastern Margin of the Tibetan Plateau: Constraints from the 2008 M_w 7.9 Wenchuan Earthquake

Mong-Han Huang and Roland Bürgmann

Introduction

The fundamental geological structure and rheology of the Tibetan plateau have been debated for decades. Two major models have been proposed: (1) the deformation in Tibet is distributed, and associated with ductile flow in the mantle or lower crustal flow (LCF); (2) the Tibetan plateau was formed during interactions among rigid blocks with localization of deformation along major faults. On 12 May, 2008, a M_w 7.9 earthquake occurred on the Longmen Shan that separates the eastern Tibetan plateau and the Sichuan basin. The earthquake ruptured ~ 235 km of the Beichuan fault (BCF) and the entire Pengguan fault (PGF) (Shen *et al.*, 2009). Geodetic inversions show more than 5 slip asperities and ~ 16 m peak slip on SW BCF (Fig. 2.12.1). All of the slip models show oblique thrusting along the SW BCF and a right-slip component gradually increases towards the NE end of the BCF. The postseismic displacement is a response to the redistribution of stresses induced by the earthquake and can be used to probe the deep rheologic properties underneath the surface (Wang *et al.*, 2012). Here we incorporate two-year long geodetic measurements and numerical modeling to examine two end-member hypotheses to provide further evidence to the deep rheology in eastern Tibetan plateau.

The Postseismic Displacement

The GPS measurements show an overall NW-SE convergent displacement in SW BCF, and turn into right lateral strike-slip motion in the NE BCF. This pattern is similar to the coseismic displacement (Fig. 2.12.1), but the peak displacement is about 40 km away from the coseismic surface rupture where the peak coseismic displacement is located (Shen *et al.*, 2009). In the hanging wall, the amplitude of displacement increases from 0-2 cm near the surface rupture to about the location of the Wenchuan-Maowen fault (WMF), and then decays from 5-7 cm at the WMF to 3-4 cm in the far field. Comparing this with the coseismic displacement (black arrows in Fig. 2.12.1), the gradient of the displacement away from the fault is much lower and might imply either a deeper slip on the fault or viscous relaxation from the deeper part of the lithosphere. In the footwall, all of the displacement moves toward the NW and the amplitude is much smaller than in the hanging wall.

Model of the Postseismic Displacement

The afterslip is the continuous slip of the fault after the main shock and is often considered down-dip of the fault rupture zone (Wang *et al.*, 2012). We use a dislocation model with layered structures to investigate the afterslip distribution by inverting the geodetic data. We modify the fault geometry proposed by Shen *et al.* (2009) and extend the fault width to 65 km depth for afterslip at the down-dip extension (afterslip model in Fig. 2.12.1). The afterslip distributes on both shallow and deep

parts of the BCF that represent the fit to both the near, and far field displacement.

We use a 3D finite element model to construct a regional rheologic model composed of an elastic Tibet upper crust and Sichuan crust, a viscoelastic Tibet lower crust, and a viscoelastic upper mantle. We use the bi-viscous Burger's rheology to represent the transient and steady state periods of the postseismic deformation. The Burger's rheology is composed of a Maxwell fluid connected in series with a Kelvin solid to represent the steady state and transient viscosities (η_1 and η_2 , respectively). The best-fitting model is composed of the LCF located between 45 and 60 km in depth and can produce more far field postseismic displacement.

The afterslip model can explain the postseismic displacement in the near field but there is larger misfit in the far field. On the other hand, the viscoelastic relaxation model can explain the far field postseismic displacement better than the near field. It appears that a single mechanism cannot solely explain the postseismic displacement. A multiple mechanism model is needed to fit both near, and far field displacements. We consider the 15 km thick LCF to be the main mechanism of the far field displacement, so the afterslip model may explain the misfit of the LCF model. The inversion (the 2nd afterslip model in the lower right in Fig. 2.12.1) of the LCF residual displacement shows a significant reduction of the deep afterslip.

As a result, the afterslip alone model requires more than 45 cm slip in the first year below Tibet's Moho that may already undergo ductile deformation, whereas the viscoelastic relaxation in a 15 km thick LCF can explain the GPS measurements. Consequently, the result of the Wenchuan postseismic displacement supports a weak lower crustal flow underneath eastern Tibet.

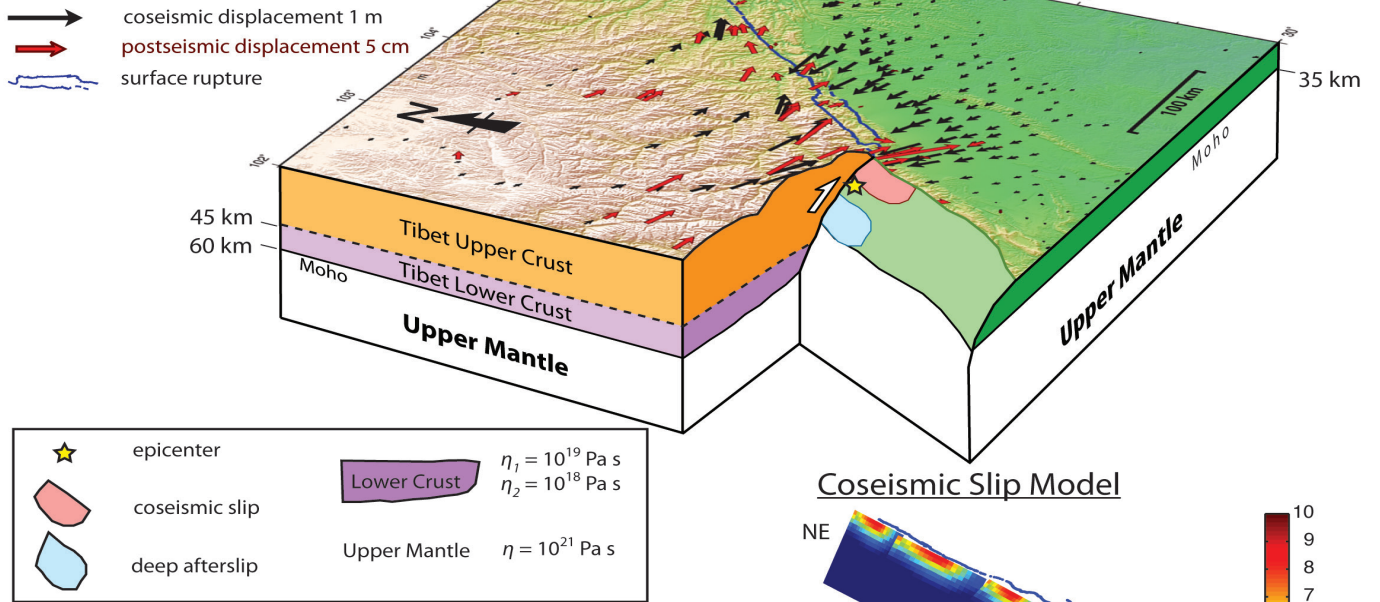
Acknowledgements

We thank Prof. Z. Shen of Beijing for providing the GPS measurements. M.-H. Huang thanks Prof. Andrew Freed for instruction on ABAQUSTM. This work is supported by the National Science Foundation (grant EAR 0738298).

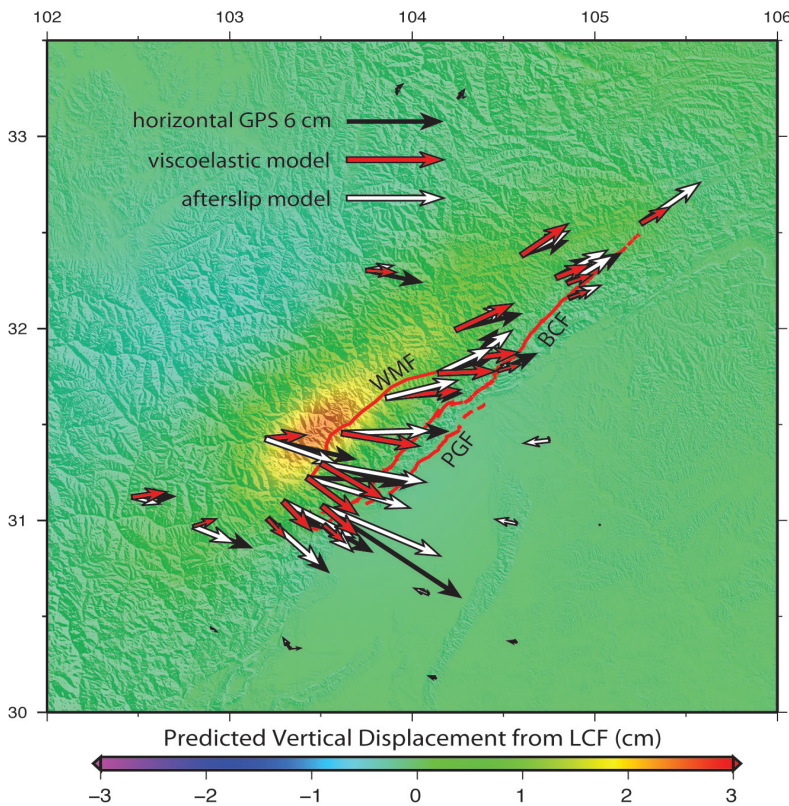
References

- Shen, Z.K., J. Sun, P. Zhang, Y. Wan, M. Wang, R. Bürgmann, Y. Zeng, W. Gan, H. Hiao, and Q. Wang, Slip maxima at fault junctions and rupturing of barriers during the 2008 Wenchuan earthquake, *Nat. Geosci.*, 2, 718-724, doi:10.1038/NGEO636, 2009.
- Wang, K., Y. Hu, and J. He, Deformation cycles of subduction earthquakes in a viscoelastic Earth, *Nature*, 484, doi:10.1038/nature11032, 2012.

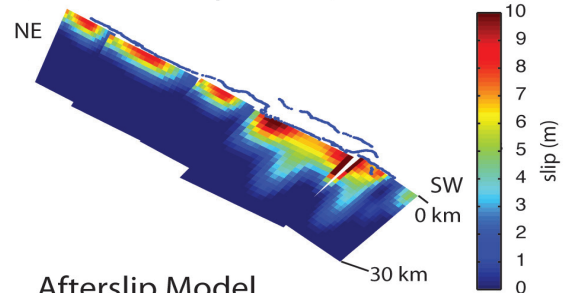
Three Dimensional Representation of Eastern Tibet



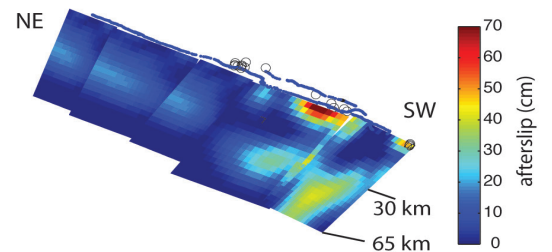
First Year Postseismic Displacement



Coseismic Slip Model



Afterslip Model



Afterslip of the Multiple Mechanism Model

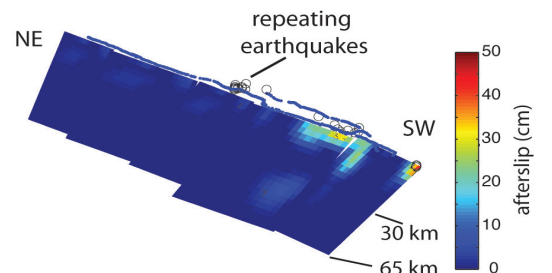


Figure 2.12.1: The 3D representation of the rheologic model in eastern Tibet and western Sichuan basin. These two geologic structures are separated by the Longmen Shan. The co- and postseismic GPS displacements are shown in the black and red arrows, respectively. The two possible mechanisms of the postseismic deformation are: (1) deep afterslip (the light blue region), and (2) lower crustal flow (the purple layer). The coseismic slip is inverted from the coseismic GPS measurements. In the lower left, the postseismic displacement during the first year is compared with the two end-member mechanisms. The two afterslip models in the lower right are inverted from the one year postseismic GPS measurements and from the LCF model residual, respectively. The deep afterslip in the multiple mechanism model is largely reduced (see text).

13 Viscoelastic Postseismic Deformation Following the 2011 M_w 9.0 Tohoku Earthquake

Yan Hu, Roland Bürgmann

Introduction

On March 11th, 2011, the surprisingly large M_w 9.0 Tohoku earthquake ruptured the interface of the subducting Pacific Plate over an area approximately 400 km long and 200 km wide and produced a devastating tsunami. As a result of the earthquake, five marine GPS-acoustic stations recorded more than 50 meters seafloor displacements near the trench (Fujiwara *et al.*, 2011). This was a first. Inversions from land and seafloor geodetic data, as well as teleseismic data, show that portions of the megathrust slipped as much as 80 meters (e.g., Ozawa *et al.*, 2011; Inuma *et al.*, 2012) (solid contours in Figure 2.13.1a). Viscoelastic relaxation in the upper mantle of the shear stresses induced by the earthquake, and aseismic afterslip of the megathrust both contribute to the very rapid crustal deformation observed since the earthquake. Land GPS stations have recorded more than one meter postseismic displacements in two years since the earthquake (red arrows in Figure 2.13.1a). The geodetic data in NE Japan, with unprecedented high spatial and temporal resolution, provide a unique opportunity to explore the rheological structure of the upper mantle and behavior of the megathrust in earthquake cycles.

In this ongoing research, we integrate the wealth of geodetic data from NE Japan and modeling experiences developed at other margins (Hu and Wang, 2012; Wang *et al.*, 2012) to investigate the effects of mantle rheology on postseismic deformation following the 2011 earthquake.

Finite Element Model

Newtonian-Maxwell rheology has been widely used to describe slow viscoelastic relaxation of the mantle in earthquake cycle deformation models and studies of postglacial rebound. In this work, we assume that the upper mantle is represented by the bi-viscous Burgers rheology that is able to describe slow, long-term deformation as well as very rapid, short-term transient deformation. A bi-viscous Burgers element consists of a Maxwell element (steady-state viscosity) in parallel with a Kelvin element (transient viscosity) (Bürgmann and Dresen, 2010).

We use a three dimensional (3D) finite element model (FEM) that is able to incorporate the complex slab geometry and tectonic structure in the real Earth. The model shown in Figure 2.13.1b consists of an elastic upper plate, an elastic subducting plate, a viscoelastic continental mantle wedge, and a viscoelastic oceanic upper mantle. Reference rock properties of each tectonic unit are also labeled in Figure 2.13.1b.

A common approach of studying afterslip is to invert the postseismic surface displacements, or the residual between observations and mantle-relaxation-model predicted motions, for distributed slip on the subduction thrust in an elastic half-space. In reality, however, afterslip is stress driven and time dependent. The conventional approach neglects the significant

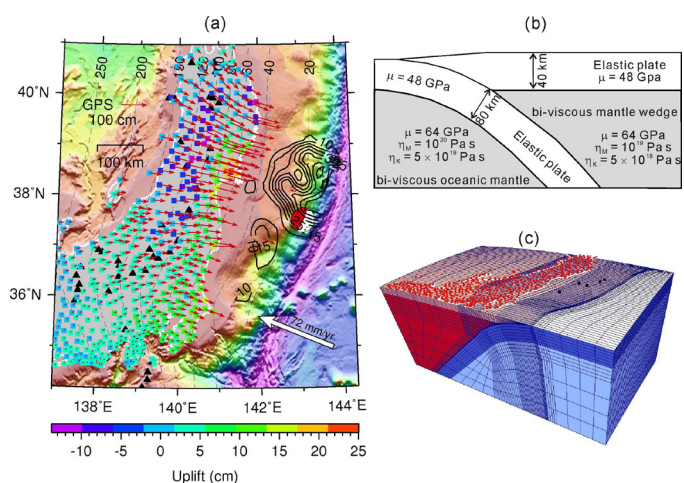


Figure 2.13.1: (a) Horizontal (red arrows) and vertical (colored contours) two-year postseismic displacements observed at land GPS stations in NE Japan. Marine GPS data (red arrows) are one year postseismic displacements. Solid contours are coseismic slip distributions at 10-meter intervals (Inuma *et al.*, 2012). Labeled dashed lines represent the depth of the subduction interface. (b) Schematic diagram of finite element model (after Hu and Wang, 2012). Each tectonic unit is labeled with its rock properties. (c) Central part of the finite element mesh. Red and black dots represent locations of land and marine GPS stations, respectively. Thick white lines denote the coastline.

relaxation of the upper mantle due to the afterslip itself and the contribution of mantle relaxation to driving afterslip. In this work, we use a narrow weak shear zone with low viscosity that is attached to the subduction interface to simulate the afterslip. Because coseismic slip of the fault induces shear stress in the shear zone, subsequent viscoelastic relaxation of the shear zone gives an approximation of the stress-driven afterslip of the fault.

Following the approach of developing the FEM mesh in Hu and Wang (2012), we manually derived thirty-two latitude-parallel profiles based on published slab geometry data (e.g., Nakajima and Hasagawa, 2006), relocated seismicity, and locations of the trench and the arc. These profiles were then used to construct the finite element mesh. The central part of the mesh is shown in Figure 2.13.1c.

Model Results

In our preliminary model, based on results deduced from post-2004 Sumatra earthquake deformation (Hu and Wang, 2012), steady-state and transient viscosities of the continental mantle wedge and the oceanic mantle are shown in Figure 2.13.1b. Steady-state and transient viscosities of the shear zone are 10^{17} and 10^{16} Pa s, respectively. The shear zone is attached to portions of the fault where the coseismic slip is less than five meters, and the afterslip zone terminates at 120 km depth.

Our model successfully reproduces the first-order pattern of

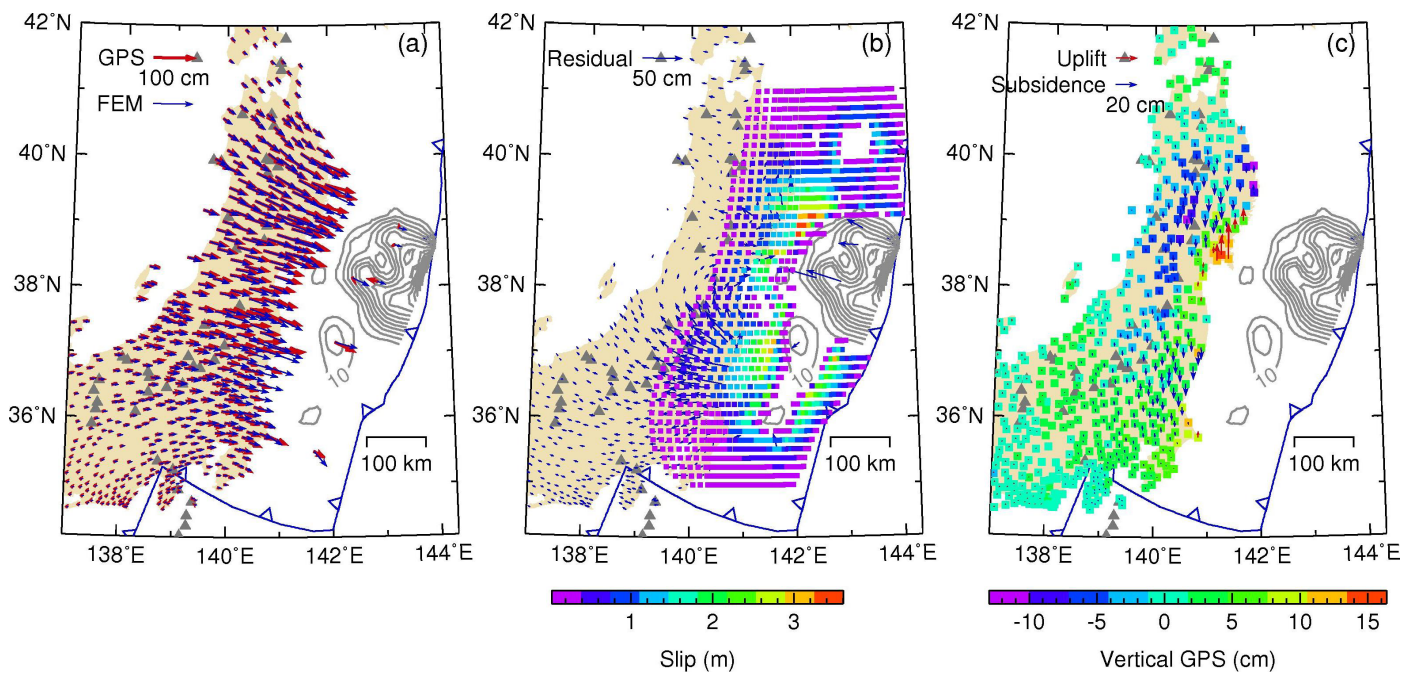


Figure 2.13.2: Comparison of postseismic GPS observations with model-predicted results one year since the earthquake. (a) Horizontal displacements. Red and blue arrows represent GPS observations and model-predicted displacements, respectively. (b) Residual between GPS observations and model-predicted results shown in (a). Colored contours represent cumulative slip of the shear zone. (c) Vertical displacements. Red and blue arrows represent model-predicted uplift and subsidence, respectively. Colored rectangles represent vertical GPS observations. Gray solid contours represent the coseismic slip of the 2011 earthquake, also shown in Figure 2.13.1a.

the observed horizontal (Figure 2.13.2a) and vertical (Figure 2.13.2c) displacements one year since the 2011 earthquake. In particular, the model predicts the order of magnitude of displacements at five marine GPS sites well (Figure 2.13.2a). The model has indicated that afterslip of the fault slows down logarithmically with time. The fault undergoes continuous afterslip of up to about three meters in the first six months since the earthquake and up to about four meters in two years (results not shown).

We have also studied the effects of two elastic subduction slabs in the south by taking into account the subducting Philippine Sea Plate and weaker lower crust below the volcanic arc. Such structure heterogeneity has minimum effects on the postseismic deformation of the 2011 Tohoku earthquake (results not shown). We are also using repeating earthquakes that periodically rupture the same segments of the megathrust (Uchida and Matsuzawa, 2013) to improve the constraints on the location and rheology of the shear zone.

Acknowledgements

We thank Paramesh Banerjee for providing processed daily GPS time series of land stations by the Geospatial Information Authority (GSI) of Japan and Kelin Wang's group at Pacific Geoscience Center, Geological Survey of Canada for the finite element code. This work is funded by NSF grant no. 1246850.

References

Bürgmann, R., and G. Dresen, Rheology of the lower crust and upper mantle: Evidence from rock mechanics, geodesy, and field observations, *Annu. Rev. Earth Planet. Sci.*, 36, 531–567, doi:10.1146/

annurev.earth.36.031207.124326, 2008.

Fujiwara, T., S. Kodaira, T. NO, Y. Kaiho, N. Takahashi, and Y. Kaneda, The 2011 Tohoku-Oki Earthquake: Displacement Reaching the Trench Axis, *Science*, 334, 1240, doi:10.1126/science.1211554, 2011.

Hu, Y., and K. Wang, Spherical-Earth finite element model of short-term postseismic deformation following the 2004 Sumatra earthquake, *J. Geophys. Res.*, 117(B5), B05404, doi:10.1029/2012JB009153, 2012.

Iinuma, T., et al., Coseismic slip distribution of the 2011 off the Pacific Coast of Tohoku Earthquake (M9.0) refined by means of seafloor geodetic data, *J. Geophys. Res.*, 117, B07409, doi:10.1029/2012JB009186, 2012.

Nakajima, J., and A. Hasegawa, Anomalous low-velocity zone and linear alignment of seismicity along it in the subducted Pacific slab beneath Kanto, Japan: Reactivation of subducted fracture zone? *Geophys. Res. Lett.*, 33, L16309, doi:10.1029/2006GL026773, 2006.

Ozawa, S., T. Nishimura, H. Suito, T. Kobayashi, M. Tobita, and T. Imakiire, Coseismic and postseismic slip of the 2011 magnitude-9 Tohoku-Oki earthquake, *Nature*, 475, 373–376, doi:10.1038/nature10227, 2011.

Uchida, N., and T. Matsuzawa, Pre- and postseismic slow slip surrounding the 2011 Tohoku-oki earthquake rupture, *Earth Planet. Sci. Lett.*, doi:10.1016/j.epsl.2013.05.021i, 2013.

Wang, K., Y. Hu, and J. He, Deformation cycles of subduction earthquakes in a viscoelastic Earth, *Nature*, 484, 327–332, doi:10.1038/nature11032, 2012.

14 Ambient Seismic Noise Monitoring for Stress-Induced Changes in the Geysers Geothermal Field, California

Voon Hui Lai, Taka'aki Taira, Douglas Dreger

Introduction

The Geysers Geothermal Field in California is one of the most seismically active zones in North America. We investigate the temporal change of the stress field within this region, by analyzing the small perturbations of the velocity structure through the correlations of ambient seismic noise. The cross correlation of ambient noise recorded between two stations over a period of time is used to extract the impulse response or the Green's function between the stations (*Shapiro and Campillo, 2004*), which can then be used to detect temporal changes in seismic velocity. We are particularly interested in detecting temporal perturbations associated with seismic velocity structure accompanying tectonic events and fluid injections.

Methodology

For this study, we follow closely the ambient noise data processing procedure described in *Seats et al. (2012)*. Our procedure consists of three phases: (1) preparation of single station seismic record, (2) cross-correlation of the data between two stations and temporal stacking, and (3) measurement of the travel time shift.

Preparation

Vertical components of the continuous record of seismic noise for over 12 months are obtained from an array of seismic stations operated by the Lawrence Berkeley National Laboratory (LBNL). This network contains 30 seismic stations distributed over the entire Geysers geothermal field with an average station distance of 2 to 3 km. This translates into 435 possible pair combinations of the stations in which some pairs have overlapping paths that allow us to verify the consistency of the Green's function along the same path.

The instrument response, mean, and trend are removed from the raw data, and a 0.1-0.9 Hz band-pass filter is applied. Finally, a whitening procedure is applied to broaden the frequency band of ambient seismic noise. For the output data, we test a few different sampling rates (20, 50 and 100 Hz) and determine that 20 Hz is the most optimum rate, with the greatest amplitude for the Green's function extracted in a frequency range of 0.1 Hz to 0.9 Hz (see Figure 2.14.2).

Cross-correlation and Stacking

We compute hourly cross-correlations of the seismic noise between two stations and stack the correlations into 1-day and subsequently 30-day stacks to obtain a reference Green's function (RGF) with high signal to noise ratio. Overlapping time windows are used to reduce any dependencies or effects of high amplitude transient signals (*Seats et al., 2012*).

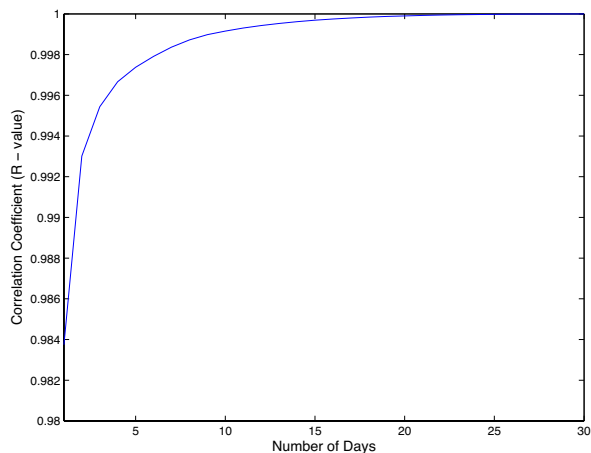


Figure 2.14.1: The mean correlation coefficient (R-value) of a month-long RGF against the stacked correlation in different numbers of consecutive days. The result shows the stacked correlation achieves a very high R-value (0.999) and begins to stabilize after a short period of 9 cumulative days.

Measurement

We estimate the relative travel time shift between the RGF and the 30-day stacked correlations in the frequency range from 0.1 to 0.9 Hz by computing a local travel time shift between the two Green's functions and measuring the slope of the travel time shifts as a function of lapse time. If the structure experiences a spatially homogeneous relative seismic velocity change due to tectonic events or fluid injections, the relative velocity change will be the opposite value of the relative travel time shift (*Brennguier et al., 2008*). The relative velocity change is typically small (less than 1%).

Discussion

On occasion, continuous data may contain gaps due to various technical problems such as failed data loggers and telemetry dropouts. As a result, these data that contain gaps are removed from the analysis. To ensure the reliability of our correlations, we perform a synthetic noise analysis by calculating the mean correlation coefficient (R-value) of a month-long RGF against the stacked correlation in different numbers of consecutive days. We find that the resulting R-value exceeds 0.999 with a 9-day stack of Green's functions (Figure 2.14.1). This shorter time window would allow us to examine time-varying seismic structure with a high temporal resolution. We plan to follow up with a more rigorous analysis to better reflect the actual data condition that includes rejected hourly data in random days in the month.

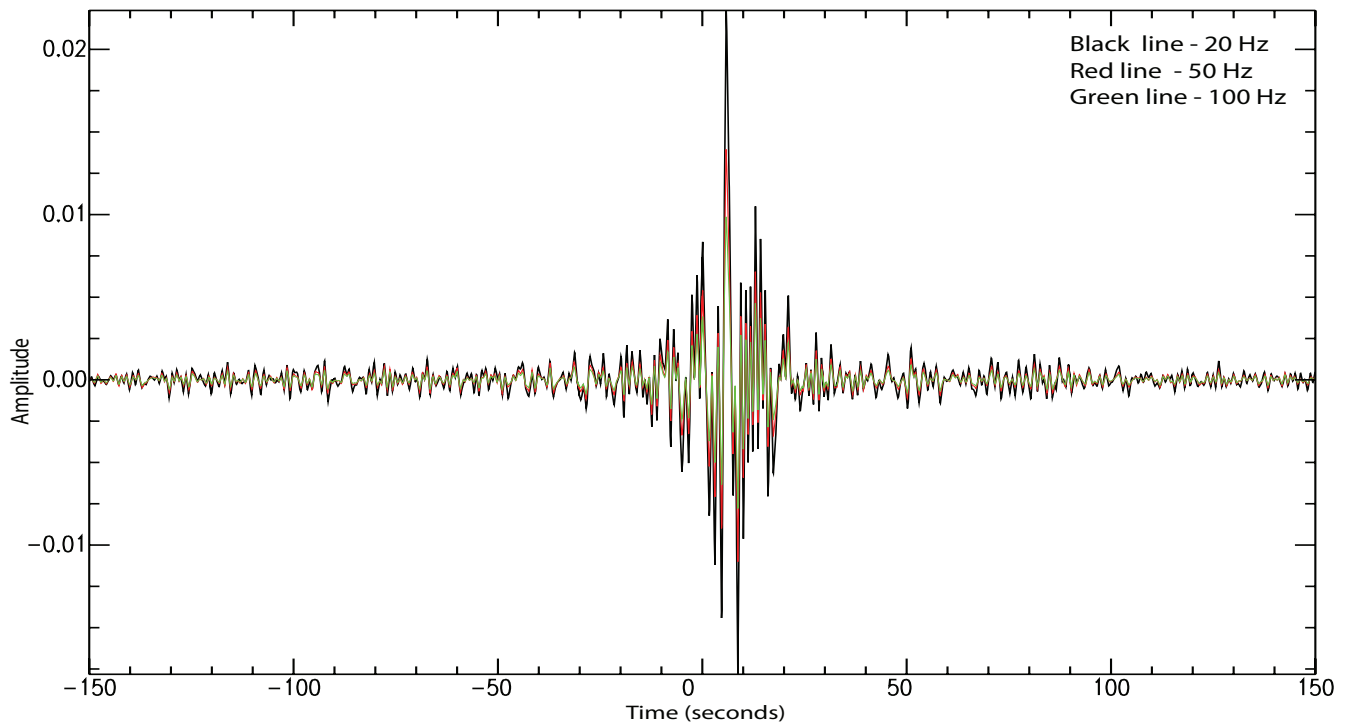


Figure 2.14.2: Stacked correlations of the same station pairs using different output sampling rates (20, 50, and 100 Hz). The resulting three outputs show great similarity in Green's function. The 20 Hz output marked with a black line shows the largest amplitude.

We also observe several gaps in the hourly data that span less than a minute. An alternative to minimize the loss of rejected data is to reduce our time window by preparing 30 minute-long data instead of hourly data. However, there will be a trade-off between retaining data and computational time.

The relative seismic velocity change within the structure after tectonic events (e.g., *Brenguier et al., 2008*) and fluid injection can provide information about stress changes in seismogenic zones such as the Geysers. As a follow up to this study, we will revisit important assumptions, in particular the ambient seismic noise source, in order to have a greater confidence in our result.

Acknowledgements

This work is funded by the National Science Foundation under award number NSF, EAR-1053211. We would also like to thank A. Nayak and S.H. Yoo for their support.

References

- Brenguier, F., N. M. Shapiro, M. Campillo, V. Ferrazzini, Z. Duputel, O. Coutant and A. Nercessian, Towards forecasting volcanic eruptions using seismic noise. *Nature Geoscience*, Vol 1, Issue: 2, p. 126-130, 2008.
- Brenguier, F., M. Campillo, C. Hadziioannou, N. M. Shapiro, R. M. Nadeau, E Larose, Postseismic Relaxation Along the San Andreas Fault at Parkfield from Continuous Seismological Observations. *Science*, Vol. 321. P. 1478- 1481, 2008.
- Seats, K. J., J. F. Lawrence and G. A. Prieto, Improved Ambient noise correlation functions using Welch's method. *Geophys. J. Int.* 188, 513-523. doi: 10.1111/j.1365-246X.2011.05263.x, 2012.
- Shapiro, N. M. and M. Campillo, Emergence of broadband

Rayleigh waves from correlations of the ambient seismic noise. *Geophys. J. Int.* 31, L07614, doi: 10.1029/2004GL019491, 2004.

15 Automated Measurement of P- and S-Wave Differential Times for Imaging Spatial Distributions of the V_p/V_s Ratio with a Moving-Window Cross-Correlation Technique

Taka'aki Taira and Aitaro Kato (Earthquake Research Institute, University of Tokyo)

Introduction

A high-resolution V_p/V_s ratio estimate is one of the key parameters needed to understand spatial variations in composition and physical states within the Earth. *Lin and Shearer (2007)* recently developed a methodology to obtain local V_p/V_s ratios in individual similar earthquake clusters, based on P- and S-wave differential times. A waveform cross-correlation approach is typically employed to measure those differential times for pairs of seismograms from similar earthquake clusters, at narrow time windows around the direct P- and S-waves. This approach effectively collects P- and S-wave differential times and requires the robust P- and S-wave time windows that are extracted to be based on manually or automatically picked P- and S-phases. We present another technique to estimate P- and S-wave differential times by exploiting temporal properties of delayed time as a function of elapsed time on the seismograms with a moving-window cross-correlation analysis (*e.g.*, *Sniieder, 2002; Niu et al., 2003*).

Methodology

Following *Lin and Shearer (2007)*, V_p/V_s ratio within similar earthquake clusters can be expressed as

$$(\delta t_s^i - \delta \bar{t}_s) = (V_p/V_s)(\delta t_p^i - \delta \bar{t}_p) \quad (1.1)$$

where δt_p^i and δt_s^i represent the P- and S-wave differential times for a single pair of earthquakes in a cluster obtained from the station i , respectively, and $\delta \bar{t}_p$ and $\delta \bar{t}_s$ are the median values of the P and S differential times from all stations.

We use a moving-window cross-correlation analysis to measure S-wave differential time. In this analysis, we evaluate time evolutions of delay times from a pair of similar earthquakes. Two seismograms aligned by the direct P-waves yield that delayed times become zero around the direct P-wave. In contrast, delayed times obtained from time windows including the direct S-wave have a non-zero value.

Our approach, in principle, is capable of measuring both P- and S-wave differential times from single-component seismograms. In an ideal case, the temporal evolution of delayed time becomes a step function with its discontinuity at the onset of the direct S-wave. The offset or constant delay time (dt) in the resulting step function would be the S-wave differential time, relative to the P-wave differential time as the two waveforms are aligned by the direct P wave.

$$dt^i = \delta t_s^i - \delta t_p^i \quad (1.2)$$

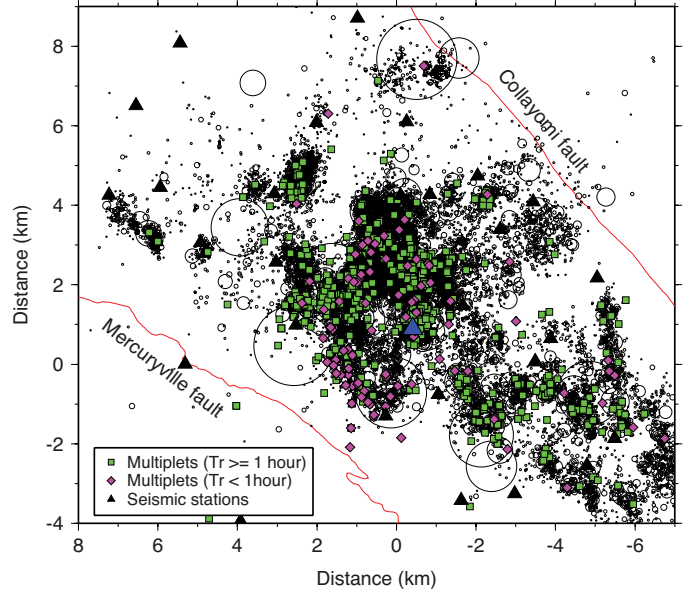


Figure 2.15.1: Map view of the Geysers similar event clusters (multiplets) identified in our analysis. Green squares and purple diamonds are the multiplets with longer (≥ 1 hour) and shorter (< 1 hour) recurrence intervals, respectively. The Black triangles are the LBNL and USGS seismic stations. The Blue triangle is station GDXB. Broadband data from station GDXB were used to identify the Geysers multiplets. Black circles are locations of relocated earthquakes in this area during 1984 to 2008 (*Waldhauser and Schaff, 2008*). Circle sizes are proportional to earthquake rupture sizes.

Analysis

We apply our moving-window cross-correlation technique to the two different data sets collected at: 1) the Wakayama district, Japan and 2) the Geysers geothermal field, California (Figure 2.15.1). Both of the target areas are characterized by earthquake swarms that provide a number of similar event clusters.

We use the following automated procedure to systematically analyze the two data sets: 1) identifying the direct P arrivals on the vertical component data by using an Akaike Information Criterion based on a phase picking algorithm introduced by *Zhang et al. (2003)*, 2) performing the waveform alignment by the P-wave with a waveform cross-correlation to obtain the P-wave differential time, δt_p^i , 3) the moving-time window analysis to estimate the S-wave differential time, $\delta \bar{t}_s$ (Figure 2.15.2).

Kato et al. (2010) have estimated the V_p/V_s ratios for a few similar earthquake clusters from the Wakayama data set, by a conventional approach to obtain differential times. As shown in Figure 2.15.3, we find that the resulting V_p/V_s ratios from

our approach for the same earthquake clusters are comparable

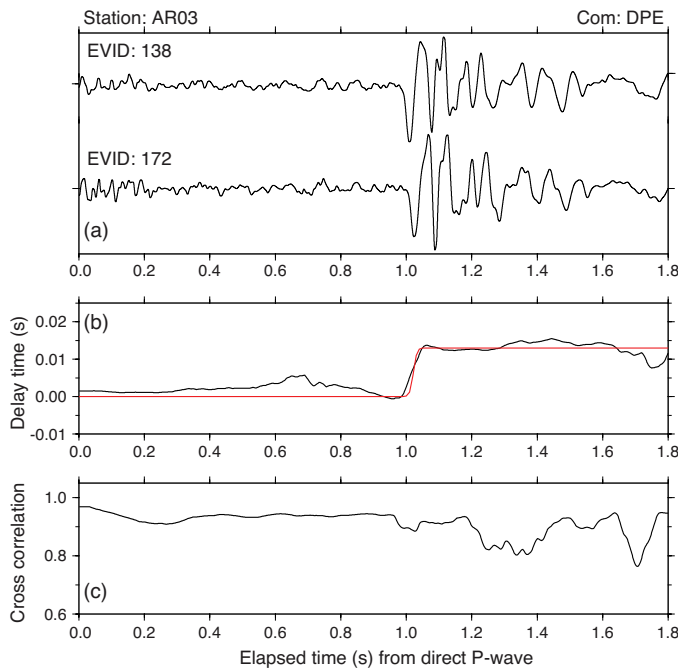


Figure 2.15.2: S-wave differential times measurement with a moving-window cross-correlation analysis. (a) Observed seismograms recorded at station AR03 in the east-west component for two Wakayama local earthquakes (evnet-ids 138 and 172). Waveforms are aligned by the direct P-wave. The resultant P-wave differential time is -0.0239 s. Amplitudes are normalized by their maximum amplitudes. (b) Delay time and (c) cross-correlation value from a moving-window cross-correlation analysis. Red line shown in (b) is the best fit step function with the offset of 0.0123 s. Using equation (15.2), the resulting S-wave differential time is -0.0116 s.

with those obtained from *Kato et al.* (2010). We also find that the moving-window cross-correlation technique effectively measures both P- and S-wave differential times for the seismograms in which the clear P- and S-phases are not observed.

Acknowledgements

We thank the Northern California Earthquake Data Center and the Lawrence National Berkeley Laboratory for data collection and distribution for the Geysers seismic data. This work is supported by the National Science Foundation grant EAR-1053211.

References

- Kato, A., S. Sakai, T. Iidaka, T. Iwasaki, and N. Hirata, Non-volcanic seismic swarms triggered by circulating fluids and pressure fluctuations above a solidified diorite intrusion, *Geophys. Res. Lett.*, 37, L15302, doi:10.1029/2010GL043887, 2010.
- Lin, G., and P.M. Shearer, Estimating local V_p/V_s ratios within similar earthquake clusters, *Bull. Seismol. Soc. Am.*, 97, 379–388, 2007.
- Niu, F., P.G. Silver, R.M. Nadeau, and T.V. McEvilly, Stress-Induced Migration of Seismic Scatterers Associated with the 1993 Parkfield Aseismic Transient Event, *Nature*, 426, 544–548, 2003.
- Snieder, R, Coda wave interferometry and the equilibration of energy in elastic media. *Phys. Rev. E.*, 66, 046615, 2002.

Waldhauser, F. and D.P. Schaff, Large-scale relocation of two decades of Northern California seismicity using cross-correlation and

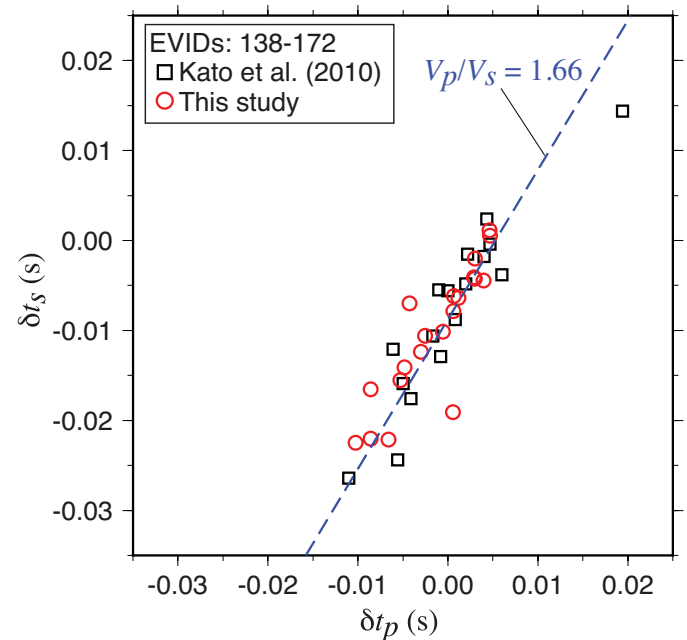


Figure 2.15.3: P differential arrival times versus S differential arrival times for a single pair of events investigated by *Kato et al.* (2010). Black squares and red circles are the P and S differential time measurements by *Kato et al.* (2010) and our study, respectively. The blue dashed line passing through the points is the best fitting line from a least-squares method. The slope of the line is 1.66, which is the resulting V_p/V_s ratio.

double-difference methods, *J. Geophys. Res.*, 113, B08311, doi:10.1029/2007JB005479, 2008.

Zhang, H.J., C. Thurber, and C. Rowe, Automatic P-wave arrival detection and picking with multiscale wavelet analysis for single-component recordings, *Bull. Seismol. Soc. Am.*, 93(5), 1904–1912, 2003.

16 Inferring a Maximum *A Posteriori* Probability Model from Geodetic Data

Jianbao Sun

Introduction

Space geodetic techniques, particularly GPS and Interferometric Synthetic Aperture Radar (InSAR), have become vital tools for earthquake and crustal deformation studies, in recent years. Data measured using these techniques have been widely used for inversion of coseismic, postseismic and interseismic slip, as well as for inferring best-fit source parameters of geophysical phenomena. A number of optimization methods exist for modeling and interpretation of geodetic data (*e.g.* Menke, 2012; Tarantola, 2005). Each approach has pros and cons for solving the geodetic inversion problems, but we mostly rely on the different forms of least squares methods for both linear and nonlinear problems. This is vital for geodetic data interpretation because InSAR provides extremely high horizontal resolution, with a few to tens-of-meter pixel size for most of the satellites, such as the Envisat satellite from the European Space Agency (ESA) or the TerraSAR-X satellite from German Aerospace Center (DLR). The high resolution, with unprecedented deformation measurement precision, requires that InSAR data be inverted with efficient algorithms. This is a challenge for geophysical studies and emergency responses, because the problems are strongly nonlinear when geodetic data are linked with geophysical models.

A class of inversion approaches for geodetic data relies on probabilistic inversion methods, which describe the inversion problem as an *a posteriori* probability density function (PDF) sampling process. The *a posteriori* PDF is composed of a prior PDF of unknown parameters and a likelihood function connecting data with theoretical models. The prior PDF is updated using the likelihood function according to Bayes' theorem. The *a posteriori* PDF is sampled with a Markov Chain Monte Carlo (MCMC) method. This is the Bayesian inversion method for geodetic inverse problems. Fukuda and Johnson (2008) developed the Fully Bayesian inversion method, which treats every unknown parameter as a nonlinear parameter and inverts in a MCMC process, without using the least squares inversion. This method is theoretically advantageous for solving the problem for all of the unknown parameters in a unified framework and one process. However, it also complicates the parameter search in a high-dimension nonlinear space with large amounts of observations, such as InSAR data. Fukuda and Johnson (2010) developed another *a posteriori* PDF for geodetic inversion problems, which uses linear least squares inversion with a MCMC sampling process for nonlinear parameters, called Mixed linear-nonlinear Bayesian inversion method. This is a reasonable treatment to geodetic problems because they have both linear and nonlinear properties. The least squares solution for linear parameters greatly reduces the computation cost compared to the solution of treating all parameters as non-linear.

A Maximum *A Posteriori* Probability Model

The Bayesian methods are still far less efficient than the pop-

ular global optimization methods, such as simulated annealing, genetic, or neighborhood algorithms. However these methods are not optimized for uncertainty estimates. In addition, the two Bayesian inversion methods risk to be trapped in low-probability regions, or might never sample disconnected regions of the parameter space, leading to divergence of the inversion. This can occur because the structure of parameter space is unknown, and we cannot guarantee that a random walk is able to explore the global parameter space. It is quite possible that the collected models close to the mathematical maximum of the *a posteriori* PDF are not geophysically reasonable.

Our solution to these problems is to use the fast global optimization algorithm—Adaptive Simulated Annealing (ASA) (Ingber, 1993)—to search the parameter space, while using constraints for both linear and nonlinear parameters to guarantee that physically reasonable models are collected (Sun *et al.*, 2013). This falls in the well known class of Maximum-*A-Posteriori* (MAP) methods. The 'mode' of the *a posteriori* PDF will be searched through the global optimization inversion. The parameter uncertainties are not obtained as conveniently as in the Bayesian methods. However, by analyzing the models collected at the later stage of the inversion, or starting an independent Bayesian inversion after the MAP inversion, it would be easy to estimate the parameter uncertainties, because the efficiency of the MCMC method depends on how far the initial solution is from the 'mode' of the posterior PDF.

We use the *a posteriori* PDF from Fukuda and Johnson (2010) as the optimization objective. By using this *a posteriori* PDF, some of the important advantages of the Bayesian method are inherited, *e.g.*, objective smoothing of slip solutions, a unified solution for all of the parameters in one process (regularization factor, data weights, unknown fault geometry parameters and fault slips). This is in contrast to using a uniform slip assumption in a prior step. Currently, we mainly use the MAP method for coseismic slip inversions, including both highly nonlinear parameters and a large number of fault-slip parameters, with high-resolution geodetic observations, such as GPS and InSAR data. However, the method is not limited to coseismic slip inversions, and other geophysical problems with both linear and nonlinear properties can be addressed with this method in a more efficient manner if the nonlinear properties are weak. The MAP method we developed here gains high efficiency due to using the very fast global optimization method ASA. It normally takes only a few minutes to obtain a solution for one-segment slip models of a blind fault, even with a large number (> 1000) of data points. For multiple fault-segment models, the computation cost depends on the number of nonlinear parameters and the matrix size of the least squares inversion. However, the MAP inversion can quickly converge to the vicinity of the *a posteriori* PDF mode in the initial stage, with the following iterations refining the solution step by step. This is particularly useful in rapid-response applications, where a first-order model is needed; *e.g.*, for stress transfer assessment after an earthquake.

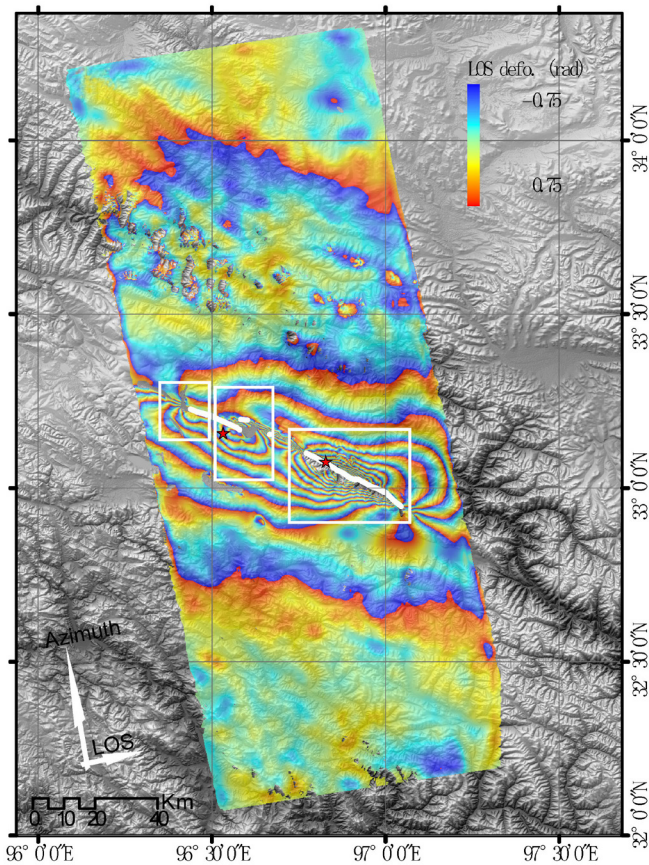


Figure 2.16.1: One of the L-band InSAR interferograms of the 2010 Yushu, China earthquake produced from ALOS PALSAR data. The white lines show the surface rupture from field investigations and the white rectangles highlight areas of high displacement gradients. The right star is the location of the maximum surface slip, and the left one is the epicenter from USGS solution. Note that the fringe between 33.5°N and 34.0°N, is likely due to atmospheric delay, rather than earthquake deformation.

Moreover, it is promising to use this method to construct a database of geophysical models from geodetic data in a unified form, so that the underlying deformation mechanisms of the lithosphere can be inferred.

A MAP Model Case of a Large earthquake

The slip model of the April 14, 2010 Mw 6.9 Yushu, China earthquake is a modestly difficulty case, composed of three segments with a sinistral strike-slip dominated mechanism. There are 3537 subsampled InSAR data points on three tracks used in the inversion (Figure 2.16.1). We failed to get the inversion to converge using Bayesian inversions of the three tracks of InSAR data; however, the inversion stably converged to the model shown in Figure 2.16.2 using the MAP method.

References

Fukuda J., and Johnson, K., A Fully Bayesian Inversion for Spatial Distribution of Fault Slip with Objective Smoothing, *Bulletin of The Seismological Society of America*, 98(3), 1128-1146, doi:10.1785/0120070194, 2008.

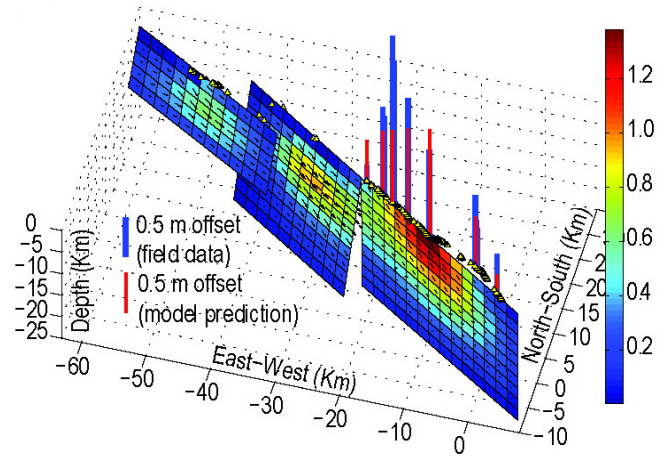


Figure 2.16.2: The MAP model of the 2010 Yushu, China earthquake. Also shown are the model offset predictions at the surface with field data for comparison.

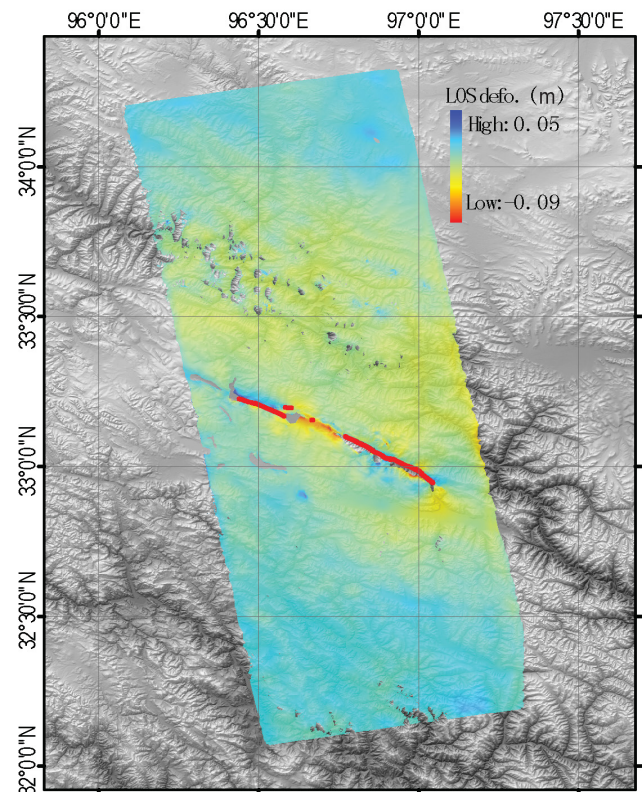


Figure 2.16.3: The residuals of the interferogram in Figure 2.16.1 after removal of the forward modeled InSAR deformation using the MAP model in Figure 2.16.2. Note that the unwrapped fringe between 33.5°N and 34.0°N still exists.

Fukuda J., and Johnson, K.M., Mixed linear-non-linear inversion of crustal deformation data: Bayesian inference of model, weighting and regularization parameters, *Geophysical Journal International*, 181(3), 1441-1458, doi:10.1111/j.1365-246X.2010.04564.x, 2010.

Sun J., Shen, Z.-K., Bürgmann, R., Wang, M., Chen, L., and Xu, X., A three-step Maximum-A-Posteriori probability method for InSAR data inversion of coseismic rupture with application to the April 14, 2010 Mw 6.9 Yushu, China earthquake, *J. Geophys. Res.*, in press, doi:10.1002/jgrb.50244, 2013.

17 Exploring Landslide and Granular Mechanics from Geodetically Derived Surface Flow Kinematics

Brent Delbridge, Roland Bürgmann, Eric Fielding, Scott Hensley, Bill Schulz

Introduction

This project focuses on improving the understanding of the physical mechanisms controlling landslide motion by studying the landslide-wide kinematics of the Slumgullion landslide in southwestern Colorado using interferometric synthetic aperture radar (InSAR) and GPS. Factors which may control the landslide motion include pore-water pressure, inertia, the geometry of the landslide boundaries, and material properties such as strength, viscosity, hydraulic conductivity, diffusivity, and density (Schulz *et al.*, 2009b, Schulz *et al.*, 2009a). Our task is to examine the relative importance of each of these factors by understanding how they manifest themselves as observable modulations of the slide deformation under different external forcing such as rainfall, snowmelt and atmospheric pressure variations.

The deformation field derived from InSAR will provide the necessary observations to interpret and identify the spatial scale-dependent processes by providing the important length scale observations necessary to go beyond kinematic slide models and use this slide as a large granular shear experiment to push our current understanding of granular media.

By utilizing the temporal resolution of real-time GPS acquired during a temporary deployment from July 22nd through August 2nd with the landslide-wide coverage of the InSAR-derived deformation, we hope to elucidate the landslide response to environmental changes such as rainfall, snowmelt, and atmospheric pressure, and consequently, the mechanisms controlling the dynamics of the system.

The results of this study will also allow us to test the agreement and commensurability with Uninhabited Aerial Vehicle Synthetic Aperture Radar (UAVSAR) derived deformation with real-time GPS observations and traditional satellite-based SAR interferometry from the COSMOSkyMed system. We will not only help mitigate the hazards associated with large landslides, but also provide information on the limitations of current geodetic imaging techniques. This unique opportunity to compare several concurrent geodetic observations of the same deformation will provide constraints and recommendations for the design and implementation of future geodetic systems for the monitoring of earth surface processes.

The Slumgullion Natural Laboratory

The Slumgullion landslide provides an ideal setting in which to study landslide mechanics because of its rapid deformation rates of up to 2 cm/day and large spatial extent in which to examine the complex interaction of different kinematic elements within the slide (3.9 km long with an estimated volume of 20×10^6 m³, Parise and Guzzi, 1992). The slide has also shown sensitivity to rainfall, snowmelt, and atmospheric pressure variations from passing storm fronts and the solid earth and ocean tides (Schulz,

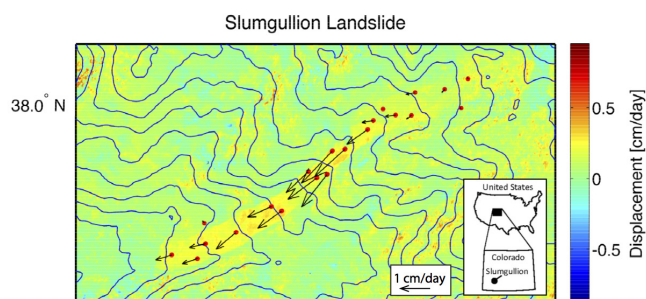


Figure 2.17.1: The colors above show the line-of-sight (LOS) displacement inferred from a pair of UAVSAR images collected one week apart on April 16th and 23rd 2012. The red circles and corresponding black vectors show GPS derived horizontal motion. The Slumgullion landslide is located in the San Juan Mountains of southwestern Colorado (inset) and has been moving for approximately the last 300 years (Crandell and Varnes, 1961) with total displacement on the order of hundreds of meters (Coe *et al.*, 2003).

2009). The clearly measurable response of the slide motion to environmental forcing makes Slumgullion a perfect natural laboratory.

Fleming *et al.* (1999) performed detailed mapping of the landslide and showed that the landslide has about a dozen kinematic units. These units are generally separated by narrow zones across which most differential displacement occurs. Fleming *et al.* (1999) measured average annual velocities of (0.5-2.0 cm/day) with lowest velocity at the landslide head (0.3 cm/day), low velocity at the toe (0.5 cm/day), and greatest velocity (2 cm/day) where the landslide is narrowest and steepest. They found that velocity varies seasonally, presumably due to changes in pore-water pressures. Coe *et al.* (2003) performed periodic surveying of surface monuments distributed across the landslide and hourly monitoring at two locations of landslide displacement, air and soil temperature, snow depth, rainfall, soil-water content, and groundwater pressures within an apparently perched aquifer. They found that the landslide moved fastest during spring and summer and slowest during winter. The time between rainfall and the landslide velocity response was less than several weeks.

Schulz and others (2009a,b) performed further sampling, field testing and monitoring at one location on the side of the landslide for three years. They found the landslide motion accelerated when pore-water pressure increased within the landslide body, but the pore-water decreased along the landslide margin. The decrease in pore pressure at the slide margins probably occurred in response to shear-induced soil dilation. Consequently, the decreased pore-water pressures increased effective stress and caused the landslide to decelerate. This hypothesis is supported by large-scale ring-shear tests on shear zone soils, precise leveling across part of the bounding shear zone, *in situ* hydrologic testing, and laboratory measurements of soil porosity (Schulz *et al.*, 2008).

Current Research

The NASA/JPL UAVSAR airborne repeat-pass SAR interferometry system imaged the Slumgullion landslide from four look directions on eight flights in 2011 and 2012. Combining the four look directions allows us to extract the full 3-D velocity field of the surface. COSMO-SkyMed(CSK) high-resolution Spotlight data was also acquired during time intervals overlapping with the UAVSAR one-week pairs, with intervals as short as one day. Interferograms made from pairs of CSK images acquired in 2010, 2011 and 2012 reveal the slide deformation on a longer timescale by allowing us to measure motion on a scale of meters and see the average rates over year-long intervals using pixel offset tracking of the high-resolution SAR amplitude images. The spatially complex deformation field derived from InSAR will provide the necessary observations to interpret and identify the spatial scale-dependent processes present by providing the important length scale observations necessary to go beyond kinematic slide models.

Additionally, TerraSAR-X repeat-pass interferometry data was acquired in 2011–2012 and TanDEM-X bistatic (single-pass interferometry) data was acquired in 2011. The TanDEM-X bistatic data will enable construction of a high-resolution InSAR digital elevation model. These observations were taken to complement and overcome the spatial limitations of ongoing yearly GPS observations from 18 monitoring points and *in situ* observations of pore-pressure and atmospheric parameters acquired by collaborator Bill Schulz from the USGS. The high resolution topography derived from our Tandem-X BiStatic data will be used to correlate the slide topology with its complex spatial deformation, which will allow me to extract the roles played by composition and geometry. We continued to build upon this work by beginning an independent field investigation consisting of the deployment of seven continuous GPS stations along the length of the slide from July 22nd to August 2nd, 2012. This time period was concurrent with the acquisition of several SAR images including a pair of four-pass UAVSAR flights July 24th–August 1st 2012. COSMO-SkyMed high-resolution Spotlight data was also acquired over the landslide during time intervals overlapping with the UAVSAR one-week pairs and GPS deployment, with time intervals as short as one day. (five CSK acquisitions total, three descending track and two ascending track). Additionally, the topographic data will also act as a unique and independent dataset allowing for quantitative geomorphometric analysis.

We believe that the synthesis of these observations will result in a more robust estimate of the total slide displacement, and yield a robust estimate of the systematic and random errors present in these observations. The temporal resolution of the real-time GPS will compliment the landslide-wide spatial coverage of the InSAR-derived deformation to provide full coverage of the surface displacement. The spatiotemporal overlap of the various geodetic datasets in this study provide a unique opportunity to quantify information on the limitations of current geodetic imaging techniques, and their application to studying earth surface processes.

3D Displacement Vectors

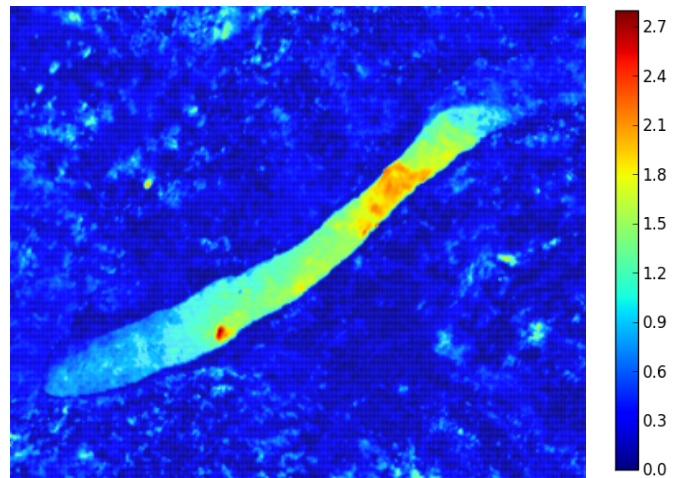


Figure 2.17.2: The image above shows the magnitude of the 3D displacement vectors which were estimated from four UAVSAR one-week interferogram pairs spanning April 16th–April 23rd 2012 (one of these images used is shown in Figure 2.17.1). The slide velocity increases with warmer colors. The narrow, rapid portion of the slide reaches the 2 cm/day previously measured by *Coe et al.*, 2003 and others. Note that the largest velocity magnitudes of 2.7 cm/day are restricted to a small isolated region near the toe of the slide, and appear to be a smaller slide piggybacking on the larger flow. The coincident acquisition of these images along four independent flight paths allowed us to extract the true physical displacement of the image ground surface. This procedure overcomes the ambiguity in determining the slide motion present in a single interferogram, which only yields deformation information in the ‘look direction’.

Acknowledgements

This has been supported by an NSF Graduate Research Fellowship and is a collaboration of The University of California Berkeley with the USGS in Colorado, and Jet Propulsion Laboratory in Pasadena, California.

References

- Coe, J. A., Ellis, W. L., Godt, J. W., Savage, W. Z., Savage, J. E., Michael, J. A., & Debray, S., Seasonal movement of the Slumgullion landslide determined from Global Positioning System surveys and field instrumentation, July 1998–March 2002, *Engineering Geology*, 68(1), 67-101, 2003.
- Fleming, R. W., Baum, R. L., & Giardino, M., Map and description of the active part of the Slumgullion landslide, Hinsdale County, Colorado, US Department of the Interior, US Geological Survey, 1999.
- Schulz, W. H., Kean, J. W., & Wang, G., Landslide movement in southwest Colorado triggered by atmospheric tides, *Nature Geoscience*, 2(12), 863-866, 2009.
- Schulz, W. H., McKenna, J. P., Kibler, J. D., & Biavati, G., Relations between hydrology and velocity of a continuously moving landslide: evidence of pore-pressure feedback regulating landslide motion?, *Landslides*, 6(3), 181-190, 2009.

18 Geodetic Tracking and Characterization of Precipitation Triggered Slow Moving Landslide Displacements in the Eastern San Francisco Bay Hills, California, USA

Julien Cohen-Waeber, Roland Bürgmann, Nicholas Sitar, Alessandro Ferretti, Chiara Giannico, Marco Bianchi

Introduction

Technologies such as continuous Global Positioning Systems (GPS) and Interferometric Synthetic Aperture Radar (InSAR) are now capable of measuring active surface displacement with as much as sub-centimeter precision and accuracy. While GPS has become such a fundamental tool that tracking discrete points in real time is common and reliable, its finite spatial extent is a shortcoming. Alternatively, the introduction of InSAR has allowed widespread surface deformation tracking, though it is still far from being real time. Evidently, these technologies are complementary and lend themselves to numerous geological engineering applications including the characterization and tracking of subsidence, seismically induced crustal deformation, or in our case, landslides. Thus, the objective of this work is to characterize, by a careful observational program, active slope deformation resulting from various static and dynamic conditions across the Lawrence Berkeley National Laboratory (LBNL) site and the San Francisco East Bay hills (Berkeley Hills). Through the instrumentation of individual landslides with a comprehensive network of continuous GPS stations, and regional monitoring of slope surface deformation by InSAR time series analysis, this study focuses on the effects and characterization of precipitation triggered slow moving landslide displacements.

InSAR Time Series Analyses

A review of three independent InSAR time series analyses of the Berkeley Hills, from separate satellite acquisitions over different time intervals from 1992-2011, shows remarkable consistency (Hilley *et al.* 2004, Quigley *et al.* 2010, Giannico *et al.* 2011). In each case, a clear precipitation dependent behavior of landslide displacement has been observed, with similar mean downslope velocities of approximately 30 mm/year and periods of higher velocities during each wet season. Furthermore, these studies suggest that internal deformation of each slide mass is noticeable when divided into groups of coherently moving masses (Quigley *et al.* 2010, Cohen-Waeber *et al.* 2013). In fact, improved InSAR methods which allow higher spatial resolution have allowed preliminary conclusions on the mechanics of displacement within these landslides as different sections of the deformable slide mass mobilize separately.

The InSAR time series analysis of permanent scatterers performed by Hilley *et al.* (2004) first showed the use of InSAR for seasonal landslide displacement tracking using European Space Agency satellites ERS-1 and ERS-2 data acquisitions from 1992 to 2001. The study observed that periods of landslide acceleration were closely related to seasonal precipitation, though non-linear in that precipitation related displacement did not

occur immediately, with lag times of up to 3 months, and did not predictably increase with larger events.

Similarly, Quigley *et al.* (2010) examined seasonal precipitation-related displacement, supplementing the same ERS data set with the Canadian Space Agency's RADARSAT-1 acquisitions from 2001 to 2006. Landslide displacement was shown not only to be of the same magnitude as for the ERS data, but was also clearly seasonal and sensitive to variations in rainfall patterns as well. Detrended and stacked (by month) observations plotted against average monthly precipitation exhibited a clear 1 to 3 month displacement response lag time and a positive correlation to the intensity of precipitation.

An important limitation of the Permanent Scatterer InSAR method used in these examples is the presence of stable coherent targets. To improve spatial resolution, a new algorithm (SqueeSAR™) developed by Tele-Rilevamento Europa (TRE) utilizes both the Permanent and Distributed Scatterer methods (Ferretti *et al.* 2011). Thus, a third InSAR time series analysis was performed over the Berkeley Hills by Giannico *et al.* (2011) applying the SqueeSAR™ method to the German Space Agency's TerraSAR-X data acquisitions from 2009-2011. Once again, landslide related displacements were clearly identifiable with similar velocities and with periods of precipitation-related acceleration, though with better spatial coverage (Figure 2.18.1, top).

The higher spatial resolution afforded by the SqueeSAR™ method allows closer observation of the landslide mechanisms as expressed at the ground surface, much like in Quigley *et al.* (2010). In this case, the downslope displacements of different areas within the Berkeley Hills landslides reveal that they are in fact moving as bodies of smaller coherent masses, much like a flow slide, with what could be called an "accordion effect" (Cohen-Waeber *et al.* 2013). Differencing the average downslope displacements of the top, middle and bottom of the landslides reveals a pattern of apparent landslide extension, followed by a landslide shortening as the precipitation progresses. During wet seasons, the lower portions of the landslides accelerate earlier than the upper portions while toward the end of wet seasons and into dry periods, the lower portions of the landslides slow and the upper portions catch up (Figure 2.18.1, Bottom).

Continuous GPS Tracking

With the installation of seven continuous GPS stations on several LBNL and Berkeley Hills landslides, ground surface displacements are being tracked at a data collection rate of 1 Hz, since January 2012. While historical ground surface displacements related to these landslides have yet to be fully characterized and quantified, a clear signal from daily solutions at several of these stations is already apparent. Through two mildly wet

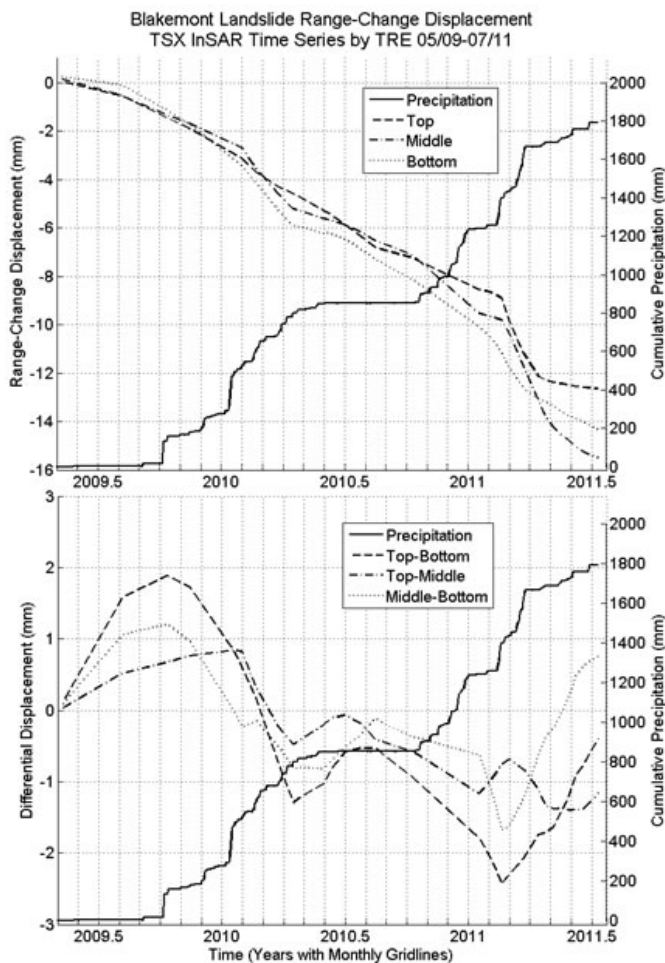


Figure 2.18.1: Average downslope range-change displacement (top) and differential of average downslope displacements from TRE SqueeSAR™ analysis of TerraSAR-X data acquisitions (2009-2011, bottom) in areas of Blakemont Landslide, versus cumulative precipitation (right axes).

seasons, GPS measurements have confirmed InSAR observations with well-defined precipitation triggered slope movement at similar average velocities and the same “accordion effect”.

Preliminary Conclusions

Overall, InSAR has demonstrated its capability to record and characterize landslide motions that otherwise would not have been observed with such level of detail. Records of landslide related surface displacement from several independent studies have similar precipitation triggered down-slope velocities, and comparable internal mechanisms exhibiting progressive accordion-like downslope failure typical to slow moving flow slides. While both methods of observation have not yet been compared on one landslide over the same period, they are complimentary and these observations have been verified by continuous GPS data. Improved InSAR spatial coverage and observations over longer periods will provide important insight on the triggering mechanisms and internal landslide behaviors described. Notably, further work is planned to explore the possibility of seis-

mically induced landslide motions. Despite recent moderate earthquakes in the region, these have not yet been documented, (Hilley et al. 2004, Cohen-Waeber et al. 2013) primarily due to the lack of temporal resolution with InSAR.

Acknowledgements

We gratefully acknowledge our financial support from the Lawrence Berkeley National Laboratory, Earth Science Division Director’s fund.

References

Cohen-Waeber J. et al., GPS Instrumentation and Remote Sensing Study of Slow Moving Landslides in the E. San Francisco Bay Hills, CA., Proceedings of the 18th Int. Conf. on Soil Mech. and Geotech. Eng., Paris, France, 2013.

Ferretti A. et al., A New Algorithm for Processing Interferometric Data-Stacks: SqueeSAR, *IEEE Geoscience and Remote Sensing* 49(9), 3460-3470, 2011.

Giannico C. and Ferretti A, SqueeSAR™ Analysis Area: Berkeley, *Processing Report*, Tele-Rilevamento Europa, Milano, IT, 2011.

Hilley G.E. et al., Dynamics of Slow Moving Landslides From Permanent Scatterer Analysis, *Science* 304, 1952-1955, 2004.

Quigley K. C. et al., Seasonal Acceleration and Structure of Slow Moving Landslides in the Berkeley Hills, Proc. of the 3rd Conf. on Earthquake Hazards in the E. San Francisco Bay Area; edited by Keith Knudsen, *CA Geol. Surv. Special Report* 219, 169-178, 2010.

19 Repeating Earthquake Slip Evolution Along 200 km of the Central San Andreas Fault

Robert M. Nadeau, Ryan C. Turner, and Roland Burgmann

Introduction

An historic catalog of micro-earthquakes and digital seismograms from the Northern California Seismic System (NCSS) extending back through 1984 enable a spatially and temporally extensive view of active faulting processes at depth using repeating earthquakes along a ~200km long section of the central San Andreas Fault (SAF) zone. We analyzed seismic data along this section to identify new repeating earthquake (REQ) sites and to update known REQ sites (Nadeau and McEvilly, 2004; Turner *et al.*, 2013) through April of 2011. This information was then used to infer the evolution of aseismic fault slip at seismogenic depth along the fault section in order to investigate the general underlying architecture and mechanics of the faulting process at the location and to assess the relationship of the REQ behavior with respect to the occurrence of larger ($> M4$) earthquakes in the region. This provides insights into the evolution and role of transient aseismic fault slip in earthquake occurrence that should ultimately lead to improved models of the earthquake cycle and aid in the development of more accurate earthquake forecasts.

Results

We searched for and updated REQs in the study zone using a waveform cross-correlation/cross-coherency method (Nadeau and McEvilly, 2004). The resulting REQ catalog consisted of 870 REQ sites comprised of 6011 repeated events (Figure 2.19.1). The REQ search region also included several 10s of km both northwest and southeast of the 200km section, but yielded little evidence of REQ activity in these presumably locked fault regions.

Deep fault creep inferred from the REQs (Nadeau and McEvilly, 2004) occurring on the SAF-proper show a clear decrease in rates (below the Pacific-North American relative plate motion rate of 3.3 cm/yr) to the northwest of the juncture of the San Andreas and Calaveras faults at about 90 km NW (Figure 2.19.1). Deep creep occurring off the SAF (i.e., to the northeast) is also observed along the Sargent fault (~140 to 160 km NW) (Turner *et al.*, 2013) and on the Paicenes-San Benito faults (~80 to 87 km NW). With the exception of the region from ~65 to 80 km NW, more complex spatial and temporal deep-creep behavior is also observed in regions of moderate to large earthquake activity ($>M4.0$).

In the Parkfield area, for example, a significant increase in the rate of creeping is observed following the M6.0 earthquake. Before the M6.0 event, cumulative creep was well behind that expected for freely creeping fault keeping pace with the relative plate motion rate of 3.3 cm/yr. However, by the end of the study period in April of 2011, the accelerated accumulation of creep resulting from the post-seismic creep released from the M6.0 appears to have resulted in a cumulative creep over the study

period that is consistent with the expected long-term accumulation of creep from tectonic plate motion, at least between +5 km and -15 km northwest.

Though a post-seismic increase in creep accumulation following the M6.0 is observed southeast of -15 km, it continues to lag behind the plate rate, indicating an increase in slip deficit of ~50-60 cm since the end of 1984 at the southeastward end of the study segment. This and the absence of identifiable REQs farther to the southeast is consistent with classification of the Cholame segment of the SAF as a type-A locked fault segment capable of rupturing in an ~M7.0 or larger earthquake (UCERF 2, 2007).

Two prominent along-strike dips in the cumulative deep creep contours are also observed centered at about 73 and 85 km NW. The 85 km dip appears to correspond well with the location of the off-SAF sequences, suggesting relative plate motion that is to be accommodated by deformation on at least two sub-parallel fault zones. The dip at 73 km has no corresponding off-fault REQ activity, but the spatial distribution of low-rate REQs appears to outline a low-repeat-rate seismicity hole, possibly indicating a zone of slip-deficit accumulation above ~6km that has dimensions of about 15 km along-strike and 5 km in depth. The slip deficit in this area is on the order of 40 cm, since 1984 and if an earthquake were to rupture over this area and release this accumulated deficit it could generate an M5 or larger earthquake.

Acknowledgements

Supported by the U.S. Geological Survey through award G10AC00093 and by the National Science Foundation through award EAR-0951430. Waveform data were provided by the Northern California Seismic System, USGS, Menlo Park by way of the Northern California Earthquake Data Center at the Berkeley Seismological Laboratory (BSL).

References

- Nadeau, R. M. and T. V. McEvilly, Periodic Pulsing of Characteristic Microearthquakes on the San Andreas Fault, *Science*, 303, 220-222, 2004.
- Turner, R.C., R.M. Nadeau and R. Burgmann, Aseismic Slip and Fault Interaction from Repeating Earthquakes in the Loma Prieta Aftershock Zone, *Geophys. Res. Lett.*, 40, 1079-1083, doi:10.1002/grl.50212, 2013.
- Waldhauser, F., and D. P. Schaff (2008), Large-scale relocation of two decades of Northern California seismicity using cross-correlation and double-difference methods, *J. Geophys. Res.*, 113, B08311, doi:10.1029/2007JB005479.
- Waldhauser, F. (2009), Near-real-time double-difference event location using long-term seismic archives, with application to Northern California, *Bull. Seism. Soc. Am.*, 99, 2736-2848, doi:10.1785/0120080294.
- Working Group on California Earthquake Probabilities (WGCEP)

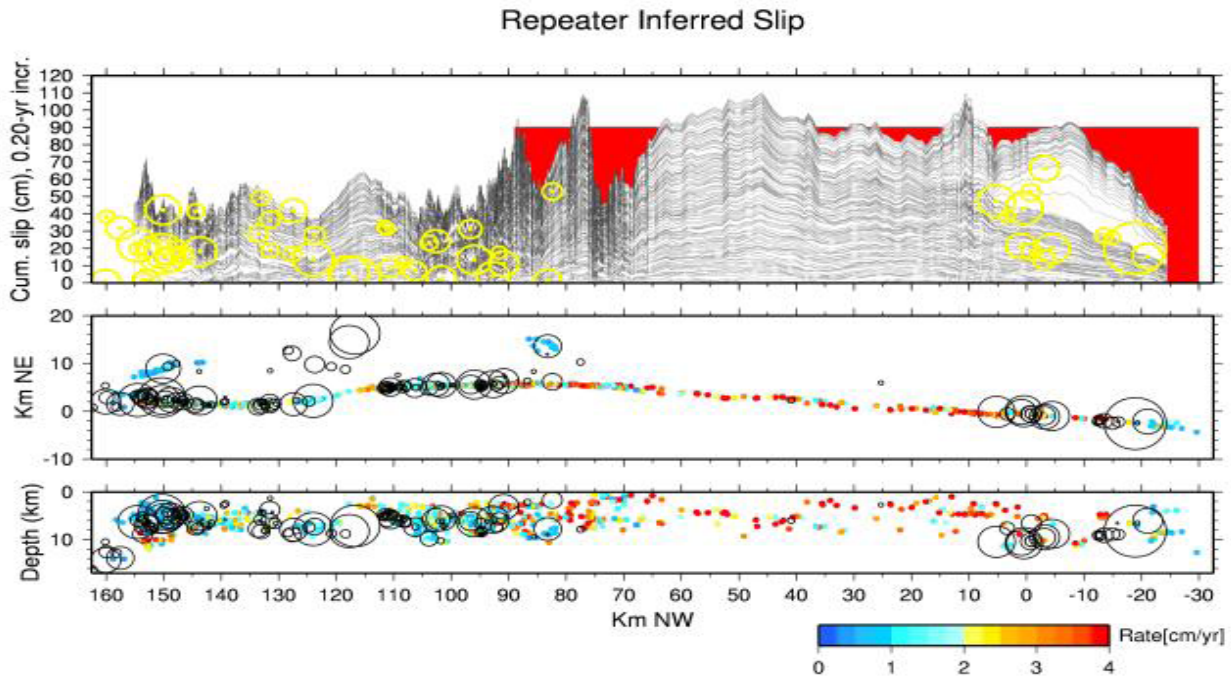


Figure 2.19.1: REQ inferred cumulative deep-creep through time (top) and Double-difference relocations (DDRT, *Waldhauser and Schaff, 2008; Waldhauser, 2009*) of 870 REQ sites along the ~ 200 km long study region (middle, bottom). Cities of Parkfield and San Juan Bautista are located at -9 and +135 km, respectively. The REQ events range in magnitude from ~ M1.4 to 3.5. Top: Contours of cumulative deep-creep from REQs from 1984 through April, 2011 at 0.2 yr intervals with along-strike smoothing of 15 REQ sequences. Yellow symbols are >M4 events occurring during this period and centered on the nearest 0.2yr contour. Red region is expected cumulative creep since 1984 assuming a tectonic rate of 3.3 cm/yr. Middle: Along-fault map view of SAF REQs color-coded to their average inferred slip rates over the entire 1984 - April 2011 study period. M4+ seismicity is shown as black circles. Bottom: Along-fault depth section of the same sequences. Off-SAF repeaters on the sargent fault (~140 to 160 km NW) and on the Paicenes-San Benito faults (~80 to 87 km NW) were not used in the slip contour calculations.

(2007), The Uniform California Earthquake Rupture Forecast, Version 2 (UCERF 2), *U.S. Geol. Surv. Open File Rep.*, 2007-1473, 1-104.

20 Variability of Fault Slip Behaviors along the San Andreas Fault in the San Juan Bautista Region, Inferred from Characteristically Repeating Earthquake

Taka'aki Taira, Roland Bürgmann, Robert M. Nadeau, Douglas S. Dreger

Introduction

An improved understanding of time history of fault slip at depth is an essential step toward understanding the underlying mechanics of the faulting process. We investigate spatially- and temporally-varying fault slip along the northernmost creeping section of the San Andreas fault near San Juan Bautista (SJB), California, by systematically examining spatiotemporal behaviors of characteristically repeating earthquakes (CRE).

Characteristically Repeating Earthquake Catalog

We have constructed the CRE catalog through a waveform cross-correlation analysis. We analyzed about 12,000 local events that occurred within a 15 km radius of the 1998 M_w 5.1 SJB earthquake. We evaluate the waveform similarity for a pair of seismograms in the vertical component with an 8-24 Hz bandpass filter based on the waveform cross-correlation coefficient and the phase coherency. To minimize the false detection of repeating earthquakes, we identify a pair of earthquakes as CREs if both the cross-correlation coefficient and the coherency are greater than 0.95 obtained from at least two stations. Our cross-correlation and coherency thresholds are comparable to those used in previous studies (e.g., *Zhao and Peng, 2009*). Our analysis identifies about 600 sequences with magnitudes ranging from -0.1 to 3.5 that are distributed in a depth range of 3 km to 10 km (Figure 2.20.1).

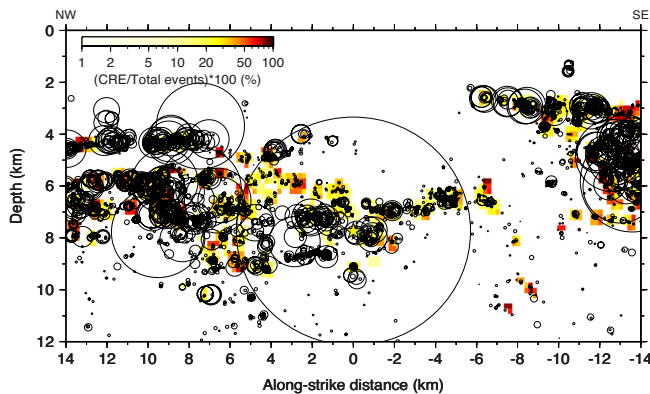


Figure 2.20.1: Spatial distribution of CREs near the 1998 M_w 5.1 SJB earthquake. Color scale indicates the CRE proportion of total seismicity. Circles are local earthquakes (1984-2012) analyzed to identify CREs, and their sizes are proportional to the rupture size. The yellow star is the 1998 SJB M_w 5.1 earthquake.

Following *Nadeau and Johnson (1998)* and *Chen et al. (2007)*, we first explore a relation between the recurrence interval (Tr) and seismic moment (M_0) for the CREs identified in the SJB region. As the Tr of CREs were significantly perturbed following the 1998 M_w 5.1 SJB earthquake, we estimated the median Tr

and M_0 in individual sequences from the CRE activity in 1990-1997. As shown in Figure 2, the Tr - M_0 relation from our study is in good agreement with those from *Nadeau and Johnson (1998)* and *Chen et al. (2007)*. This would indicate that the SJB CRE can be used to infer temporal evolutions of the fault slip (d) near the CRE rupture area, with the empirical relation between d - M_0 introduced in *Nadeau and Johnson (1998)*:

$$\log(d) = -2.36 + 0.17 \log(M_0) \quad (1.1)$$

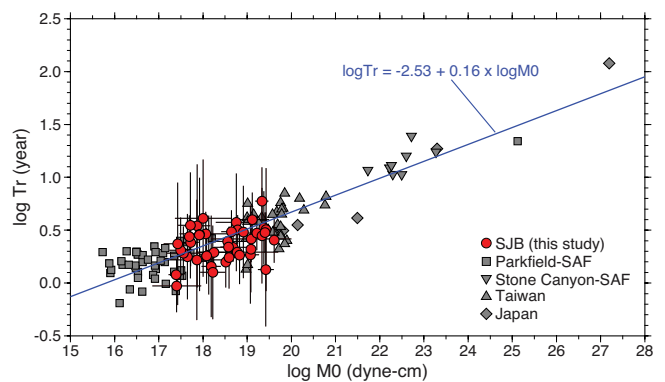


Figure 2.20.2: Recurrence interval (Tr) as a function of seismic moment (M_0) from *Chen et al. (2007)* and this study. Red circles are the SJB CRE sequences.

Temporal behaviors of fault slip are determined from CREs with equation (20.1) on the characteristic fault path where CREs occurred. We discretize a 28 km long, 12 km deep plane with 1 km x 1 km segments in the strike and dip directions, respectively. In each segment, we used CRE sequences that occurred within a 3 km radius from the center of the segment, and computed average fault slips when at least 3 sequences are available (Figure 2.20.3).

Spatial Variation in Interseismic Slip Rate

We evaluated the spatial distribution of the interseismic slip rate from CREs that occurred before the 1998 M_w 5.1 SJB earthquake at individual segments. Our analysis identifies a low-creep (0.1-0.2 cm/year) or locked asperity near the 1998 M_w 5.1 SJB earthquake (Figure 2.20.4). The geodetic slip rate in this area is about 2.3 cm/year (e.g., *Johanson and Bürgmann, 2005*). This suggests a considerable slip deficit was accumulated in the low-creep rate zone.

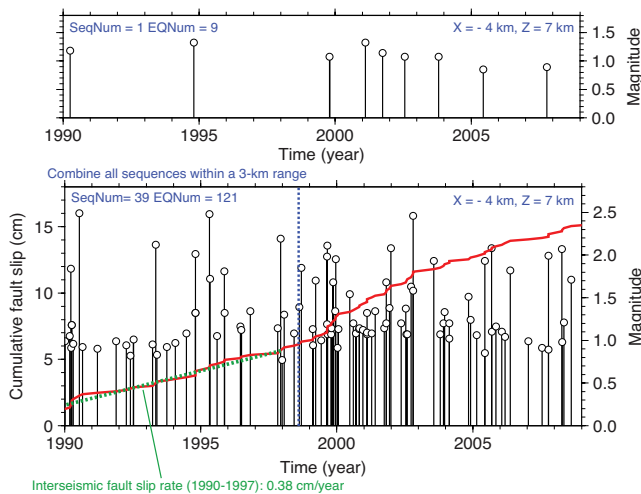


Figure 2.20.3: Fault slip estimate from CRE activity. Top panel shows the time history of a single sequence at the $X=-4$ and $Z=7$ grid point. The bottom panel shows the CRE activities from all sequences that occurred within a 3 km radius from this grid point. Red line is the time history of the average fault slip with equation (20.1), and dashed blue line is the origin time of the 1998 SJB M_w 5.1 earthquake. Also shown is the interseismic slip rate estimate (dashed green line) with the CRE activity in 1990–1997.

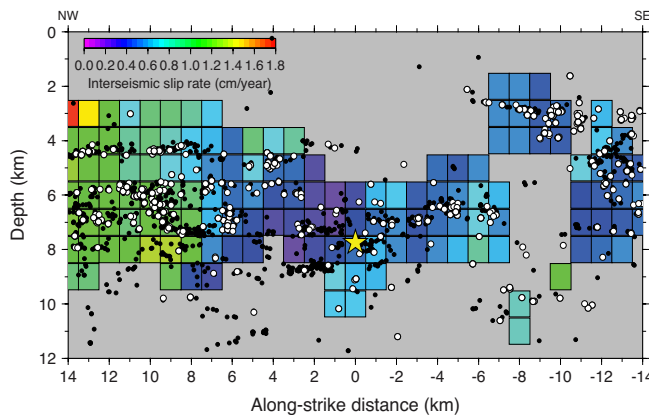


Figure 2.20.4: Spatial variation in interseismic slip rate (1990–1997) inferred from the characteristically repeating earthquakes. White and black circles indicate repeating and non-repeating earthquakes, respectively. The yellow star is the 1998 SJB M_w 5.1 earthquake.

Spatiotemporal Evolution of Postseismic Slip following the 1998 SJB M_w 5.1 Earthquake

In the postseismic period following the 1998 M_w 5.1 mainshock, the CRE activity was significantly increased in a zone at a depth of 5–10 km about 2–7 km northwest of the 1998 SJB mainshock (Figure 2.20.5), which indicates a triggering of substantial aseismic slip induced by the 1998 SJB mainshock. The largest accumulated postseismic slip is about 6 cm at this zone in the first 1000-day postseismic period. It appears that a considerable aseismic slip release occurred in the low-creep rate zone shown in Figure 2.20.4.

The spatial migration of the postseismic slip was inferred from CREs activities (Figure 2.20.6). Initial postseismic migration within the first 100 days was dominantly along the

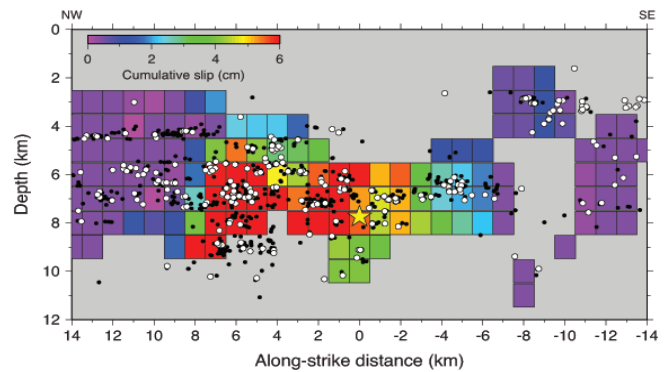


Figure 2.20.5: Spatial variation in postsic slip in the first-1000 day postseismic period.

strike of the San Andreas fault, toward the northwest fault segment. After this postseismic period, another migration of postseismic slip was initiated, which was propagated into the southeast fault segment from the hypocenter of the 1998 M_w 5.1 SJB earthquake.

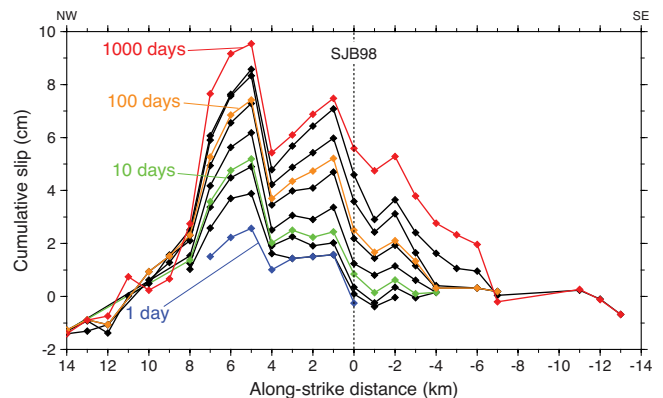


Figure 2.20.6: Cumulative postseismic slip inferred from CRE sequences.

Acknowledgements

We thank K.H. Chen for providing us with the CRE data, and the Northern California Earthquake Data Center for data collection and distribution for the seismic data in the northern California. This work is supported by the National Science Foundation grant EAR-0951430.

References

- Chen, K.H., R.M., Nadeau, and R.J. Rau, Towards a universal rule on the recurrence interval scaling of repeating earthquakes?, *Geophys. Res. Lett.*, 34, L16308, 2007.
- Johanson, I. A., and R. Bürgmann, Creep and quakes on the northern transition zone of the San Andreas fault from GPS and InSAR data, *Geophys. Res. Lett.*, 32, L14306., 2005.
- Nadeau, R.M., and L.R. Johnson, Seismological studies at Parkfield VI: Moment release rates and estimates of source parameters for small repeating earthquakes, *Bull. Seismol. Soc. Am.*, 88, 790–814, 1998.
- Zhao, P., and Z. Peng, Depth extent of damage zones around the central Calaveras fault from waveform analysis of repeating earthquakes, *Geophys. J. Int.*, 179, 1817–1930, 10.1111/j.1365-246X.2009.04385.x, 2009.

21 Seismic Quiescence Following Large Magnitude Earthquakes

Christopher Johnson and Roland Bürgmann

Introduction

Stress perturbations produced by large-magnitude earthquakes impact seismicity at regional and global distances by altering the stress on a fault plane and advancing or delaying earthquake nucleation. Regional changes in seismicity are observed in aftershock locations with areas of increased or decreased activity correlating to areas of positive or negative Coulomb stress changes, respectively (Stein, 1999). At distances beyond two fault lengths, *i.e.* the region experiencing significant static Coulomb stress change, seismic waves from large magnitude earthquakes have been shown to trigger small earthquakes (Gomberg *et al.*, 2001). This dynamic transfer of stress from seismic waves is also observed to trigger microseismicity and tremor in regions of geothermal activity as well as non-volcanic tremor in deep fault zones immediately during the passage of the waves and in the hours to days following (Brodsky, 2006; Peng *et al.*, 2010). Less frequently, immediate triggering of small earthquakes ranging from $3 > M < 5$ are detected during the surface wave train (Husker and Brodsky, 2004; Tape *et al.*, 2013). Above $M > 5$, dynamic triggering is not observed at distances beyond the 2-3 fault lengths of a large-magnitude event (Parsons and Velasco, 2011). An exception to this finding is the M_w 8.6 2012 east Indian Ocean event that resulted in above-average global seismicity for events $> M5.5$ in the six days following the mainshock and is an example of delayed dynamic triggering which suggests that the stress perturbations experience during the teleseismic surface waves were large enough to advanced the earthquake cycle of multiple $> M5$ events (Pollitz *et al.*, 2012). As a result, questions remain regarding the dynamic triggering of large earthquakes at global distances and the influence of earthquake nucleation times following dynamic stress perturbations on active faults.

Subsequent to the global increase of seismicity as a result of the 2012 east Indian Ocean event is a 95 day period of quiescence for $M \geq 6.5$ events (Pollitz *et al.*, Submitted). The observable rate decrease following the 2012 Indian Ocean event prompted this study to examine if a magnitude threshold exists for seismic quiescence following a period of dynamically triggered earthquakes. Here we investigate the idea of global “dynamic shadowing” in order to determine if a spatial and temporal relationship to large magnitude events exists for periods of reduced global seismicity. This study builds on the previous work by Parsons and Velasco (2011) who concluded that an increase in $M > 5$ seismicity is confined to the region within 2-3 fault lengths of the rupture and activity returned to background rates within 36 hours following a $M > 7$ event. Using a similar methodology we explore the suppression of global activity with respect to background earthquake activity following large magnitude events. The goal of this study is to determine if a dynamic shadow results in a reduction of seismicity at a distinguishable level below the background seismicity over various temporal and spatial ranges.

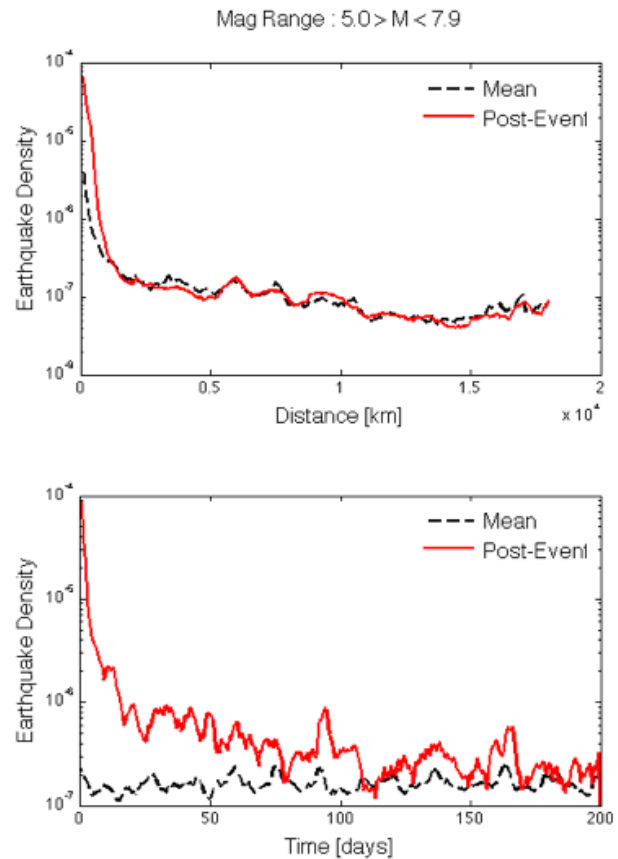


Figure 2.21.1: All events from 1977–2013 are considered between $5 > M < 7.9$ for the analysis. The top panel indicates a return to mean rates at a distance of ~ 1000 km. The bottom panel indicates increased activity for > 100 days following a $M \geq 7.9$ event. Significant activity below the mean rate is not observed.

Methods

Establishing a change in earthquake rates requires a robust background rate for subsequent comparisons. Utilizing 35 years of earthquake catalog data obtained from the Advanced National Seismic System (ANSS), we analyze seismic rate changes following large magnitude earthquakes. Similar to Parsons and Velasco (2011) we compile earthquake catalogs within select magnitude ranges, one containing the range of magnitudes that possibly experience a rate change and the second catalog containing all remaining larger events. For each magnitude range considered, a spatial and temporal stacking of the events is used to calculate an earthquake density. The background rate is determined by randomly combining the event times using different locations within the compiled catalog of smaller events in order to scatter the foreshock and aftershock activity. By varying the magnitude range and time intervals around the large earthquakes, we will establish if a relationship exists between suppressed seismicity and very large magnitude events.

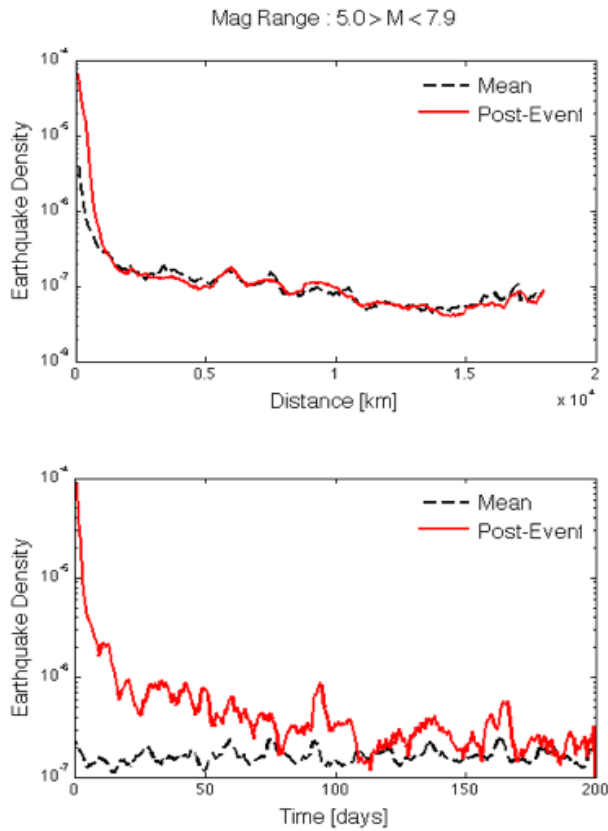


Figure 2.21.2: All events from 1977–2013 are considered between $6.0 > M < 7.9$. Similar to the lower magnitude range, no increased activity is detected beyond ~ 1000 km. The bottom panel indicates a return to background rates within 25 days. Brief periods of activity below the mean are observed but the significance is not supported when considering the third catalog.

Initial Results

Catalog data from 1977–2012 includes 36 $M \geq 7.9$ events and three catalogs are compiled containing all other events within $5.0 > M < 7.9$, $6.0 > M < 7.9$, and $6.5 > M < 7.9$. Using a time window of 200 days and distances extending to 18,000 km, an earthquake density is computed by stacking all events relative to the large events in 12 hr bins at 100 km interval. The mean density is calculated using the preceding 200 days of events in each catalog. Each magnitude range indicates a return to background rate within ~ 1000 km of the mainshock. This is consistent with a 2–3 fault length aftershock zone. The temporal increase in activity resembles an Omori decay with $6.5 > M < 7.9$ activity returning to background rates within three days and activity for $M > 5$ is increased for ~ 100 days. No magnitude range demonstrates an extended decrease in activity below the mean rate. Continued examination of different magnitude, spatial, and temporal ranges is to be completed.

Acknowledgements

This work is based upon work supported by the National Science Foundation Graduate Research Fellowship for C.W. Johnson

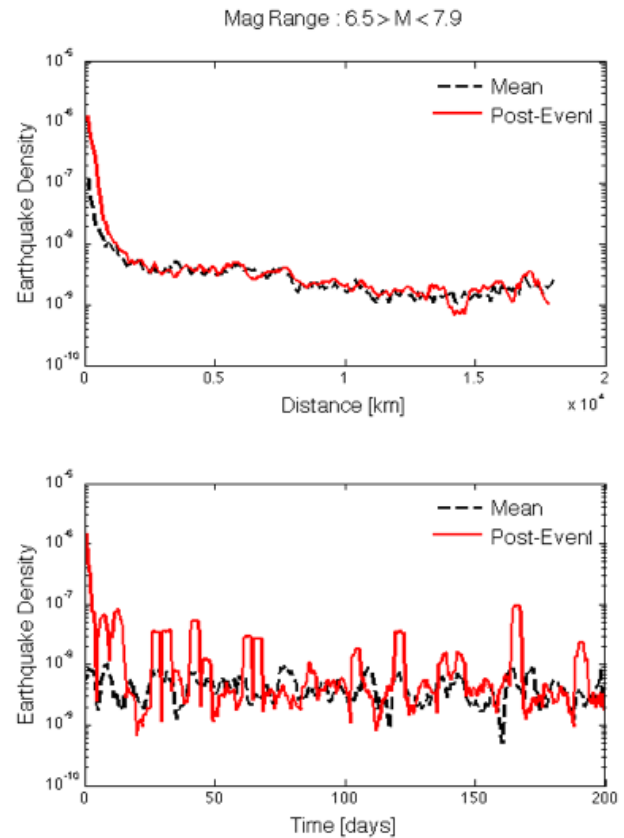


Figure 2.21.3: No significant suppression of activity is observed for events $6.5 > M < 7.9$. Activity returns to mean rates within 1000 km and three days without a period of reduced activity.

References

- Brodsky, E. E., Long-range triggered earthquakes that continue after the wave train passes, *Geophys. Res. Lett.*, 33, L15313, doi:10.1029/2006GL026605, 2006.
- Gomberg, J., Reasenberg, P.A., Bodin, P., and Harris, R.A., Earthquake triggering by seismic waves following the Landers and Hector Mine earthquakes, *Nature*, 411, 462–466, 2001.
- Husker, A.L. and Brodsky, E.E., Seismicity in Idaho and Montana triggered by the Denali Fault earthquake: A window into the geologic context for seismic triggering, *Bull. Seis. Soc. Am.*, 94, S310–S316, 2004.
- Parsons, T. and Velasco, A.A., Absence of remotely triggered large earthquakes beyond the mainshock region, *Nature Geosci.*, 4, 312–316, 2011.
- Peng, Z., D. P. Hill, D. R. Shelly, and C. Aiken, Remotely triggered microearthquakes and tremor in central California following the 2010 Mw 8.8 Chile earthquake, *Geophys. Res. Lett.*, 37, L24312, doi:10.1029/2010GL045462, 2010.
- Pollitz, F.F., Stein, R.S., Sevilgen, V. and Bürgmann, R., The 11 April 2012 east Indian Ocean earthquake triggered large aftershocks worldwide, *Nature*, 490, 250–253, 2012.
- Stein, R.S., The role of stress transfer in earthquake occurrence, *Nature*, 402, 605–609, 1999.
- Tape, C., West, M., Silwal, V., and Ruppel, N., Earthquake nucleation and triggering on an optimally oriented fault, *Earth and Plan. Sci. Lett.*, doi:10.1016/j.epsl.2012.11.060, 2013.

22 Laboratory Investigations into Micromechanical Mechanisms Controlling the Onset of Stick-slip Instabilities

Paul A. Selvadurai, Steven D. Glaser and Rani H. Kiwan

Introduction

Improving our understanding of the factors controlling spontaneous shear rupture nucleation on a frictional fault would help better define the important physical processes contributing to earthquake rupture and faulting. Our current laboratory investigations (Selvadurai and Glaser, 2013) quantify the local stress states on a laboratory fault, which control the transition from stable (quasi-static) to unstable (dynamic) sliding. We propose that the initiation of the unstable phase occurs at the displacement incongruities where compliant, ‘creeping’ segments of the fault transition into stiff, ‘locked’ sections. These transition regions can exhibit swarms of smaller earthquakes, localized in time and space, prior to the larger subsequent earthquake. Similarities between our laboratory results (specifically the acoustic emission measurements), and those observed in geological settings are briefly described here.

Laboratory Facilities

The laboratory model consisted of two sandblasted Poly(methyl methacrylate) (PMMA) surfaces pressed together by a normal stress (σ_p) and then sheared at a constant velocity (v_p) in a direct shear configuration. Figure 2.22.1 provides a general view of the direct shear apparatus where the PMMA base plate and slider block measured 950 x 950 x 60 mm and 400 x 80 x 10 mm, respectively. A non-contact eddy current sensor array, mounted near the interface, measured the slow, quasi-static motions near the fault and, in nature, are evident in GPS and InSAR data. To measure the relatively quick dynamic stress changes, an array of 16 piezoelectric acoustic emission (AE) sensors were placed along the underside of the base plate; drawing parallels to seismometers deployed in the field. The AE sensors have been accurately calibrated using known source-time functions induced by glass capillary fractures. During the application of the normal pressure, contacting asperities are formed due to the interaction between the two randomly rough surfaces. These interactions are believed to be consistent with processes occurring on natural geological faults. A pressure sensitive film (FUJI™ prescale 12-50 MPa) was used to initially localize, quantify, and measure the heterogeneous normal stresses resulting from the population of asperity contacts.

Laboratory Procedure

Details of the experimental facilities, procedure and material properties of the PMMA are given by Selvadurai and Glaser (2013). Briefly, the fault was firstly characterized using the pressure sensitive film by compressing it throughout the interface using a known nominal stress (σ_p) for a controlled amount of time (t_{hold}) at a known reference location. Using the electro-mechanical shear actuator, the rigid loading platen was driven at a set-point velocity (v_p) to simulate far-field tectonic actions.

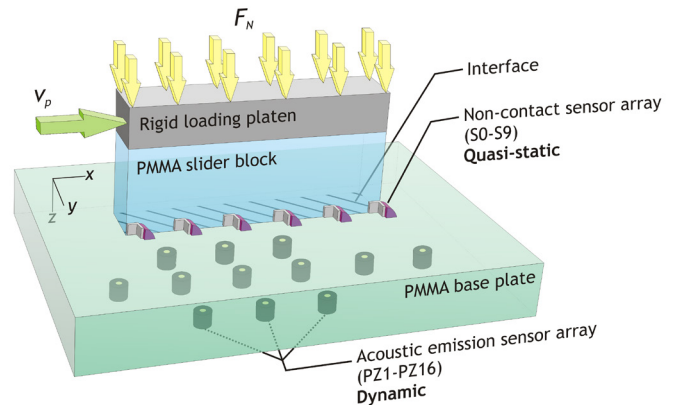


Figure 2.22.1. General schematic view of the overall direct shear apparatus including general locations of the sensors arrays.

Current experimental suites employed constant velocities ranging from 0.010 to 0.030 mm/s but only the results from the faster loading rate, $v_p = 0.030$ mm/s, will be presented here. Shear stress (τ_p), normalized over the nominal interface area, measured between the loading platen and shear actuator, increased gradually and slow, aseismic ‘creeping’ displacements were observed using the non-contact sensors until a ‘mainshock’ occurred. The mainshock was characterized by a sizable decrease in the bulk shear force (~50-70% drop from maximum) coupled with rapid, coseismic displacements in the direction of applied shear.

Experimental Observations: Foreshocks Preceding the Mainshock

Detectable physical changes, such as ground deformations associated with the premonitory movements are difficult (if not impossible) to detect using current geodetic and seismic sensing tools. On some natural faults, smaller earthquakes have occurred within a region tens of kilometers of the eventual hypocenter of the larger earthquake, weeks to seconds beforehand. The physics and mechanics of these ‘foreshocks’ are not well understood with respect to their influence on the larger mainshock.

In Figure 2.22.2, while loading the fault slowly ($v_p = 0.030$ mm/s) prior to the mainshock, we observe small dynamic emissions detected using the AE array.

During these ‘foreshock’ emissions, there was no discernible drop in the bulk shear force (τ_p) sustained by the fault, but they must represent changes in local stress states due to some physical phenomena which we are currently investigating.

Spatio-temporal distributions can also be analyzed. Location and timing of the foreshocks were determined from first arrival P-waves using multiple AE sensors and are shown in Figure 2.22.3. The size of the circular region represents the spatial error associated with the p-wave location algorithm. Locations

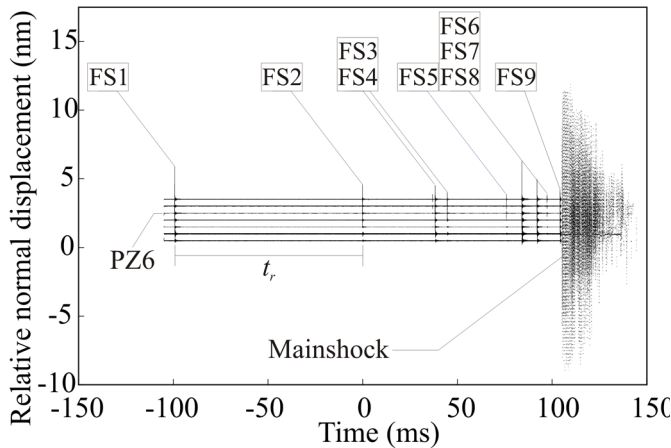


Figure 2.22.2. Acoustic emission measurements for nine foreshocks (FS1-FS9) creating a sequence that preceded a larger mainshock event ($v_p = 0.030$ mm/s). The recurrence time, t_r between FS1 and FS2 is shown as an example.

of the foreshocks have been superimposed over the initial contact measurements provided from the pressure sensitive where the hotter (red) colors indicate contact and the cooler (blue) represents zero stress or no initial contact.

Preliminary Discussion

Observational seismology has, in some cases, observed foreshock sequences preceding larger mainshock events (e.g., *Dodge et al., 1995*) not dissimilar to our preliminary laboratory results. While the scale of the two results are distinctly different (in both space and time) we have currently begun an investigation that employs similar techniques and models to characterize our experimental findings. These techniques may help develop scaling relations from the laboratory to the field that have been difficult to characterize in the past. These foreshock bursts may be useful contributors to short-term earthquake probability estimates (*Chen and Shearer, 2013*).

Acknowledgements

Funding for this work is provided by NSF Grant # 1131582.

References

Chen, X. and Shearer, P. M., California foreshock sequences suggest aseismic triggering process: *Geoph. Res. Lett.*, v. 40, p. 1-6, doi:10.1002/grl.50444, 2013.

Dodge, D. A., Beroza, G. C. and Ellsworth, W. L., Foreshock sequence of the 1992 Landers, California, earthquake and its implications for earthquake nucleation: *J Geophys. Res.*, v. 100, no. B7, p. 9865-9880, 1995.

Selvadurai, P. A. and Glaser, S. D., Experimental evidence of micromechanical processes that control localization of shear rupture nucleation: Presented at the *47th US Rock Mechanics / Geomechanics Symposium* in San Francisco, CA, USA, 2013.

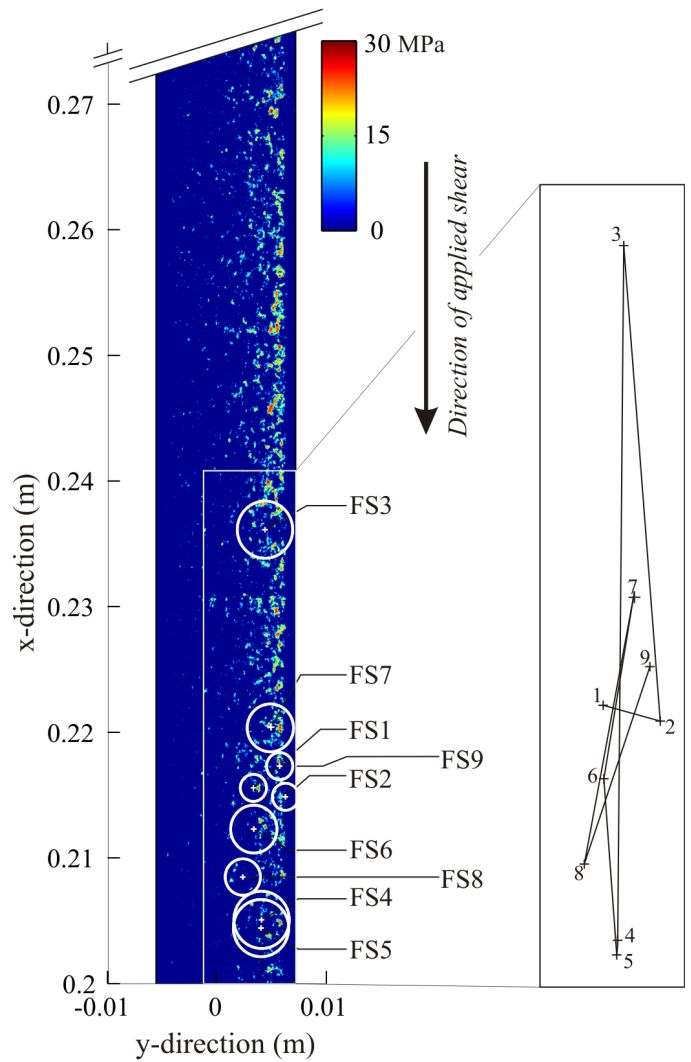


Figure 2.22.3. Locations of the foreshocks shown in Figure 2.22.2 determined using P-wave travel times from multiple sensors. The locations were superimposed on the pressure measurements obtained from the pressure sensitive film. Locations exhibiting higher normal stress appear red while the blue background assumes no normal stress was transferred (i.e., no contact occurred). The inlay shows an enlarged view of the movement of the foreshock sequence where the distribution appears to be random in space.

23 Source Characterization of Underground Explosions from Combined Moment Tensor and First Motion Analysis

Andrea Chiang and Douglas S. Dreger

Introduction

The use of regional distance long-period, complete waveform data to determine the seismic moment tensor and discriminate the source-type of earthquakes, underground cavity collapses and nuclear explosions has been demonstrated for events in the western United States (Dreger *et al.*, 2008; Ford *et al.*, 2008; Ford *et al.*, 2009a), and for the recent 2006 and 2009 North Korean nuclear tests (Ford *et al.*, 2009b; Ford *et al.*, 2010). In these studies populations of earthquakes, underground cavity collapses and nuclear explosions are found to separate when considered on a Hudson *et al.* (1989) source-type diagram. Ford *et al.* (2010) utilized the Hudson *et al.* (1989) source-type representation to develop a network sensitivity solution (NSS) to determine the best fitting solution, the uncertainty in the solution, and the capabilities of the method given the station topology. The regional distance moment tensor inversion, coupled with NSS analysis and first motion constraints, enables the discrimination of source-type in conditions of relatively sparse regional distance monitoring.

Data and Methods

In this study we investigate the September 14, 1988 US-Soviet Joint Verification Experiment (JVE) nuclear test at the Semipalatinsk test site in Eastern Kazakhstan, and two nuclear explosions conducted at the Chinese Lop Nor test site. These events were very sparsely recorded by stations located within 1600 km, and in each case only 3 or 4 stations were available in the far-regional distance range (Figure 2.23.1) for moment tensor analysis. Following the results of Ford *et al.* (2009b) we incorporated first-motion data from regional stations, as well as teleseismic stations to provide additional constraint in the NSS analysis. The results show that unique discrimination of these events is possible under these extremely sparse monitoring conditions when long-period regional waveforms and P-wave first-motion polarities are combined.

To assess the confidence of the moment tensor solution, we implemented the Network Sensitivity Solution (NSS) technique developed by Ford *et al.* (2010). The technique presents the level of fit between data and the different theoretical solutions described by the source-type diagram for a given station configuration, Earth model, and frequency band. From the NSS of a given event we can determine whether or not the best fitting full moment tensor solution from the inversion is well resolved to make useful interpretations about the source. We included regional and/or teleseismic P-wave first motions in addition to waveform data in the NSS analysis (Ford *et al.*, 2012) to better constrain the moment tensor solution by comparing observed P-wave polarities to predicted P-wave polarities.

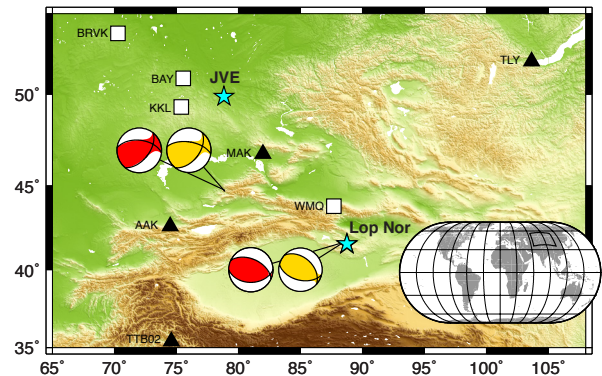


Figure 2.23.1. Event locations (star) and seismic stations (triangle and square) used in the moment tensor analysis. The two Lop Nor events are located very closely hence the overlapping stars. Black triangles represent the stations used in the analysis of the May 15th, 1995 Lop Nor explosion and the June 8th, 1996 Lop Nor explosions, and white squares are the stations used in the September 14th, 1998 Soviet JVE. Focal mechanisms of local earthquakes used in the velocity model calibration are also plotted. Gold is the solution from this study and red is the Harvard GCMT solution.

Network Sensitivity Solutions (NSS)

Here we present the combined waveform and first motion analysis for the three explosions (Figure 2.23.2). For the 1988 JVE, the regional waveforms only the NSS solution shows a similar trend compared to other nuclear explosions (Ford *et al.*, 2010), with the best-fitting full moment tensor solution plotting near the theoretical opening crack. The colors of the shaded contour regions correspond to different scaled variance reduction (sVR), in which the sVR is scaled to the moment tensor solution in the NSS that has the maximum VR. In the case of using just the waveform data, source mechanisms without a significant explosive component can fit the observed data just as well as a dominantly explosive mechanism. However, when regional and teleseismic P-wave first motions are included in the computation of the NSS a solution that is predominately explosive is obtained. The NSS results show significant improvement in discrimination capabilities when we include additional constraints from P-wave first motions, especially for moment tensor solutions fitting better than sVR of 90%.

The two Lop Nor explosions illustrate that when good teleseismic data is not available, using only regional P-wave polarities also improves monitoring capabilities. Waveform-only NSS for the 1995 Lop Nor event show a wide range of possible sources fitting $\geq 90\%$ of the best fitting moment tensor solution, which is largely the result of the large Love wave amplitudes and the sparse station coverage. However, if we use both waveform data and P wave polarities observed at regional distances we see the combined analysis significantly reduces the distribution of

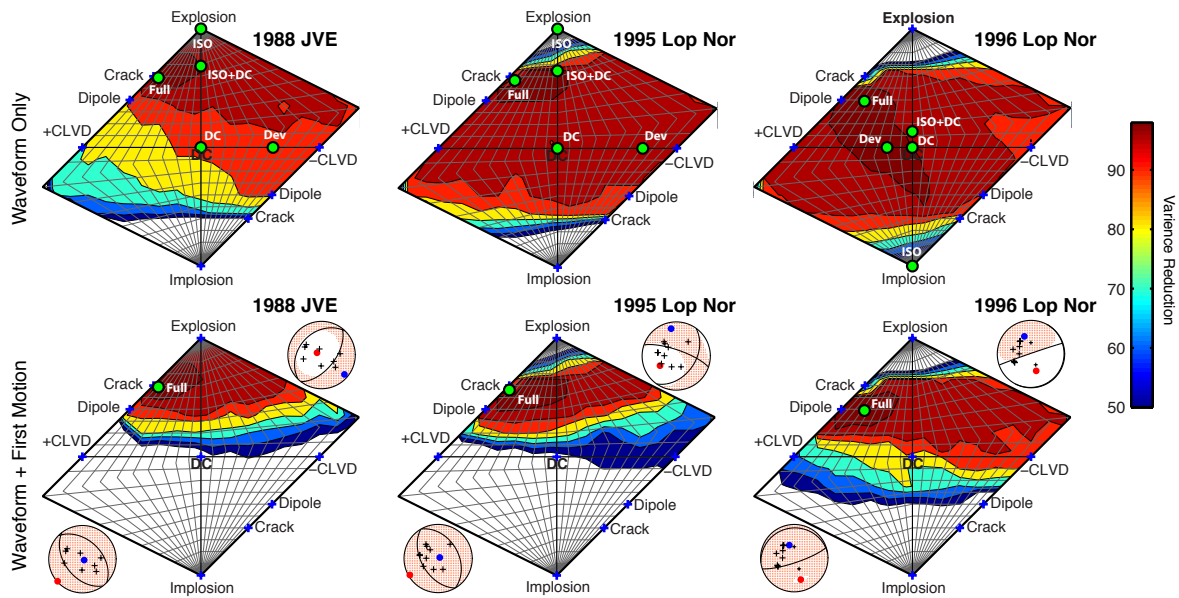


Figure 2.23.2: Network Sensitivity Solutions (NSS) for the 1988 JVE, 1995 and 1996 Lop Nor Shaft Explosions. Green circles are best fitting full, deviatoric, pure double couple (DC), ISO+DC and pure isotropic (ISO) source mechanisms; blue crosses are the theoretical mechanisms; shaded regions are color-coded by their scaled variance reduction (sVR); black crosses, blue dots and red dots plotted on the best fitting full and deviatoric mechanisms are P-wave up first motions, T- and P-axes. Here we compare NSS using regional waveform and combined waveform and P-wave first motion. For the JVE we used both regional and teleseismic first motions, and for the two Lop Nor explosions we used only regional first motions.

solutions with high sVR ($\geq 90\%$) and uniquely discriminates the event as consistent with other nuclear explosions and inconsistent with earthquakes and collapses (Figure 2.23.2).

Similarly, waveform-only NSS for the 1996 Lop Nor event cannot uniquely discriminate the event as a explosive source due to strong Love waves, sparse station coverage, and possible Rayleigh wave reversal. However, after incorporating regional P-wave first motions, the NSS results now show similar trends as observed in the 1995 Lop Nor test and the 1988 Soviet JVE, though contours showing solutions with $sVR \geq 90\%$ are more extensive and cross slightly over to the horizontal deviatoric line (Figure 2.23.2). Although the combined waveform and first motion NSS does not give a unique discrimination, it identifies the source as non-DC. Unlike earthquakes, the distribution of moment tensor solutions is not situated around the pure DC mechanism but shifted along the vertical volumetric axis and towards an opening linear vector dipole.

Conclusions

We have performed seismic moment tensor inversions for the 1988 Soviet JVE test and two Lop Nor nuclear tests. These cases represent sparse monitoring conditions. In each case we have shown that the use of long-period waveform data comprised mostly of regional surface waves results in solutions with large isotropic components that are consistent with solutions for other studied nuclear tests (Ford *et al.*, 2009a; Ford *et al.*, 2009b; Ford *et al.*, 2010). Using only regional waveforms, the distribution of solutions on the source type diagram of Hudson *et al.* (1989) do not cleanly discriminate the event either because of the known explosion negative compensated linear vector dipole (CLVD) tradeoff (case of the JVE event) or due to

large observed Love waves (cases of the two Lop Nor tests). In each case, however, the inclusion of regional P-wave polarities, and ideally observations from teleseismic arrays when available, reduces area of solutions that provide a good level of fit to the data, providing good separation from double-couple solutions and solutions on the deviatoric line.

Acknowledgements

We acknowledge funding from the Air Force Research Laboratory, contract FA9453-10-C-0263 that is supporting this research.

References

- Dreger, D. S., Ford, S. R., and Walter, W. R., Source Analysis of the Crandall Canyon, Utah, Mine Collapse, *Science*, 321, 217, 2008.
- Ford, S. R., Dreger, D. S. and Walter, W. R., Source Characterization of the 6 August 2007 Crandall Canyon Mine Seismic Event in Central Utah, *Seismol. Res. Lett.*, 79, 637-644, 2008.
- Ford, S. R., Dreger, D. S. and Walter, W. R., Source Analysis of the Memorial Day Explosion, Kimchaek, North Korea, *Geophys. Res. Lett.*, 36, 2009
- Ford, S. R., Dreger, D. S. and Walter, W. R., Identifying Isotropic Events Using a Regional Moment Tensor Inversion, *J. Geophys. Res.*, 114, 2009.
- Ford, S. R., Dreger, D. S. and Walter, W. R., Network Sensitivity Solutions for Regional Moment-Tensor Inversions, *Bull. Seismol. Soc. Am.*, 100, 1962-1970, 2010
- Ford, S. R., Walter, W. R. and Dreger, D. S., Event Discrimination Using Regional Moment Tensors, *Bull. Seismol. Soc. Am.*, 102, 867-872, 2012
- Hudson, J. A., Pearce, R. G., and Rogers, R. M., Source type plot for inversion of the moment tensor, *J. Geophys. Res.*, 94, 765-774. 1989.

24 Moment Tensor Inversion of Seismic Events Associated with the Sinkhole at Napoleonville Salt Dome, Louisiana

Avinash Nayak and Douglas S. Dreger

Introduction

Napoleonville Salt Dome is located near Bayou Corne, Assumption Parish, southeast Louisiana. Caverns in salt domes such as this one are used for brine mining and storage of hydrocarbons and industrial waste. Beginning in June 2012, residents of Bayou Corne reported unusual gas bubbling in surface waters and frequent tremors. The parish requested the assistance of the United States Geological Survey (USGS) to monitor the continuous seismic activity. A temporary network of broadband seismic stations was established which revealed a complex and rich sequence of numerous seismic events. On August 3, 2012, a large sinkhole (Figure 2.24.1) was reported close to the western edge of the salt dome leading to an emergency declaration and evacuation of nearby residents. The sinkhole, filled with a slurry of water, crude oil and debris, has since swallowed Cypress trees and has been growing in surface area ever since (presently > 20,000 m²). Subsidence, bubbling of natural gas and intermittent seismicity have been observed in the region. Preliminary investigation suggests that sidewall collapse of a cavern, OXY GEISMAR #3, might be a possible cause of the sinkhole. Readers are referred to public briefings reports on the Department of Natural Resources, Louisiana website for further details (<http://dnr.louisiana.gov/index.cfm?md=pagebuilder&tmp=home&pid=1051>).

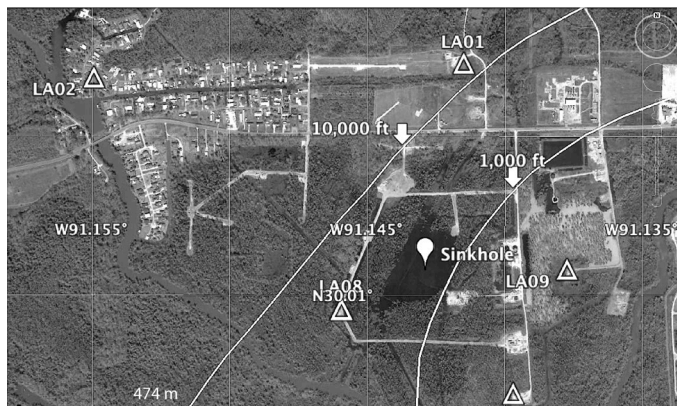


Figure 2.24.1: Google Earth image (dated – March 12, 2013) of the study region showing locations of USGS stations (triangles), sinkhole (balloon) and approximate contours (solid lines) of the edge of Napoleonville salt dome at 1,000 feet and 10,000 feet depth.

This region (-91.16°E to -91.13°E, 30°N to 30.025°N,) has been previously aseismic, with no events reported in the *National Earthquake Information Center* catalog between January 1973 and April 2012. Therefore, the sudden intense seismicity occurring simultaneously with development of the sinkhole indicates that the two phenomena are probably related. In this study, we implement an approach for automatic detection, location and moment tensor inversion of seismic events at the sinkhole.

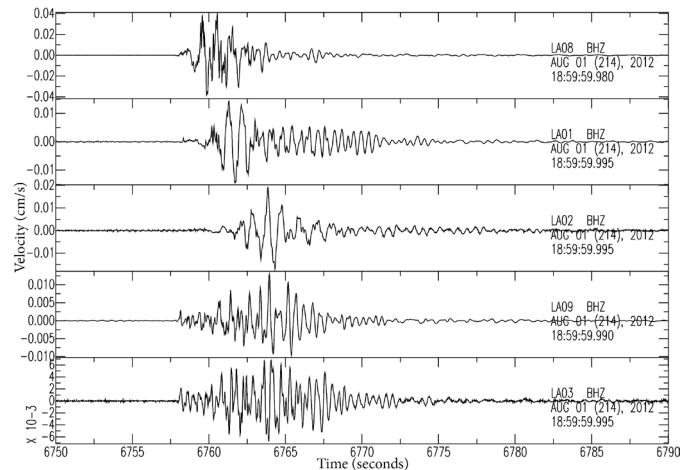


Figure 2.24.2: Velocity waveforms of a representative event.

Data and Methodology

Figure 2.24.2 shows velocity waveforms of a seismic event on August 1, 2012 as recorded at five USGS stations. The records primarily show that strong surface waves and waveforms of multiple events are quite similar to each other, indicating closely spaced hypocenters and a repetitive source process. Three of these stations, LA01, LA02 and LA08, are on the sedimentary strata surrounding the sinkhole and show similar waveforms, but are quite different from waveforms at stations LA03 and LA09, which are on sedimentary deposits over the salt dome. The difference in waveforms is reflected in the available seismic velocity models (*William Ellsworth, personal comm.*), which show the salt dome to be a fast half-space, overlain and surrounded by slow layers of sediments with velocities smoothly increasing with depth. To study source mechanisms of these events, we perform six-component point source seismic moment tensor inversion allowing for both deviatoric mechanisms and volume changes (*Minson and Dreger, 2008*). Due to the uncertainties in travel-time locations and depths owing to lack of clear seismic phases in waveforms and presence of numerous seismic events, we employ the grid search approach of *Kawakatsu (1998)* which continuously scans the seismic wavefield and performs moment tensor inversion of low frequency waveforms assuming virtual sources distributed over a 3D grid. For a given window of data, the source location and moment tensor solution which give the best Variance Reduction (VR), a measure of normalized fit between observed and synthetic waveforms, is assumed to be the true seismic source. We assume that seismic paths to stations LA01, LA02 and LA08 conform to sediment velocity model and seismic paths to stations LA03 and LA09 conform to salt dome velocity model. Fundamental Green's functions for the 1D velocity models are computed using *FKRPROG (Saikia, 1994)*. Displacement records are bandpass filtered between 0.1 to 0.2

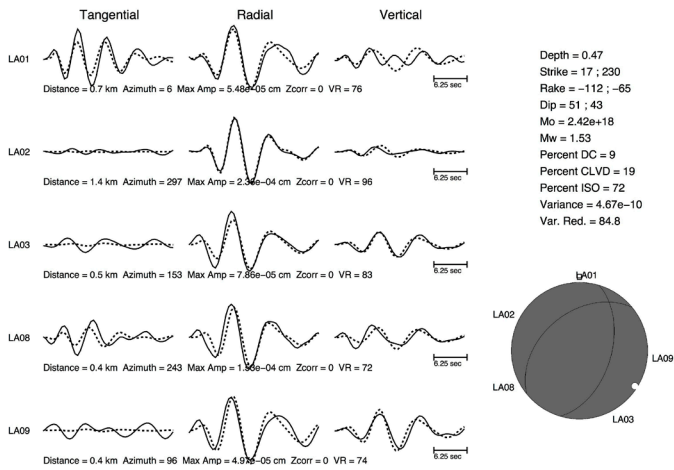


Figure 2.24.3: Observed (solid lines) and synthetic (dashed lines) waveforms and the moment tensor solution for one event.

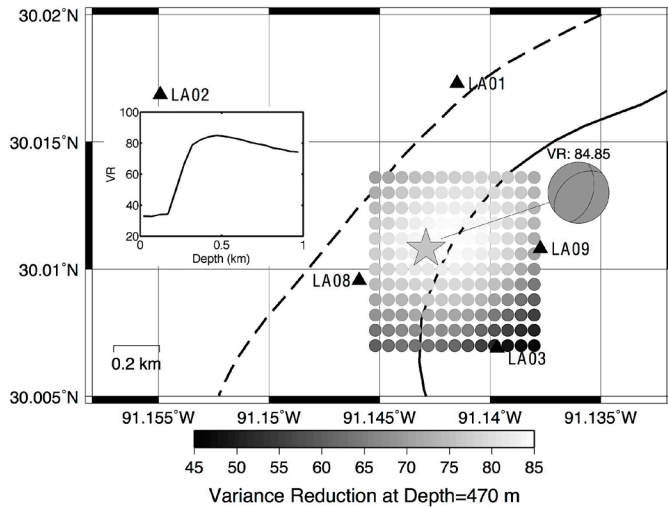


Figure 2.24.4. Figure showing distribution of VR in horizontal directions at best depth and distribution of best VR with depth (inset).

Hz, which simplifies the waveforms while maintaining the signal to noise contrast for larger events. The same causal filter is used for Green's functions. Then, the moment tensor inversion is performed for each grid point using 25-second data windows with time steps of 0.25 seconds. Here we discuss results for 5 hours of data from 17:00 hours to 24:00 hours on August 01, 2012. We were able to detect 23 events using a threshold of 70% VR during this time period. The details of the moment tensor solution and corresponding waveform fits for one of the events are shown in Figures 2.24.3. This event was located at -91.1422°E , 30.0112°N , depth 0.47 km and centroid time 20:52:39.00 hours. The solution fits the data very well at 84% VR and can explain most of the strong radial and vertical components. We find a dominant volume increase component in the solution (Isotropic > 70%). The distribution of VR in space (Figure 2.24.4) shows that our location is well constrained. All solutions are quite similar showing a dominant volume increase component (Isotropic 64-74%) and are concentrated at a depth of ~ 470 m at the western edge of the salt dome, very

close to the present location of the sinkhole. Magnitudes range from M_w 1.3 to 1.7.

Discussions

The moment tensor solutions are opposite to what one would expect in a collapse environment, if the energy release were purely due to gravity-driven tectonic collapse alone. However, the presence of large volume increase components as well as occurrence of harmonic tremors and long period events in the region indicates the role of fluids in controlling the seismic source processes, which can be inferred to be due to tensile failure of a near-vertical crack, or a crack-double-couple on a normal fault in the salt. Future work will include studying sensitivity of moment tensor solutions to velocity models, modeling waveforms at higher frequencies and possible explanations of the source mechanisms in terms of physical processes and their relationships with the sinkhole.

Acknowledgements

We thank William Ellsworth (USGS) for preliminary velocity models, data, mapping resources and helpful discussions. We also thank Aurelie Guilhem (ETH Zurich) and Seung Hoon Yoo (BSL) for helpful discussions. A. Nayak wishes to acknowledge the BSL Byerly/Tocher grant in supporting this work.

References

- Kawakatsu, H., On the realtime monitoring of the long-period seismic wavefield: *Bull. Earthq. Res. Inst.*, 73, 267-274, 1998.
- Minson, S.E., and D.S. Dreger, Stable Inversion for complete moment tensor: *Geophys. J. Int.*, 174, 585-592, 2007.
- Saikia, C.K., Modified frequency-wavenumber algorithm for regional seismograms using Filon's quadrature: modeling Lg waves in eastern North America: *Geophys. J. Int.*, 118, 142-158, 1994.

25 Full Moment Tensor Solutions Constrained using First Motion Polarities for Seismicity at the Geysers Geothermal Field, California

Voon Hui Lai, Sierra Boyd, Douglas Dreger

Introduction

The Geysers Geothermal Field is one of the most seismically active regions in North America. There have been previous efforts to study the source parameters of these earthquakes with magnitude greater than M_w 3.0 in this region by computing the deviatoric and full moment tensor solutions for these events (Boyd, 2013). However, for earthquakes that have a small volumetric term, statistical analysis such as the F-test is insufficient to provide good measure of significance to the full moment tensor (FMT) solutions. Hence, we incorporate first motion polarities to provide the additional constraint to the FMT solutions.

Methodology

Five earthquakes are chosen for further investigation. The first motion polarity data takes into account four parameters: station azimuth from the epicenter, takeoff angle, polarity (up or down) of first P arrivals, and a weighing factor. An average of 150 seismic stations from Northern California (NCSN), Berkeley Digital (BDSN), and Lawrence Berkeley National Lab (LBNL) Seismic Networks are used to ensure good azimuthal coverage. Both azimuth and takeoff angle for each station are obtained from the Northern California Earthquake Data Center (NCEDC) catalog and the polarities of the vertical component of each station are visually reviewed using Seismic Analysis Code (SAC) and Jiggle, developed by U.S. Geological Survey (USGS). A weighting is introduced to account for the uncertainties in determining the first motion polarities, which primarily stem from: (1) emergent signals which are common for head waves (or Pn phase), (2) low signal to noise ratio and (3) acausal ringing for stations that use an acausal filter and are situated close to the epicenter. Impulsive signals are assigned higher weight to reflect higher confidence in picking; lower weights are assigned to emerging polarities. Ambiguous polarities are removed from the analysis.

The first motion polarities are then incorporated into the Network Sensitivity Solutions (NSS) developed by Ford *et al.* (2010). NSS calculates the variance reduction (VR) for each synthetic source and plots it as a function of source-type parameter on a source-type plot. Using NSS, we first compute 200 million possible moment tensor solutions using the waveform data. Solutions with positive values of VR are then tested against the first motion data, and a combined VR is computed. The maximum VR fit surface is plotted on the Hudson *et al.* (1989) source-type diagram.

Results and Discussion

For events occurring on March 1, 2011 and February 24, 2008, we observe that using the combined dataset, the region representing the best-fit source model with VR greater than

95% in the source-type diagram (see Figure 2.25.1b) is significantly reduced in area. For the March 1, 2011 event, the best-fit source model is composed of 79% double couple (DC), 3% +compensated linear vector dipole (+CLVD) and 18% isotropic (ISO) components. For the February 24, 2008 event, the best-fit source model is composed of 22% DC, 30% +CLVD, and 48% ISO components. For both events, the constrained FMT solution shows consistency on the ISO component compared to the unconstrained FMT solution.

For both events, the first motion constrained FMT solution provides superior fit to the first motion polarities, closely followed by the unconstrained FMT solution (see Figure 2.25.1). In contrast, the deviatoric solution does not fit well the polarity data as demonstrated by the negative fit value. In conclusion, there is a higher confidence in the FMT solution as it fits better with the first motion polarities. The polarity data is also useful in determining the source parameters for an earthquake by providing a good constraint to the FMT solution. The preferred source mechanism for the earthquake is the best-fit source model obtained from NSS using both waveform data and first motion polarities.

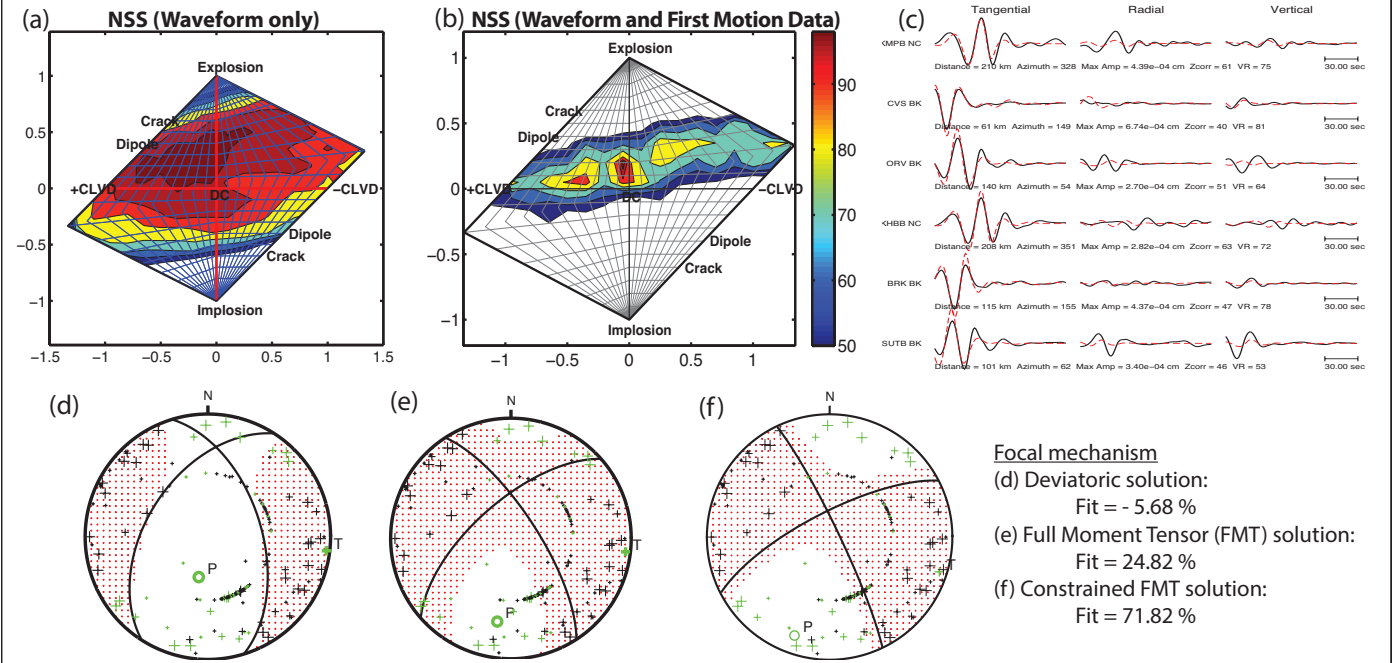
Acknowledgements

This work is supported by the Department of Energy Geothermal Technologies Program under Award Number DD-EE0002756-002. We would like to thank A. Chiang, A. Guilhem, P. Hellweg, P. Lombard, and S.H. Yoo for their support.

References

- Boyd, O. S., D. S. Dreger, V. H. Lai, and R. Gritto, Full Moment Tensor Analysis Using First Motion Data at the Geysers Geothermal Field. PROCEEDINGS, 38th Geothermal Reservoir Engineering Workshop, SGP-TR-98, 2013.
- Ford, S. R., D. S. Dreger and W. R. Walter, Network sensitivity solutions for regional moment tensor inversions, *Bull. Seism. Soc. Am.*, 100, 1962-1970, 2010.
- Hudson, J. A., Pearce, R. G., and Rogers, R. M., Source type plot for inversion of the moment tensor, *J. Geophys. Res.*, 94, 765-774, 1989.

MARCH 1, 2011 (EVENT ID: 71530230)



FEBRUARY 24, 2008 (EVENT ID: 51197011)

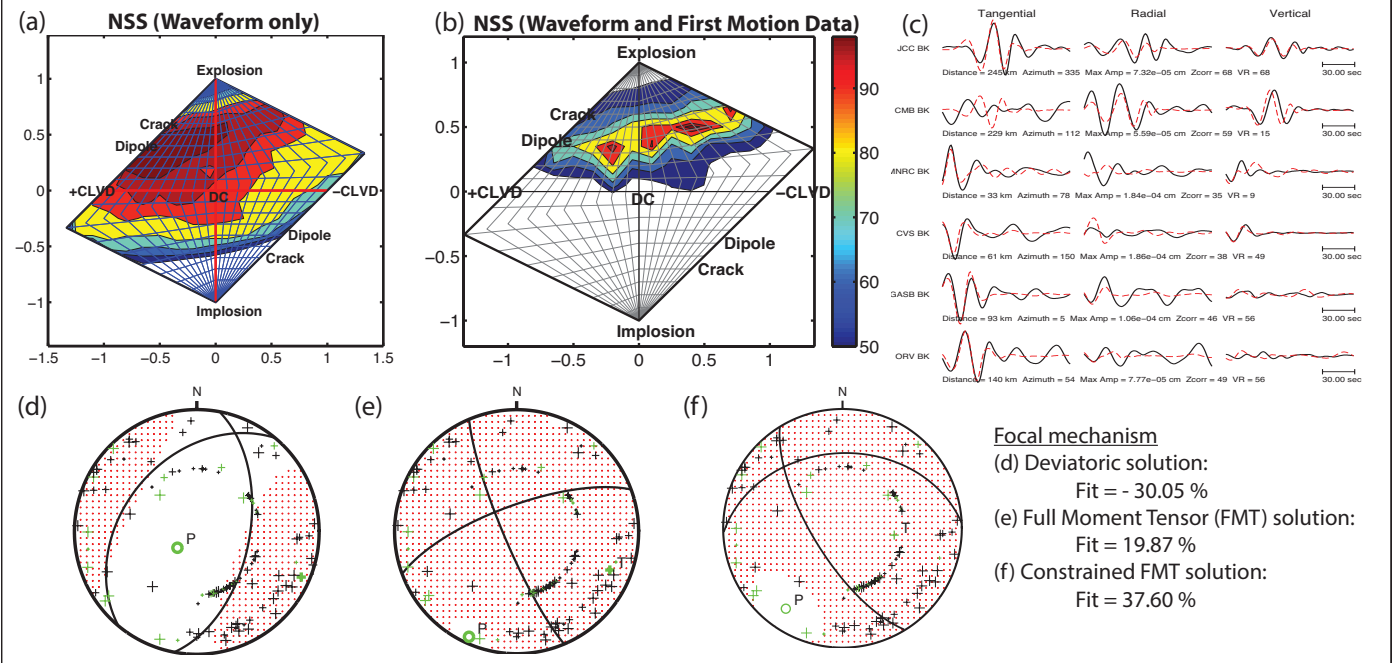


Figure 2.25.1: Source type plots for the NSS result using (a) waveform data and (b) the waveform constrained with first motion polarities. Warmer colors represent higher VR for the best-fit source model for each event. The plots show the VR scaled to the maximum fit value for each case. We also compare (c) the synthetic waveform computed using the constrained full moment tensor (FMT) solution (indicated by the black solid line) with the observed waveform data (indicated by the red dashed line) and show that they compare reasonably well with high variance reduction, particularly for March 1, 2011 event which its VR equals to 74.1%. Focal mechanisms of (d) deviatoric solution, (e) unconstrained FMT solution and (f) constrained FMT solution overlaid with the polarity information are also shown here. Red shaded region represents compressional which is dominated by “up” first motions (shown by black “+” signs) while the white region represents dilatation, dominated by “down” first motions (green “+” signs). The weighting corresponds to the size of the “+” sign where the bigger “+” sign means higher confidence in picking. The “+” signs in the inner circle typically represent head-wave arrivals at stations with small takeoff angle and are useful to constrain the nodal planes

26 TremorScope: Imaging the Deep Workings of the San Andreas Fault

Roland Bürgmann, Richard Allen, Douglas Dreger, Robert Nadeau, Barbara Romanowicz, Taka'aki Taira, Margaret Hellweg

Introduction

Until recently, active fault zones were thought to deform via seismic slip during earthquakes in the upper, brittle portion of the crust, and by steady, aseismic shear below. However, in the past decade, this view has been shaken by seismological observations of seismic tremor deep in the roots of active fault zones. First recognized on subduction zones in Japan and the Pacific Northwest, tremor has also been found to be very active on a short section of the San Andreas Fault to the southeast of one of the most densely monitored fault segments in the world, near Parkfield, CA (Nadeau and Dolenc, 2005). This deep (~20-30 km) zone of activity is located right below the nucleation zone of the great 1857 Fort Tejon earthquake, estimated to be an $M7.9$ event. Thus, learning more about the temporally and spatially complex faulting processes in this zone may help us better understand the conditions that lead to such large ruptures.

The Project Plan and Implementation

The tremor source region is southeast of existing seismic networks around Parkfield, along the San Andreas Fault. We are adding eight seismic stations—the TremorScope (TS) network—in this area to complement existing instrumentation.

Now, all sites for the TS network have been permitted and all four surface stations have been installed, two in this past year. Figure 2.26.1 shows the installation of the seismometer vault at station TRAM, just above the centroid of the tremor sources. Surface installations have a broadband seismometer, an accelerometer and a digitizer. Station TRAM will also host one of the four boreholes. The borehole sites, with a hole about 300 m deep, will have an accelerometer at the surface. Seismometers, accelerometers and geophones will be installed at the bottom of these boreholes, where the levels of environmental and human-induced noise are much lower than at the surface, so the weak tremor signals will be more easily detected and analyzed. We defined the specifications for the boreholes, including target depth and casing options. In late-June, we hosted a pre-bid walk-through for prospective drilling companies to introduce them to the drilling sites in preparation for their bids. Down-hole will be a three-component set of gimballed, 2 Hz geophones. Three boreholes will also be equipped with a Guralp downhole sensor package, consisting of a three-component broadband seismometer, a three-component accelerometer and a digitizer. At all locations, data will be logged onsite and forwarded to Berkeley for real-time processing. The data will be used in real-time earthquake monitoring (see Operational Section 3.1) as well as for tremor studies. Data are now being archived and analyzed from the four surface stations.

Figure 2.26.2 shows non-volcanic tremor in the Parkfield region on May 8th, 2013. This type of tremor is hard to detect at just one station because it has a low diffuse signal that lasts for minutes. The TS network is located very near the source of these tremors and we can clearly pick up the signal on multiple



Figure 2.26.1. Installation of the seismic vault at TremorScope station TRAM.

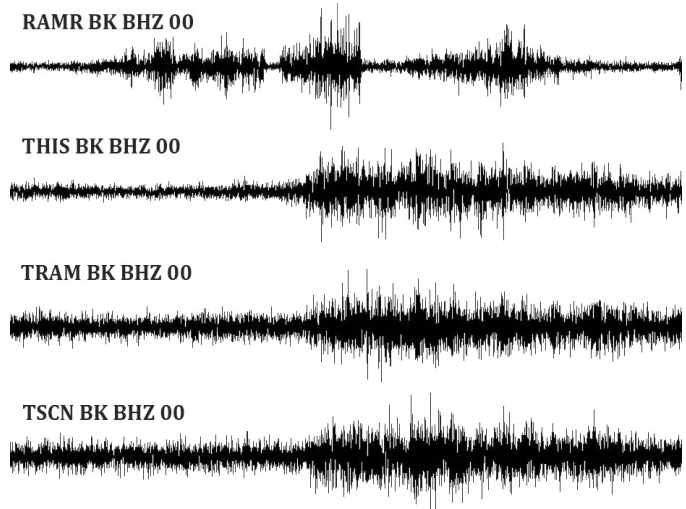


Figure 2.26.2: Non-volcanic tremor as seen on the TS network in the Parkfield, CA region on May 8th, 2013. The concurrence of the signal on the lower three seismograms shows that this is not locally generated noise. Station RAMR, however, is farther away and does not pick up the tremor.

stations (THIS, TRAM, TSCN) and confirm that this is indeed tremor. In contrast, station RAMR is located about 50 km away from the source region and no identifiable tremor signal is visible.

Results

Figure 2.26.3 depicts a map of the Parkfield, California area. The stars are locations of tremor bursts occurring 90 days prior to June 9th, 2013. Red stars are the five most recent tremor bursts. The solid and dotted lines in both panels represent the locked and creeping portions of the San Andreas Fault, respect-

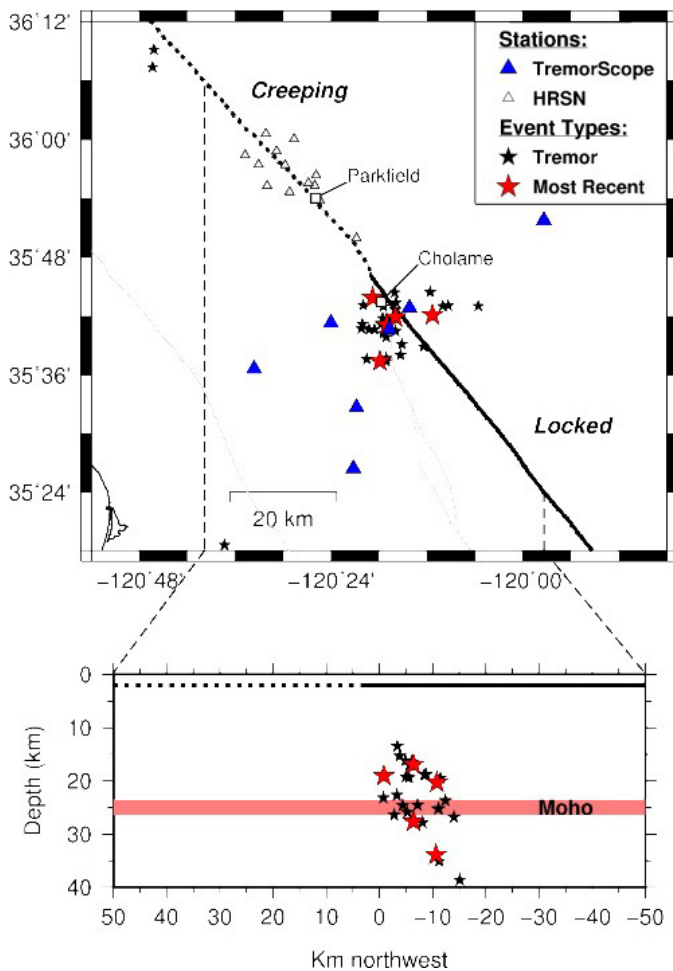


Figure 2.26.3: Map showing the 90 days of tremor prior to June 9th, 2013.

ively. The white triangles are sensitive borehole stations of the High Resolution Seismic Network (HRSN) used in the detections, and the Tremorscope stations are shown as blue triangles. The towns of Parkfield and Cholame are the labeled squares. The bottom panel shows the locations of the tremor episodes in depth section along the fault. The pink horizontal line represents the Moho in the area. To look at the most recent tremor, go to http://seismo.berkeley.edu/research/recent_tremor.html

Perspectives

Data from the TremorScope project will improve earthquake tremor monitoring in the region south of Parkfield. Insights from the project will also contribute to an understanding of tremor and slip in other regions of the world where such phenomena have been observed, but are not nearly as accessible. Should a great San Andreas earthquake occur during this experiment, the network would also provide unprecedented and exciting insights into the seismic rupture process. In addition, the BSL received the go-ahead from the university to submit a “major research initiative”, or MRI, proposal to the National Science Foundation for tracking fault processes on the deep San Andreas with a high-sensitivity seismic array of borehole

stations. This project would use the TremorScope instrumentation as leverage to increase and improve seismic monitoring throughout the area and improve our understanding of the transition in fault behavior between the locked San Andreas Fault in the Fort Tejon/Carizo Plains segment and the creeping section to the northwest of Parkfield.

Acknowledgements

This work is funded by grant 2754 from the Gordon and Betty Moore Foundation.

References

Nadeau, R., and Dolenc, D., Nonvolcanic tremors deep beneath the San Andreas fault, *Science*, 307, 389, doi:10.1126/science.1107142, 2005.

27 Near Real-Time Infragravity Noise Removal for the Monterey Ocean Bottom Broadband (MOBB) Station

Zhao Zheng, Taka'aki Taira, Barbara Romanowicz

Introduction

The Monterey Ocean Bottom Broadband (MOBB) seismic station is located 40 km offshore in the Monterey Bay, CA, at a water depth of ~1,000 m (Romanowicz *et al.*, 2003; 2006). Since 2009, data have been available in real time via cable connection to the nearby MARS (Monterey Accelerated Research System) node (<http://www.mbari.org/mars>) (Romanowicz *et al.*, 2009). So far, MOBB is the only offshore permanent broadband station in central California besides the island-based Farallon Islands station (FARB). It therefore provides important complementary azimuthal coverage for seismicity on the San Andreas Fault system.

However, the usage of MOBB seismic data for purposes such as regional moment tensor (MT) determination has been greatly restricted due to severe noise from seafloor deformation forced by ocean infragravity (IG) waves. Given the water depth at MOBB, the IG-induced noise on the vertical component seismogram peaks in 20-200s (Dolenc *et al.*, 2005), which overlaps with the band (10-100 s) for regional MT analysis.

Fortunately, MOBB contains a Differential Pressure Gauge (DPG) which provides continuous water pressure recordings at a sufficiently high sampling rate (1 sps). It has been noticed that a strong correlation exists between seafloor vertical ground motion and pressure in the IG band (Dolenc *et al.*, 2005). A transfer function (TF) between the two components can therefore be defined and utilized to remove the IG noise from vertical component seismogram (Webb and Crawford, 1999; Crawford and Webb, 2000; Crawford *et al.*, 2006; Dolenc *et al.*, 2007). If the TF is time invariant, then it can be pre-computed and used in a real-time fashion for noise removal.

Method

Following Webb and Crawford (1999), the transfer function $T(\omega)$ can be expressed as

$$T(\omega) = \gamma(\omega) \sqrt{G_{SS}(\omega)/G_{PP}(\omega)} \quad (27.1)$$

where $G_{SS}(\omega)$ and $G_{PP}(\omega)$ are the one-sided auto-spectral density functions for the vertical component seismic and the pressure records, respectively, and $\gamma(\omega)$ is the coherence between the two components defined as (Bendat and Piersol, 1986):

$$\gamma(\omega) = G_{SP}(\omega) / \sqrt{G_{SS}(\omega)G_{PP}(\omega)} \quad (27.2)$$

with $G_{SP}(\omega)$ being the one-sided cross-spectral density function between seismic and pressure records. Following Crawford and Webb (2000), we estimate $G_{SS}(\omega)$, $G_{PP}(\omega)$, and $G_{SP}(\omega)$ from $S(\omega)$ and $P(\omega)$, the spectrum of the seismic and the pressure record:

$$G_{SS}(\omega) = \left(\frac{2}{NL}\right) \sum_{i=1}^N |S_i(\omega)|^2 \quad (27.3)$$

$$G_{PP}(\omega) = \left(\frac{2}{NL}\right) \sum_{i=1}^N |P_i(\omega)|^2 \quad (27.4)$$

$$G_{SP}(\omega) = \left(\frac{2}{NL}\right) \sum_{i=1}^N S_i^*(\omega)P_i(\omega) \quad (27.5)$$

where i is the index of the data segment that enters the average, N the number of data segments, and L the length of each segment. In this study, we calculate the G terms for each day by breaking 1 day's data into 8 non-overlapping 3-hour segments and taking the average. We have tried other values of N and L and determine that this set is optimal.

The part of energy that is coherent with the pressure record is then subtracted from the seismogram:

$$S'(\omega) = S(\omega) - T_i^*(\omega)P(\omega) \quad (27.6)$$

Then an inverse Fourier transform of $S'(\omega)$ is taken to obtain the corrected seismogram in the time domain.

The success of the method relies upon the high coherence between the seismogram and the DPG in the IG band. In a related study (Taira *et al.*, 2013), the authors have confirmed that the coherence is indeed high ($\gamma^2(\omega)$ median > 0.995 in the period range of 30-200s) for MOBB.

Results

We systematically calculate the TFs from each day from Apr 2009–Feb 2010 and July 2011–June 2012 when data are available (the gap in between was due to a cable trawl incident). We have also examined the time before 2009, however these data have many issues. These 1-day TFs are then compared to examine their temporal variability (Fig. 2.27.1). We discover that the TF is generally stable over time, except for an abrupt change from 2010 to 2011, which was due to a DPG replacement in July 2011. One reference TF is obtained for 2009-2010 and 2011-2012, respectively. As a side note, despite nominally being identical, different DPGs have notably different calibrations, which may be a relevant concern for other OBS deployments and related studies. The reference TF needs to be recalibrated every time the instrument is replaced.

We then utilize the reference TF for noise removal. Fig. 2.27.2 shows an example of an M_w 4.3 local earthquake. The method proves successful. We then include the cleaned MOBB data for MT inversion. As shown in Fig. 2.27.3 for several local earthquakes, significant improvements in variance reduction are achieved. This noise removal method has been incorporated in the MT determination code of the Northern California Seismic System.

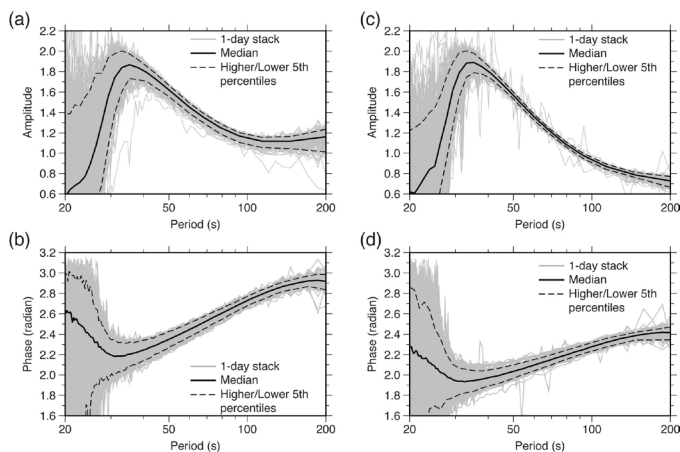


Figure 2.27.1: Amplitude (a,c) and phase (b,d) responses of the 1-day transfer functions (TFs) in the time intervals 2009-2010 (left) and 2011-2012 (right). In each plot, the individual TFs are the cluster of gray curves; the solid curve shows the median, and the two dashed curves show the higher and lower 5th percentiles of the ensemble.

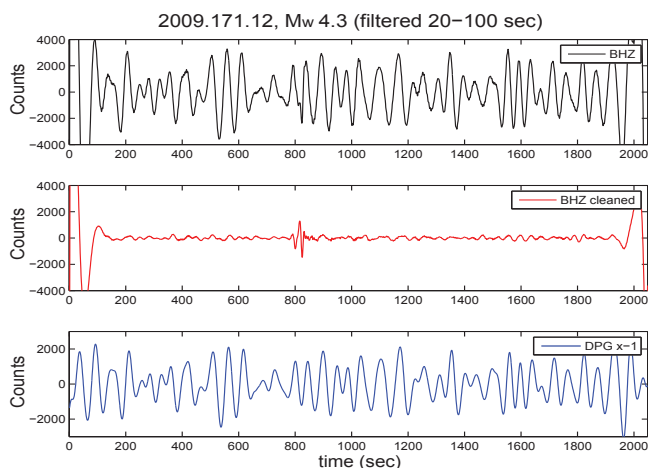


Figure 2.27.2: MOBB waveforms for an M_w 4.3 local earthquake. From top to bottom: the vertical component seismogram before the noise removal using the reference TF for the time interval of 2009–2010; the vertical component seismogram after the noise removal; the DPG record (sign flipped). All traces are filtered in 20-100 seconds.

Acknowledgements

MOBB data are downloaded from the NCEDC. D. Dolenc kindly provided us with the codes for computing power spectral density and transfer functions. This study was supported by the NSF Grant OCE-9911392 and OCE-0648302.

References

- Bendat, J. S., and A. G. Piersol, Random Data: Analysis and Measurement Procedures, John Wiley and Sons, New York, 1986, 566 pp.
- Crawford, W. C., and S. C. Webb, Identifying and removing tilt noise from low-frequency (<0.1 Hz) seafloor vertical seismic data, *Bull. Seismol. Soc. Am.* 90(4), 952–963, 2000.
- Crawford, W. C., Stephen, R. A., and Bolmer, S. T., A second look at low-frequency marine vertical seismometer data quality at the

OSN-1 site off Hawaii for seafloor, buried, and borehole emplacements, *Bull. Seismol. Soc. Am.* 96(5), 1952–1960, 2006.

Dolenc, D., Romanowicz, B., Stakes, D., McGill, P., and Neuhauser, D., Observations of infragravity waves at the Monterey ocean bottom broadband station (MOBB). *Geochem. Geophys. Geosyst.*, 6, Q09002, 2005.

Dolenc, D., B. Romanowicz, R. Uhrhammer, P. McGill, D. Neuhauser, and D. Stakes, Identifying and removing noise from the Monterey ocean bottom broadband seismic station (MOBB) data, *Geochem. Geophys. Geosyst.*, 8, Q02005, 2007.

Romanowicz, B., Stakes, D., Uhrhammer, R., McGill, P., Neuhauser, D., Ramirez, T., and Dolenc, D., The MOBB experiment: A prototype permanent off-shore ocean bottom broadband station. *Eos Trans., AGU* 84(34), 325, 2003.

Romanowicz, B., Stakes, D., Dolenc, D., Neuhauser, D., McGill, P., Uhrhammer, R., and Ramirez, T. The Monterey Bay broadband ocean bottom seismic observatory. *Ann. Geophys.* 49, 607–623. 2006.

Romanowicz, B., McGill, P., Neuhauser, D., and Dolenc, D. Acquiring real time data from the broadband ocean bottom seismic observatory at Monterey Bay (MOBB). *Seism. Res. Lett.*, 80(2), 197–202, 2009.

Taira, T., Zheng, Z. and Romanowicz, B., On the Systematic Long Period Noise Reduction on Ocean Floor Broadband Seismic Sensors Collocated with Differential Pressure Gauges, *Bull. Seism. Soc. Am.*, in review, 2013.

Webb, S. C., and W. C. Crawford, Long period seafloor seismology and deformation under ocean waves, *Bull. Seis. Soc. Am.* 89, 1535–1542, 1999.

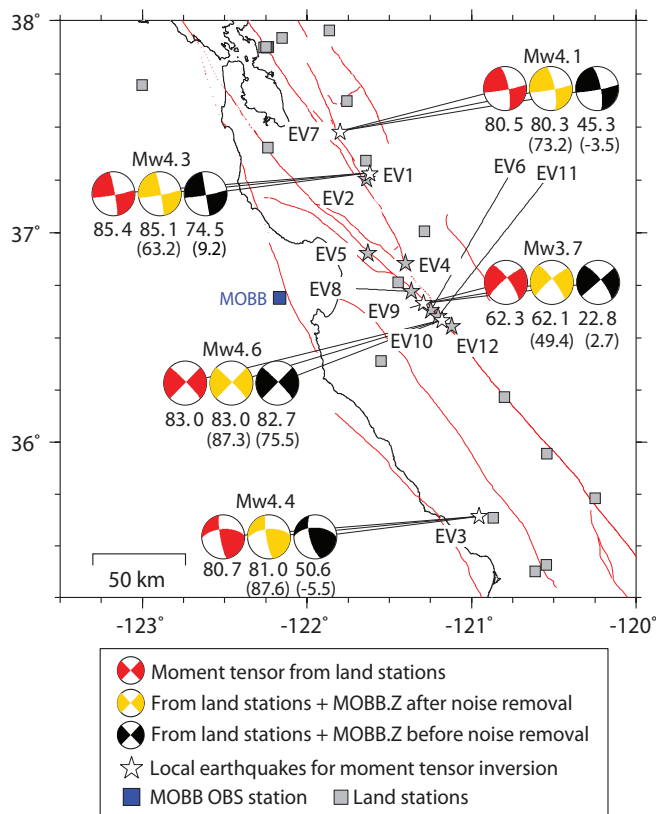


Figure 2.27.3. Comparison of moment tensor solutions with cleaned and uncleaned MOBB data for five local earthquakes. The number below each beachball is the variance reduction (VR) of waveform fit. The numbers in parentheses are the VR when only MOBB is used.

28 Potential Applications Using a Smartphone Network

Qingkai Kong, Richard Allen

Introduction

We are continuing to explore the use of the accelerometer in smartphones to detect earthquakes and the potential scientific applications of using such a dense network. Although the smartphone network does not exist at this point, we are starting to think about how we could use the data for scientific research and applications by using an analogous dataset. We are using the Nodal Seismic Array deployed by the NodalSeismic Company. This array has a nominal station spacing of about 120 m and was designed for active source exploration of petroleum resources. It occupied over 5200 sites with 10 Hz vertical component seismometers in the heavily urbanized area of Long Beach, CA. The dimensions of the array are 7 km by 10 km.

Methodologies

(1) P-wave arrival time residual

We first picked the P-wave arrival time of a magnitude 2.4 earthquake (2011-05-14 04:19:15) for each of the stations using the STA/LTA algorithm (Allen 1978) combined with manual picking. Then we extracted a 1D structure model from the 3D velocity model for southern California (Magistrale *et al.* 1996). We used TauP package (Crotwell *et al.* 1999) to predict the arrival time of the P wave using the extracted velocity model. We then subtracted the observed travel time from the predicted time. Removing the linear trend produced the residual travel time map in Figure 2.28.1

(2) Helmholtz Tomography

We implemented the Eikonal/Helmholtz tomography method first proposed by Lin *et al.* 2009. This method uses the Eikonal equation (e.g. Wielandt 1993; Shearer 1999)

$$\frac{1}{c_i(r)^2} = |\nabla\tau(r_i, r)|^2 - \frac{\nabla^2 A_i(r)}{A_i(r)\omega^2} \quad (1.1)$$

which is derived directly from the Helmholtz equation. In this equation, c_i is the phase speed for traveltime surface i at position r , ω is the frequency and A is the amplitude of an elastic wave at position r . From this equation, we can directly relate the travel time of the waves with the phase velocity at each station point without doing an inversion. Using the above equation to get the phase velocity is called Helmholtz tomography. If high frequencies are used, or the spatial variation of the amplitude field is small compared with the gradient of the travel time surface, then the second term on the right-hand side can be dropped. This forms the basis of Eikonal tomography. Lin applied this Eikonal tomography to ambient noise of this dense array and then inverted this into a 3D structure. We apply this Helmholtz tomography method to the same earthquake we used above, and get a phase velocity structure as shown in Figure 2.28.2.

Initial results and future work

From the two figures, we can see some evidence of the shallow structure in this area (the depth of the earthquake is 11.9 km, and the distance from the epicenter to the edge of the array is about 6.5 km). Some obvious structures associated with the faults can be seen. With only one small earthquake, it is hard to tell the real structure in this area. But this shows the potential of using the dense network, like the smartphone network, to study the earth structure. We are now developing our 2nd generation application for the smartphones for collecting earthquake data, and building a prototype smartphone network with Deutsche Telecom (Silicon Valley Innovation Center). A network consisting of these smartphones may work as a supplement network to the current traditional network for scientific research and real-time application.

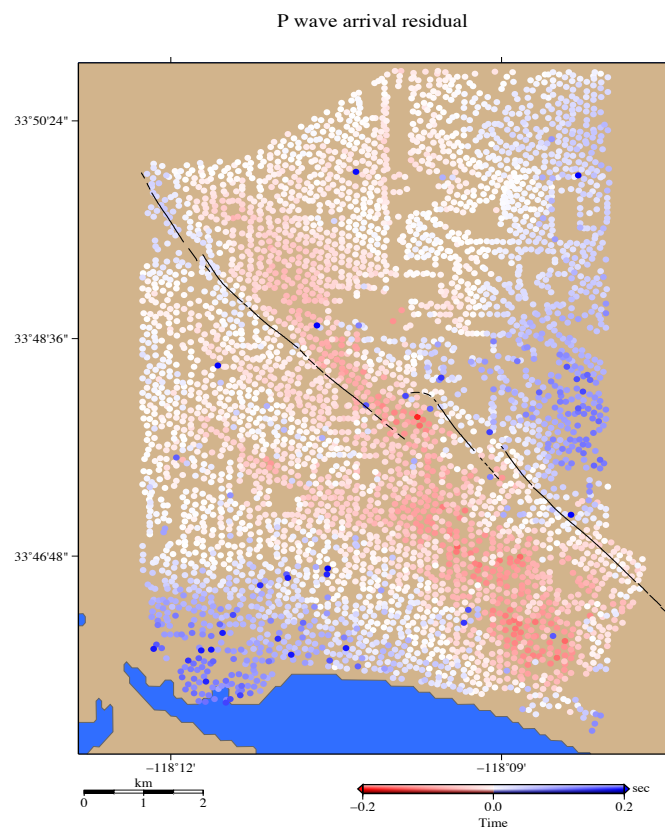


Figure 2.28.1. P-wave arrival time residual from the magnitude 2.4 earthquake. Red dots show the observed arrival time later than the predicted time, and the blue dots are the stations at which the observed p-wave arrival time is earlier than the predicted time. Black lines are the faults in this area.

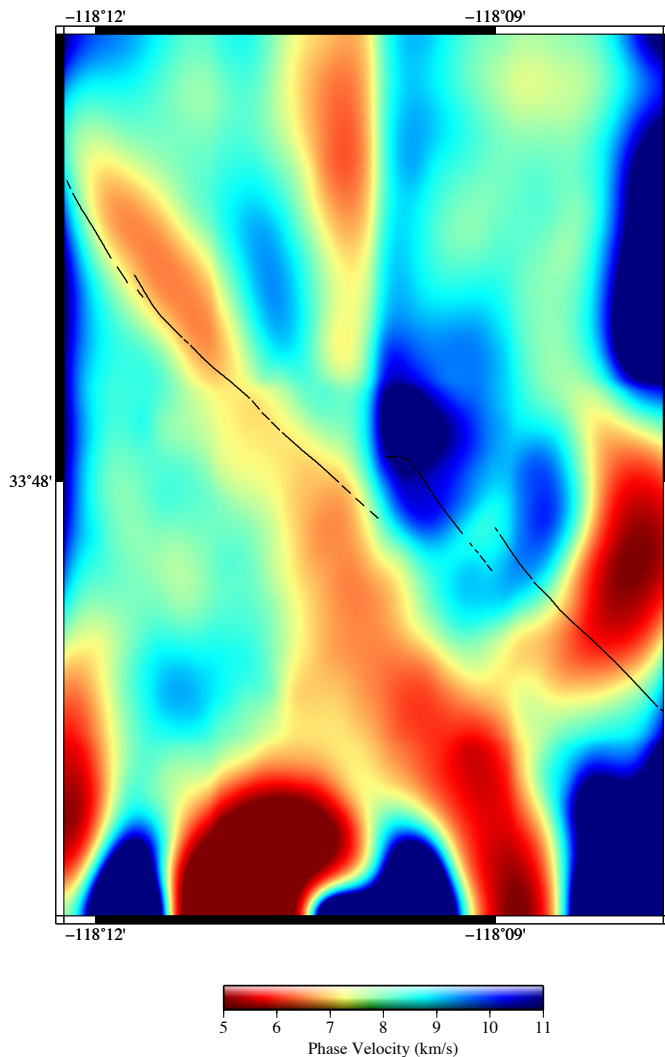


Figure 2.28.2. P wave phase velocity computed from the Helmholtz tomography. The red areas are slow velocities and the blue areas are fast velocities. The black lines are the faults in this area.

Acknowledgements

We thank Dan Hollis from NodalSeismic Company for providing the data for us to analyze. This project is funded by Deutsche Telekom and CITRIS. Patrick McEvoy, Markus Neubrand, Angela Nicoara, Louis Schreier, and Arno Puder from Deutsche Telekom provided the android phones and the myShake application.

References

- Allen, R., Automatic earthquake recognition and timing from single traces: *Bulletin of the Seismological Society of America*, 68, 1521-1532, 1978.
- Crotwell, H. P., T. J. Owens, and J. Ritsema, The TauP Toolkit: Flexible seismic travel-time and ray-path utilities, *Seismological Research Letters* 70, 154-160, 1999
- Lin, F. C., Ritzwoller, M.H. & Snieder, R., Eikonal tomography: surface wave tomography by phase front tracking across a regional broadband seismic array, *Geophysical Journal International*, 177(3),

1091-1110, 2009.

Lin, F., and M. H. Ritzwoller, Helmholtz surface wave tomography for isotropic and azimuthally anisotropic structure, *Geophysical Journal International*, 186, 1104-1120, 2011a.

Magistrale, H., K. McLaughlin, and S. Day, A geology based 3-D velocity model of the Los Angeles basin sediments, *Bulletin Seismological Society of America* 86, 1161-1166, 1996.

Shearer, P., Introduction to Seismology, Cambridge University Press, Cambridge, 1999.

Wielandt, E., Propagation and structural interpretation of non-plane waves, *Geophys. J. Int.*, 113, 45-53, 1993.

29 ShakeAlert: A Unified EEW System for California

Margaret Hellweg, Richard Allen, Maren Böse (Caltech), John Clinton (ETH), Egill Hauksson (Caltech), Thomas Heaton (Caltech), Ivan Henson, Serdar Kuyuk, Doug Neuhauser, Ingrid Johanson, Ronni Grapenthin

Introduction

Earthquake Early Warning (EEW) is a method of rapidly identifying an earthquake in progress and transmitting alerts to nearby population centers before damaging ground shaking arrives. The first few seconds of the initial P-wave arrivals at one or more stations are used to detect the event, and predict magnitude and peak shaking. Detections from several stations are combined to locate the event. A warning of imminent shaking can be used to activate automatic safety measures, such as slowing trains, isolating sensitive equipment, or opening elevator doors. Warnings can also be sent directly to the public via cell phone, computer, television, or radio.

With support from the United States Geological Survey (USGS) and the Gordon and Betty Moore Foundation, the California Integrated Seismic Network (CISN) now moves into Phase III of the ShakeAlert project. This move transitions the focus from creating an end-to-end demonstration system for real time EEW solely in California, to developing a prototype for a West Coast EEW system. The University of Washington now joins the collaboration with the Berkeley Seismological Laboratory (BSL), the California Institute of Technology (Caltech), and the Swiss Institute of Technology Zürich (ETH). Phase III of the ShakeAlert development will provide a blueprint for future public alerts.

Project Status

The ShakeAlert system combines the best aspects of the three methods from the proof-of-concept project. Caltech's *OnSite* algorithm uses P-wave data from the single station nearest the epicenter to provide extremely rapid estimates of likely ground shaking. The BSL's ElarmS algorithm and ETH's Virtual Seismologist use data from several stations around an event epicenter to produce a slightly slower, but more reliable estimate of magnitude and location. Often, ElarmS is the first to send out an alert due to constant improvements to the algorithm made possible in part by Ivan Henson's system performance tools. Combining the three methods produces an algorithm, which has the speed of a single-station method, but is augmented by the confirmation and updated adjustments as additional station data become available.

When an identified event exceeds a defined combination of magnitude, ground shaking intensity, and statistical likelihood, information is broadcast to system users. Currently, during the demonstration and prototype phases, only project participants and a small cadre of beta users receive event information. Recipients include the state's emergency operations center at the California Office of Emergency Services (CalOES), Bay Area Rapid Transit (BART), Google, and the San Francisco Department of Emergency Management (SFDEM). A schematic diagram of the end-to-end system can be found at: <http://www.cisn.org/eew/EEWProject.html>.

ElarmS Development

The newest version of ElarmS (ElarmS2) began publishing alerts in March 2012 for the entire state of California. The improved algorithm in the new production-grade version of the code maximizes the performance, given the current seismic network configuration, and hardware and software capabilities, improving both the speed of the early warning processing and the accuracy of the result. ElarmS2 successfully detected 26 of the 29 earthquakes ($M > 3.5$) across California and only issued two false alarms in a five-month period. Since April 2012 (for the BK network), and August 2012 (for the CI network), the stations are now equipped to send data in one-second packets to the waveform processing centers and be processed directly, shaving up to 6 seconds off of alert times. Event filters were also added to minimize the publication of false events. With all of these enhancements integrated, an alert can now be issued by ElarmS2 within 12.37 ± 5.21 sec of the origin time (see Figure 2.29.1). The tail in the alert time histogram is mainly caused by events offshore of Cape Mendocino and events located in poorly instrumented areas such as the northern and northeastern regions of California.

G-larmS Development

This year, the BSL has ramped up development of real-time GPS-based approaches to EEW through the use of displacement time series for rapid source parameter estimation. The G-larmS module uses data from GPS stations throughout Northern California to provide estimates of earthquake size and rupture length within seconds following a large ($M > 7$) event. G-larmS is complementary to seismic EEW methods, providing precision for higher magnitude estimates where seismic methods tend to saturate and in turn relies on seismic data to provide event triggering. Preliminary testing of the offset determination module using simulated real-time GPS data from the 2010 $M_w 7.2$ El Mayor-Cucupah earthquake found that the offset estimate stabilized quickly, even in the presence of earthquake shaking, and that the method provides results within 1-2 cm of the expected values. Work continues on the G-larmS module that will invert for fault slip and update magnitude estimates; it should be ready for operation by the end of this year.

Perspectives

This year we are continuing Phase III of the EEW project in collaboration with our partners at Caltech and the University of Washington, with funding from the USGS and the Moore Foundation. We look forward to continuing to maintain, operate, and improve the system as it transitions from a demonstration product to a working prototype. Phase III will highlight the increased importance of the EEW users and their interactions with the system.

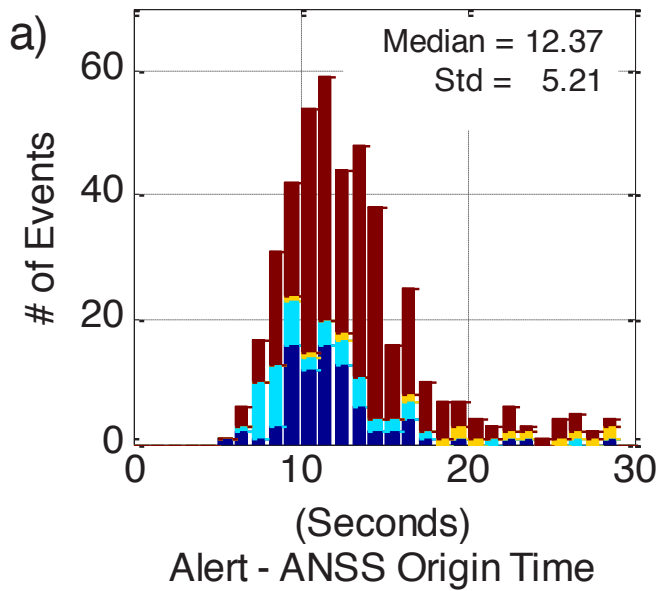


Figure 2.29.1: Latencies reflecting the difference in time between the first alert publication and the origin time of the earthquake in the Advanced National Seismic System (ANSS) catalog tallied for earthquakes detected by ElarmS2 from October 2, 2012 to February 15, 2013. The histogram is color coded by the epicenter's regional location: Bay Area (blue), LA Area (cyan), Offshore (yellow), and all others (red).

Acknowledgements

This project is supported at UC Berkeley by USGS Cooperative Agreement G12AC20348, at Caltech by Agreement G12AC20343, at USC/SCEC by Agreement G12AC20339, and at ETH Zurich by Agreement G12AC20342. Funding from the Gordon and Betty Moore Foundation is under project number GALA 3024.

30 Optimal Seismic Network Density for Earthquake Early Warning: A Case Study from California

H. Serdar Kuyuk and Richard M. Allen

Introduction

One of the challenges with Earthquake Early Warning Systems (EWS) is minimizing the “blind zone”—the region around an earthquake epicenter where no warning is possible because the strong shaking has already occurred by the time the alert is generated. There are factors that influence the radius of the blind zone area that are simply out of our control. For example, we cannot dictate exactly where and when earthquakes occur and how far individuals are from the earthquake epicenter. However, there are many things we can do to reduce the size of the blind zone. For example, improvements can be made to increase the warning time by some seconds by: a) using the most advanced telecommunication technologies that can potentially decrease the current telemetry delay; b) decreasing data packet size to less than 0.5 seconds; c) improving event detection and alert filtering algorithms; and d) well developed seismic networks with improved station density deployed across seismogenic zones. The degree to which these improvements can be made depends on how close the seismic stations are to the earthquake epicenter, as well as the distance between the warning site and the earthquake epicenter, the depth of earthquake, the density of the seismic network, the telemetry delay, and the time needed for decision making in regards to the type of warning that should be issued. For any practical use, the blind zones will be larger depending on the time required for a specific action.

We estimate how the average blind zone radius changes with varying interstation distances by examining inter-station distances from 1 km to 100 km (Figure 2.30.1). In our calculations, we first model typical California earthquakes, which, on average, have a relatively shallow depth of 8 km. We find that by increasing the station density 10 times (interstation distances from 100 to 31 km), the radius of the blind zone decreases by 57% from 73 km to 32 km. Increasing mesh density an additional 10 times (interstation distances from 31 to 10 km), the blind zone radius drops by another 37% from 32 km to 20 km. Increasing the station density by another factor of 10 (interstation distances from 10 to 3 km) reduces the radius by only 15% from 20 km to 17 km. We can also compute these estimates for the spatial extent of the blind zone area. A decrease of 57%, 37%, and 15% in blind zone radius corresponds to an 80%, 60% and 28% drop respectively in total blind zone area

We explored the distribution of interstation distances within the California Integrated Seismic Network (CISN). At each of the California stations we assign an average interstation distance value, which is computed from the average distance to the three closest stations. From these values we create a contour map of interstation distances using a linear interpolation between stations (Figure 2.30.2a).

We find that ~50% of California have an average interstation distance of 50 km or more (Figure 2.30.2a, primarily yellow

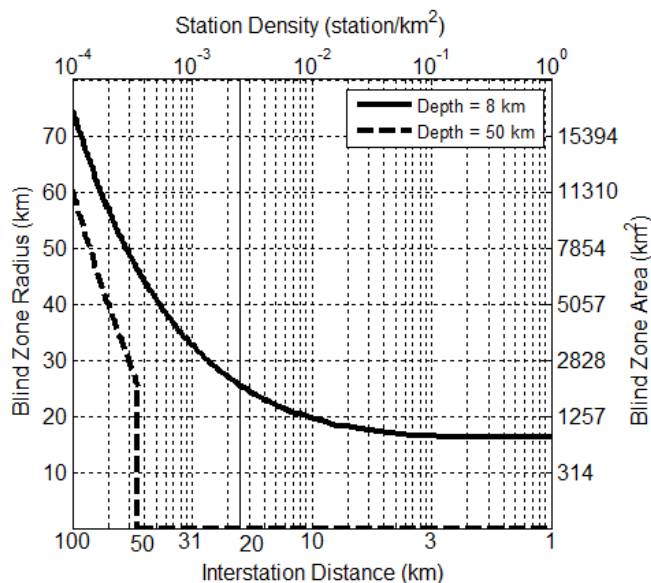


Figure 2.30.1: Relationship between network density (or, equivalently interstation distance) and blind zone radius (or, equivalently area) computed for earthquakes of different depths. The smaller 8 km depth (solid line) is consistent with the average depth of earthquakes in California and the larger 50 km depth (dashed line) is consistent with what might be expected beneath the on-shore regions of the Pacific Northwest of the US from a subduction zone earthquake.

regions), whereas highly populated areas, such as the San Francisco Bay and the Los Angeles regions have less than 30 km spacing (Figure 2.30.2a, green colors).

An EWS should be devised to be the most robust at issuing alerts in regions identified as having high shaking potential from earthquakes, in combination with a large population base from the standpoint of probabilistic seismic hazard. For California, we assess which regions have both a high shaking potential (Figure 2.30.2b) and a large population density (Figure 2.30.2c). The seismic networks have been designed to have higher station densities in the regions of higher population. Qualitatively, regions that have both large populations as well as a high likelihood of experiencing strong shaking include: the extended Los Angeles and San Francisco Bay regions, and the southern part of the San Andreas Fault.

For the southern part of the Central San Andreas Fault (SAF), between San Jose and Los Angeles, we find there are an inadequate number of stations. In this critical part of California, the interstation distance varies from 30 to 50 km

Based on quantitative estimates of the current CISN/EWS infrastructure, we conclude that the blind zone radius throughout California is very heterogeneous. The minimum blind zone radius is ~16 km for typical California earthquakes with 8 km depth when a system requires at least four station detections

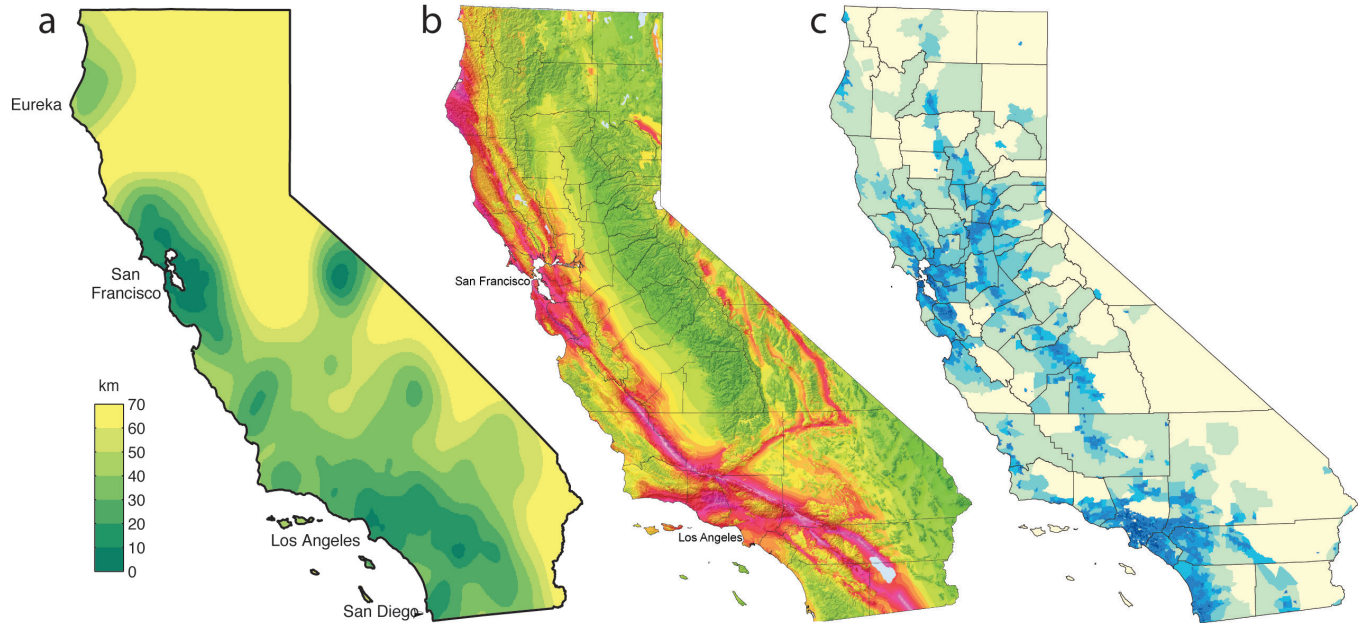


Figure 2.30.2: a) Seismic station interstation density map where yellow colors indicate lower densities. For a given station location, the interstation density is determined by averaging the distance to the nearest 3 stations, b) Probabilistic seismic hazard map (from the State of California), c) Population density of California (from the U.S. Census Bureau). For larger resolution images see the References section that has the appropriate links.

and there is a four second processing/communications delay. Therefore, based on current constraints, there will be no time to issue a warning for any location within 16 km of a large earthquake. This limit of 16 km could be decreased if we address technical and algorithmic issues such as reducing the telemetry delay, decision-making time, etc.

The blind zone radius increases with larger interstation distance. Throughout most of the greater San Francisco Bay area and the Los Angeles area, blind zone radius is less than 30 km. These regions would likely get warnings for earthquakes that occur at distances greater than 20 km. In other regions of California, particularly in Northern California where the station spacing is much sparser (e.g., interstation distances of > 70 km), the blind zone radius is much larger. Our results show that successful warnings could only be issued for earthquakes at distances of 50 km from the earthquake location.

Three key factors which affect the optimization of interstation distance and station distribution are: I) budget, II) population/property distribution, and III) probability of expected earthquakes (past seismicity/known faults). In our budget-limited reality, however, optimum performance is also not achieved by even station distribution. Stations should be (1) densest (~10 km) in the urban areas that are above hazardous faults, (2) fairly dense (~20 km) along hazardous faults away from urban centers, and (3) least dense in other regions. Based on the current distribution of stations and hazards in California, the areas between San Jose and northern LA, and between Eureka and the San Francisco Bay Area need immediate attention if we would like to enhance EEWs in California.

Acknowledgements

This work is funded by USGS/NEHRP awards G09AC00259 and G12AC20348, and by the Gordon and Betty Moore Foundation through Grant GBMF3024 to UC Berkeley.

References

- Kuyuk H.S., Allen, R.M., Optimal seismic network density for earthquake early warning: A case study from California, *Seismological Research Letters*, in press, 2013.
- State of California, Department of Conservation, Regional Geologic Hazards and Mapping Program, Probabilistic seismic hazard map (<http://www.consrv.ca.gov/cgs/rghm/psha/Pages/Index.aspx> last accessed 02 March 2013)
- U.S. Census Bureau, U.S. Department of Commerce, Economics and Statistics Administration. (http://www2.census.gov/geo/maps/dc10_thematic/2010_Profile/2010_Profile_Map_California.pdf)

31 Designing a Network-Based Earthquake Early Warning System for California: ElarmS-2

H. Serdar Kuyuk, Richard M. Allen, Ivan Henson, Holly Brown, Margaret Hellweg, and Douglas Neuhauser

Introduction

The California Integrated Seismic Network (CISN), funded by the USGS, is developing an Earthquake Early Warning (EEW) system for California. Within this “California Shake-Alert” project, three algorithms are being tested, one of which is the network based Earthquake Alarm Systems (ElarmS) EEW. Over the last 3 years, the ElarmS algorithms have undergone a large-scale reassessment and have been re-coded to solve technical and methodological challenges. The improved algorithms in the new production-grade version of the code (E2) maximize the current seismic network’s configuration, hardware, and software performance capabilities improving both the speed of the early warning processing and the accuracy of the result. E2 is designed as a modular code and consists of a new event monitor module with an improved associator that allows more rapid association with fewer triggers, while also adding several new alert filter checks that help minimize false alarms.

Performance of E2

The performance statistics we present here are for the on-line real-time E2 system, versions E2.3.1 and E2.3.2, which have been running in real-time since October 2, 2012 (Figure 2.31.1.). The changes made in E2.3.2 only affect the performance speed, so we are maximizing the time window and number of events by considering performance for both versions. We find that E2 detected 26 of the 29 Advanced National Seismic System (ANSS) earthquakes which had $M_{ANSS} \geq 3.5$. We also investigate the performance in the most populated and the most instrumented regions of the state, the San Francisco Bay Area and the Los Angeles region and find that in these regions, all events were detected and there was only one false event. E2 also successfully detected most earthquakes just outside the CISN networks, including offshore of Cape Mendocino in Northern California and south of the California/Mexico border. However, the estimates for earthquakes that are at the edge or outside of our network have larger errors than is typical of detections within the network footprint.

E2 issued five false alert messages, none of which were in the highly populated San Francisco Bay Area or Los Angeles region. Instead, these false alerts were caused by events outside of California. One event was the M_w 6.3 earthquake off the west coast of Baja, California on December 14, 2012. This was more than 300km from the network, yet triggered many Southern California stations. These triggers were associated into four simultaneous separate/split events because the offshore event had a poor initial estimate of location (false events 1a, b, c, d in Figure 2.31.1). The other false event was from a M_w 5.1 earthquake 72km west of Tonopah, Nevada on December 13, 2012. The closest station to this Nevada event was 80 km away, resulting in a significant initial mislocation. The E2 system did adequately

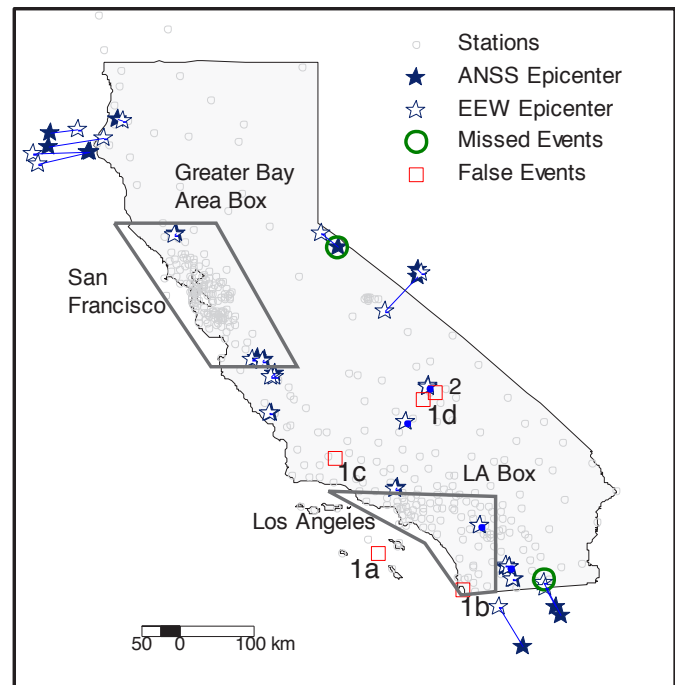


Figure 2.31.1: All detected California events (29), false events (squares, 2), and missed events (circles, 3) with $M_{ANSS} \geq 3.5$ that occurred between October 2, 2012 and February 15, 2013. ANSS epicenters (filled stars) and the corresponding E2 epicenters (open stars) are connected with a line.

locate this earthquake in later iterations; however, later station triggers also generated another event (false alert 2 in Figure 2.31.1).

The differences between ANSS and E2 source parameters are calculated for $M_{ANSS} \geq 3.5$ and $M_{ANSS} \geq 3.0$ events. We compute errors in earthquake magnitude, origin time and location by subtracting the E2 results from ANSS results (Figure 2.31.2). For $M_{ANSS} \geq 3.0$ events we find the median magnitude error is -0.05 ± 0.39 , where the negative -0.05 value indicates that on average E2 slightly overestimates the magnitude by 0.05 magnitude units. For only the larger events ($M_{ANSS} \geq 3.5$) the error is 0.09 ± 0.46 .

Errors in origin time and location are both strongly influenced by the location algorithm. The origin time errors are not normally distributed, instead the mean and standard deviations of the origin time errors are -0.29 ± 1.16 for $M > 3$ and -0.10 ± 1.59 for $M > 3.5$. The median error in the epicentral location (*i.e.*, distance between true and estimated epicenters) of E2 is 3.78 km. The median location error decreases to 2.01 km for larger events ($M > 3.5$).

On Nov/Dec 2012, we made some small changes to the waveform processor that makes E2 a little faster:

- No longer process the data aligned on second boundaries. Simply process packets as soon as they arrive.

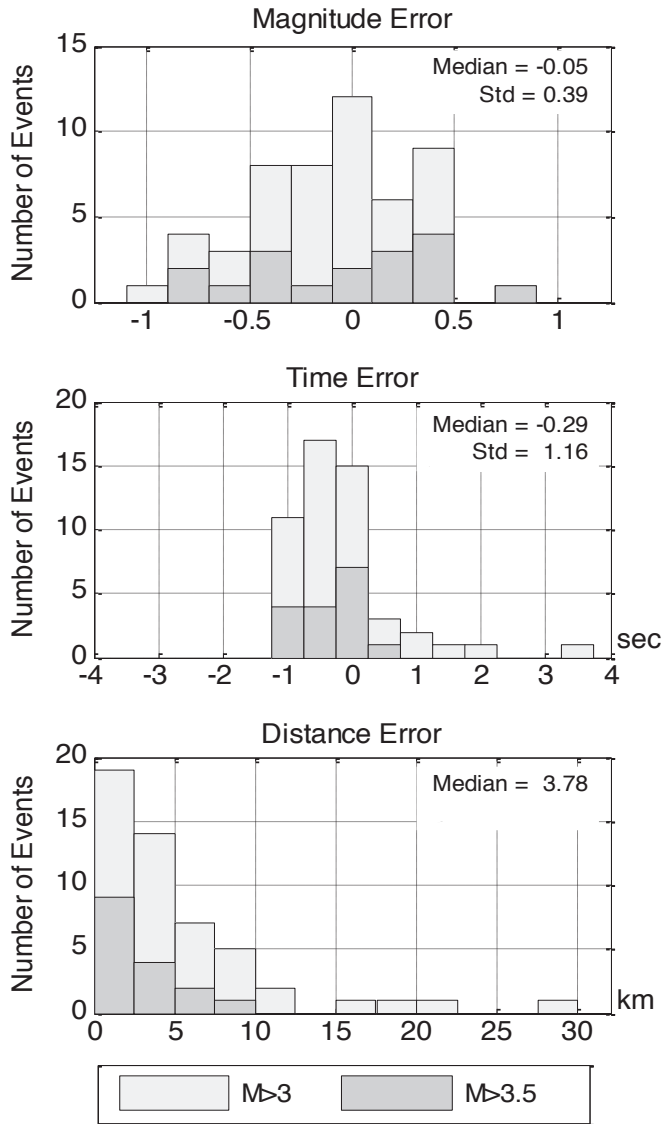


Figure 2.31.2: Histograms of magnitude, time and location errors for E2. The lighter histograms are errors for all events with $M_{ANSS} \geq 3.0$ and darker histograms are for events with $M_{ANSS} \geq 3.5$.

- No longer wait for a half second before sending a trigger (this was to compute τ_p^{\max}). Now send triggers immediately.
- Reduce trigger buffer from 0.5 to 0.05.

These changes probably decreased trigger latencies by 1.0 to 1.5 seconds on average.

In June 2013, the speed of the E2 location algorithm was improved by using four processing threads to do the grid search, instead of one. This makes E2 about three times faster for off-line processing. The online performance from October 2, 2012 to February 15, 2013 shows, on average, E2 currently issues an alert 8.68 ± 3.73 s after the first P-wave detection for all events across California. This processing latency, is calculated by the alert time minus the time of the first P-wave arrival at the closest stations (Figure 2.31.3). Currently, E2 processing latency is the smallest in the Los Angeles Area with a median of 6.72 ± 3.96

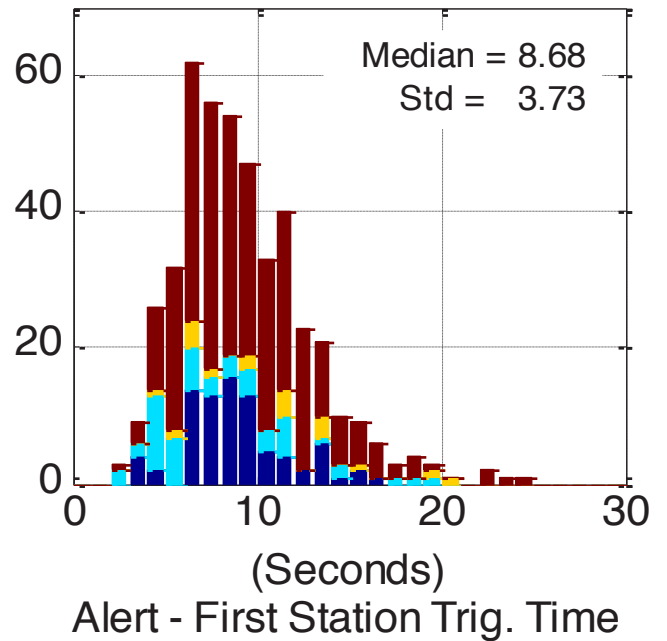


Figure 2.31.3: E2 processing latency, which is alert time minus the time of the first P-wave arrival at a seismic station. This shows the total time the network and E2 require to issue an alert for an event. The median is 8.68 ± 3.73 seconds. Alerts are faster for the San Francisco Bay (blue) and Los Angeles area (cyan).

seconds, which is almost two seconds faster than the latency in the San Francisco Bay Area. This is due to the additional delays from NC stations, which make up a large fraction of the stations in Northern California.

Acknowledgements

This project is possible thanks to the collaborative efforts of many people working at the CISE operating institutions: UC Berkeley, Caltech, USGS Menlo Park and USGS Pasadena. This work is funded by USGS/NEHRP awards G09AC00259 and G12AC20348, and by the Gordon and Betty Moore Foundation through Grant GBMF3024 to UC Berkeley.

References

Allen, R.M., Seconds before the big one, *Scientific American*, 2011.
 Brown, H., Allen, R.M., Hellweg, M., Khainovski, O., Neuhauser, D., Souf, A., Development of the ElarmS methodology for earthquake early warning: Realtime application in California and offline testing in Japan, *Soil Dynamics and Earthquake Engineering*, 31, 188-200, 2011.
 Kuyuk H.S., Allen, R.M., Brown, H., Hellweg, M., Henson, I., and Neuhauser, D., Designing a network-based earthquake early warning system for California: ElarmS-2, *Bull. Seismol. Soc. Am.*, accepted, 2013.

32 G-larmS—Integrating Real-Time GPS into Earthquake Early Warning I: Implementation

Ronni Grapenthin, Ingrid Johanson, Richard Allen

Introduction

In an effort to improve earthquake parameter estimation in Earthquake Early Warning (EEW) for large earthquakes (such as moment magnitude and finite fault geometry), the BSL is working to integrate information from real-time GPS, and now generates and archives real-time position estimates using data from 62 GPS stations in the greater San Francisco Bay Area. This includes 26 stations that are operated by the BSL as part of the Bay Area Regional Deformation (BARD) network, 8 that are operated by the USGS, and 29 stations operated by the Plate Boundary Observatory (PBO).

Data from these sites are processed in a fully triangulated network scheme in which neighboring station pairs are processed with the software TrackRT (Herring *et al.*, 2010). Positioning time series are produced operationally for 172 station pairs (Figure 2.32.1); additional station pairs will be added as more real-time stations become available.

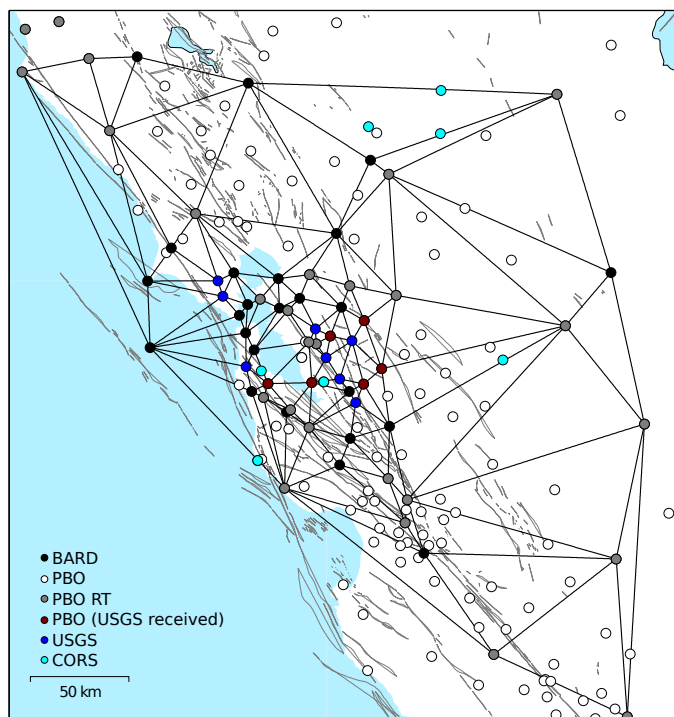


Figure 2.32.1: Map of the greater San Francisco Bay Area with high-rate GPS stations. Lines connecting the stations indicate station pairs (172) we use in the processing. White circles are non real-time PBO stations.

G-larmS, the geodetic alarm system, sits on top of real-time GPS processors such as TrackRT and analyzes real-time positioning time series, determines and broadcasts static offsets from these, and will ultimately derive fault and magnitude information (not fully implemented). This prototype Python im-

plementation is tightly integrated into seismic alarm systems as it uses their P-wave detection alarms to trigger its processing.

Architecture and Data Processing

The G-larmS architecture and process flow are depicted in Figure 2.32.2. Most notably, G-larmS consists of two independent modules for offset estimation and earthquake parameter estimation. Within these, the actual methods to get the respective values are easily exchangeable and could be easily exported to other agencies in other geographic regions.

A list of 172 station pairs (baselines) forms the basis of the Bay Area network. Each of these baselines is processed by an individual TrackRT process to generate position time series. For event response and quality assessment, we consider the most recent 10 minutes of data. Multipath and other noise treatment will be implemented in the future. We categorize time series as ‘good’ or ‘bad’ based on a few metrics such as standard deviation over the 10 minute time window. These quality parameters are passed along with the derived offsets.

The GPS system listens to CISN ShakeAlert (Hellweg *et al.*, 2013) to get earthquake alarms. Once the seismic system is triggered, we estimate and publish the offset evolution for a subset of baselines (see below). In parallel, the parameter estimator prepares to ingest these offsets to invert them for rupture length and magnitude.

Offset Estimation

Offset estimation is triggered by the seismic system, which broadcasts messages containing location, and preliminary magnitude information. The magnitude estimate is used to determine a cut-off radius around the alerted epicenter. This defines an area for which we expect static offsets. We limit our analysis to the stations in this region to manage computing resources.

To estimate co-seismic offsets from the east, north, and vertical component of each baseline time series, we implement the following algorithm:

1. Determine pre-event position by averaging time series over 10 minute time window.
2. Estimate S-wave arrival (shaking and static offset arrive).
3. Average each new datum after predicted S-wave arrival to determine post-event position.
4. Update static offset by subtracting average pre-event position from average post-event position.

Parameter Estimation

Offset Estimation

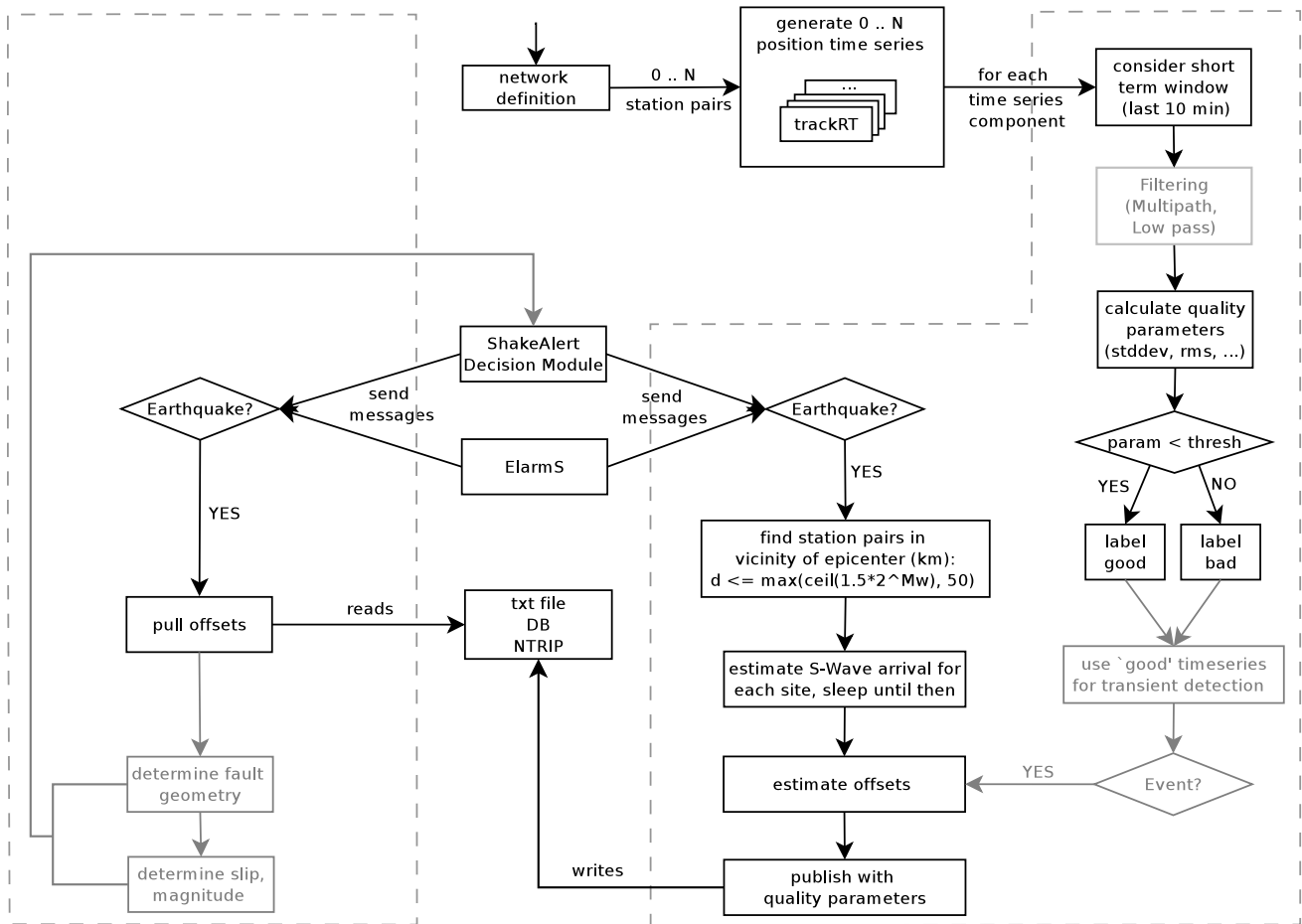


Figure 2.32.2: G-larmS flowchart showing its two independent components for offset and parameter estimation. The light gray boxes indicate planned but not yet implemented components.

Outlook

The plan for the near future includes the finalization of the earthquake parameter estimation module (similar to *Colombelli et al., 2013*) and the implementation of a mechanism to broadcast the results. Once this is in place, G-larmS will be run in test-mode for careful performance evaluation.

In the mid to long term we intend to include sidereal filtering and other methods to eliminate noise in the time series, which will improve the detection limits and likely enable autonomous transient detection. The latter would turn G-larmS into a valuable asset in volcanic environments.

Acknowledgements

This work is supported through the Gordon and Betty Moore Foundation, and CISN partners. We use real time data services provided by the Plate Boundary Observatory operated by UN-AVCO for EarthScope (www.earthscope.org) and supported by the National Science Foundation (grants no. EAR-0350028 and EAR-0732947).

References

Colombelli, S., et al., Application of real-time GPS to earthquake early warning in subduction and strike-slip environments, *J. Geophys. Res. Solid Earth*, 118, doi:10.1002/jgrb.50242, 2013.

Herring, R. T. A. et al., GAMIT/GLOBK Reference Manuals, Release 10.4 (*MIT Technical Reports*), 2010.

Hellweg, M. et al., Operating and Improving Earthquake Early Warning for Northern California and the US West Coast, SSA Annual Meeting, 2013.

33 G-larmS—Integrating Real-Time GPS into Earthquake Early Warning II: Testing

Ronni Grapenthin, Ingrid Johanson, Richard Allen

Introduction

Testing the results of real-time GPS for Earthquake Early Warning (EEW) under realistic conditions, and for scenarios that are relevant to the San Francisco Bay Area’s tectonic environment, is a major step toward having our work accepted for integration with an operational EEW system. While Northern California has many small earthquakes (*i.e.*, $M_w < 4$) that are used to validate the seismic system, it is only for very large earthquakes ($M_w > 6.5$) that real-time GPS is expected to provide a significant contribution. This is because for larger events, seismic systems need additional information to correctly estimate magnitude and finite fault extent, and because real-time GPS suffers from a lower signal-to-noise ratio than post-processed data.

Here, we follow two strategies to test G-larmS (see Research section 2.32): (1) add simulated static offsets to real-time time series, and (2) replay archived data that contain static and dynamic motion due to a real event. We test the prototype system for the Bay Area using synthetic data for a M_w 6.9 Hayward Fault Scenario and with data for the 2010 M_w 7.2 El Mayor-Cuicapah earthquake. Because the earthquake parameter module is in development, tests are limited to offset estimation.

To facilitate testing of the full software stack, we include 3 options in G-larmS: (1) a replay of archived data, (2) adding simulated offsets to replayed or real-time data, and (3) simulate the receipt of CISN ShakeAlert messages, *i.e.* an earthquake alarm.

M_w 6.9 Hayward Fault Scenario

Due to the accumulated slip deficit since the last large earthquakes along the Hayward-Rodgers Creek fault zone, its earthquake probability is the highest of any fault in the San Francisco Bay Area (*e.g.*, Bürgmann *et al.*, 2000). We use this region to test G-larmS’ ability to recover static offsets from time series because this is where our network is the densest.

We use Okada’s (1985) equations to simulate static offsets (Figure 2.33.1) due to 1 m of slip along the entire Hayward Fault (M_w 6.9) and convert the absolute offsets into offsets along baselines (see Figure 2.32.1). Using G-larmS’ replay mode, these relative offsets are added to archived real-time positioning time series after the simulator in G-larmS generates a CISN ShakeAlert alarm. This contains time and location information for the theoretical earthquake. G-larmS estimates the expected S-wave arrival time for each baseline at which the simulated offsets are added to the respective time series. The offset estimation algorithm is triggered in the same way as for a real event. We repeat this offset recovery experiment 224 times and recover offsets close to the simulated values within the variation of real-time noise (± 1 -2 cm, Figure 2.33.2), which gives us confidence that the algorithms work as expected.

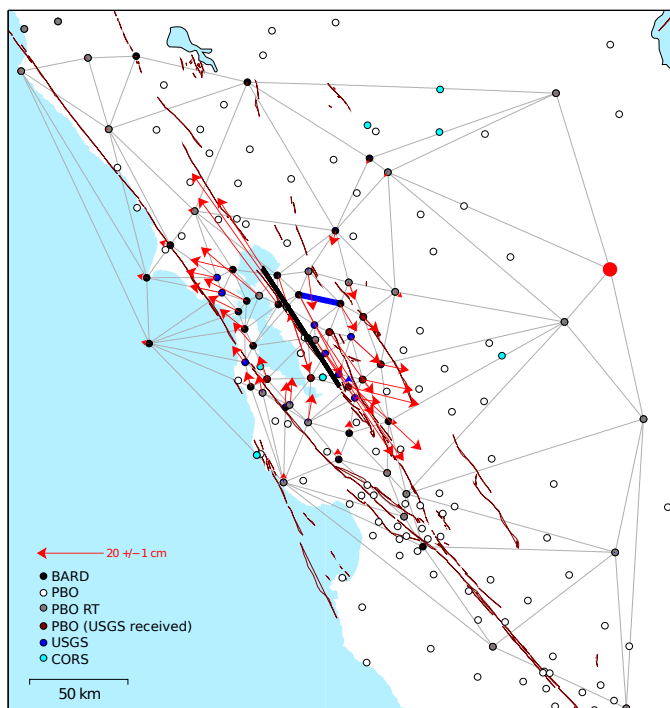


Figure 2.33.1: Simulated co-seismic offsets due to a Hayward Fault scenario of 1 m of slip along the entire fault (the black line is the fault model). The displacements are given with respect to station CMBB (red circle). The blue line marks baseline DIAB-BRIB for which we show the offset evolution below.

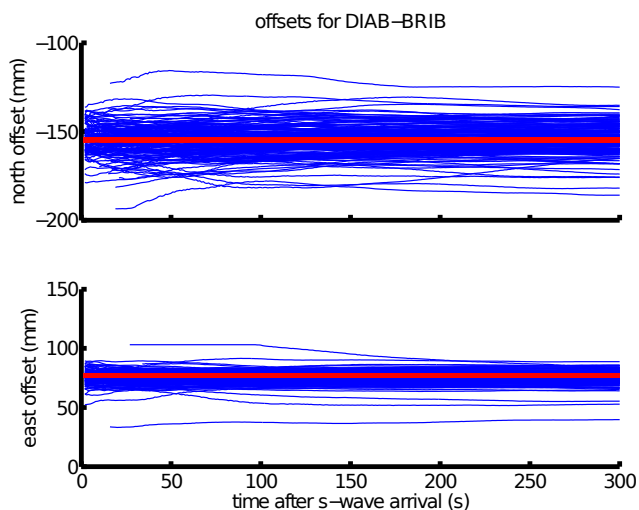


Figure 2.33.2: Time series of offset recovery (blue lines) after adding simulated offsets to archived real-time time series along baseline DIAB-BRIB (see Figure 2.33.1). Time series are with respect to expected S-wave arrival time, though the simulated offsets do not contain any dynamic deformation. The red lines show the simulated offset. 224 offset time series based on randomly selected data between Nov 2012 and Apr 2013. The spread of the results is within data variance; no ‘bad’ time series have been removed for this experiment.

2010 M_w 7.2 El Mayor-Cucapah

The M_w 7.2 El Mayor-Cucapah earthquake (e.g., *Hauksson et al.*, 2011) occurred on April 04, 2010 at 22:40:47 UTC (USGS) south of the US border in Mexico. This event was well sampled by a dense network of high-rate GPS sites (Figure 2.33.3). We process these data (obtained from SOPAC), which contain static offsets and dynamic motion due to surface waves, with TrackRTr (*Herring et al.*, 2010) and predicted IGS orbits to simulate a real time situation. The resulting time series are analyzed in G-larmS' replay mode. We generate a CISN ShakeAlert message with the final USGS parameters for origin time, location and magnitude for the event. This triggers the offset estimation for the network as detailed above.

Figure 2.33.4 shows the evolution of co-seismic offset estimates along the two blue baselines in Figure 2.33.3 and provides a comparison to the final co-seismic offset estimates from SOPAC (red line). While the dynamic motion impacts these sites to some degree, the results converge quickly to the co-seismic offsets.

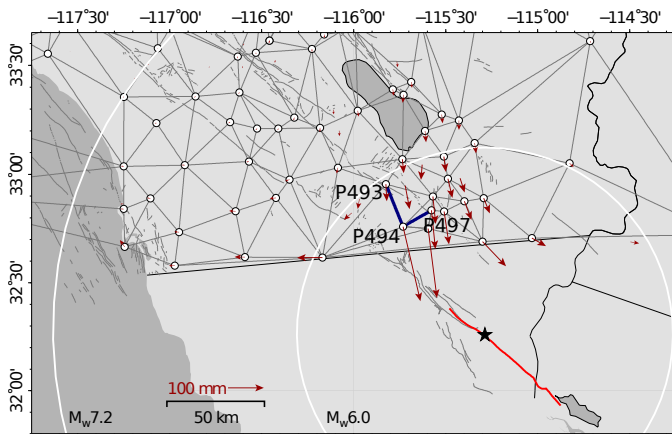


Figure 2.33.3: Subset of baselines used for the El Mayor-Cucapah earthquake. Arrows show absolute offsets, the star marks the epicenter. White circles mark G-larmS' threshold radius for M_w 6.0 and 7.2. The blue lines mark baselines P493-P494, and P494-P497 for which we show offsets in Figure 2.33.4.

Conclusions and Outlook

The tests suggest that G-larmS' offset estimation is implemented correctly and the strategy recovers quickly from dynamic motion due to S-waves. The impact of these results on magnitude estimation will have to be tested in the future. Other future work will include the use of more realistic static offset estimations for the Hayward fault (*provided courtesy Brad Aagaard*, USGS) and investigate the timing of GPS contributions to earthquake early warning in the Bay Area.

Acknowledgements

This work is supported through the Gordon and Betty Moore Foundation, and CISN partners. We use data provided by the Plate Boundary Observatory operated by UNAVCO for EarthScope and supported by the NSF (grants no. EAR-0350028 and EAR-0732947).

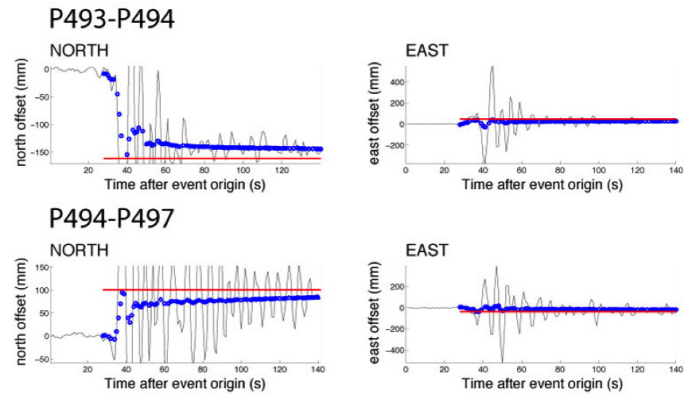


Figure 2.33.4: Offset time series (blue) estimated from displacements (black) shown with respect to event origin time for baselines P493-P494 and P494-P497 (Figure 2.33.3). Red lines are the final co-seismic offset derived from GPS solutions provided by SOPAC. Our results quickly converge to the final solutions even through the dynamic motion.

References

- Bürgmann, R. et al., Earthquake Potential Along the Northern Hayward Fault, California, *Science* 289, 1178, DOI: 10.1126/science.289.5482.1178, 2000.
- Hauksson, E. et al., The 2010 M_w 7.2 El Mayor-Cucapah earthquake sequence, Baja California, Mexico and southernmost California, USA: Active seismotectonics along the Mexican Pacific margin, *Pure Appl. Geophys.*, doi:10.1007/s00024-010-0209-7, 2011.
- Herring, R. T. A. et al., GAMIT/GLOBK Reference Manuals, Release 10.4 (*MIT Technical Reports*), 2010.
- Okada, Y., Surface Deformation due to Shear and Tensile Faults in a Half-Space, *BSSA* 75(4), pp 1135-1154, 1985.

34 Application of Seismic Array Processing to Earthquake Early Warning

Lingsen Meng, Richard Allen

Introduction

Earthquake early warning (EEW) systems are essential in mitigating seismic hazard by issuing warnings prior to the arrival of strong ground shaking during an earthquake. Many of the currently operating EEW systems work on the basis of magnitude-amplitude/frequency scaling for a point source, which is invalid for magnitude estimation of $M > 7.5$ earthquakes. This issue is particularly highlighted in EEW performance of the M9.0 Tohoku-Oki earthquake (Hoshiya *et al*, 2011). Failing to take into account the finite rupture propagation, the magnitude estimated by the Japanese EEW system saturated at M8.1. The Japanese Meteorological Agency (JMA) issued warnings of strong seismic intensity only for the Tohoku region. However, the Kanto region experienced much larger ground motions than that predicted by JMA. The example of the Tohoku-Oki earthquake demonstrates the need for characterizing the finite fault dimension in real time for EEW systems of large earthquakes to be successful.

Among the ongoing efforts to determine the finite fault extent in real time, GPS approaches provide more reliable static displacements and thus, magnitude, than do seismic methods (Colombelli *et al*, 2013). The FinDer approach is also proposed to determine linear fault geometry based on the amplitude difference in near/far field seismic waveform, provided dense station coverage.

Alternatively, we explore the concept of imaging the rupture process of large earthquakes in real time using clusters of dense seismic arrays located near an active fault. Back tracing the waveforms of earthquakes recorded by such arrays allows the estimation of the rupture directivity, size, duration, speed, and segmentation, which enables the EEW of $M > 6$ earthquakes. The principle is analogous to the location and tracking of moving sources by antennas in a variety of military and civilian applications. Figure 2.34.1 illustrates the concept of seismic array processing for EEW. Strong, high-frequency (HF) seismic waves usually radiate from the rupture front. Tracking the source of the HF seismic waves during large earthquakes recovers the movement of the rupture front. The trajectory of the rupture front marks the fault extent involved in the earthquake.

Method

The direction of the incoming HF waves can be determined by analyzing the phase of coherent seismic signals across an array with various array-processing techniques. For small-scale arrays, the impinging wave front can be approximated as a plane wave. The back azimuth of the plane wave is then projected onto an assumed fault plane to resolve the location of the rupture front. Here, we adopt the correlation stacking technique to perform the array analysis. The correlation stacking beamforms the normalized cross-correlation coefficients instead of the waveforms to improve robustness against scattering and multi-pathing in the shallow crustal environment (Fletcher *et*

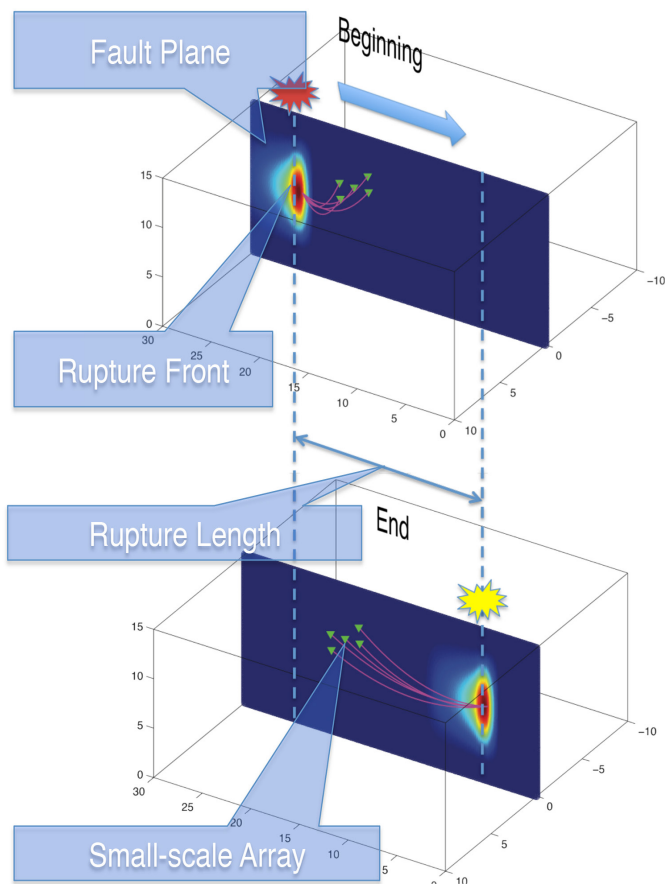


Figure 2.34.1: 3D schematic of imaging seismic rupture with a small scale array. The color contours mark the rupture front with high slip velocity. The red and yellow “bang” symbols represent surface projections of the rupture front. The green triangles are the stations. The pink curve is the ray path of the incoming seismic waves. The dashed lines mark the spatial extent of the rupture.

al., 2006). The stacked correlation cc_{ij} can be calculated by :

$$cc_{ij} = \left[\frac{\sum_t x_i(t)x_j(t - \tau_{ij})}{\sum_t x_i^2 \sum_t x_j^2} \right]^{1/2}$$

where i, j are station indices, x_i is the seismic signal recorded at the i th station, t is the time, τ_{ij} is the timing delay of a testing wave direction between the station i and j .

The 2004 Parkfield Earthquake

We implemented the proposed methodology to the 2004 M6 Parkfield earthquake in a simulated real-time environment. The earthquake is one of the few big events ($M > 6$) that are recorded by a local small-scale seismic array (UPSAR array). Fletcher *et al*, 2006 shows that the rupture kinematics can be retrieved by

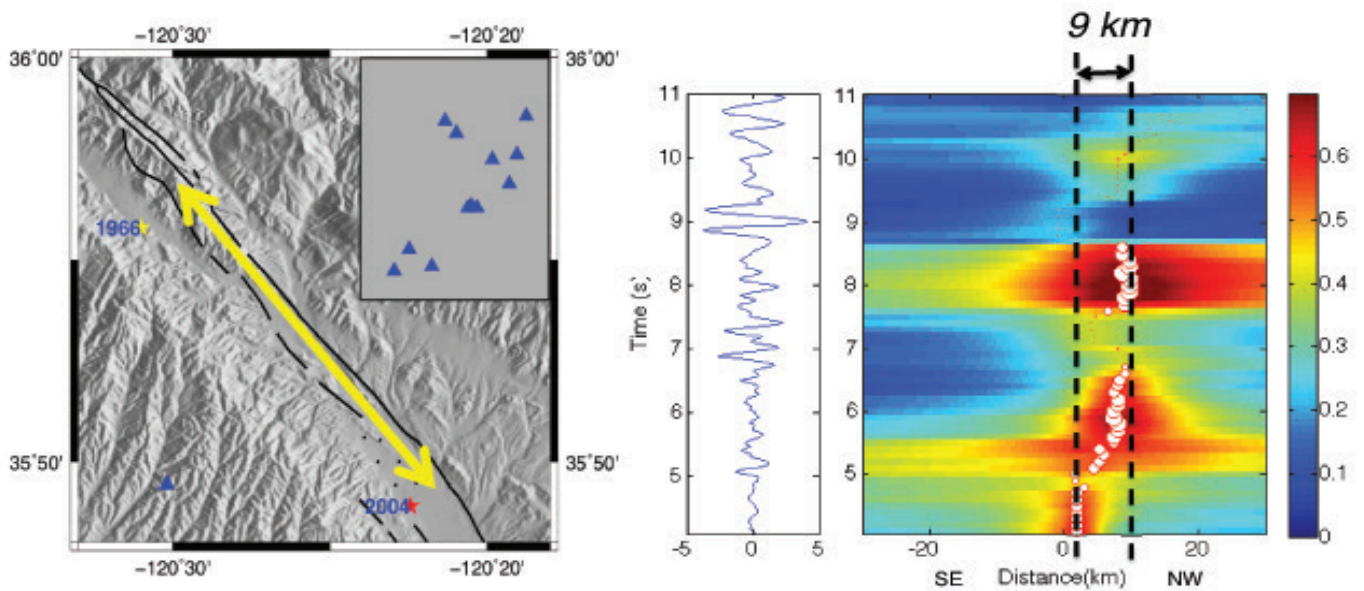


Figure 2.34.2: Array analysis of the 2004 M_6 Parkfield earthquake. Left: mapview of the Parkfield area. The yellow arrows mark the approximated region of the rupture. The yellow and red stars are the epicenters of the 1966 and 2004 event, respectively. The blue triangle is the location of the UPSAR array with the distribution of the stations in the inset map. Right: stacked correlation coefficient as a function of along-strike position with respect to the hypocenter and time after P wave arrival is shown in color. The white dots are the peak location in each time frame sized by the correlation coefficient. The black dashed lines mark the beginning and end of the HF energy source which gives a rupture size estimate of 9 km.

the UPSAR array. The earthquake is dominated by a unilateral rupture along the San Andreas Fault towards the northwest. The rupture is composed of three subevents that radiated strong high frequency signals. The first subevent is close to the hypocenter.

The two later subevents are closely spaced in the along-strike location near the end of the rupture. The interpretation is that these two subevents might occur at different depths consistent with the bimodal distribution of the aftershocks. In addition, we find that the dipping layer beneath the array causes the bias of the back azimuth and thus rupture length. After corrections, the estimated rupture length of 9 km is consistent with the distance between the two main subevents identified by back-projection using all local stations.

Conclusion

We explored the possibility of using seismic array processing in real time and developed an efficient methodology for rapid characterization of the earthquake rupture directivity and of the rupture area extent, using a correlation-stacking method. The strategy we propose can potentially prompt more reliable earthquake early warnings for large earthquakes. In terms of the future work, the optimal design of the array geometry and position, and real-time implementation strategy need to be further investigated.

Acknowledgements

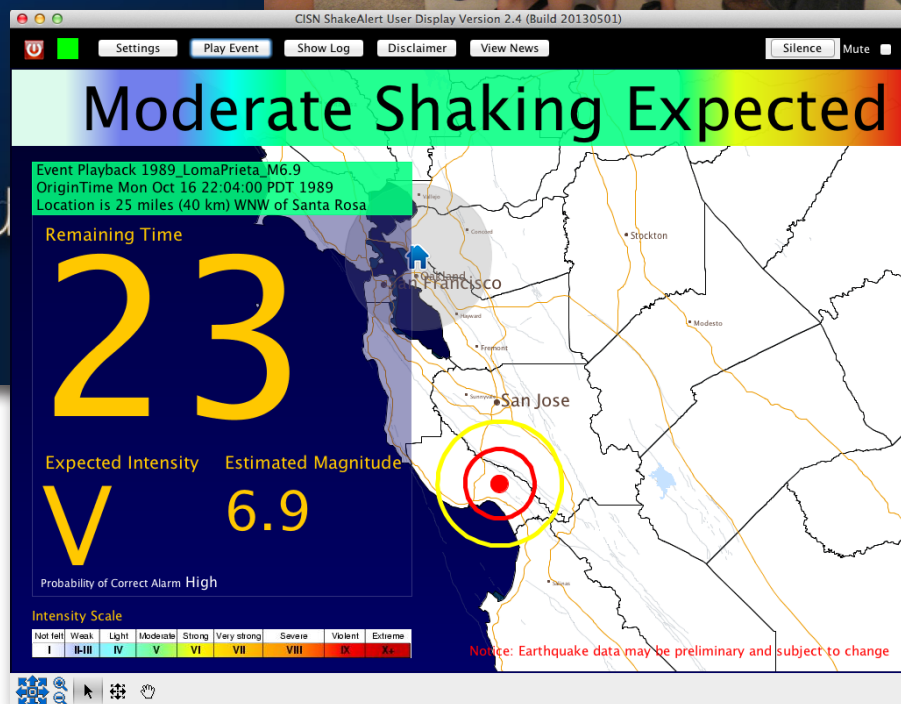
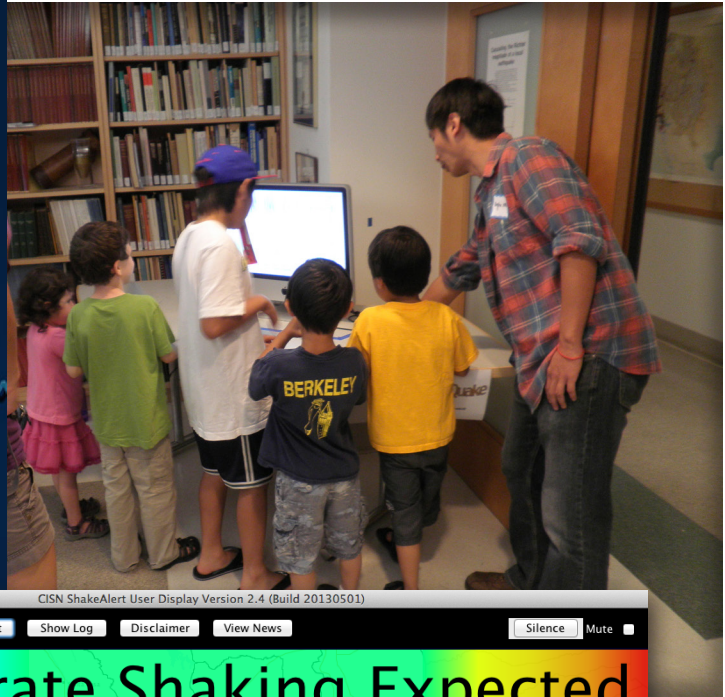
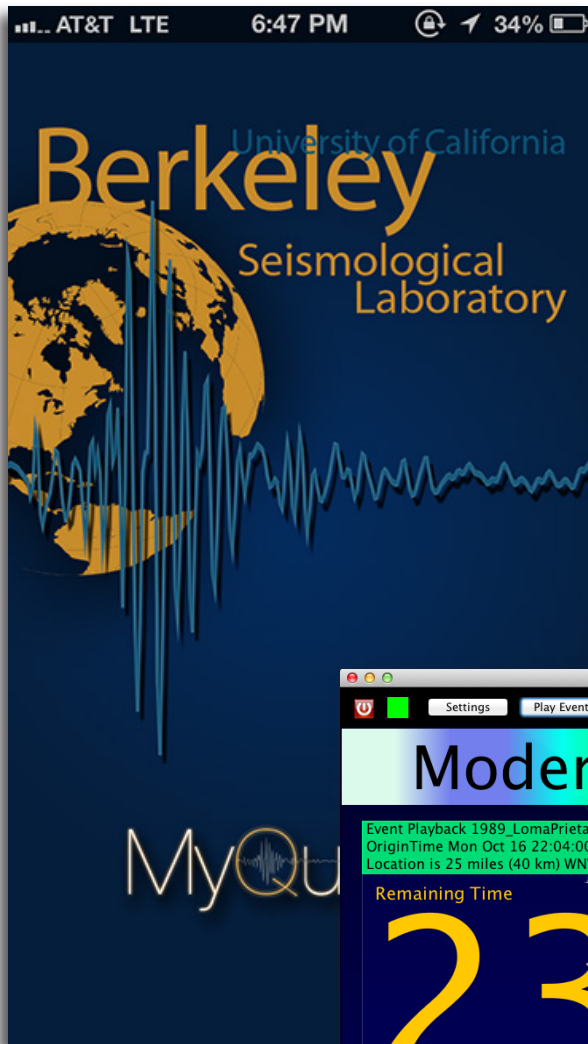
We thank Pablo Ampuero for his constructive discussions and suggestions. This work is funded by the Earthquake Early Warning grant of U.C. Berkeley from the Gordon and Betty Moore Foundation.

References

- Colombelli, S., Allen, R.M., and Zollo, A., Application of real-time GPS to earthquake early warning in subduction and strike-slip environments, *J. Geophys. Res. Solid Earth*, 118, doi:10.1002/jgrb.50242, 2013.
- Fletcher, J., Spudich, P., and Baker, L., Rupture propagation of the 2004 Parkfield, California, earthquake from observation at the UPSAR, *Bull. seism. Soc. Am.*, 96, S129–S142, 2006.
- Hoshihara, M., Iwakiri, K., Hayashimoto, N., Shimoyama, T., Hirano, K., Yamada, Y., Ishigaki, Y., and Kikuta, H., Outline of the 2011 off the Pacific coast of Tohoku earthquake (Mw 9.0)—Earthquake early warning and observed seismic intensity, *Earth Planets Space*, 63(7),547–551, 2011.

Chapter 3

Broadening Engagement



1 Earthquake Research Affiliates Program

Introduction

The Earthquake Research Affiliates (ERA) program at the BSL promotes the support of seismological research through industrial and governmental involvement. The program has recently expanded to include speaking engagements, council meetings, and the publication of its first online newsletter.

Earthquake Research Affiliates Program

The BSL draws on the diversity of the interdisciplinary earthquake and solid earth research community at UC Berkeley. Augmenting these efforts, the ERA program provides a forum for the exchange of ideas and information between industry and public sector organizations with an interest in BSL research and the scientists themselves. The mission of the ERA program is to inspire, nurture, and sustain vibrant public-private and industrial-academic partnerships focused on the development and use of innovative earthquake information products, including alert services, and other novel seismological measurement technologies. The program is designed to promote the application of new research and technology, and to provide a forum for inviting optimal and essential users to participate in the development and testing of new technologies, with the goal of introducing these new technologies into the marketplace. Current ERA members include the Bay Area Rapid Transit District (BART), the University of California Police Department, Berkeley (UCB-PD), the San Francisco Department of Emergency Management (SFDEM), and Google.

Regular interaction with each group is a key aspect of the program. Recently, we have engaged Google's Public Alerts group to address whether and how earthquake early warning can be melded with the online experience. Beta Users on UC Berkeley campus (see the UserDisplay section) are brainstorming, in collaboration with the ERA, ways in which the campus can proactively mitigate earthquake hazards using early warnings. Monthly meetings with our counterparts at Caltech and the University of Washington are supporting this endeavor.

Senate Bill SB135

A California bill calling for the creation of a public earthquake early warning system for the state was put forward by State Senator Alex Padilla (D-District 20). After being passed unanimously by two State Senate committees, including Appropriations, it also received a unanimous vote on the Senate Floor. The bill is slated to go before the State Assembly committee on governmental organization on August 7th, 2013. The bill, as amended, tasks the California Governor's Office of Emergency Services (CalOES) with defining funding sources to support the build-out and operations costs for the project.

The Berkeley Seismological Laboratory, and in particular Director Richard Allen, have been intimately involved in providing support and scientific expertise for this endeavor. Dr. Allen

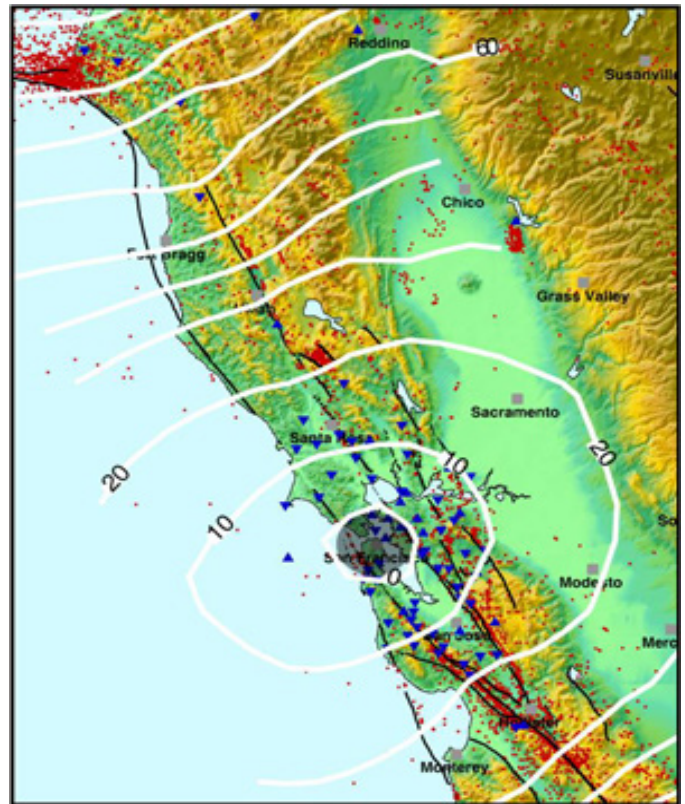


Figure 3.1.1: The lines on this map show warning times for San Francisco resulting from hypothetical major earthquakes at various locations, which are quickly detected by an early warning system. The gray area marks the "blind zone." There will be no warning for earthquakes in this area.

and Dr. Jennifer Strauss made several trips to the State Capitol to inform and update legislators on the ShakeAlert system, and Dr. Allen provided testimony at key points during the bill's progress.

UserDisplay 2.4

At 9:56 a.m. on March 11, 2013, ShakeAlert User Displays state-wide began alerting a small cadre of scientists, emergency managers, ERA members, and other Beta testers to the oncoming waves of the M_w 4.7 Anza earthquake. Thirty seconds later, our colleagues in Pasadena felt mild shaking just as the countdown hit zero. This moderate event—close to a population center—brought the focus of the earthquake early warning project a bit closer to home. Rather than relying on reams of data to discern system fidelity, this was a tangible example of how powerful a full public system could be for the State of California and the West Coast.

The newest version of the earthquake early warning User Display GUI was released on May 8th to the project's Beta Users. This distribution included many improvements based on user feedback, and includes revised intensity calculations and stability upgrades.

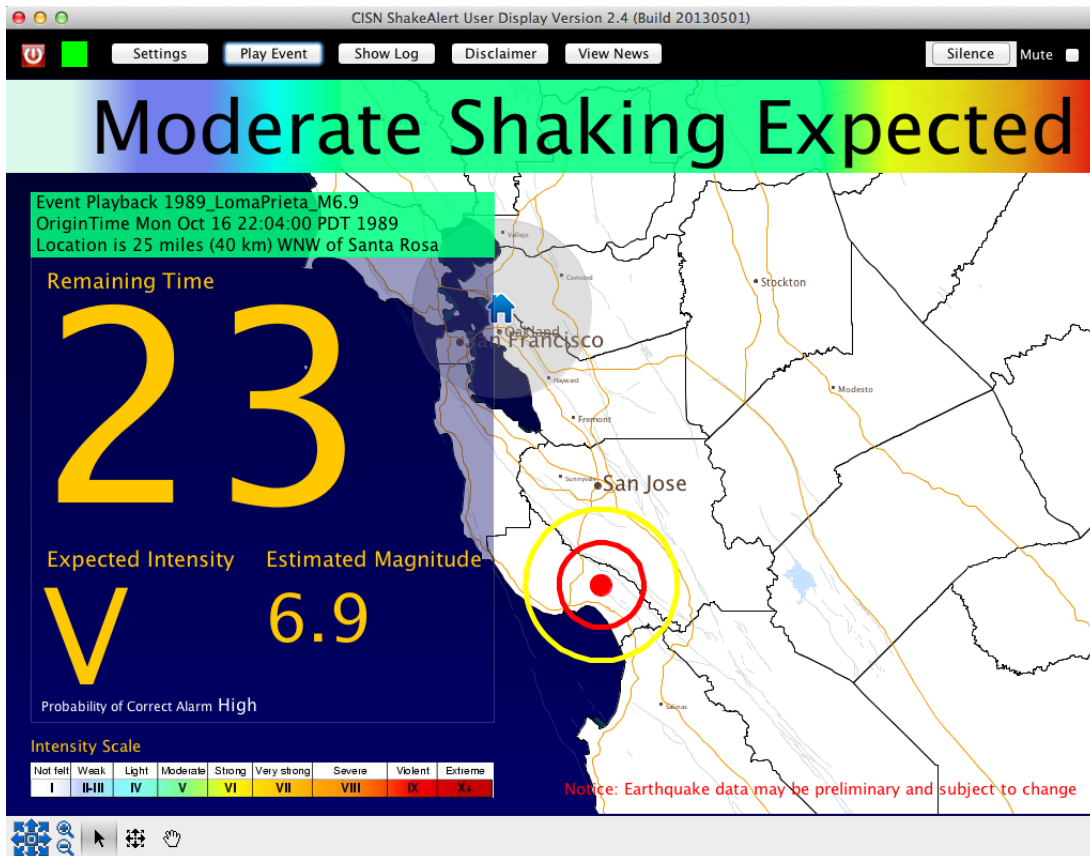


Figure 3.1.2: The CISN ShakeAlert User Display. Here we have simulated the $M6.9$ Loma Prieta earthquake of 1989. As the earthquake waves propagate out, we collect more data and update the magnitude and expected intensity estimates, issuing more accurate warnings.

Continuing Engagement

The BSL is fostering a dialog between public safety organizations and seismologists through public presentations and civic groups. On March 28, Dr. Jennifer Strauss, the External Relations Officer for the ERA, gave a primer on earthquakes at the tri-annual training workshop of San Leandro's Community Emergency Response Team (CERT). CERT brings volunteer members of the community together and trains them in basic disaster response skills so that they may assist others in their neighborhood or workplace following an event, when professional responders may not be immediately available to help. She was also part of the San Francisco Emergency Management Delegation to Haifa, Israel. While she was unable to join them physically in the Middle East, she prepared a joint presentation with Fuad Sweiss, the Director of Infrastructure for the Department of Public Works, San Francisco, on earthquake early warning. Later that year, she presented earthquake hazard and mitigation information to the Business Managers Recovery Association's (BRMA) July meeting. Interactions with other groups, including the San Francisco Office of Earthquake Safety, the Lifelines Council, and the Community Action for Seismic Safety groups, is ongoing.

LBNL Prep Fair

Lawrence Berkeley Lab hosts an annual Emergency Preparedness Fair and Road Safety Day to help employees prepare

for and react to future emergencies, as well as to raise their awareness of safe road behavior. This year, on June 18 from 11 a.m. to 1:30 p.m., the BSL manned a booth to provide earthquake hazard mitigation and early warning information. Dr. Strauss was joined by graduate student Qingkai Kong and post-doc Dr. Serdar Kuyuk for the event. Dr. Kuyuk highlighted his research on QwVR, while Mr. Kong demonstrated his smart-phone accelerometer application for attendees.

Acknowledgements

Jennifer Strauss heads the Earthquake Research Affiliates program with oversight by Richard Allen and Peggy Hellweg. Jennifer Strauss and Peggy Hellweg contributed to the preparation of this section.

2 Engaging the Public

Introduction

One of the core missions of the Berkeley Seismological Laboratory is to enable the broad consumption of earthquake information and solid earth science through education and outreach to all sectors of society. While many of our outreach and education activities focus on lectures, tours, and public events, we also engage the public through collaborative initiatives and products. Highlights from this year include contributions to Bloom, MyQuake, and Science on a Sphere.

Bloom

This year, the BSL took advantage of a unique opportunity to encourage the experience of seismology through the lens of art. *Bloom* is an internet-based Earthwork on exhibit at the Nevada Museum of Art from February 16–June 16, 2013. Created by collaborators Ken Goldberg, Sanjay Krishnan, Fernanda Viégas, and Martin Wattenberg, *Bloom* uses a live data feed from BSL's Hayward fault station to provide a moving visual commentary on the growth and fragility of the natural world.

The colorful exhibit (which can be viewed online at <http://j.mp/Bloom-Art>) is a constantly evolving field of circular blossoms. The size and position of each blossom is based on real-time changes in the Earth's motion (as measured by the seismometer), but which are not necessarily seismic in nature. The positioning of the blossoms is not random, but rather arrayed according to the time, rate of change and time lapse between recorded events.

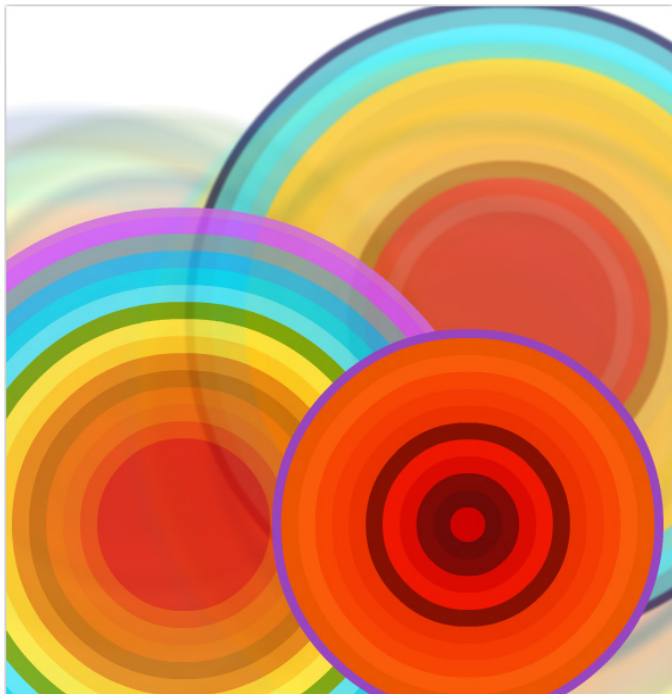


Figure 3.2.1: Snapshot of Bloom taken at 1:20 p.m. (PDT) on Friday, July 19th, 2013. In the exhibit, colors are derived from photographs of flowers.

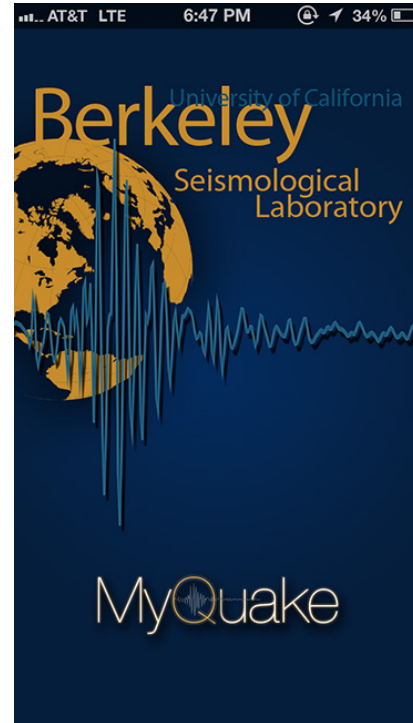


Figure 3.2.2: Opening screen for the BSL's new iPhone app: MyQuake.

MyQuake

The MyQuake app (released in July 2013) is the product of an undergraduate student research project in collaboration with the BSL. Rohan Agarwal (computer science) and Cora Bernard (geophysics) developed the app.

MyQuake maps earthquakes that occurred recently in the California region and across the globe. It also provides information about large damaging historic earthquakes in California, and calculates the shaking intensity at user-defined locations for both the historic and current earthquakes. For example, it calculates that at Berkeley, the shaking for the 1868 Hayward earthquake was Intensity VII, while for the 1906 Great San Francisco earthquake it was Intensity VIII. The app then links to videos that show what it is like to experience shaking of that intensity.

MyQuake is completely ad-free and provides a smooth, intuitive user interface to facilitate learning everything about earthquakes, keeping the user informed and preparing them for the next big earthquake.

MyQuake is now available for free at the iTunes store.

Science on a Sphere

In partnership with the Lawrence Hall of Science (LHS), the lab is developing earthquake-related content for joint display on a flat screen together with NOAA's Science on a Sphere (SOS, http://sos.noaa.gov/What_is_SOS/index.html). The goal

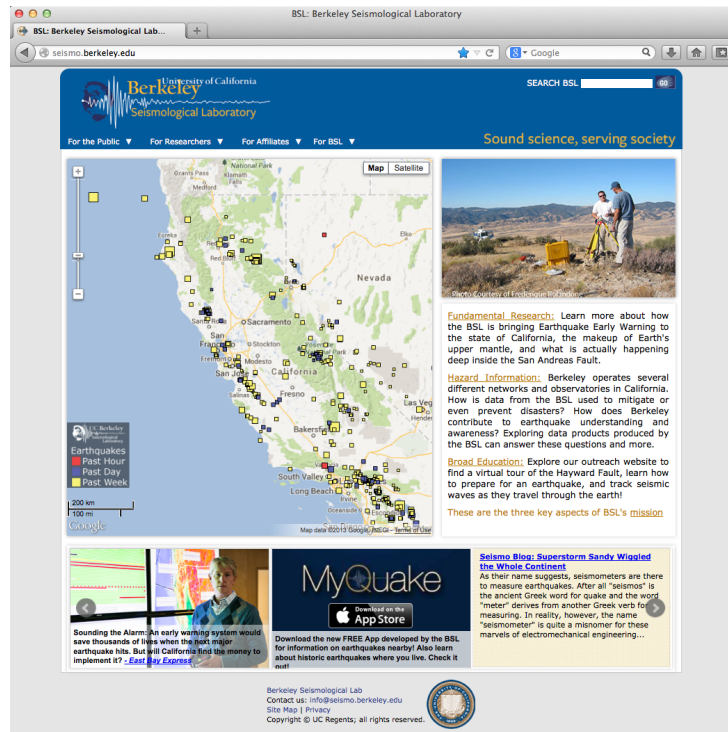


Figure 3.2.3: The redesigned homepage of the Berkeley Seismological Lab. Notice the real-time earthquake map that organizes earthquakes by date and magnitude.

of SOS is to amass display products and project them on a six-foot diameter sphere to foster education and discovery in the realm of environmental processes. The final products from all institutions will be made available to both the Science on a Sphere members and to the IRIS Active Earth Display Kiosk (IAEDK) network (see http://www.iris.edu/hq/programs/education_and_outreach/museum_displays/active_earth). The BSL is tasked with content and scientific accuracy for this project, while the LHS is in charge of technical aspects and evaluation of pedagogical content.

The BSL's contributions consist of two main themes: "Seismic Waves" and "Disasters". This year, Jennifer Taggart, Clay Miller, and William Hawley have assembled content, media, and graphics for inclusion on the IAEDK slides and popups, with a focus on three earthquake-related disasters: Liquefaction, Tsunamis, and Building Collapse. The Tsunami slides explain tsunami generation and discuss the 2011 Tohoku and 2004 Sumatra tsunamis. Building collapse compares and contrasts the 2010 Haiti disaster with the low level of shaking damage in Sendai after the much larger Tohoku earthquake. Finally, the liquefaction slides explain what liquefaction is and give examples of how it can be dangerous (infrastructure damage during the 2011 Christchurch earthquake, landslides in the 2008 Wenchuan earthquake, buildings tilting and then toppling over in a 1964 Japan quake, San Francisco Marina district damage after the 1989 Loma Prieta quake).

We plan to demo the project at the American Geophysical Union (AGU) fall meeting, using a smaller-scale sphere.

BSL Website

This academic year, the BSL's web pages went through several phases of modernization. The most prominent change is the real-time earthquake map on our homepage. Visitors to the homepage are now greeted with a dynamic map showing all earthquakes detected in California. Earthquakes appear in real time as squares, colored by age in days and sized by magnitude in order to give the most emphasis to the earthquakes likely to be felt widely. Each individual square can be clicked on, initiating a popup balloon containing the event's magnitude, date and time, depth, and distance to the nearest town, as well as links to ShakeMaps and other earthquake information products. Users can zoom and pan to explore earthquakes around the world as well as in particular regions like The Geysers, CA. When an earthquake above magnitude 3.5 occurs in the state's reporting area, the default map zooms to that earthquake and stays there for 48 hours (or until a larger earthquake happens). A manual override allows BSL seismologists to hold the map's focus at a particular point, should one or more events of particular interest occur.

In addition to the real-time earthquake map, the homepage is complemented by a slideshow and clickable carousel created from the popular jQuery plugin, bxSlider. Our navigation menu has been improved to funnel visitors toward the pages most relevant to them. Visitors now hover over a menu item describing who they are, such as "For Researchers," which triggers a two-column dropdown menu containing an organized list of pages targeted toward their interests. Last but not least, the BSL webpages are now served up as <http://earthquakes.berkeley.edu> as well as our old URL, <http://seismo.berkeley.edu>.

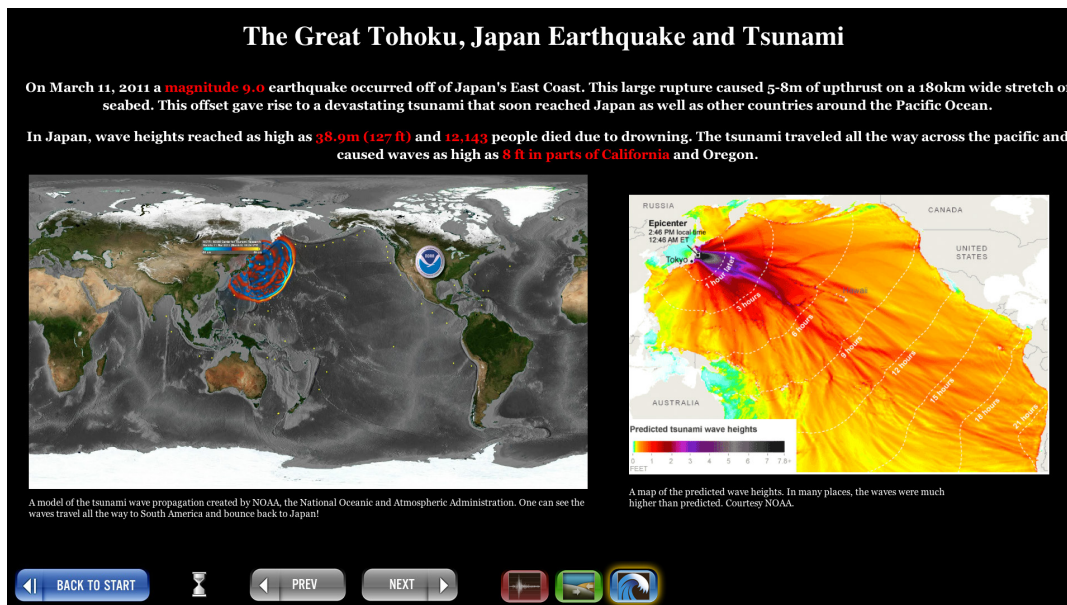


Figure 3.2.4: One of the slides of the IRIS AED the BSL has customized and displayed in McCone Hall. This slide has an animation of wave propagation from the tsunami caused by the M9.0 Tohoku earthquake. The image to the right shows predicted wave heights of the tsunami.

The BSL continues to educate and inform the public through our webpages, providing a seismology blog (<http://seismo.berkeley.edu/blog>), videos, an earthquake FAQ, and resources for teachers and those who wish to dig deeper. Our “seismic networks” web pages also serve the research community, providing detailed information about each of our seismic stations.

Media

This year, the BSL continued its outreach to the public by providing numerous and varied media sources with interviews and information. The bulk of media requests we get are for newspaper and other print sources, however, we also gave interviews to KQED, a public radio station, as well as to MBC, a Korean broadcasting company. This year was particularly important and busy for media inquiries due to the pronounced status of our Earthquake Early Warning efforts. There were several major events that caused particular interest, including a cooperation with Bay Area Rapid Transit (BART) and the announcement of California Senate Bill 135 (see Broadening Engagement Section 1).

<http://www.wired.com/threatlevel/2013/05/newitz-disasters/>

Displays

In addition to the more modern look of the BSL's web pages, we have also added several engaging displays throughout our building (McCone Hall) to encourage public education, awareness, and fascination.

In the first floor lobby we have showcased an interactive display that allows visitors to explore current earthquakes and learn about the science of earthquakes. The display was created using an IRIS web-based Active Earth Display (AED) template. The template allows the BSL to create up to 25 unique slides with completely customized content that users can cycle

through using a touch pad. The 25 slides are broken into three categories and users can click on the category they want to view. When the display has been inactive for five minutes, it reloads the home slide, which is a real-time seismogram of the last three days of data from station BKS.BK, located on the UC Berkeley campus. The display is shown on a large monitor and it has been optimized for our specific setup. However, it is web-based, so it can be accessed anywhere. If one wishes to view the display, they can go to <http://www.iris.edu/aed2/index.phtml?code=BSL2012>.

On the 2nd floor of McCone Hall, with the same setup as in the 1st floor lobby, we have a looping Google Earth tour flythrough. The tour shows viewers faults and historic earthquakes in California and takes them to the sites of a few of our stations, including an underwater site. It does all this by seamlessly “flying” from place to place, taking advantage of Google’s visually stunning databases of topography and city data.

In the BSL conference room, we have three different displays running on four monitors. On one of the monitors is a seismogram from the last four days of data from station BKS.BK, a seismic station located on UC Berkeley’s campus. The data is displayed through the SWARM program. We also use the SWARM program to create a vibrant map of California, overlaid with the location of our BK network of seismic stations. We have enabled a few of these stations to show the last 10 minutes of data in real time. With these seismograms displayed throughout the state, one can see seismic activity throughout California in real time.

On our last monitor, we alternate between two programs. The first and most common is *seisnetwatch*, and the other is the California Integrated Seismic Network (CISN) User Display. *Seisnetwatch* is a tool the BSL uses to monitor station quality and health. It allows us to see the stations of the Berkeley Digital Seismic Network (BDSN) and their health for the past month. The CISN User Display is part of an effort at the BSL to

create a Earthquake Early Warning System (EEWS), see Broadening Engagement Section 1. The display will issue an alert of an earthquake before strong shaking is felt at our location (provided the epicenter is not too close).

Acknowledgements

Peggy Hellweg oversees the Public Engagement projects at the BSL. Stephane Zuzlewski created the earthquake map for the BSL homepage. Our seismology blog is written by Horst Rademacher.

Special acknowledgements to our external collaborators: Ken Goldberg, Rohan Agarwal, and Cora Bernard, Toshi Komatsu and Gretchen Walker at LHS. Jennifer Taggart, Clay Miller, Peggy Hellweg, and Jennifer Strauss contributed to the preparation of this section.

References

Ken Goldberg, Sanjay Krishnan, Fernanda Viégas, and Martin Wattenberg, *BLOOM (detail)*, 2012. Custom software with live data feed, size variable. Courtesy of the Artists. Commissioned by the Nevada Museum of Art.

3 Science and Society

Introduction

BSL faculty, staff, and graduate students are involved in a wide variety of outreach activities, ranging from public lectures to tours of the Hayward Fault geomorphology on campus. This year, we continued our involvement in CalDay and other traditional activities, while adding participation in the statewide Golden Guardians exercise.

Lawson Lecture

The Lawson Lecture is a free, public lecture hosted by the BSL each year around the anniversary of the 1906 San Francisco earthquake. This year, on April 8, 2013, BSL's own Dr. Richard Allen gave the lecture. His topic was "Warning California: Science and Technology to Reduce the Growing Earthquake Threat". The talk highlighted efforts at the BSL, along with those of collaborators from other institutions, to develop the science and technology necessary to reduce the impacts of future earthquakes to society, through the delivery of rapid alerts for earthquakes and tsunamis.

He began by discussing the growing threat to societies around the world from earthquakes. As they and their infrastructure become more interconnected, the potential long-term impacts of earthquakes also become more unpredictable. New technologies, including high accuracy real-time GPS (which can now track the rupture of faults) and harnessing the accelerometers in smartphones to detect earthquakes and transmit the warning ahead of the shaking are providing opportunities to improve and deliver warnings in more locations around the world.

A key feature of the presentation was the description of the earthquake early warning project, which is of great interest to many of the BSL's industry partners. Thus, this year, the hour-long public lecture was followed by a reception, where members of the BSL's Earthquake Research Affiliates program were able to engage in discussions other attendees, be they members from other industry groups, journalists or researchers.

The Lawson Lectures are viewable as Flash video at http://earthquakes.berkeley.edu/news/lawson_lecture.html.

Golden Guardians

First implemented by former Governor Arnold Schwarzenegger in 2004, the Golden Guardian is California's annual series of statewide emergency exercises. This year's theme was a major earthquake in Northern California. The BSL worked with the Chair of the California Earthquake Clearinghouse (Clearinghouse), Anne Rosinski, to create an earthquake early warning scenario for the aftershock portion of the exercise on May 15th.

The mission of the Clearinghouse is to provide a temporary virtual location where engineers, geologists, seismologists sociologists, economists, and other professionals can gather and share information immediately after a damaging earthquake. The Clearinghouse tested their Unified Incident Command and Decision Support (UICDS) middleware that is also being used



Figure 3.3.1: BSL Graduate Student Qingkai Kong engages students during the 2013 CalDay Open House.

by CalOES.

With the aid of Dr. Maren Böse and Claude Felizardo at CalTech, a simulated M_w 6.5 aftershock in Northern California was created and played on the ShakeAlert UserDisplay. This allowed Dr. Jennifer Strauss to create a movie, which the Clearinghouse could incorporate into their UICSD test strategy. Dr. Strauss liaised with the Clearinghouse both before and during the Golden Guardians aftershock scenario to foster discussion on how earthquake early warning can be used for hazard mitigation before, and planning strategies after a major event.

CalDay-BSL Open House

Just two weeks after the very successful Lawson Lecture, the BSL participated in UC Berkeley's CalDay—an open house for prospective students and general day of fun for community members. Many departments have exhibits and demonstrations for everyone and every interest. The Berkeley Seismological Lab is proud to share in this tradition. Visitors included all age groups and we had something fun for everyone. The youngest visitors played with demos of earthquake mechanics and got to "make their own quake" by jumping up and down near an accelerometer as the results were broadcast on a computer screen. The young guests also received their very own seismogram of an earthquake, and all guests watched BSL seismic data in real time through the SWARM application. Guests could also watch the 2013 Lawson Lecture and learn about Earthquake Early Warning, or scroll through our interactive display and learn about earthquakes and tsunamis.

CalDay ran from 10:00 AM–3:00 PM on Saturday April 20, 2013.

Tours

During 2012–2013, many groups, ranging from mid-

dle-school students to international guests, visited the BSL for talks, tours, and hands-on science experiences.

Thirty-five middle-school students from First Baptist Christian School were lead by Jennifer Taggart on a tour of the Hayward Fault in September. Dr. Peggy Hellweg led a similar tour for the UC Section Club in March, while Undergraduate student William Hawley guided Camp DaVinci 6th–9th graders on this hike later in June. Clay Miller lead a group of international students from the Stamford School in England on a tour of the BSL and the Hayward fault on July 15, 2013. Dr. Jennifer Strauss also gave this group a brief primer on the seismology of the area.

Ongoing Activities

As in previous years, the members of the BSL gave several external lectures. This year was particularly exciting because Dr. Barbara Romanowicz was invited to give the Chancellor's Research Lecture on Tuesday, April 20 at the International House. The lecture was entitled: Imagining the Earth's Interior. While the original title was slated to be: Imaging the Earth's Interior, this fortuitous typo brought to light the creative aspects of seismology.

Dr. Ingrid Johanson gave an outreach talk to the Stockton chapter of Delta Kappa Gamma—an honor society for women educators. Dr. Jennifer Strauss began interfacing with the Community Action Plan for Seismic Safety (CAPSS) group as they work on the safety implementation plan for the City of San Francisco. She also presented a talk to the City's Director of Earthquake Safety, Patrick Otellini.

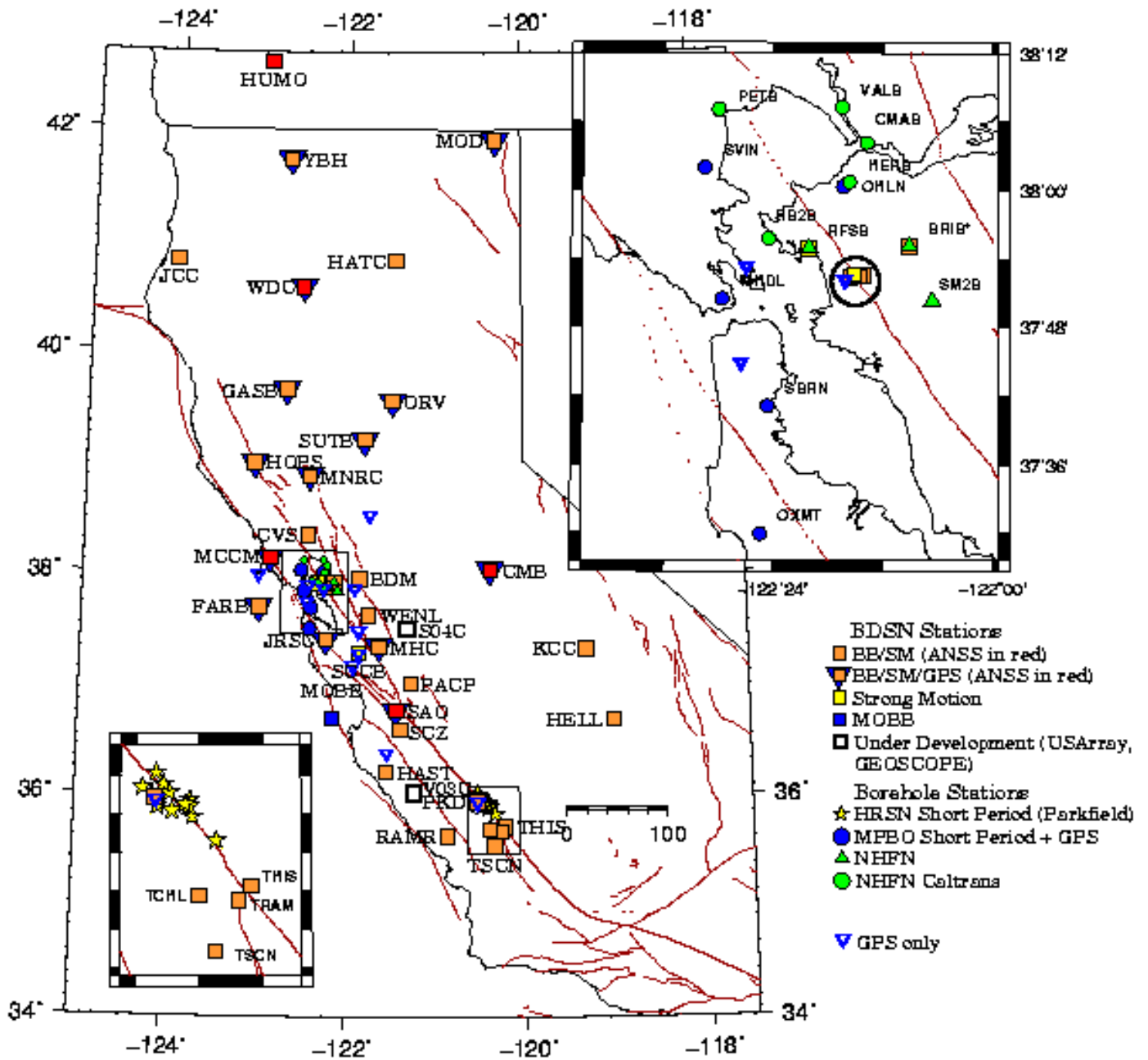
Recorded information on current earthquake activity is updated regularly on our information hotline (510-642-2160).

Acknowledgements

Peggy Hellweg oversees the outreach activities at the BSL. Richard Allen, Bob Urhammer, Jennifer Taggart, Clay Miller, Jennifer Strauss, and many other faculty, staff, and students at the BSL contribute to the outreach activities. Peggy Hellweg, Jennifer Taggart, Clay Miller, and Jennifer Strauss contributed to the preparation of this section.

Chapter 4

Operations



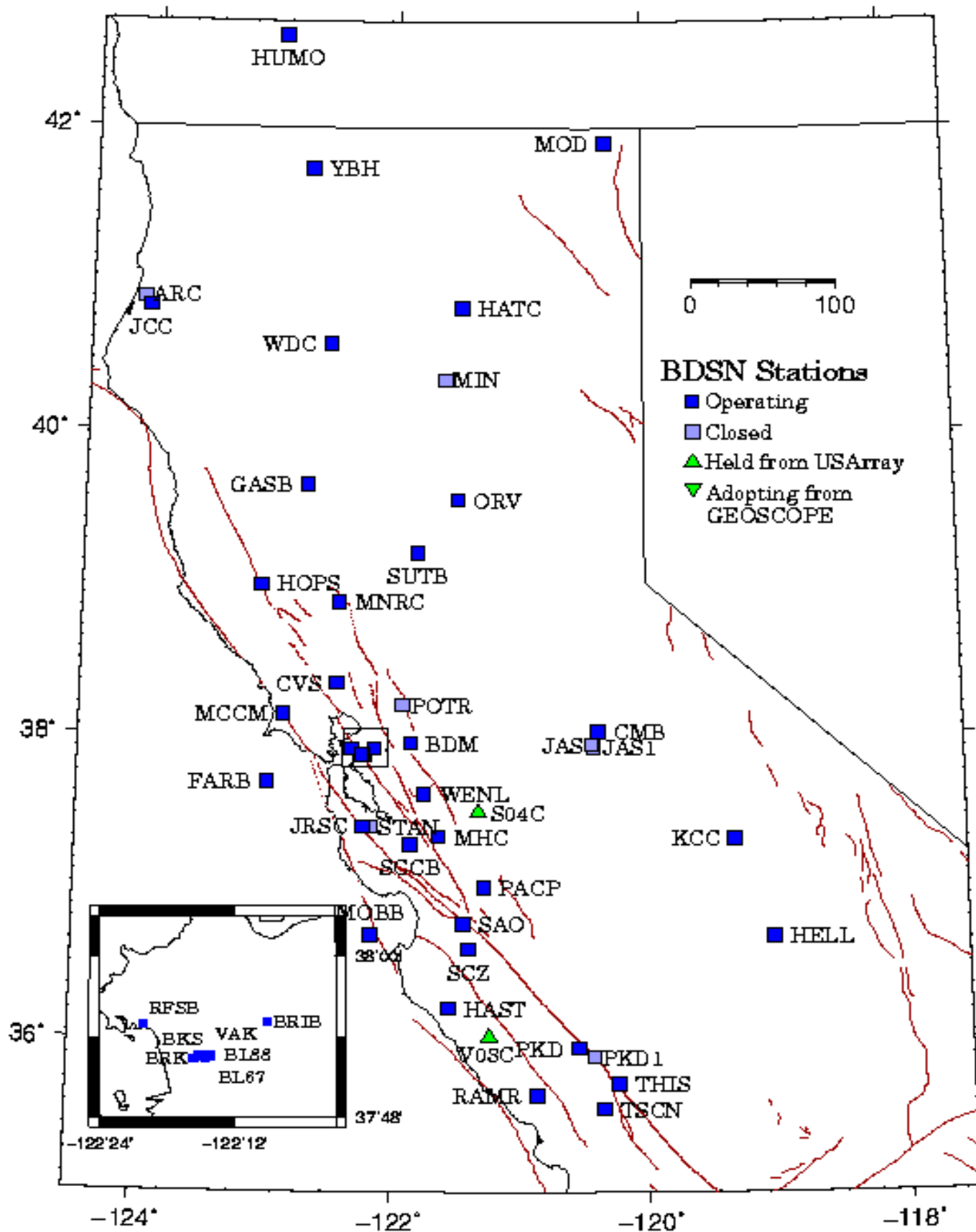


Figure 4.1.1: Map illustrating the distribution of BDSN stations in Northern and Central California. In the inset map, the order of the stations from left to right is: RFSB, BRK, BL88, VAK, BL67, BKS, BRIB.

1 Berkeley Digital Seismic Network

Introduction

The Berkeley Digital Seismic Network (BDSN) is a regional network of very broadband and strong motion seismic stations spanning Northern California and linked to UC Berkeley through continuous telemetry (Figure 4.1.1 and Table 4.1.1). The network is designed to monitor regional seismic activity as well as to provide high quality data for research in regional and global broadband seismology.

Since 1991, the BDSN has grown from the original three broadband stations installed in 1986-87 (BKS, SAO, MHC) to 40 stations, including an ocean-bottom seismometer in Monterey Bay (MOBB). We take particular pride in high quality installations, which often involve lengthy searches for appropriate sites away from sources of low-frequency noise as well as continuous improvements in installation procedures and careful monitoring of noise conditions and problems. This year, field and operation efforts have been directed toward the installation of stations for the TremorScope project (see Research Section 2.26), the adoption of the Geoscope station SCZ and, of course, upgrades, maintenance and repair as necessary. Engineering and research efforts were also devoted to several projects to test instrumentation (see Operational Section 4.6). In the past year, we huddle-tested eight Quanterra environmental add-ons with SETRA pressure sensors, the QEP; recorded data from tilt meters and compared it to signals from broadband horizontal sensors; and compared accelerometers from several manufacturers.

The expansion of our network to increase the density of state-of-the-art strong motion/broadband seismic stations and to improve the joint earthquake notification system in this seismically hazardous region—one of BSL's long term goals—is coordinated with other institutions and is contingent on the availability of funding. With equipment provided by Lawrence Berkeley National Laboratory (LBNL), we continue to work toward installing a station in the Lawson Adit on the UCB campus, very close to the fault. This effort is close to bearing fruit. We also continue our efforts to install all the stations of the TremorScope project funded by the Gordon and Betty Moore Foundation (see Research Section 2.26). As part of this exciting project for monitoring non-volcanic tremor sources along the San Andreas Fault south of Parkfield, the BDSN is being augmented by a network of four high-quality borehole stations and four surface stations. All four surface stations are now installed and are collecting data. Finally, in the past year, we were approached by the University of California Santa Cruz (UCSC) and Geoscope (France), which have operated the station SCZ in the Coast Ranges near the city of Salinas, CA. Geoscope can no longer maintain the data logger at the station. The BSL has now adopted the station, installed a new data logger, and is providing the data to UCSC.

Data quality and the integrity of the established network are at least as important as network growth, so existing network stations must be preserved. With equipment and funds from the America Recovery and Reinvestment Act (ARRA), the BSL was

able to replace almost all of its old data loggers. We continue to operate broadband seismometers from the first generation, however. Some of which were installed more than 25 years ago. As funds become available, we upgrade their electronics and do our best to keep them operating well. We continue to exercise vigilance and to commit time and resources to repairs and upgrades as necessary.

BDSN Overview

Thirty-five BDSN sites are equipped with three-component broadband seismometers and strong-motion accelerometers, and with 24- or 26-bit digital data acquisition systems or data loggers. Three sites (BL88, RFSB and SCCB) consist of a strong-motion accelerometer and a 24-bit digital data logger. The ocean-bottom station MOBB is equipped with a three component broadband seismometer with integrated digitizer and a differential pressure gauge (DPG). Currently, the station SCZ has two broadband seismometers, a set of STS-1s and a STS-2, installed for comparison purposes. After we confirm the instrument response of the STS-1s, we will install an accelerometer in place of the STS-2, so SCZ will become a standard BDSN site. Data from all BDSN stations are transmitted to UC Berkeley using continuous telemetry, including the ocean-bottom site, MOBB. In order to avoid data loss during utility disruptions, each site has batteries to supply power for three days. The combination of high-dynamic range sensors and digital data loggers ensures that the BDSN has the capability to record the full range of earthquake motion required for source and structure studies. Table 4.1.2 lists the instrumentation at each site.

Most BDSN stations have Streckeisen STS-1 or STS-2 three-component broadband sensors (*Wielandt and Streckeisen*, 1982; *Wielandt and Steim*, 1986). Exceptions are: BRIB, where a Guralp CMG-3T broadband sensor contributed by LLNL is deployed in a post-hole installation; Guralp CMT-3T broadband seismometers at the new TremorScope sites; and a Guralp CMG-1T at MOBB. All stations, except the TremorScope sites and JRSC, have Kinematics FBA-ES-T accelerometers with $\pm 2g$ dynamic range. At TremorScope, accelerometers are Guralp CMG-5Tc units, also with $\pm 2g$ dynamic range, and JRSC has Metrozet TSA-100. Since July 2011, there are no longer any Q680, Q730, or Q4120 Quanterra data loggers in the BDSN collecting data from seismic sensors. The sites with Quanterras all have Q330, Q330HR or Q330S data loggers. The Quanterra data loggers employ FIR filters to extract data streams at a variety of sampling rates. The same is true for the Guralp DM24 digitizers at the TremorScope sites and at MOBB. With the ARRA data logger upgrade, several conventions changed: All sites received SEED location codes, with the data logger for the broadband and strong motion sensors having the location code "00," and accelerometer channels are now designated with "HN?" rather than "HL?." Where there is a second broadband seismometer, as at YBH, it is designated with the location code "50". In addition, the BDSN stations now record continuous data at 0.1,

Code	Net	Latitude	Longitude	Elev (m)	Over (m)	Date	Location
BDM	BK	37.954	-121.8655	219.8	34.7	1998/11 -	Black Diamond Mines, Antioch
BKS	BK	37.8762	-122.2356	243.9	25.6	1988/01 -	Byerly Vault, Berkeley
BL67	BK	37.8749	-122.2543	736.18	0	2011/04 -	LBNL Building 67, Berkeley
BL88	BK	37.8772	-122.2543	602.21	0	2011/01 -	LBNL Building 88, Berkeley
BRIB	BK	37.9189	-122.1518	219.7	2.5	1995/06 -	Briones Reservation, Orinda
BRK	BK	37.8735	-122.261	49.4	2.7	1994/03 -	Haviland Hall, Berkeley
CMB	BK	38.0346	-120.3865	697	2	1986/10 -	Columbia College, Columbia
CVS	BK	38.3453	-122.4584	295.1	23.2	1997/10 -	Carmenet Vineyard, Sonoma
FARB	BK	37.6978	-123.0011	-18.5	0	1997/03 -	Farallon Island
GASB	BK	39.6547	-122.716	1354.8	2	2005/09 -	Alder Springs
HAST	BK	36.3887	-121.5514	542	3	2006/02 -	Carmel Valley
HATC	BK	40.8161	-121.4612	1009.3	3	2005/05 -	Hat Creek
HELL	BK	36.6801	-119.0228	1140	3	2005/04 -	Miramonte
HOPS	BK	38.9935	-123.0723	299.1	3	1994/10 -	Hopland Field Stat., Hopland
HUMO	BK	42.6071	-122.9567	554.9	50	2002/06 -	Hull Mountain, Oregon
JCC	BK	40.8175	-124.0296	27.2	0	2001/04 -	Jacoby Creek
JRSC	BK	37.4037	-122.2387	70.5	0	1994/07 -	Jasper Ridge, Stanford
KCC	BK	37.3236	-119.3187	888.1	87.3	1995/11 -	Kaiser Creek
MCCM	BK	38.1448	-122.8802	-7.7	2	2006/02 -	Marconi Conference Center, Marshall
MHC	BK	37.3416	-121.6426	1250.4	0	1987/10 -	Lick Obs., Mt. Hamilton
MNRC	BK	38.8787	-122.4428	704.8	3	2003/06 -	McLaughlin Mine, Lower Lake
MOBB	BK	36.6907	-122.166	-1036.5	1	2002/04 -	Monterey Bay
MOD	BK	41.9025	-120.3029	1554.5	5	1999/10 -	Modoc Plateau
ORV	BK	39.5545	-121.5004	334.7	0	1992/07 -	Oroville
PACP	BK	37.008	-121.287	844	0	2003/06 -	Pacheco Peak
PKD	BK	35.9452	-120.5416	583	3	1996/08 -	Bear Valley Ranch, Parkfield
RAMR	BK	37.9161	-122.3361	416.8	3	2004/11 -	Ramage Ranch
RFSB	BK	37.9161	-122.3361	-26.7	0	2001/02 -	RFS, Richmond
SAO	BK	36.764	-121.4472	317.2	3	1988/01 -	San Andreas Obs., Hollister
SCCB	BK	37.2874	-121.8642	98	0	2000/04 -	SCC Comm., Santa Clara
SCZ	BK	36.598	-121.403	261	0	2013/04 -	Chualar Canyon, Santa Cruz
SUTB	BK	39.2291	-121.7861	252	3	2005/10 -	Sutter Buttes
TCHL	BK	35.68812	-120.40092	431	0	2013/06 -	Clark Property, Shandon
THIS	BK	35.714	-120.237	623	0	2012/05 -	South End of Cholame Valley, Shandon
TRAM	BK	35.67691	-120.27093	642	0	2012/12 -	Private Property, Shandon
TSCN	BK	35.544	-121.3481	476.47	0	2012/03 -	Shell Creek North, Shandon
VAK	BK	37.8775	-122.2489	266	10	2010/08 -	LBNL Building 46, Berkeley
WDC	BK	40.5799	-122.5411	268.3	75	1992/07 -	Whiskeytown
WENL	BK	37.6221	-121.757	138.9	30.3	1997/06 -	Wente Vineyards, Livermore
YBH	BK	41.732	-122.7104	1059.7	60.4	1993/07 -	Yreka Blue Horn Mine, Yreka

Table 4.1.1: Stations of the Berkeley Digital Seismic Network currently in operation. Each BDSN station is listed with its station code, network ID, location, operational dates, and site description. The latitude and longitude (in degrees) are given in the WGS84 reference frame, and the elevation (in meters) is relative to the WGS84 reference ellipsoid. The elevation is either the elevation of the pier (for stations sited on the surface or in mining drifts) or the elevation of the well head (for stations sited in boreholes). The overburden is given in meters. The date indicates either the upgrade or installation time.

Code	Broadband	Strong-motion	Data logger	GPS	Other	Telemetry	Dial-In
BDM	STS-2	FBA-ES-T	Q330HR			FR	
BKS	STS-1	FBA-ES-T	Q330HR		QEP, E300, Baseplates	FR	X
BL67	CMG-3T	FBA-ES-T	Q330S			LAN	
BL88		FBA-ES-T	Q330S			R	
BRIB	CMG-3T	FBA-ES-T	Q330HR	X	Strainmeter, EM	FR	X
BRK	STS-2	FBA-ES-T	Q330HR			LAN	
CMB	STS-1	FBA-ES-T	Q330HR	X	QEP, E300, Baseplates	FR	X
CVS	STS-2	FBA-ES-T	Q330HR			FR	
FARB	STS-2	FBA-ES-T	Q330HR	X		R-FR/R	
GASB	STS-2	FBA-ES-T	Q330HR	X		R-FR	
HAST	STS-2	FBA-ES-T	Q330HR			R-Sat	
HATC	STS-2	FBA-ES-T	Q330HR			T1	
HELL	STS-2	FBA-ES-T	Q330			R-Sat	
HOPS	STS-1	FBA-ES-T	Q330HR	X	QEP, E300, Baseplates	FR	X
HUMO	STS-2	FBA-ES-T	Q330HR			VSAT	X
JCC	STS-2	FBA-ES-T	Q330HR			FR	X
JRSC	STS-2	TSA-100S	Q330HR	X	EM	Mi-LAN	X
KCC	STS-1	FBA-ES-T	Q330HR		QEP, E300, Baseplates	R-Mi-FR	X
MCCM	STS-2	FBA-ES-T	Q330HR			VSAT	
MHC	STS-1	FBA-ES-T	Q330HR	X		FR	X
MNRC	STS-2	FBA-ES-T	Q330HR	X		Sat	X
MOBB	CMG-1T		DM24		OCM, DPG	LAN	
MOD	STS-1*	FBA-ES-T	Q330HR	X	Baseplates	VSAT	X
ORV	STS-1	FBA-ES-T	Q330HR	X	Baseplates	FR	X
PACP	STS-2	FBA-ES-T	Q330HR			Mi/FR	
PKD	STS-2	FBA-ES-T	Q330HR	X	EM	R-Mi-T1	X
RAMR	STS-2	FBA-ES-T	Q330			R-FR	X
RFSB		FBA-ES-T	Q330HR			FR	
SAO	STS-1	FBA-ES-T	Q330HR	X	QEP, E300, Baseplates, EM	FR	X
SCCB		FBA-ES-T	Q330HR	X		FR	
SCZ	STS-1, STS-2		Q330HR		QEP, E300, Baseplates	?	?
SUTB	STS-2	FBA-ES-T	Q330HR	X		R-FR	
TCHL	CMG-3T	CMG-5TC	DM24			R-Mi	
THIS	CMG-3T	CMG-5TC	DM24			R-Mi	
TRAM	CMG-3T	CMG-5TC	DM24			R-Mi	
TSCN	CMG-3T	CMG-5TC	DM24			R-Mi	
VAK	CMG-3T	FBA-ES-T	Q330S			R	
WDC	STS-2	FBA-ES-T	Q330HR	X		FR	X
WENL	STS-2	FBA-ES-T	Q330HR			FR	
YBH	STS-1, STS-2	FBA-ES-T	Q330HR, Q330**	X	E300, Baseplates	FR	X

Table 4.1.2: Instrumentation of the BDSN as of 06/30/2012. Except for BL88, RFSB, SCCB, and MOBB, each BDSN station consists of collocated broadband and strong-motion sensors, with a 24-bit or 26-bit data logger and GPS timing. The stations BL88, RFSB, and SCCB are strong-motion only, while MOBB has only a broadband sensor. Additional columns indicate collocated GPS receivers as part of the BARD network (GPS) and additional equipment (Other), such as warpless baseplates, new STS-1 electronics (E300) or electromagnetic sensors (EM). The OBS station MOBB also has an ocean current meter (OCM) and differential pressure gauge (DPG). The main and alternate telemetry paths are summarized for each station. FR - frame relay circuit, LAN - ethernet, Mi - microwave, R - radio, Sat - Commercial Satellite, T1 - T1 line, VSAT - USGS ANSS satellite link. An entry like R-Mi-FR indicates telemetry over several links, in this case, radio to microwave to frame relay. (*) During 2011-2012, the STS-1 at this station was replaced by an STS-2. (**) YBH is CTBT auxiliary seismic station AS-109. It has a high-gain STS-2.

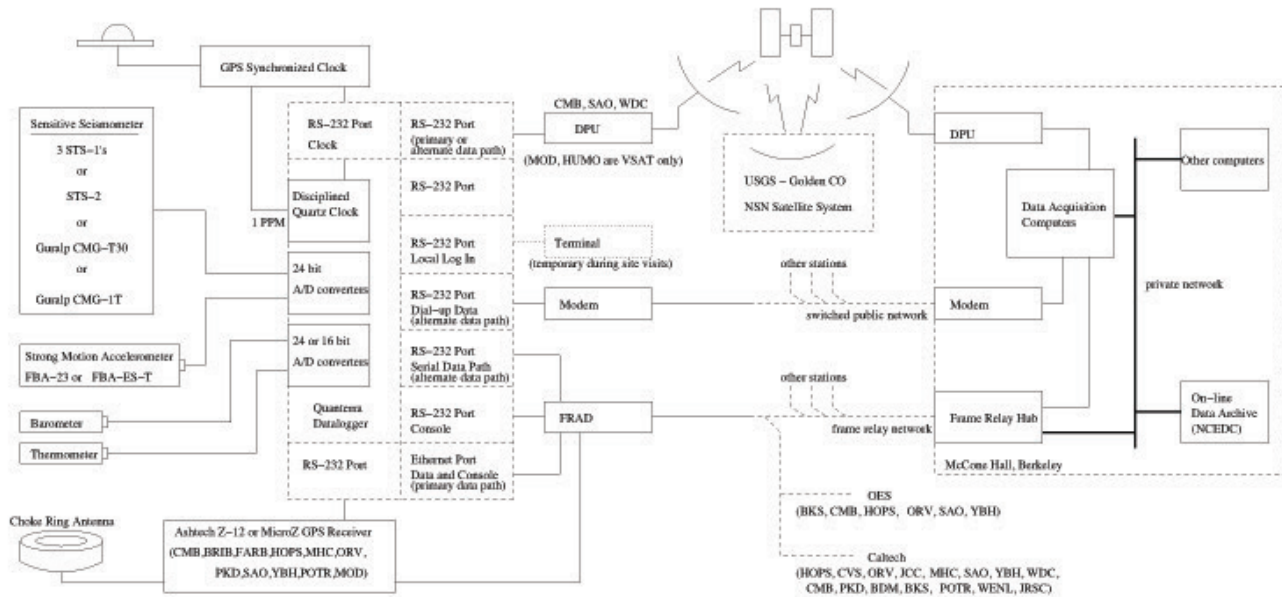


Figure 4.1.2: Schematic diagram showing the flow of data from the sensors through the data loggers to the central acquisition facilities of the BSL.

Sensor	Channel	Rate (sps)	Mode	FIR
BB	VH?	0.1	C	Ac
BB	LH?	1	C	Ac
BB	BH?	40	C	Ac
BB	HH?	100	C	Ca
SM	LN?	1	C	Ac
SM	BN?	20/40	C	Ac
SM	HN?	100/200	C	Ca/Ac

Table 4.1.3: Typical data streams currently acquired at BDSN stations, with channel name, sampling rate, sampling mode, and the FIR filter type. BB indicates broadband; SM indicates strong-motion; C continuous; Ac acausal; Ca causal. The HH? and HN? channels are now all recorded and telemetered continuously at 100sps (200sps for the accelerometers at the TremorScope sites) and most have causal filtering. In the past, SM channels have been named HL? (BL?, LL?). For past sampling rates, see earlier annual reports.

1.0, 40, and 100 or 200 samples per second (Table 4.1.3). In the past, other sample rates may have been available (see past annual reports).

When the broadband network was upgraded during the 1990s, a grant from the CalREN Foundation (California Research and Education Network) in 1994 enabled the BSL to convert data telemetry from analog leased lines to digital frame relay. The frame-relay network uses digital phone circuits which support 56 Kbit/s to 1.5 Mbit/s throughput. Today, 21 of the BDSN sites rely on frame-relay telemetry for all or part of their communications system. We are looking for alternatives, as the phone companies will soon deprecate frame-relay services. Other stations send their data to the data center via satellite, Internet, microwave, and/or radio (see Table 4.1.2).

As described in Operational Section 4.6, data from the

BDSN are acquired centrally at the BSL. These data are used for rapid earthquake reporting as well as for routine earthquake analysis (Operational Sections 4.2 and 4.1). As part of routine quality control (Operational Section 4.6), power spectral density (PSD) analyses are performed continuously and are available on the Internet (<http://www.ncedc.org/ncedc/PDF/>).

The occurrence of a significant teleseism also provides the opportunity to review station health and calibration. Figure 4.1.3 displays BDSN waveforms for the M_w 8.3 earthquake that occurred beneath the Sea of Okhotsk on May 24, 2013.

Special Projects in the BDSN

TremorScope

In 2010 the Gordon and Betty Moore Foundation funded the BSL to complete an exciting project for monitoring non-volcanic tremor sources along the San Andreas Fault south of Parkfield. For this project, the BDSN is being augmented by a network of four high-quality borehole stations and four surface stations. Progress on this project is described in Research Section 4.26), and in the “2012–2013 Activities” section below. All four surface stations are now installed and are collecting data.

The Monterey Bay Ocean Bottom Seismic Observatory (MOBB)

The Monterey Ocean Bottom Broadband observatory (MOBB) is a collaborative project between the Monterey Bay Aquarium Research Institute (MBARI) and the BSL. Supported by funds from the Packard Foundation to MBARI, from NSF/OCE, and from UC Berkeley to the BSL, its goal has been to install and operate a long-term seafloor broadband station as a first step toward extending the onshore broadband seismic net-

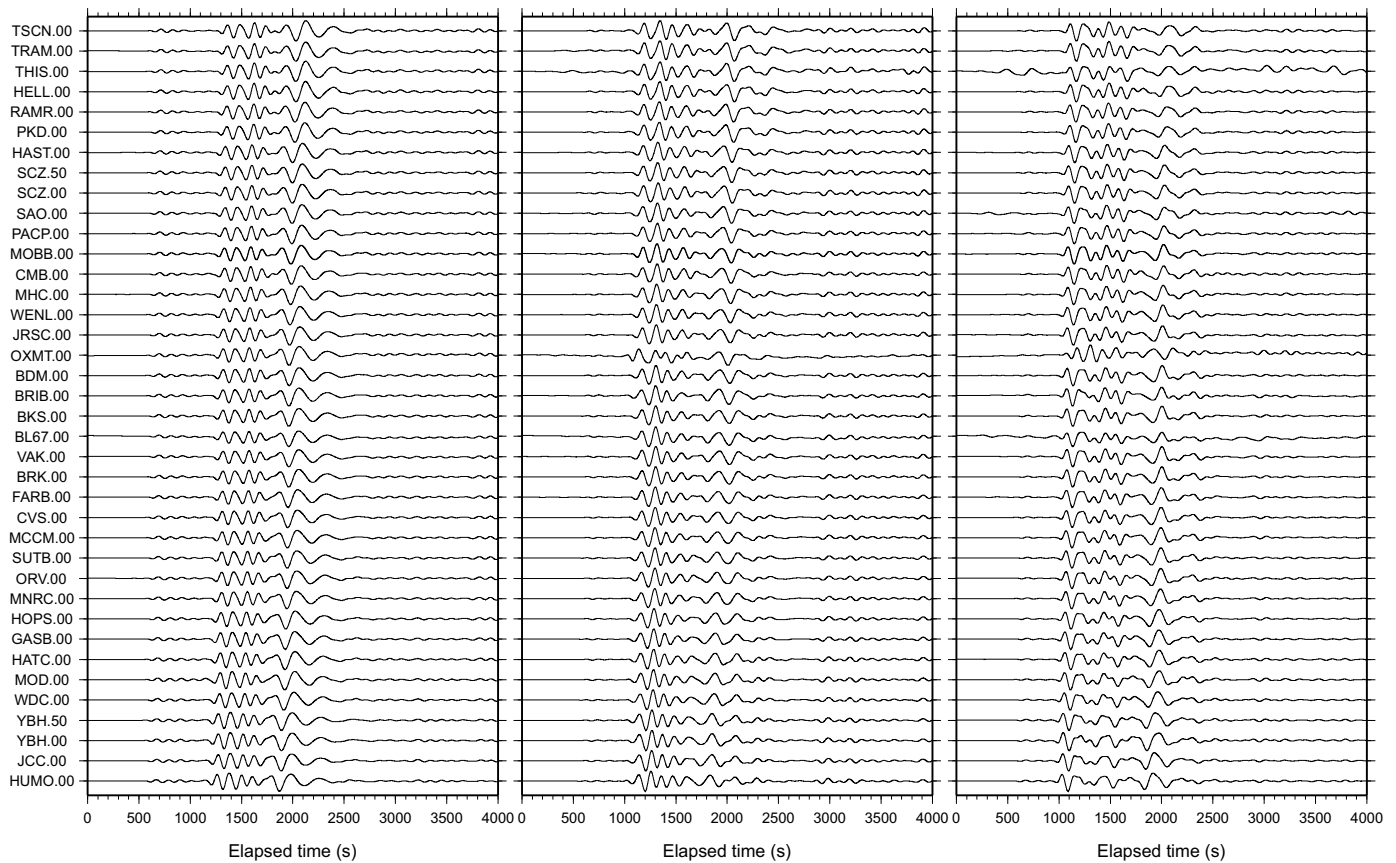


Figure 4.1.3: Long period (100-333 s period) waveforms recorded across BDSN from the M_w 8.3 teleseismic earthquake which occurred on May 24, 2013, Sea of Okhotsk at 54.874 N, 153.281 E. The panels show data from the vertical, north-south and east-west components, respectively. The traces are deconvolved to ground velocity, scaled by their maximum values, and ordered from bottom to top by distance from the epicenter. The highly similar waveforms recorded across the BDSN provide evidence that the broadband sensors are operating within their nominal specifications. The newest station, TCHL was installed in June 2013, after this earthquake occurred. BDSN data are archived and available at the Northern California Earthquake Data Center. This is described in detail in Operational Section 4.8.

work in Northern California to the seaward side of the North America/Pacific plate boundary, providing better azimuthal coverage for regional earthquake and structure studies. It also serves the important goal of evaluating background noise in near-shore buried ocean floor seismic systems, such as may be installed as part of temporary deployments of “leap-frogging” arrays (e.g., Ocean Mantle Dynamics Workshop, September 2002). The project has been described in detail in BSL annual reports since 2002 and in several publications (e.g., Romanowicz *et al.*, 2003, 2006, 2009). More information about the project can be found at <http://seismo.berkeley.edu/bdsn/mobb.overview.html>.

MOBB is now continuously providing data through a cable connected to the Monterey Accelerated Research System observatory (MARS, <http://www.mbari.org/mars/>), a sea-floor node in Monterey Bay connected to a shore facility in Moss Landing by a 52 km electro-optical cable. The cable was deployed in the spring of 2007, and node installation was completed in November 2008.

MOBB, located ~3 km from the node, was connected on February 28, 2009, through an extension cable installed by the ROV Ventana, with the help of a cable-laying tool sled. Technical information about the installation and cabling are provided

in past annual reports. After one year of continuous operation, the MOBB real-time telemetry ceased abruptly when the extension cable snapped as a result of repeated trawling, even though the observatory is located in a protected zone. With funds from NSF/OCE to replace the 3.2 km cable, we decided to “go the extra mile” to bury the cable to protect it better. MOBB has been on-line again since the cable was replaced in June 2012, as described in the 2011-2012 Annual Report. The station has been running well since then, except for “timing” problems due to the way time information is provided through the MARS node. We are working with MBARI to resolve those problems. As of 2012, we have implemented a method for removing infragravity induced noise from data of the vertical seismic channel and are exploring other means to further improve data for use in analysis. As can be seen in Figure 4.1.4, at very long periods (1.5 - 5 mHz) the data at MOBB are comparable with those from the other stations of the BDSN. For more information about MOBB, please visit

Electromagnetic Observatories

The BSL’s first electromagnetic observatories were deployed in 1995, in collaboration with Dr. Frank Morrison. Well characterized electric- and magnetic-field measuring systems were

Sensor	Channel	Rate (sps)	Mode	FIR
Magnetic	VT?	0.1	C	Ac
Magnetic	LT?	1	C	Ac
Magnetic	BT?	40	C	Ac
Electric	VQ?	0.1	C	Ac
Electric	LQ?	1	C	Ac
Electric	BQ?	40	C	Ac

Table 4.1.4: Typical MT data streams acquired at SAO, PKD, BRIB, and JRSC with channel name, sampling rate, sampling mode, and FIR filter type. C indicates continuous; Ac acausal. Data loggers for these systems have not been upgraded/replaced, but tests are on-going with new data loggers.

installed at two BDSN sites along the San Andreas Fault. These reference sites, now referred to as ultra-low frequency electromagnetic (ULFEM) observatories, are collocated with seismometer sites so that the field data share the same time base, data acquisition, telemetry, and archiving systems as the seismometer outputs. The original UC Berkeley sites were installed at San Andreas Geophysical Observatory (SAO), outside Hollister, halfway between San Francisco and Parkfield; and at the Parkfield earthquake prediction experiment (PKD), 300 km south of the San Francisco Bay Area (Figure 4.1.1). Each of the two sites is equipped with three induction coils and two 100 m electric dipoles. In addition, PKD has two 200 m electric dipoles. The magnetotelluric (MT) data are continuously recorded at 40 Hz, 1 Hz and 0.1 Hz and archived at the NCEDC (Table 4.1.4). For a history of instrumentation siting, see past annual reports.

In 2004, the NSF’s Earthscope program funded a Stanford-USGS-Berkeley collaboration, led by Simon Klemperer, Jonathan Glen and Darcy McPhee, to install three additional ULFEM sites within the San Francisco Bay Area. Sites were selected close to the San Andreas fault on Stanford lands at Jasper Ridge (JRSC), on Marin Headlands (MHDL), and in the East Bay near the Hayward fault on UC land near Briones Regional Park (BRIB). All these three sites are significantly affected by electromagnetic noise from the BART electric train system, but were sited in the populated San Francisco Bay area on the premise that if ULFEM signals were ever detected as precursors to earthquakes, such a discovery would have greater societal benefit in a populated area than in more remote parts of California. The new instrumentation was installed at JRSC in 2004, MHDL in 2006 and BRIB in 2007. JRSC, BRIB and MHDL have three orthogonal EMI-Schlumberger magnetic coils. JRSC and BRIB each also have two independent sets of orthogonal 100 m electric dipoles, each with a shared, common electrode, an arrangement mandated by the limited number of recording channels on the Quanterra digitizing system. MHDL lacks electric sensors due to National Park Service restrictions on land access. Data at the EM/MT sites are currently fed to Quanterra data loggers synchronized in time by GPS, and sent to the BSL via dedicated communication links. The installations use proprietary electric-field and magnetic-field “signal conditioners”

between the electrodes or magnetometers and the Quanterra digitizers.

The availability of new funding from NASA in 2009 led to a joint effort by the USGS, the BSL and Stanford towards improving operation and maintenance of the EM/MT sites. BSL engineers met scientists from the USGS and Stanford at SAO in October 2008 to assess the condition of the EM/MT system. The EM coils were not working; they were removed and returned to EMI Schlumberger, the manufacturer. EM/MT equipment at PKD was evaluated in August 2008. There, the data logger was removed from the PKD EM/MT system and has not yet been returned. At the same time, the Stanford-USGS sites were suffering from intermittent failures, due to lack of full-time maintenance staff.

In 2008, the BSL began developing a low-cost digitizer intended to be a lower-power, lower-cost replacement for both the signal conditioners and the Quanterra. At the inception of the design process, it was hoped that this new digitizer – while not as feature-rich as commercially available data loggers – might serve both seismic and electromagnetic communities. Subsequently, the design process moved to become a Stanford-USGS responsibility. A prototype 24-bit digitizer was developed and field-tested (Bowden *et al.*, 2010). A significantly modified version is being re-tested in the summer of 2013.

The site JRSC is now being used as a test-bed for new MT field installations and electronic equipment. Duplicate recording equipment can be installed there alongside the permanent MT station to check the fidelity of new equipment. As of September 2013, the replacement ULFEM digitizer is recording data from magnetometers temporarily installed alongside the permanent magnetometers that are recorded on a Quanterra. Data from identical magnetometers recorded by the old and new systems are being compared, to verify that the ULFEM digitizer has acceptable performance before it is installed at any station permanently. In the 2004–2007 original Bay Area deployments, magnetometers were buried directly inside of a plastic conduit. At JRSC a new installation system has been implemented for the horizontal magnetic coils. Now, brackets are set in concrete to support the plastic conduit that can be accurately levelled, and it can be drained to prevent build up of condensation. In the summer of 2013, the horizontal magnetometers at MHDL, BRIB and SAO are being reinstalled using this new system. In the original installations it was further assumed that the magnetometer coils were stable electronically, and no provision was made for regular calibration. A calibration coil system has now been developed and is being tested. In this system, a coil is permanently installed around the magnetometers; it will be pulsed at midday every day with a fixed voltage at known frequencies (Connor *et al.*, 2012). The calibration pulse is intended to be automatically initiated from the ULFEM digitizer. Calibration coils will be installed at JRSC, MHDL, BRIB and SAO as soon as the ULFEM digitizer is accepted to replace the existing Quanterras.

Although the Stanford-USGS-Berkeley ULFEM network will be significantly refurbished and improved as a result of summer 2013 field activities, no progress has been made on re-installing the PKD system. Existing grants from federal agencies expire in 2013, and until we succeed in winning new grants, we antic-

ipate no new progress in maintaining or improving recording systems, but we will instead focus on data analysis to justify new grant proposals.

2012-2013 Activities

Station Upgrades, Maintenance, and Repairs

Given the remoteness of the off-campus stations, BDSN data acquisition equipment and systems are designed, configured, and installed so that they are both cost effective and reliable. As a result, there is little need for regular station visits. Nonetheless, repair, maintenance and upgrade visits are occasionally required, especially since many of the broadband seismometers installed by BSL are from the first generation and are about 25 years old.

In the summer of 2009, the USGS received ARRA funds, among other things, to upgrade and improve seismic stations operated as part of the Advanced National Seismic System (ANSS). The BSL continues to benefit from those funds, in the form of a reduction in maintenance and repair visits to our sites. We received the new model of Quanterra data logger, the Q330HR, as government-furnished equipment (GFE). Over the course of the following two years, we installed the Q330HR, replacing the old Quanterras at 25 BDSN seismic stations. In addition, under the ARRA all remaining Kinemetrics FBA-23 accelerometers were replaced with Kinemetrics' newer, lower noise model, the FBA-ES-T. Some ARRA money was used to purchase Quanterra Environmental Packages (QEP) and SETRA pressure sensors for our quietest sites. Over the years the environmental sensors (pressure, temperature, humidity) installed at many of the sites had died. In addition, the Q330 only has 6 input channels, which we use for the seismometer and accelerometer components. The QEPs offer additional digitizing capacity as well as rudimentary environmental sensors (pressure, temperature, humidity). We purchased the SETRA pressure sensors to ensure high quality pressure measurements for reducing long period noise in the very broadband recordings. During the Spring 2012, we installed all QEP packages and SETRA pressure sensors in a huddle test on the roof of McCone Hall. Data from that test are discussed in the Operations section 4.6. We began installing the QEPs this year. They are now installed at BKS, CMB, HOPS, KCC, SAO and SCZ.

In addition, over the past three years, we have been able to purchase and install new electronics, E300s from Metrozet, for our STS-1 sites. Including work from this year, seven sites now have E300s: BKS, CMB, HOPS, KCC, SAO, YBH, and the site we adopted from UCSC and Geoscope, SCZ. Funds for the E300s have come from our IRIS/GSN grant, and from our support from the California Office of Emergency Services (CalOES), and from the Federal Emergency Management Agency, through CalOES.

New Stations

TremorScope: Two new stations were installed as part of the TremorScope project in the past year, TRAM and TCHL. These two stations are surface stations, installed in vaults made

from plastic septic tanks. To provide thermal mass and reduce noise, the tanks are surrounded by several cubic yards of concrete. Data flow from the stations by radio to USGS microwave hubs at Black Mt. and Hog Canyon. All four borehole locations have been permitted, one will be colocated with the surface site TRAM. We developed specifications for the boreholes and have worked with UC Berkeley's Capital Projects office to prepare for contracting the drilling. In late June and early July 2013, we had site visits with staff from interested drilling companies, so they could prepare their bids.

Geoscope Station SCZ: In the Fall of 2012, we were approached by staff from Geoscope, the French international seismic network, which installed and has operated the station SCZ in cooperation with UCSC since 1986. They asked if we would be interested in adopting SCZ, since Geoscope was upgrading their data loggers and data collection system, and would not have equipment to upgrade the system at SCZ. We found that SCZ, which is installed in a short adit into metamorphic rock in the Coast Ranges east of Salinas, CA, is a very quiet station. Geoscope had installed, and was leaving a set of STS-1 seismometers. UC Santa Cruz agreed to continue to cover the satellite telemetry expenses, and to purchase a FBA-ES-T accelerometer for the site. The BSL provided a Q330-HR, E300 electronics for the STS-1s and a QEP and SETRA. The initial installation took place in the spring of 2013. Rather than installing the FBA-ES-T immediately, we installed a STS-2 in parallel with the STS-1s to be able to evaluate and confirm their response. Some troubleshooting was necessary during the transition, as several elements, such as the centering motor of the STS-1 N component, did not work immediately. We have now collected enough data in parallel, and will exchange the STS-2 with the FBA-ES-T during the early fall of 2013.

Repair, Maintenance and Upgrades

As always, some of the BSL's technical efforts were directed toward maintaining and repairing existing instrumentation, stations, and infrastructure. We have benefitted greatly from the data loggers provided and installed through the ARRA upgrade, and from the installation of the E300s at our STS-1 sites. They allow better remote access, troubleshooting and reconfiguration. Now, field visits can be better prepared for and more effective. Remotely performed activities will not be reported here. They include seismometer recenters at many sites, remote calibration at sites with STS-1s and E300s and upgrades of the firmware for both Q330s and Balers at all sites.

BKS: We installed the first QEP and SETRA at this site. The accelerometer test also took place here (see Operational Section 4.6).

BL67: This station is installed in a concrete vault on a west sloping hillside at Lawrence Berkeley National Lab (LBNL). Because of this, the temperature in the vault regularly exceeded 60°C during the summer months. We insulated the seismometer to reduce temperature-related variation and performed extensive troubleshooting on the ethernet bridge, through which the data flow. Eventually, the consumer-grade ethernet bridge succumbed to high temperatures, and with funds from LBNL, we were able to replace it with a more robust bridge. Since then,

there have been no further telemetry problems at the site.

BRIB: This station, near Briones Regional Park experienced both power and telemetry problems during the past year. From the vault to the Observatory, where the data are collected and forwarded to the data center, data were running over fiber optic cables. Our last few pairs finally died. After exploring various options, we now have a radio link to carry data between the vault and the Observatory, which will be less susceptible to both earth movements and animals. In addition, as part of our transition away from Frame Relay, we have moved all of our data (broadband, borehole, EM/MT and GPS) to the Department of Astronomy T-1.

CMB: During the year, we had several discussions with our hosts at Columbia College about the possibility of replacing our “copper” data infrastructure with fiber. In June, the first steps were finally taken, and we visited the site to ensure that none of our equipment would be impacted by the digging.

GASB: The GPS clock for the Q330HR was replaced.

HAST: This station, on UC’s Hastings Reserve in the Coast Ranges south of Monterey, was adopted from the Transportable Array (TA) deployment. It is powered by solar panels and batteries. A site visit was required to replace the batteries, and to replace the GPS clock, which was no longer providing time to the Q330.

HATC: This site, just north of Mt. Lassen, was adopted from the Transportable Array (TA) deployment. Here both the batteries and the accelerometer were replaced.

HELL: During a visit to our other former transportable array site, HELL, to determine how best to provide additional insulation for the STS-2, we discovered ~5 cm of water in the vault. We troubleshot the pump, which is supposed to pump out the water, and accidentally reoriented the FBA-ES-T. In a subsequent site visit we corrected that sensor’s orientation.

KCC: At KCC, in a Southern California Edison (SCE) tunnel in the Sierra Nevadas, the STS-1 seismometers continue to experience problems, despite the replacement of their original electronics with E300s. We suspected that splices in the cables connecting the E300 to the data logger were their source. With funds from IRIS/GSN, we purchased 50 ft cables to replace the spliced cables. They were installed in June. At the same time, we met SCE personnel to troubleshoot the telemetry problem that had begun early in 2013. It seems that the problem was caused when a new card was installed in SCE equipment, but not correctly enabled. We are pleased to again be collecting data from KCC in real time and have retrieved all available data, about 3 months worth, from the on-site recordings. During the site visit, a QEP and SETRA were also installed. Another site visit is required to this station to remove some equipment that is no longer used, to replace one of the memory sticks in the Baler and to create a serial connection to the E300. It has not been possible during the summer, due to nearby forest fires.

PACP: Although the rest of the equipment at PACP continued to function well, the accelerometer appeared to have died. During a site visit, we discovered the good news, that “only” the fuse of the system providing power to the accelerometer had blown. Following its replacement, our accelerometer at the site again produces ground motion data.

PKD: Our broadband station at Parkfield normally works well and does not require visits. In the past year, we had to replace the data logger, which was GFE and was returned to the ANSS Depot for repair. We also experienced recurrent telemetry problems, which were found to have their source at the solar powered repeater site. Replacing the batteries and the charge controller finally resolved the telemetry problems.

RAMR: This station was adopted from the Transportable Array (TA) deployment, six years ago. The batteries installed during the transition no longer provided enough power and were replaced.

SAO: This site at the San Andreas Fault south of the town of Hollister is one of the BSL’s oldest stations, and was one of the sites where STS-1 seismometers were installed early on. Unlike many of our other STS-1 stations, the seismometer vault here is exposed to strong temperature swings, to humidity (and occasional flooding) and, despite recent upgrades to the entry, to vermin. This has been hard on the STS-1 electronics, and when we discovered renewed problems with them, we replaced them with the new E300 electronics. The replacement did not resolve all the problems, and was followed by several site visits to troubleshoot possible problem sources in the cables. Our final determination is that these, very old STS-1s have idiosyncratic characteristics which will not allow them to be calibrated using the standard E300 procedures. We are working to develop alternatives. During the site visits, a QEP was also installed with its accompanying SETRA.

SCCB: The TSA-100S accelerometer at SCCB died again, apparently due to flooding. It was replaced with a FBA-ES-T from BSL inventory. Additional efforts were made to reduce the possibility of water again collecting in the vault, such as adding a drain at its bottom.

TremorScope sites THIS, TRAM, TSCN: Following the initial deployment of the three TremorScope sites, we noticed problems with the data logger, including that the memory sticks occasionally experienced data losses, and that the data loggers shut down when the outside temperature dropped. Working together with Guralp Systems, we found the sources of the problems, repaired the systems that had not yet been deployed and then replaced those in the field. The retrieved data loggers were then also repaired. Also, the CMG-3T that was installed at THIS had a 120 s hum on the E component, due to a faulty feedback circuit. The seismometer was replaced and repaired, and is now installed at TCHL. The initially installed fence at THIS was also improved.

WENL: Yet again, the STS-2 at WENL exhibited problems and was replaced.

YBH: Since upgrading the STS-1 electronics at YBH with an E300, we have been experiencing problems with the performance of the E component. One speculation was that the spliced Q330-E300 cables were degrading and causing the problems. With funds from our IRIS/GSN grant, we purchased a set of ~120 ft cables to make the connection with no splices. They were installed in May 2013, but do not seem to have alleviated the problem. We are currently considering and exploring other options for resolving the problem, probably with a replacement of the E sensor. Other activities performed during the same visit

included the preparation of a power circuit for a satellite dish heater for the CTBT satellite telemetry. They CTBTO requested the circuit, so that their telemetry will not go down when it snows. They have, however, not yet installed the heated dish.

Perspectives for 2013-2014

We have several goals for 2013-2014. One of them is to provide separate insulation for the STS-2s at the former Transportable Array sites (HAST, HATC, HELL, RAMR, SUTB) to explore how this may reduce noise on the horizontal components. We will also complete the installations of QEPs and SETRAs at our STS-1 sites and again record local pressure and temperature data for correcting signals at very long periods. Finally, we will be working more closely with our USGS colleagues to retrieve and archive data at sites where we operate collocated equipment. At our mini-PBO stations in the Bay Area, we collect geophone and GPS-deformation data. Our USGS colleagues asked if we could also adopt their tilt and strain sensors. We already record the strain data on our GFE Basalt data loggers. Together, we developed a plan to replace the Basalt data loggers with Quanterra Q330 data loggers and QEPs. This will allow the collection of nine channels of time series and as well as air pressure data from a SETRA, and pore pressure data from the Paroscientific down-hole. We are also exploring the possibility of recording data from USGS accelerometers in Parkfield that are collocated with some of our borehole stations there. This would also involve an upgrade of our radio telemetry system.

Very Long Period Data from the BDSN

Great earthquakes excite normal modes in frequency bands around 1 mHz, well below those of smaller earthquakes. The May 24, 2013, M_w 8.3 earthquake which occurred in the Sea of Okhotsk provided an opportunity to look at the noise levels in these bands at our broadband BDSN stations. Figure 4.1.4 shows spectra in the band from 0.15 mHz to 5.5 mHz for all our broadband stations, which have both a variety of sensors (see Table 4.1.2), and different types of installations. We are pleased that in this band, the normal mode signals are well above the noise at all stations. We propose to further explore the performance of our stations in this band using a suite of earthquakes of various sizes.

Acknowledgements

Under Richard Allen's general supervision, Peggy Hellweg oversees the BDSN operations. Doug Neuhauser is responsible for organizing BDSN data acquisition operations, and Peggy Hellweg coordinates the engineering team. Nicole Crisosto, Aaron Enright, John Friday, Joshua Miller, Sarah Snyder Taka'aki Taira, and Bob Uhrhammer contribute to the operation of the BDSN. The network equipment upgrades and improvements were funded through the ARRA (American Recovery and Reinvestment Act), under USGS award number G09AC00487. The new STS-1 electronics, E300s, installed at seven of our stations, were purchased with funds from an IRIS/GSN grant and from CalOES and FEMA. The new Q330-E300 cables for KCC and YBH were purchased with funds from the IRIS/GSN grant.

The TremorScope deployment is funded by Grant 2754 from the Gordon and Betty Moore Foundation.

MOBB is a collaboration between the BSL and MBARI. From the BSL, Barbara Romanowicz, Taka'aki Taira, and Doug Neuhauser participate in the project. The MBARI team is headed by Paul McGill and has included many others over the years. The MOBB effort at the BSL is supported by UC Berkeley funds. MBARI supports the dives and data recovery. The MOBB seismometer package was funded by NSF/OCE grant #9911392. The development of the interface for connection to the MARS cable is funded by NSF/OCE grant #0648302.

Taka'aki Taira, and Peggy Hellweg contributed to the preparation of this section.

References

- Bowden, D.C., Engelland-Gay, H., Enright, A., Gardner, J., Klemperer, S.L., McPhee, D.K., Glen, J.M., Stanford-USGS Ultra-low frequency electromagnetic network: hardware developments in magnetometer calibration and recording. *EOS Trans. AGU*, Abstract NH31A-1338 presented at 2010 Fall Meeting, AGU, San Francisco, CA, 2010.
- Connor, D., Klemperer, S.L., Glen, J.M., and McPhee, D.K., Stanford-USGS Ultra-Low Frequency Electromagnetic Network: Magnetometer Calibration Developments, Poster presented at 2012 Annual Biomedical Research Conference for Minority Students (ABRCMS), San Jose, CA, 11/28/2012, 2012.
- Romanowicz, B., D. Stakes, R. Uhrhammer, P. McGill, D. Neuhauser, T. Ramirez, and D. Dolenc, The MOBB experiment: a prototype permanent off-shore ocean bottom broadband station, *EOS Trans. AGU*, Aug 28 issue, 2003.
- Romanowicz, B., D. Stakes, D. Dolenc, D. Neuhauser, P. McGill, R. Uhrhammer, and T. Ramirez, The Monterey Bay Broadband Ocean bottom seismic observatory, *Ann. Geophys.*, 49, 607-623, 2006.
- Romanowicz, B., P. McGill, D. Neuhauser and D. Dolenc, Acquiring real time data from the broadband ocean bottom seismic observatory at Monterey Bay (MOBB), *Seismol. Res. Lett.*, 80, 197-202, 2009.
- Wielandt, E., and J. Steim, A digital very broadband seismograph, *Ann. Geophys.*, 4, 227-232, 1986.
- Wielandt, E., and G. Streckeisen, The leaf spring seismometer: design and performance, *Bull. Seis. Soc. Am.*, 72, 2349-2367, 1982.

Mw8.3 Sea of Okhotsk, 2013 May 24, 120-h-long data

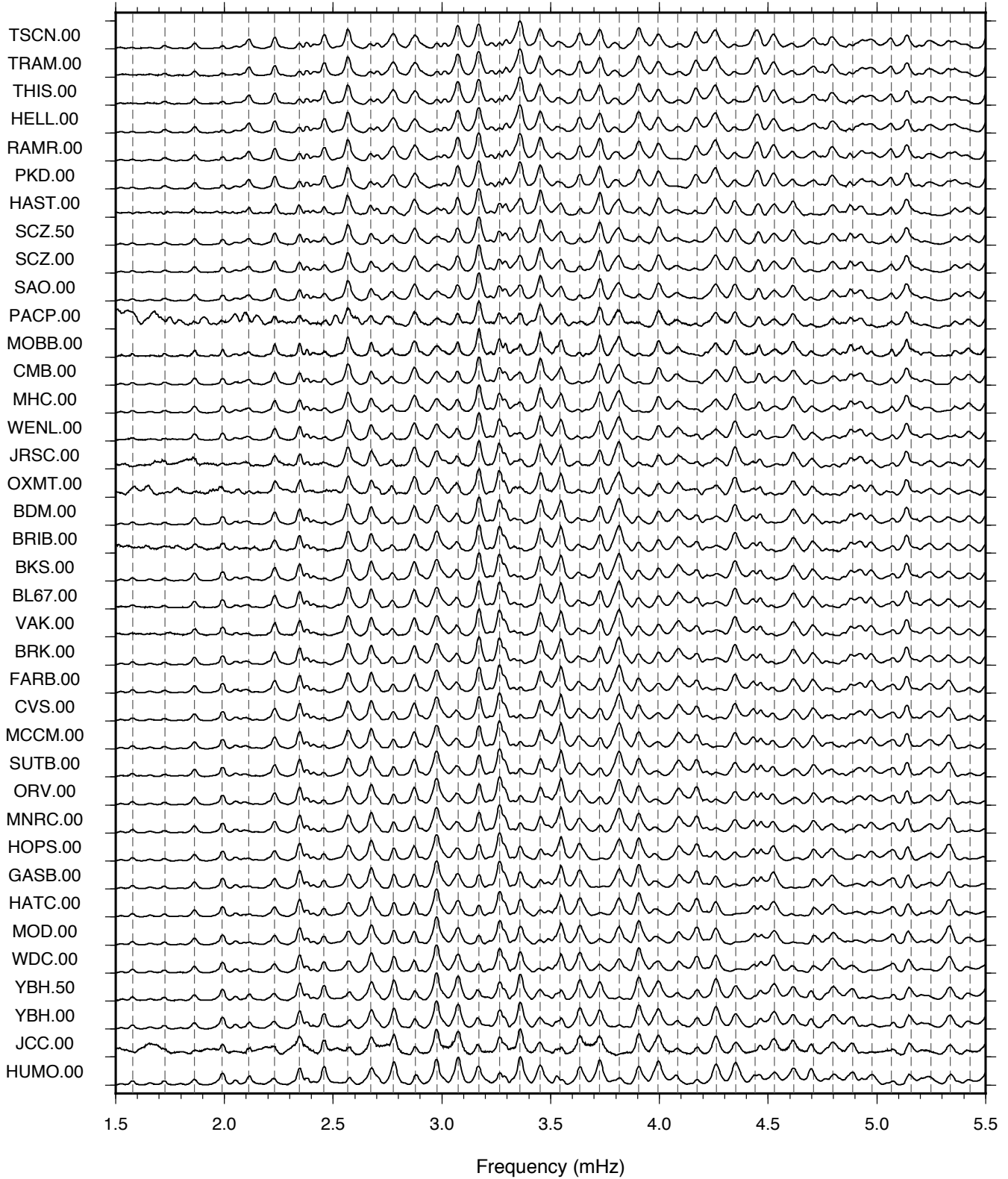


Figure 4.1.4: Amplitude spectra of vertical components of ground acceleration for the 120-hour-long data recorded at the BSN stations following the May 24, 2013 M_w 8.3 Okhotsk teleseismic event. The spectra are normalized by their maximum amplitudes. Dashed lines are expected spheroidal modes with the PREM model.

2 California Integrated Seismic Network

Introduction

Advances in technology have made it possible to integrate separate earthquake monitoring networks into a single seismic system, as well as to unify earthquake monitoring instrumentation. In California, this effort began in the south with the TriNet Project. There, Caltech, the California Geological Survey (CGS), and the USGS created a unified seismic system for Southern California. With major funding provided by the Federal Emergency Management Agency (FEMA), the California Governor's Office of Emergency Services (CalOES), and the USGS, monitoring infrastructure was upgraded and expanded, combining resources in a federal, state and university partnership. In 2000, the integration effort expanded to the entire state with the formation of the California Integrated Seismic Network (CISN, see 2000–2001 Annual Report). To this end, UC Berkeley and the USGS Menlo Park and Pasadena offices joined forces with Caltech and the CGS. The CISN is now in the thirteenth year of collaboration and its twelfth year of funding from CalOES.

CISN Background

Organization

The organizational goals, products, management, and responsibilities of the CISN member organizations are described in the founding memorandum of understanding and in the strategic and implementation plans. To facilitate activities among institutions, the CISN has three management centers:

- *Southern California Earthquake Management Center: Caltech/USGS Pasadena*
- *Northern California Earthquake Management Center: UC Berkeley/USGS Menlo Park*
- *Center for Engineering Strong Motion Data: California Geological Survey/USGS National Strong Motion Program*

The Northern and Southern California Earthquake Management Centers operate as twin statewide earthquake processing centers, serving information on current earthquake activities, while the Center for Engineering Strong Motion Data is responsible for producing engineering data products and distributing them to the engineering community.

The Steering Committee, made up of two representatives from each core institution and a representative from CalOES, oversees CISN projects. The position of chair rotates among the institutions; John Parrish from CGS took over as chair of the Steering Committee in January 2013 from Ken Hudnut.

An external Advisory Committee represents the interests of structural engineers, seismologists, emergency managers, industry, government, and utilities, and provides review and oversight. The Advisory Committee is chaired by Loren Turner of Caltrans. It last met in March 2013. Agendas and reports from the meetings may be accessed through the CISN website

(<http://www.cisn.org/advisory>).

The Steering Committee has commissioned other committees, including a Program Management Group to address planning and coordination, and a Standards Committee to resolve technical design and implementation issues.

In addition to the core members, other organizations contribute data that enhance the capabilities of the CISN. Contributing members include: University of California, Santa Barbara; University of California, Santa Cruz; University of California, San Diego; University of Nevada, Reno; University of Washington; California Department of Water Resources; Lawrence Berkeley National Lab; Lawrence Livermore National Lab; and Pacific Gas and Electric Company.

CISN and ANSS

The USGS Advanced National Seismic System (ANSS) has developed along a regionalized model. Eight regions have been organized, with the CISN representing California. David Oppenheimer of the USGS represents the CISN on the ANSS National Implementation Committee (NIC).

As the ANSS moves forward, committees and working groups are established to address issues of interest. BSL faculty and staff have been involved in several working groups of the Technical Integration Committee, including Doug Dreger, Peggy Hellweg, Pete Lombard, Doug Neuhauser, Bob Uhrhammer, and Stephane Zuzlewski.

CISN and CalOES

CalOES has long had an interest in coordinated earthquake monitoring. The historical separation between Northern and Southern California and between strong-motion and weak-motion networks resulted in a complicated situation for earthquake response. Thus, CalOES has been an advocate of increased coordination and collaboration in California earthquake monitoring and encouraged the development of the CISN. In FY 01–02, Governor Gray Davis requested support for the CISN, to be administered through CalOES. Funding for the California Geological Survey, Caltech and UC Berkeley was made available in the spring of 2002, officially launching the statewide coordination efforts. Following the first year of funding, CalOES support led to the establishment of 3-year contracts to UC Berkeley, Caltech, and the California Geological Survey for CISN activities. We have just completed the second year of the fourth three-year contract (2011–2014). Unfortunately, state funding to the CISN has been decreasing as the state's budget problems have increased, putting pressure on our earthquake monitoring and reporting activities. Past CISN-related activities are described in previous annual reports.

2012-2013 Activities

We have just completed the fourth full year of operation in the NCEMC (Northern California Earthquake Management Center) with a new suite of earthquake monitoring software.

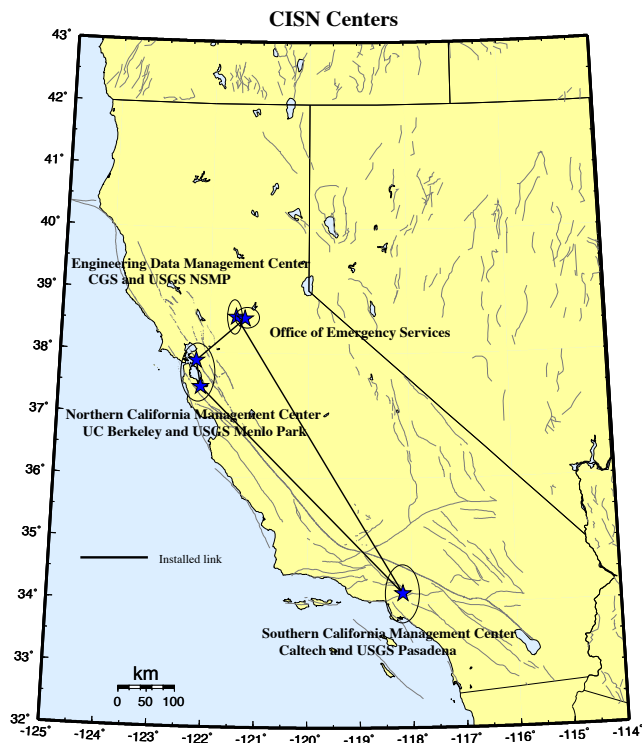


Figure 4.2.1: Map showing the geographical distribution of the CISN partners and centers. The communications “ring” is shown schematically with installed links (solid lines). It was initially a ring of dedicated T1 connections between the partners. The connections are now less robust, as reduced funding has required that the dedicated service was discontinued. Connections are now available as Internet tunnels.

In the past, this system was called the CISN software. In 2008, it was adopted by the ANSS as the system to be used by US regional networks for their operations and earthquake reporting, and it is now called the ANSS Quake Monitoring System, or AQMS. As AQMS is being implemented by other regional networks, BSL staff members are providing information and software support to the operators of those networks. The NCEMC transitioned from a hybrid system of software for earthquake monitoring and reporting to the AQMS software package in June 2009. The software is now operating at the BSL and in Menlo Park. CISN funding from CalOES contributed to this transition, and has also supported other software development and operational activities at the BSL during the past year as well.

Northern California Earthquake Management Center

As part of their effort within the CISN, the BSL and the USGS Menlo Park are operating the AQMS software as the Northern California joint earthquake information system. Operational Section 4.1 describes the operation of this system and reports on progress in implementation and improvements.

For monitoring earthquakes in Northern California, the USGS Menlo Park and BSL have improved their communications infrastructure. The BSL and the USGS Menlo Park are currently connected by two dedicated T1 circuits. One circuit is supported by CalOES funds, while the second circuit was installed in 2004-2005 (Figure 4.2.3) to support dedicated

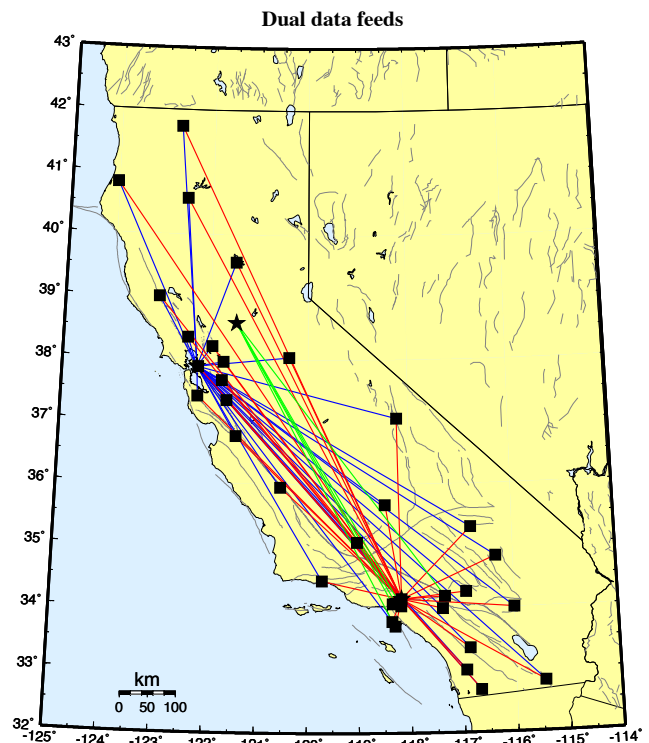


Figure 4.2.2: Map showing the original 30 stations selected to send data directly to the Northern and Southern California processing centers, and the 5 stations that send data directly to the Engineering Data Center and the Southern California processing center. Due to reductions in funding, now data from only 8 SC stations arrive directly at UCB and data from 12 UCB stations are sent to Caltech.

traffic between Berkeley and Menlo Park above and beyond that associated with the CISN.

Due to the decrease in funding, BSL has eliminated its second T1 for incoming data. BDSN data acquisition is now again limited to a single frame-relay circuit, resulting in the reintroduction of a single point of failure.

In the long term, the BSL and USGS Menlo Park hope to be connected by high-bandwidth microwave or satellite service. Unfortunately, we have not yet been able to obtain funding for such an additional communication link, although we have recently explored prospects of a very high speed radio link between the two data centers.

Statewide Integration

Despite the fact that AQMS software is now operating in both Northern and Southern California, efforts toward statewide integration continue. BSL staff are involved in many elements of these efforts. The Standards Committee, chaired by Doug Neuhouser, continues to define and prioritize projects important to the ongoing development and operation of the statewide earthquake processing system and to establish working groups to address them (meeting minutes can be found at <http://www.cisn.org/standards/meetings.html>).

Dual Station Feeds: Early in the existence of CISN, “dual station feeds” were established for 30 stations (15 in Northern

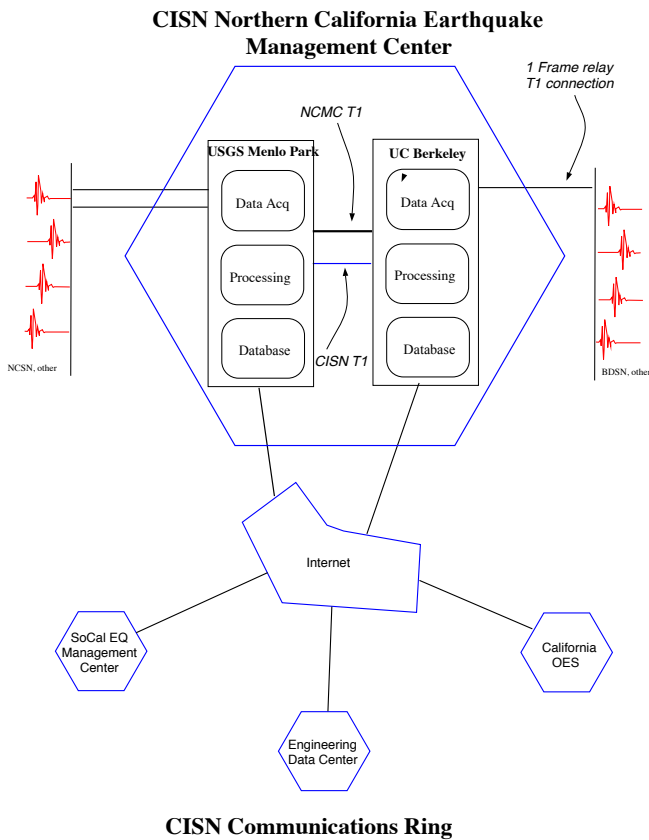


Figure 4.2.3. Schematic diagram illustrating the connectivity between the real-time processing systems at the USGS Menlo Park and UC Berkeley, forming the Northern California Management Center, and with other elements of the CISN.

California and 15 in Southern California) (see Figure 4.2.2). Because of decreases in funding, closing of stations and changes in telemetry paths, Northern California now sends data from 12 stations to Southern California in real time, and Southern California sends data from 8 to Northern California. The NCEMC uses data from the Southern California stations to estimate magnitudes on a routine basis. In addition, data from some of the stations are used in moment tensor inversions, a computation that is sensitive to the background noise level.

Data Exchange: Part of the AQMS software allows reduced amplitude timeseries to be produced and exchanged. Currently, these timeseries are being exchanged in the NCEMC, but not yet statewide. Using a common, and recently improved, format, the CISN partners continue to rapidly exchange observations of peak ground motion with one another following an event or a trigger. This step increases the robustness of generating products such as ShakeMap, since all CISN partners exchange data directly. This also improves the quality of ShakeMaps for events on the boundary between Northern and Southern California, by allowing all data to be combined in a single map. Finally, this is a necessary step toward the goal of generating statewide ShakeMaps. In addition, datasets for events of interest to engineers are provided automatically to the Center for Engineering Strong Motion Data (CESMD) in V0 format. We are now im-

proving data exchange with the University of Nevada, Reno, for events near the California/Nevada border.

Software Calibration & Standardization: CISN partners have calibrated and standardized much of the software used for automatic earthquake processing and earthquake review, now the AQMS software. The AQMS software now serves as the real-time system operating in the NCEMC. The transition was made in June 2009.

Local Magnitudes: Since the transition to the AQMS software in Northern California in June 2009, local magnitudes are calculated throughout the state using the new $\log A_0$ function and the associated station-specific corrections for broadband/strong motion stations, and also for strong-motion only stations. We are now focusing magnitude development on adding vertical components, whether short period or broadband, and short period horizontal components to the new local magnitude system. A final component of the magnitude efforts is the determination of a magnitude reporting hierarchy. For the near future, each region will continue to use its own preferences for magnitude reporting.

ShakeMap: At present, ShakeMaps are generated on five systems within the CISN. Two systems in Pasadena generate “SoCal” Shakemaps; two systems in the Bay Area generate “NoCal” Shakemaps; and one system in Sacramento generates ShakeMaps for all of California. The Sacramento system uses PDL (Product Distribution Layer) to collect the authoritative event information for Northern and Southern California. In the CISN, we evaluated the new release of the program, ShakeMap 3.5. ShakeMaps have been recalculated for all scenario events, and are about to be published. We will also soon recalculate ShakeMaps for all events in the catalog. This is necessary for two reasons. First, ShakeMap 3.5 adds additional products to the suite, such as ground motion uncertainties. Second, for ShakeMaps produced before November 2006 when the first steps toward AQMS implementation were made, there is a discrepancy between the event ID number on the Shakemap and that in the database.

We continue to work toward the goal of improving the robustness of ShakeMap generation and delivery by taking advantage of the fact that ShakeMaps are generated in the Bay Area, Pasadena, and Sacramento.

Moment Tensor Analysis: We have implemented an upgraded version of the complete waveform moment tensor code. This version allows the calculation of full moment tensor solutions, including an isotropic element. In the real time system, only deviatoric solutions will be allowed, but a reviewer may “turn on” the capability to allow full solutions. Using this new package, we recalculated moment tensors for earthquakes in the Geysers and Long Valley regions, which appeared anomalous using the deviatoric code. We also added code which allows us to use pressure-corrected data from our ocean-bottom station, MOBB (see Operational Section 4.1). We are working to implement the capability to use data from strong motion sensors in the moment tensor interface. This is useful in large events such as the 2010 Cucapa-El Mayor earthquake in Baja California. All broadband stations out to about 600 km were clipped.

Location Codes: The CISN adopted a standard for the use of “location” codes (part of the Standard for the Exchange of Earthquake Data [SEED] nomenclature to describe a timeseries based on station-network-channel-location code) in the late fall of 2003. USGS and UC Berkeley developers modified the Earthworm software to support their use. After the transition at USGS Menlo Park away from the CUSP analysis system to *Jiggle* in late November 2006, all networks in the CISN implemented location codes in their systems. Now all stations in the BK and BP networks operated by the BSL have non-blank location codes. The major effort in this transition was made along with the ARRA-funded upgrades of the data loggers. Surface data loggers digitizing seismic equipment have location code “00.” Borehole seismic stations have the location code “40.” At station YBH, we are operating a second broadband sensor for CTBTO monitoring. It has the location code “50”.

Metadata Exchange: Correct metadata are vital to CISN activities, as they are necessary to ensure valid interpretation of data. CISN is working on issues related to their reliable and timely exchange. The CISN Metadata Working Group compiled a list of metadata necessary for data processing and developed a model for their exchange. In this model, each CISN member is responsible for the metadata for its stations and for other stations that enter into CISN processing through it. For example, Menlo Park is responsible for the NSMP, Crest, and PG&E stations, while Caltech is responsible for data from the Anza network. At the present time, dataless SEED volumes are used to exchange metadata between the NCEMC and the SCEMC. The Metadata Working Group has made progress toward implementing Station XML format in this year. This is a format for metadata exchange. This vehicle is expandable, and will probably allow exchange of a more comprehensive set of metadata than dataless SEED volumes, some of which may be necessary for other systems, for example in V0 formatted data.

Standardization: The CISN’s focus on standardization of software continues. The complete AQMS system is now implemented and providing real-time earthquake information in the NCEMC (see Operational Section 4.1). The software is currently being implemented at other regional networks of the ANSS.

Earthquake Early Warning: Caltech, the BSL and the ETH Zurich have been using CISN data in real time to test Earthquake Early Warning (EEW) algorithms and to develop a demonstration Earthquake Early Warning system (see Broadening Engagement Section 3.1; see also http://seismo.berkeley.edu/research/early_warning, <http://www.shakealert.org/> and <http://www.cisn.org/eew>). In 2010-2011, we achieved end-to-end processing, with events being published to a user display. The User Display is now running at the CalOES Warning Center in Sacramento. We have also recruited other test users, including Bay Area Rapid Transit (BART), UC Berkeley Police Department, Google and other companies, agencies and organizations throughout California. Since August 2012, BART is slowing trains based on information from our EEW

system.

CISN Display

CISN Display is an integrated Web-enabled earthquake notification system designed to provide earthquake information for emergency response at 24/7 operations centers. First and emergency responders, and organizations with critical lifelines and infrastructure with a need for rapid and reliable earthquake information can request an account at <http://www.cisn.org/software/cisndisplay.htm>.

The application provides users with maps of real-time seismicity and automatically provides access to Web-related earthquake products such as ShakeMaps. CISN Display also offers an open source GIS mapping tool that allows users to plot freely available layers of public highways, roads and bridges, as well as private layers of organizational-specific infrastructure and facilities information. The current version of CISN Display is 1.4.

Earthquake Information Distribution

The USGS hosted a workshop in October 2004 to develop plans for the installation and use of the EIDS software. Doug Neuhauser and Pete Lombard participated in this workshop, which resulted in a document outlining the steps necessary for the installation and migration of the earthquake notification system from the current Quake Data Distribution Services (QDDS) to the Earthquake Information Distribution System (EIDS). During the time EIDS was operating, shortcomings were noticed, particularly as earthquake information products became larger and more complex. During the past year, the NCEMC has transitioned from using EIDS system for publishing most of its earthquake information to the new tool, developed by the USGS, the Product Distribution Layer (PDL). This tool was initially deployed for transferring so-called add-on information, such as ShakeMaps. The BSL has been using a PDL system to publish ShakeMaps since June, 2011. During FY 12–13, we worked with the USGS in Golden to test and implement PDL for delivery of all real-time products, such as complete event information which includes the picks and amplitudes used for determination of location and magnitude; and other products such as moment tensors and fault plane solutions. Pete Lombard is fundamental to our progress in this effort. We currently publish all products through PDL except “origin” information, which is awaiting developments so that CISN Display will continue to work. The BSL and NCEMC are the “guinea pig” for the implementation and will provide its codes for using PDL with AQMS to the other regional networks, when the development is complete.

Outreach

Since FY 05–06, servers for the CISN website (<http://www.cisn.org>) are located at Berkeley and Caltech. The Web servers were set up so that the load could be distributed between them, providing improved access during times of high demand. With these servers, the CISN provides access to certain earthquake products directly from <http://www.cisn.org>. For example, ShakeMaps are now served directly from the CISN website, in

addition to being available from several USGS Web servers and the CGS. The design and content of <http://www.cisn.org> continues to evolve. The website is an important tool for CISN outreach as well as for communication and documentation among the CISN partners. We are now developing an updated version of this website.

The CISN supports a dedicated website for emergency managers. This website provides personalized access to earthquake information. Known as “myCISN,” the website is available at <http://eoc.cisn.org>. To provide highly reliable access, the website is limited to registered users.

As part of the CISN, the BSL contributes each year to efforts to raise awareness of earthquakes and earthquake preparedness. The BSL is a member of the Earthquake Country Alliance, a state-wide organization of people, institutions and agencies associated with earthquake response and research. In the past year, we publicized the state-wide ShakeOut on October 18, 2012 and participated in it. Due in part to our efforts, the entire UC Berkeley campus participated. We are now working toward the statewide California ShakeOut on October 17, 2013 at 10:17 a.m. (see <http://www.shakeout.org> for more information and to sign up).

Acknowledgements

CISN activities at the BSL are supported by funding from the California Office of Emergency Services, CalOES. Richard Allen and Peggy Hellweg are members of the CISN Steering Committee. Peggy Hellweg and Doug Neuhauser are members of the CISN Program Management Group, and Peggy leads the CISN project at the BSL with support from Doug Neuhauser. Doug Neuhauser is chair of the CISN Standards Committee, which includes Peggy Hellweg, Pete Lombard, Taka’aki Taira, and Stephane Zuzulewski as members.

Because of the breadth of the CISN project, many BSL staff members have been involved, including: Aaron Enright, Nicole Crisosto, John Friday, Peggy Hellweg, Ivan Henson, Ingrid Johanson, Pete Lombard, Joshua Miller, Doug Neuhauser, Charley Paffenbarger, Sarah Snyder, Taka’aki Taira, Stephen Thompson, Bob Uhrhammer, and Stephane Zuzlewski.

Peggy Hellweg contributed to this section. Additional information about the CISN is available through reports from the Program Management Group.

3 Northern Hayward Fault Network

Introduction

Complementary to the regional surface broadband and short-period networks, the Hayward Fault Network (HFN) (Figure 4.3.1 and Table 4.3.2) is a deployment of borehole-installed, wide-dynamic range seismographic stations along the Hayward Fault and throughout the San Francisco Bay toll bridges system. Development of the HFN was initiated through a cooperative effort between the BSL (Berkeley Seismological Laboratory) and the USGS, with support from Caltrans, Electric Power Research Institute (EPRI), the University of California Campus/Laboratory Collaboration (CLC) program, LLNL (Lawrence Livermore National Laboratory), and LBNL (Lawrence Berkeley National Laboratory). The project's objectives included an initial characterization phase followed by a longer-term monitoring effort using a backbone of stations from among the initial characterization station set. Funding from Caltrans has, in the past, allowed for some continued expansion of the backbone station set for additional coverage in critical locations.

The HFN consists of two components. The first is the Northern Hayward Fault Network (NHFN), operated by the BSL, consists of 29 stations in various stages of development and operation. These include stations located on Bay Area bridges, at free-field locations, and now at sites of the Mini-PBO (mPBO) project (installed with support from NSF and the member institutions of the mPBO project). The NHFN is considered part of the Berkeley Digital Seismic Network (BDSN) and uses the network code BK. The second component of the HFN is the Southern Hayward Fault Network (SHFN) is operated by the USGS and currently consists of five stations. This network is considered part of the Northern California Seismic Network (NCSN) and uses the network code NC.

The purpose of the HFN is fourfold: 1) to contribute operational data to the Northern California Seismic System (NCSS) for real-time seismic monitoring, for response applications, and for the collection of basic data for long-term hazards mitigation; 2) to substantially increase the sensitivity of seismic data to low amplitude seismic signals; 3) to increase the recorded bandwidth for seismic events along the Hayward Fault; and 4) to obtain deep bedrock ground motion signals at the bridges from more frequent, small to moderate sized earthquakes.

In addition to the NHFN's contribution to real-time seismic monitoring in California, the mix of deep NHFN sites at near- and far-field sites and the high-sensitivity (high signal to noise ratio) and high-frequency broadband velocity and acceleration data recorded by the NHFN also provide unique data for a variety of scientific objectives, including: a) investigating bridge responses to deep strong ground motion signals from real earthquakes; b) obtaining a significantly lower detection threshold for microearthquakes and possible non-volcanic tremor signals in a noisy urban environment; c) increasing the resolution of the fault-zone seismic structure (e.g., in the vicinity of the Rodgers Creek/Hayward Fault step over); d) improving monitoring

of spatial and temporal evolution of background and repeating seismicity (to magnitudes below M_0) to look for behavior indicating the nucleation of large, damaging earthquakes and to infer regions and rates of deep fault slip and slip deficit accumulation; e) investigating earthquake and fault scaling, mechanics, physics, and related fault processes; f) improving working models for the Hayward fault; and g) using these models to make source-specific response calculations for estimating strong ground shaking throughout the Bay Area.

Below, we focus primarily on the BSL operational activities concerning the NHFN component of the HFN.

NHFN Overview

The initial characterization period of HFN development ended in 1997. During that period, the NHFN sensors initially provided signals to on-site, stand-alone Quanterra Q730 and RefTek 72A-07 data loggers, and manual retrieval and download of data tapes was required. Also during the characterization period, the long-term monitoring phase of the project began, involving the gradual transition of backbone monitoring sites to 24-bit data acquisition and communication platforms with data telemetry to the BSL.

Over the years, Caltrans has provided additional support for the upgrade of some non-backbone sites to backbone operational status and for the addition of several entirely new sites into the monitoring backbone. Efforts at continued expansion have been stymied due to propriety issue disputes between Caltrans and UC Berkeley at the administrative level. In February of 2007, the stations of the mPBO project were also folded into the NHFN monitoring scheme, increasing the NHFN by five sites.

Of the 29 stations considered part of the NHFN history, nine (E17B, E07B, YBAB, W05B, SAFB, SM1B, DB1B, DB2B, DB3B) are non-backbone stations and were not originally envisioned as long-term monitoring stations. Because the borehole sensor packages at these sites could not be retrieved (having been grouted in downhole), the sites were mothballed for possible future reactivation. Support for reactivation of two of these mothballed sites (W05B and E07B) was eventually forthcoming and their reactivation is currently planned, pending completion of the Bay Bridge retrofit and resolution of the propriety issued mentioned above. Efforts at acquiring funds for reactivation/upgrade of additional mothballed sites are also pending for similar reasons.

12 of the remaining 20 stations are currently operational (VALB, PETB, CMAB, HERB, BRIB, RFSB, SM2B, SVIN, MHDL, SBRN, OXMT, RB2B). Operation of an additional site (OHLN) has been temporarily interrupted due to outside parties having severed the power cable during local construction and restoration of operations is pending repairs. Operation of our site outside the Cal Memorial Stadium (CMSB) was also interrupted, due to accidental destruction of the borehole site during retrofit work on the stadium. Responsibility for the destruction

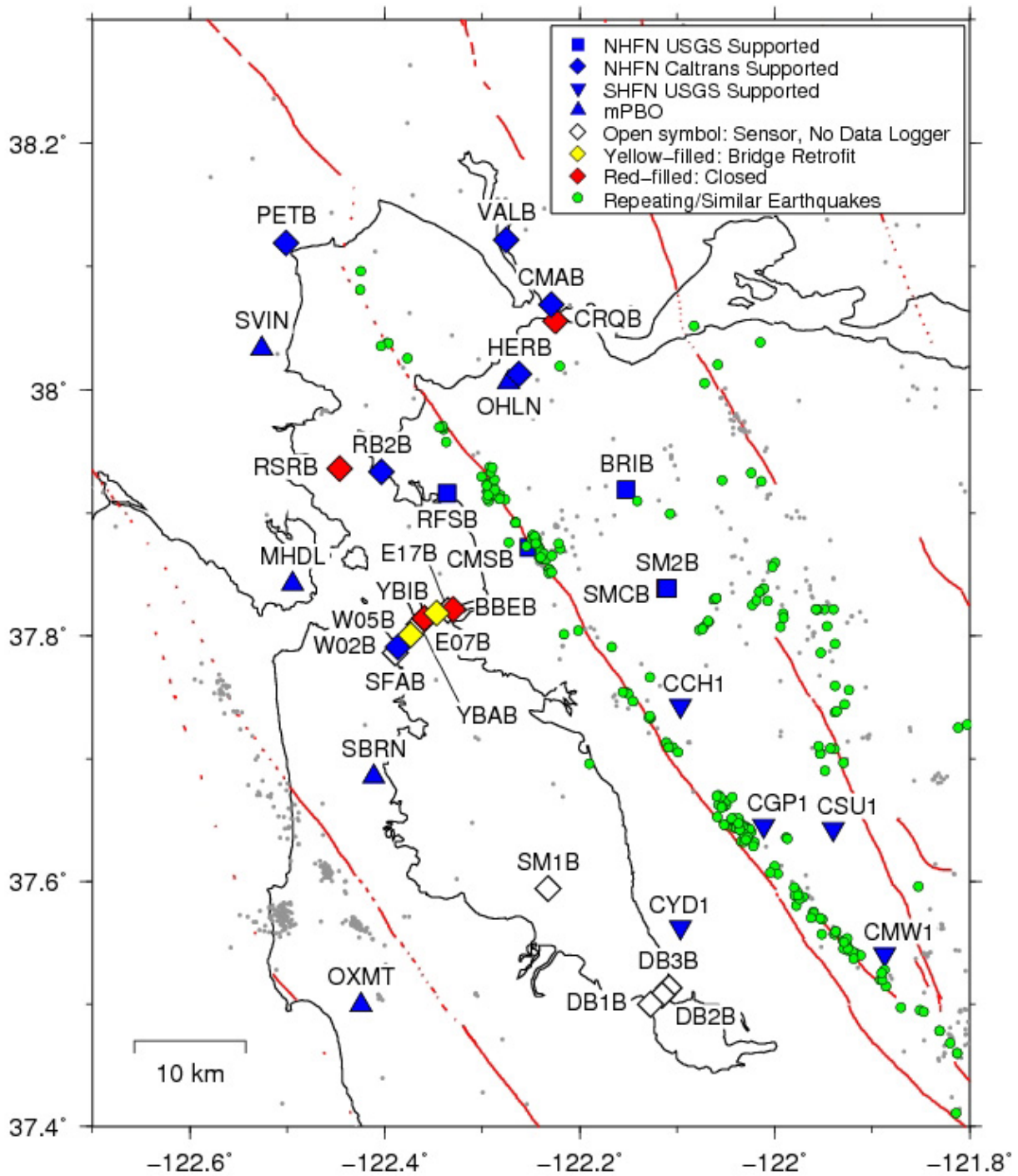


Figure 4.3.1: Map of HFN and mini-PBO stations. Diamonds are NHFN stations operated by the UC Berkeley Seismological Laboratory (BSL). Squares are BSL NHFN operated sites currently funded by the USGS. Inverted triangles are USGS SHFN sites. Triangles are former mini-PBO stations now part of the NHFN, operated by the BSL and funded by the USGS. Blue (black) are currently operational stations. Red (dark gray) are stations that recorded data in the past but are now closed, either due to replacement by higher quality installations (CRQB, SMCB) or due to complications and/or damage from earthquake retrofit activity on Bay Area bridges (RSRB, BBEB, YBIB). The color yellow represents sites whose installation is suspended pending completion of the Bay Bridge retrofit (W05B, E07B) and resolution of Caltrans and UC Berkeley proprietary issues. Currently, station BBEB operates only as a telemetry repeater site due to damage from retrofit work. Other sites that have downhole sensors but are currently non-operational are represented as open symbols. These could potentially be brought on-line with funding support. Since 2007, the NHFN has been contributing arrival time picks to the Northern California Seismic System (NCSS) for location of Bay Area earthquakes. The small gray dots are double-difference real-time relocations (<http://ddrt.ideo.columbia.edu/catalog/NCAeqDDRT.v201001>) of events occurring this year that have made use of the NHFN picks. Green circles are locations of similar/repeating events occurring in the area (*Takaaki Taira, personal communication*). Data for current and previously active NHFN and SHFN monitoring sites are all available through the NCEDC Web portal (<http://ncedc.org>).

Sensor	Channel	Rate (sps)	Mode	FIR
Accelerometer	CL?	500	T	Ca
Accelerometer	CN?	500	T	Ca
Accelerometer	HL?	200	C	Ca
Accelerometer	HL?	100	C	Ca
Accelerometer	HN?	200	C	Ca
Accelerometer	BL?	20	C	Ac
Accelerometer	BN?	20	C	Ac
Accelerometer	LL?	1	C	Ac
Accelerometer	LN?	1	C	Ac
Geophone	DP?	500	T,C	Ca
Geophone	EP?	200	C	Ca
Geophone	EP?	100	C	Ca
Geophone	BP?	20	C	Ac
Geophone	SP?	20	C	Ac
Geophone	LP?	1	C	Ac

Table 4.3.1: Typical data streams acquired at NHFN sites, with channel name, sampling rate, sampling mode, and FIR filter type. C indicates continuous, T triggered, Ca causal, and Ac acausal. Typically, the DP1 continuous channel is archived and the remaining high sample rate data (i.e., CL?, CN?, DP2 and DP3 channels) are archived as triggered snippets. As telemetry options improve, progress is being made towards archiving higher sample rate and continuous data on more channels. Prior to September 2004, only triggered data was archived for all high sample rate channels. Of the stations that are currently operational, CMAB, HERB, BRIB, RFSB, CMSB, SM2B, W02B, and RB2B record at maximum sample rates of 500 Hz; VALB and PETB at maximum 200 Hz; and mPBO sites (SVIN, OHLN, MHDL, SBRN, OXMT) at maximum 100 Hz.

was identified and funds recovered to drill a new borehole in the same area. Drilling was completed in September of 2013. Acquisition of funds for replacement of sensors and cables are currently under negotiation. Operation of station W02B on the western span of the Bay Bridge has been suspended due to the cessation of access to the site previously provided by Caltrans. Access pending the resolution of the proprietary issues between Caltrans and UC. Berkeley is expected.

These 15 sites include the five stations folded in from the mPBO project. They telemetered seismic data streams continuously into the BSL's BDSN processing stream with subsequent archival in the Northern California Earthquake Data Center (NCEDC).

The five remaining stations have been decommissioned for various reasons ranging from the sites' replacement with nearby higher quality installations (SMCB, CRQB) to irreparable site damage by outside influences such as bridge retrofit activity and construction (BBEB, YBIB, RSRB). Station BBEB, however, continues to be operational as a possible telemetry relay site for W02B should access to the station be made available.

Installation/Instrumentation

The NHFN Sensor packages are generally installed at depths ranging between 100 and 200 m, the non-backbone, non-oper-

ational Dumbarton Bridge sites are exceptions with sensors at multiple depths (Table 4.3.2). The five former mPBO sites that are now part of the NHFN have three-component borehole geophone packages. Velocity measurements for the mPBO sites are provided by Mark Products L-22 2 Hz geophones (Table 4.3.3). All the remaining backbone and non-backbone NHFN sites have six-component borehole sensor packages. The six-component packages were designed and fabricated at LBNL's Geophysical Measurement Facility and have three channels of acceleration, provided by Wilcoxon 731A piezoelectric accelerometers, and three channels of velocity, provided by Oyo HS-1 4.5 Hz geophones.

The 0.1-400 Hz Wilcoxon accelerometers have lower self-noise than the geophones above about 25-30 Hz, and remain on scale and linear to 0.5 g. In tests performed in the Byerly vault at UC Berkeley, the Wilcoxon is considerably quieter than the FBA-23 at all periods, and is almost as quiet as the STS-2 between 1 and 50 Hz.

Currently six of the NHFN backbone sites have Quanterra data loggers, and nine of the sites have been upgraded with BASALT data loggers. When operational, all 15 of these sites telemeter data continuously to the BSL. Signals from these stations are digitized at a variety of data rates up to 500 Hz at 24-bit resolution. The data loggers employ causal FIR filters at high data rates and acausal FIR filters at lower data rates (Table 4.3.1).

Data Rates and Channels

Because of limitations in telemetry bandwidth and local disk storage, 7 of the 10 (excluding CMAB, VALB and PETB) six-component NHFN stations transmit maximum 500 Hz data continuously for only 1 geophone channel (i.e., when functional, on their vertical channel). Triggered 500 Hz data for three additional channels with 180-second snippets are also transmitted. Station VALB also transmits data from only four channels; however, continuous data for all four channels are transmitted at a maximum of 200 Hz sampling. PETB transmits maximum 200 Hz data continuously on all six channels (three geophone, three accelerometer), and CMAB transmits maximum 500 Hz data continuously on all six channels. Continuous data for the channels of all 10 of these stations are also transmitted to the BSL at reduced sampling rates (20 and 1 sps). A Murdock, Hutt, and Halbert (MHH) event detection algorithm (*Murdock and Hutt, 1983*) is operated independently at each station on 500 sps data for trigger determinations. Because the accelerometer data is generally quieter, the MHH detections are made locally using data from the Wilcoxon accelerometers when possible. However, there is a tendency for these powered sensors to fail, and, in such cases, geophone channels are substituted for the failed accelerometers. The five mPBO-originated sites all transmit their three-component continuous geophone data streams to the BSL at 100, 20, and 1 sps.

Integration with the NCSS, SeisNetWatch, and Seis-miQuery

The NHFN is primarily a research network that complements regional surface networks by providing downhole recordings of very low amplitude seismic signals (e.g., from mi-

croearthquakes or non-volcanic tremor) at high gain, to high frequencies and with low noise. In addition, data streams from the NHFN are also integrated into the Northern California Seismic System (NCSS) real-time/automated processing stream for response applications and collection of basic data for long-term hazards mitigation. The NCSS is a joint USGS (Menlo Park) and Berkeley Seismological Laboratory (BSL) entity with earthquake reporting responsibility for Northern California, and data from networks operated by both institutions are processed jointly to fulfill this responsibility. Through this integration, the NHFN picks, waveforms, and NCSS event locations and magnitudes are automatically entered into a database where they are immediately available to the public through the NCEDC and its DART (Data Available in Real Time) buffer. The capability for monitoring state of health information for all NHFN stations using SeisNetWatch also exists, and up-to-date dataless SEED formatted metadata is made available through the NCEDC with the SeisQuery software tool.

Station Maintenance

Identifying network maintenance issues involves, in part, automated and semi-automated tracking of power, telemetry and data gaps. In addition, regular inspection of the seismic waveforms and spectra are carried out on samples of background noise and of significant local, regional and teleseismic earthquakes. These efforts are carried out to identify problems that can result from a variety of operational issues including changes in background noise levels from anthropogenic sources; ground loops; failing, damaged or stolen instrumentation; and power and telemetry issues. Troubleshooting and remediation of such problems are carried out through a coordinated effort between data analysts and field engineers.

In addition to routine maintenance and trouble shooting efforts, performance enhancement measures are also carried out. For example, when a new station is added to the NHFN backbone, extensive testing and correction for sources of instrumental noise (e.g., grounding related issues) and telemetry through-put are carried out to optimize the sensitivity of the station. Examples of maintenance and enhancement measures that are typically performed include: 1) testing of radio links to ascertain reasons for unusually large numbers of dropped packets; 2) troubleshooting sporadic problems with excessive telemetry dropouts; 3) manual power recycle and testing of hung data loggers; 4) replacing blown fuses or other problems relating to dead channels identified through remote monitoring at the BSL; 5) repairing telemetry and power supply problems when they arise; and 6) correcting problems that arise due to various causes, such as weather or cultural activity.

Quality Control

Power Spectral Density Analyses:

One commonly used quality-check on the performance of the borehole installed network includes assessment of the power spectral density (PSD) distributions of background noise. We have developed and implemented an automated estimation of

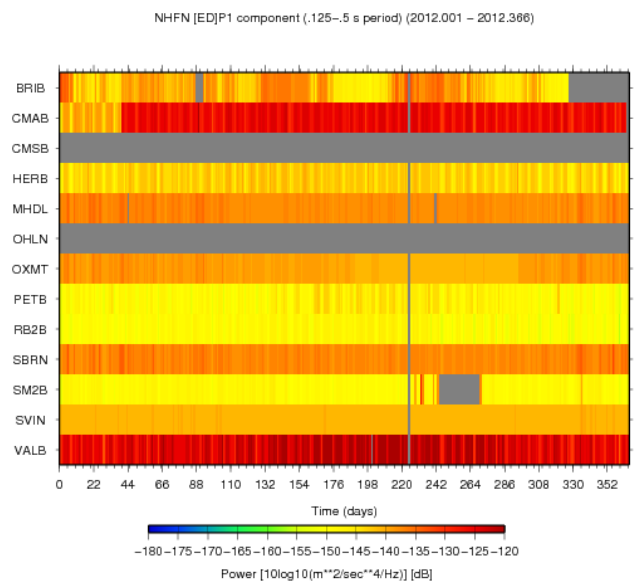


Figure 4.3.2: One-year summary plots for 2012 showing typically observed background noise PSD levels for the vertical DP1/EP1 channels of NHFN borehole stations. The mean PSD (dB) ranking (lowest to highest) of the non-mPBO stations (top panel) in operation at the time given at 3 Hz obtained from all available 2012 data on these channels are:

RB2B.BP.DP1	-140.827
SM2B.BP.DP1	-139.176
SVIN.BP.EP1	-138.676
PETB.BP.EP1	-136.503
OXMT.BP.EP1	-136.070
MHDL.BP.EP1	-135.637
HERB.BP.DP1	-132.916
SBRN.BP.EP1	-131.866
BRIB.BP.DP1	-130.980
CMAB.BP.DP1	-116.911
VALB.BP.EP1	-111.225

PSDs for HFN/mPBO the following stations are not available: CMSB (closed) and OHLN (power issue) due to construction. Variations in PSD noise among the stations are generally attributable to the stations' proximity to different cultural noise sources such as freeways or train-tracks, differences in depth of sensor installation, or to differences in local geologic conditions.

the power spectral density (PSD) distributions of background noise for all recorded NHFN channels and have developed summary PSD plots of these estimations to promote rapid evaluation of the noise levels through time.

Shown in Figure 4.3.2 are power spectral density (PSD) plots of background noise for 13 vertical NHFN channels in operation during 2012 for the 2-8 Hz frequency band. By continuously updating such plots in a variety of bands, we can rapidly evaluate changes in the network's station response to seismic signals across the wide band high-frequency spectrum of the borehole NHFN/mPBO sensors.

Changes in the responses often indicate problems with the power, telemetry, or acquisition systems, or could also be associated with changing conditions in the vicinity of station installations. In general, background noise levels of the borehole

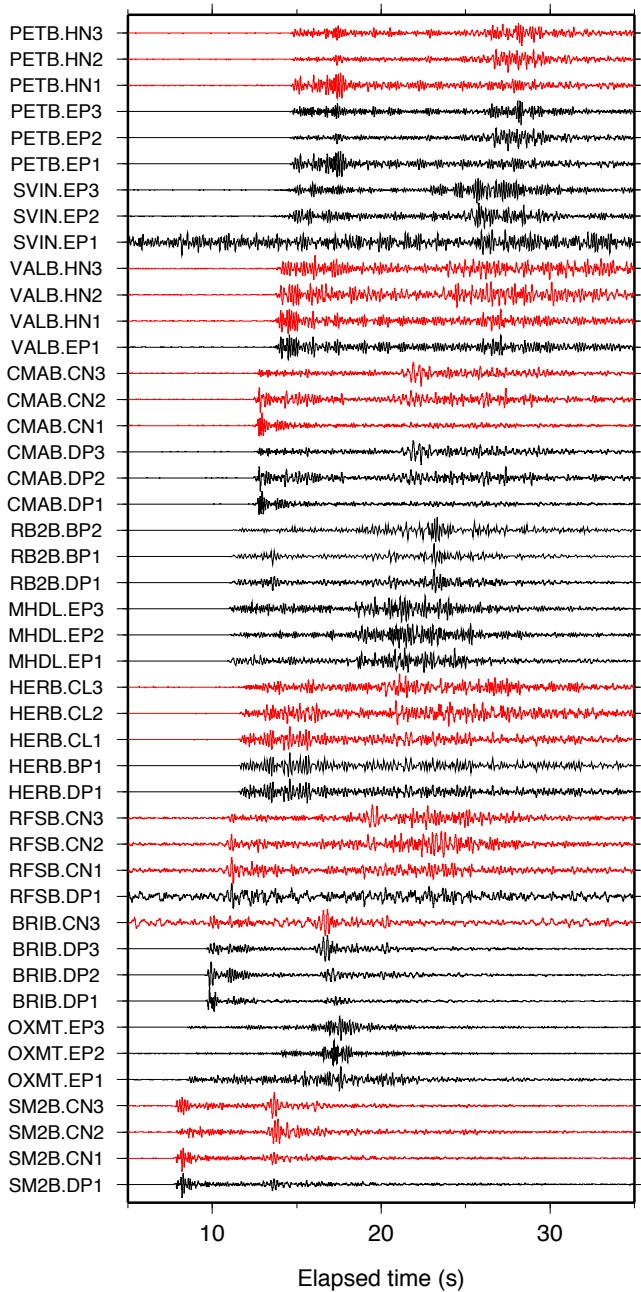


Figure 4.3.3: Plot of ground accelerations recorded on the geophones (black traces) and accelerometers (red/gray traces) of the 11 NHFN borehole stations in operation at the time of a recent Bay Area earthquake (February 24, 2013, $M_{2.9}$ near Fremont, CA). The traces are filtered with a 1-8 Hz bandpass filter, scaled by their maximum values, and ordered from bottom to top by distance from the epicenter.

NHFN stations are more variable and generally higher than those of the Parkfield HRSN borehole stations (see Operations section 4.4). This is due in large part to the significantly greater cultural noise in the Bay Area and the proximity of several near-field NHFN sites to Bay Area bridges. On average, the mPBO component of the NHFN sites (MHDL, OXMT, SBRN, SVIN in Figure 4.3.2) are more consistent with each other and throughout their spectral range. This is due in large part to the greater average depth of the mPBO sensors, the locations of

mPBO stations in regions with generally less industrial and other cultural noise sources, and possibly the absence of powered sensors (i.e. accelerometers) in their borehole sensor packages. The maximum sampling rate of 100 sps at these sites also limits their spectral range to a maximum of 40 Hz, below 60 Hz where power-line noise often becomes a problem.

One of the most pervasive problems at the other NHFN stations with higher sampling rates is power line noise (60 Hz and its harmonics at 120 and 180 Hz). This noise reduces the sensitivity of the MHH detectors and can corrupt research based on full waveform analyses. When NHFN stations are visited, the engineer at the site and a seismologist at the BSL frequently work together to identify and correct ground-loop and inductive-coupling problems, which are often at the root of this contamination.

Real Event Displays

Another method for rapid assessment of network performance is to generate and evaluate the seismograms from moderate local and large teleseismic earthquakes recorded by the NHFN stations. This is an essential component of NHFN operations because the seismic data from local, regional, and teleseismic events is telemetered directly to the BSL and made available to the Northern California Seismic System (NCSS) real-time/automated processing stream for seismic response applications within a few seconds of being recorded by the NHFN.

Shown in Figure 4.3.3 is an example display of NHFN geophone and accelerometer channels for a recent local Bay Area earthquake (February 24, 2013, $M_{2.9}$ near Fremont, CA). It is apparent from this simple display that in general both the velocity and accelerometer channels are operating correctly. However, the channels SVIN.EP1, RFSB.DP1 and BRIB.CN3 show excessive levels of noise that will need to be addressed. Stations CMSB and OHLN were off-line at the time, due to landowner construction related issues at those locations.

Figure 4.3.4 shows seismograms of the recent teleseismic M_w 8.3 deep earthquake in Sea of Okhotsk (Lat.: 54.874N; Lon.: 153.281E; depth 609 km) occurring on May 24, 2013 05:44:49 (UTC). On this date and for this frequency band (0.05-0.10 Hz), network performance appears good for the vertical (DP1 and EP1) channels for 12 of the stations in operation at the time. As with the local event in Figure 4.3.3, the SVIN.EP1 and RFSB.DP1 channels have unacceptably high levels of noise that need to be addressed.

Owing to their near similar source-receiver paths, signals from teleseismic events also serve as a good source for examining the relative polarities and responses of the BK borehole network station/components to seismic ground motion, after correction for differences in instrument response among the stations. By rapidly generating such plots (particularly with correction for instrument response) following large teleseismic events, quick assessment of the NHFN seismometer responses and polarities to real events is easily done and, if needed, corrective measures implemented with relatively little delay.

Both Figures 4.3.3 and 4.3.4 serve to illustrate the value of routine evaluation of both local (higher frequency) and teleseismic (lower frequency) events when monitoring the state

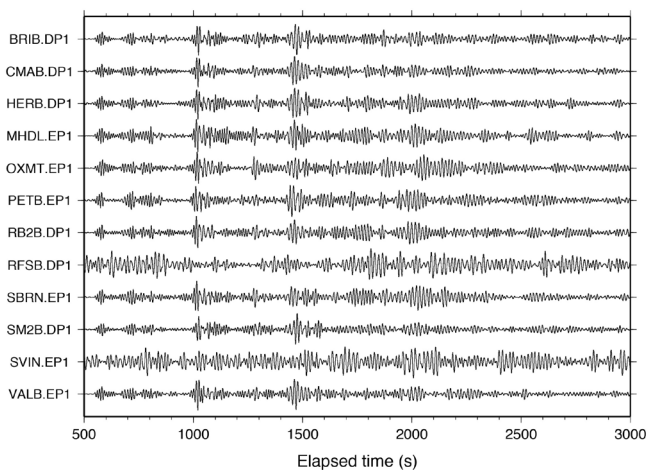


Figure 3.3.4: Plot of P-wave seismograms of the teleseismic M_w 8.3 deep earthquake in Sea of Okhotsk (Lat.: 54.874N; Lon.: 153.281E; depth 609 km) occurring on May 24, 2013 05:44:49 (UTC) recorded on the DP1/EP1 (vertical) channels of the 12 operational NHFN borehole stations. Here, vertical component geophone (velocity) data have been 0.05-0.10 Hz bandpass filtered and normalized by the maximum amplitude for each trace.

of health of NHFN stations.

2012-2013 Activities

Every year, routine maintenance, operations, quality control, and data collection play an important part in our activities. Other NHFN project activities have included: a) specific station issues; b) efforts to obtain additional funds for future upgrade and expansion of the network; and c) efforts to leverage NHFN activities through partnerships with various institutions outside of BSL

Specific Station issues

BRIB: This year data collection from station BRIB has continued to be problematic. As with most NHFN sites, the BRIB installation is a complex integration of telemetry, power, recording, and sensor instrumentation. The BRIB station is particularly complex in that it collects coincident multi-component surface, borehole, broadband, short-period velocity and accelerometer data. Hence, getting at the root of the problems there has taken considerable effort with multiple site visits and contacts with the property administrators and power/telemetry providers. Considerable progress has been made for problems related to the power system at the site, and efforts to resolve several additional issues are continuing.

OHLN: The dense Bay Area population requires that most NHFN stations be sited on developed land, and permission to use the sites is at the discretion of generous private or public landowners. Consequently, property development by the landowners sometimes requires temporary cessation and modifications to our station installations to accommodate both the landowners and our needs. This continues to be the case for station OHLN, and it continues to be off-line. However, notable progress has been made at modifying the power scheme at the

site, and we expect OHLN to be back on-line soon.

W02B: Over the years, Caltrans has provided field and financial support for the operation and maintenance of W02B and several additional stations in the NHFN. However this support has now been stymied by disputes over data propriety between Caltrans and the UC. Berkeley at the administrative level. The site is experiencing what appears to be a failure in the data acquisition system. It is also located on the western span of the Bay Bridge and access to the site is limited, requiring travel on Caltrans boats. Due to the absence of maintenance support for this previously Caltrans supported site, operation of the station has had to be suspended. Although we are hopeful, we have concerns that resolution of the proprietary issues between Caltrans and UC. Berkeley will not be worked out soon. Once the issues are resolved, however, we can regain access to the site and carry out long overdue maintenance as well as install a badly needed BASALT data logger.

CMSB: Operation of our site outside the Cal Memorial Stadium (CMSB) was interrupted in late 2010, due to retrofit work on the stadium. It was later discovered that the borehole was accidentally destroyed during landscaping following the retrofit work. Responsibility for the destruction was identified and funds recovered to drill a new borehole in the same area. Drilling was completed in September of 2013. We are now in the process of working with the UC administration to acquire funds for replacement of the sensors and cable that were also destroyed as part of the landscaping. Once these funds become available, we will purchase and install the seismic equipment in the borehole and initiate data collection from the new replacement site.

Additional Funding

Operation of the Northern Hayward Fault Network is supported by the Advanced National Seismic System (ANSS) and in the past through a partnership with the California Department of Transportation (Caltrans). ANSS provides operations and maintenance (O&M) support for a fixed subset of nine operational stations that were initiated as part of previous projects in which the USGS was a participant. Caltrans has in the past provided field and financial support for development and O&M for the remaining stations that have been added to the network through Caltrans partnership grants. In the past, Caltrans also provided additional support for upgrade and expansion of the network, when possible.

Due to the state budget crisis in the late 2000s, Caltrans began reviewing and modifying its financial commitments and its accounting practices relating to its funding of external projects, such as the NHFN project. This severely complicated efforts to receive previously approved NHFN funding from Caltrans, and it imposed many additional administrative roadblocks to acquiring additional Caltrans support. In June of 2010, our team held two meetings at Berkeley with our Caltrans contact and made a presentation at Caltrans in Sacramento to argue against O&M funding reductions and for further upgrade and expansion of the NHFN. These efforts resulted in a request by Caltrans for a proposal to install surface instruments at up to six of our borehole installations and to reactivate three currently

mothballed NHFN sites. We submitted our proposal in September of 2010. Subsequently, a reduction in the Caltrans budget for external support resulted in a request from Caltrans for us to reduce the scope of the proposal we submitted. We promptly responded to this request and tentative approval was promised. Funding was held up for over a year, however, by bureaucratic concerns and issues of proprietary rights. Haggling over these issues between the University of California (reaching as high as the UC Office of the President) and Caltrans continued into this year and the resolution was less than beneficial. Both sides have agreed that they cannot come to an agreement, and progress has come to a halt with approval for the proposed project being withdrawn by Caltrans.

This has put on hold any further work on improving and expanding the NHFN with Caltrans help. At this time, maintenance of previously supported Caltrans stations that are accessible without Caltrans assistance is continuing using some internal BSL funding, though at a greatly reduced effort. This is resulting in significantly longer downtime for failed stations and significantly degraded data. Eventually, if future support is not forthcoming, these sites will need to be closed. Sites such as W02B, where access through Caltrans is required, have had to have operations suspended when failures occur.

Partnerships

The NHFN is heavily leveraged through partnerships with various institutions, and we have continued to nurture and expand these relationships. Over the past year, we have continued our collaborative partnerships with the USGS, St. Mary's College, and the Cal Maritime Academy, and we have continued to strive to renew collaboration with Caltrans. In addition, the BSL has continued to coordinate with Lawrence Berkeley National Laboratory (LBNL) in their project to develop an LBNL array of borehole stations that provide complementary coverage to the HFN.

Acknowledgments

Thomas V. McEvelly, who passed away in February 2002, was instrumental in developing the Hayward Fault Network, and, without his dedication and hard work, the creation and continued operation of the NHFN would not have been possible.

Under Peggy Hellweg's, Robert Nadeau's and Doug Dreger's general supervision, Doug Neuhauser, Taka'aki Taira, and the engineering team (Sarah Snyder, Joshua Miller, Nicole Crisosto and John Friday) all contribute to the operation of the NHFN. Robert Nadeau and Taka'aki Taira prepared this NHFN operations section of the BSL Annual Report.

Support for the NHFN this year was provided by the USGS through the cooperative networks grant program (grant number G10AC00093). In previous years, Pat Hipley of Caltrans has been instrumental in the effort to continue to upgrade and expand the network. Larry Hutchings and William Foxall of LLNL have also been important collaborators on the project in past years.

References

- Rodgers, P.W., A.J. Martin, M.C. Robertson, M.M. Hsu, and D.B. Harris, Signal-Coil Calibration of Electromagnetic Seismometers, *Bull. Seism. Soc. Am.*, 85(3), 845-850, 1995.
- Murdock, J. and C. Hutt, A new event detector designed for the Seismic Research Observatories, *USGS Open-File-Report 83-0785*, 39 pages, 1983.
- Waldhauser, F. and D.P. Schaff, Large-scale relocation of two decades of Northern California seismicity using cross-correlation and double-difference methods, *J. Geophys. Res.*, 113, B08311, doi:10.1029/2007JB005479, 2008.

Code	Net	Latitude	Longitude	Elev (m)	Over (m)	Date	Location
VALB	BK	38.1215	-122.2753	-24.5	155.8	2005/11 - current	Napa River Bridge
PETB	BK	38.1189	-122.5011	-30	113	2010/09 - current	Petaluma River Bridge
CMAB	BK	38.06892	-122.22914	0	142.2	2009/12 - current	Cal Maritime Academy
CRQB	BK	38.05578	-122.22487	-25	38.4	1996/07 - 2010/05	CB
HERB	BK	38.01239	-122.26217	-18	217	2001/09 - current	Hercules
BRIB	BK	37.91886	-122.15179	222.2	108.8	1995/07 - current	BR, Orinda
RFSB	BK	37.91608	-122.3361	-27.3	91.4	1996/02 - current	RFS, Richmond
CMSB	BK	37.87195	-122.25168	94.7	167.6	1995/06 - current	CMS, Berkeley
SMCB	BK	37.83881	-122.11159	180.9	3.4	1998/02 - 2007/06	SMC, Moraga
SM2B	BK	37.83874	-122.11022	200	150.9	2007/06 - current	SMC, Moraga
SVIN	BK	38.03318	-122.52632	-27.5	152.4	2003/08 - current	mPBO, St. Vincent's school
OHLN	BK	38.00625	-122.27299	-0.5	196.7	2001/11 - current	mPBO, Ohlone Park
MHDL	BK	37.84232	-122.49431	94.5	151.9	2006/05 - current	mPBO, Marin Headlands
SBRN	BK	37.68561	-122.41127	4	161.5	2002/08 - current	mPBO, San Bruno Mtn.
OXMT	BK	37.49936	-122.42431	209.1	194.3	2003/12 - current	mPBO, Ox Mtn.
BEB	BK	37.8216	-122.32975	-30.8	182.9	2002/09 - 2007/11	BB, Pier E23
E17B	BK	37.82086	-122.33534	TBD	160	1995/08 - unknown *	BB, Pier E17
E07B	BK	37.81847	-122.34688	TBD	134	1996/02 - unknown +	BB, Pier E7
YBIB	BK	37.8142	-122.35923	-27	61	1996/07 - 2000/08	BB, Pier E2
YBAB	BK	37.8094	-122.3645	TBD	3	1998/06 - unknown *	BB, YB Anchorage
W05B	BK	37.801	-122.3737	TBD	36.3	1997/10 - unknown +	BB, Pier W5
W02B	BK	37.79112	-122.38632	-45	57.6	2003/06 - current	BB, Pier W2
SFAB	BK	37.7861	-122.3893	TBD	0	1998/06 - unknown *	BB, SF Anchorage
RSRB	BK	37.93575	-122.44648	-48	109	1997/06 - 2001/04	RSRB, Pier 34
RB2B	BK	37.93335	-122.40314	-18	133.5	2009/12 - current	RSRB, Pier 58
SM1B	BK	37.59403	-122.23242	TBD	298	not recorded *	SMB, Pier 343
DB3B	BK	37.51295	-122.10857	TBD	1.5	1994/09 - 1994/11 *	DB, Pier 44
					62.5	1994/09 - 1994/09 *	
					157.9	1994/07 - unknown *	
DB2B	BK	37.50687	-122.11566	TBD		1994/07 - unknown *	DB, Pier 27
					189.2	1992/07 - 1992/11 *	
DB1B	BK	37.49947	-122.12755	TBD	0	1994/07 - 1994/09 *	DB, Pier 1
					1.5	1994/09 - 1994/09 *	
					71.6	1994/09 - 1994/09 *	
					228	1993/08 - unknown *	
CCH1	NC	37.74332	-122.09657	345	119	1995/06 - current	Chabot
CGP1	NC	37.64545	-122.01128	461	121	1995/06 - current	Garin Park
CSU1	NC	37.64303	-121.9402	623	124	1995/11 - current	Sunol
CYD1	NC	37.56289	-122.0967	114	137	1996/11 - current	Coyote
CMW1	NC	37.54053	-121.88743	498	155	1995/06 - current	Mill Creek

Table 4.3.2: Stations of the Hayward Fault Network. Station code, network ID, location, period of available data, and site description are included. For entries with “*” and “+” in the date column, no monitoring data is available. For these sites, the dates are periods when data was downloaded manually. These manually retrieved data are not available at the NCEDC, but may be available from Larry Hutchings (now at LBNL). Latitude and longitude (in degrees) are in WGS84 reference frame. The well head elevation (in meters) is relative to the WGS84 reference ellipsoid. Abbreviations: TBD - to be determined; BB - Bay Bridge; BR - Briones Reserve; CMS - Cal Memorial Stadium; CB - Carquinez Bridge; DB - Dumbarton Bridge; mPBO - Mini-Plate Boundary Observatory; RFS - Richmond Field Station; RSRB - Richmond-San Rafael Bridge; SF - San Francisco; SMB - San Mateo Bridge; SMC - St. Mary's College; and YB - Yerba Buena. At the end of the initial characterization phase of the HFN project, the stations labeled with “*” were mothballed with borehole sensors remaining cemented in place. Incorporation of the “+” stations into the monitoring backbone is work in progress. Proposal to Caltrans requesting support to bring more mothballed sites into the NHFN backbone is pending. Due to damage from Bay Bridge retrofit work, station BEB no longer records seismic data but continues to operate as a telemetry relay station. Data collection at site CMSB has also been suspended temporarily to accommodate construction at Cal Memorial Stadium on the UC Berkeley campus. At OHLN, temporary suspension of data collection also occurred to accommodate landowner construction. W02B has been turned off due to equipment failure and cessation of access previously provided by Caltrans.

Site	Geophone	Accelerometer	Z	H1	H2	data logger	Notes	Telem.
VALB	Oyo HS-1	Wilcoxon 731A	-90	336	246	Q330		FR
PETB	Oyo HS-1	Wilcoxon 731A	-90	TBD	TBD	Q330		FR/Rad.
CMAB	Oyo HS-1	Wilcoxon 731A	-90	161	251	BASALT		Rad./VPN
CRQB	Oyo HS-1	Wilcoxon 731A	-90	68	338	None at Present		FR
HERB	Oyo HS-1	Wilcoxon 731A	-90	160	70	Q4120		FR
BRIB	Oyo HS-1	Wilcoxon 731A	-90	79	169	BASALT	Acc. failed, Dilat.	FR
RFSB	Oyo HS-1	Wilcoxon 731A	-90	346	256	BASALT		FR
CMSB	Oyo HS-1	Wilcoxon 731A	-90	19	109	Q4120		FR
SMCB	Oyo HS-1	Wilcoxon 731A	-90	76	166	None at present	Posthole	FR
SM2B	Oyo HS-1	Wilcoxon 731A	-90	TBD	TBD	BASALT		FR
SVIN	Mark L-22		-90	319	49	BASALT	Tensor.	FR/Rad.
OHLN	Mark L-22		-90	300	30	BASALT	Tensor.	FR
MHDL	Mark L-22		-90	64	154	BASALT	Tensor.	FR
SBRN	Mark L-22		-90	6	96	BASALT	Tensor.	FR
OXMT	Mark L-22		-90	120	210	BASALT	Tensor.	FR
BBEB	Oyo HS-1	Wilcoxon 731A	-90	19	109	None at present	Acc. failed	Radio
E17B	Oyo HS-1	Wilcoxon 731A	-90	TBD	TBD	None at present		
E07B	Oyo HS-1	Wilcoxon 731A	-90	TBD	TBD	None at present		
YBIB	Oyo HS-1	Wilcoxon 731A	-90	257	347	None at present	Z geop. failed	FR/Rad.
YBAB	Oyo HS-1	Wilcoxon 731A	-90	TBD	TBD	None at present		
W05B	Oyo HS-1	Wilcoxon 731A	-90	TBD	TBD	None at present		
W02B	Oyo HS-1	Wilcoxon 731A	-90	TBD	TBD	Q4120		Radio
SFAB	None	LLNL S-6000	TBD	TBD	TBD	None at present	Posthole	
RSRB	Oyo HS-1	Wilcoxon 731A	-90	50	140	None at present	2 acc. failed	FR
RB2B	Oyo HS-1	Wilcoxon 731A	-90	252	162	Q4120	1 acc. failed	FR
SM1B	Oyo HS-1	Wilcoxon 731A	-90	TBD	TBD	None at present		
DB3B	Oyo HS-1	Wilcoxon 731A	-90	TBD	TBD	None at present	Acc. failed	
DB2B	Oyo HS-1	Wilcoxon 731A	-90	TBD	TBD	None at present		
DB1B	Oyo HS-1	Wilcoxon 731A	-90	TBD	TBD	None at present	Acc. failed	
CCH1	Oyo HS-1	Wilcoxon 731A	-90	TBD	TBD	Nanometrics HRD24	Dilat.	Radio
CGP1	Oyo HS-1	Wilcoxon 731A	-90	TBD	TBD	Nanometrics HRD24	Dilat.	Radio
CSU1	Oyo HS-1	Wilcoxon 731A	-90	TBD	TBD	Nanometrics HRD24	Dilat.	Radio
CYD1	Oyo HS-1	Wilcoxon 731A	-90	TBD	TBD	Nanometrics HRD24	Dilat.	Radio
CMW1	Oyo HS-1	Wilcoxon 731A	-90	TBD	TBD	Nanometrics HRD24	Dilat.	Radio

Table 4.3.3: Instrumentation of the HFN as of 06/30/2013. Every HFN downhole package consists of collocated three-component geophones and accelerometers, with the exception of mPBO sites which have only three-component geophones and are also collecting tensor strainmeter data. Six HFN sites (five of the SHFN and one of the NHFN) also have dilatometers (Dilat.). The five SHFN sites have Nanometrics data loggers with radio telemetry to the USGS and eventually from there to the NCEDC for archiving. Currently, six NHFN sites have Quanterra data loggers, eight have been upgraded with ARRA funding and one (CMAB) with Caltrans funding to BASALT data loggers with local storage capacity. Of these 15 sites, 12 are currently telemetering continuous data to the BSL for archiving at the NCEDC. One site (CMSB) is temporarily shutdown due to construction at the Cal Memorial stadium on the UC Berkeley Campus. One site (OHLN) is temporarily down to accommodate landowner construction, and one site (W02B) has been turned off due to equipment failure and cessation of access for maintenance, previously provided by Caltrans. Five additional backbone sites have been decommissioned for reasons ranging from the sites' replacement with nearby higher quality installations (SMCB, CRQB) to irreparable site damage by outside influences such as bridge retrofit activity and construction (BBEB, YBIB, RSRB). Station BBEB, however, continues to operate as a telemetry relay site. The component orientation of the sensors (vertical (Z): -90 → positive counts up; horizontals (H1 and H2): azimuthal direction of positive counts in degrees clockwise from north) are given when known or labeled as "TBD" if they are yet to be determined. VPN stands for Virtual Private Network.

4 Parkfield Borehole Network (HRSN)

Introduction

The operation of the High Resolution Seismic Network (HRSN) at Parkfield, California began in 1987 as part of the United States Geological Survey (USGS) initiative known as the Parkfield Prediction Experiment (PPE) (*Bakun and Lindh, 1985*).

Figure 4.4.1 shows the location of the HRSN, its relationship to the San Andreas fault, several sites of significance from previous and ongoing experiments using the HRSN, the clusters of repeating earthquakes being monitored by the network, the nonvolcanic tremors recorded by the network and located using envelope alignment arrival-times and a migrating grid search location method (*Uhrhammer et al., 2001*) and the epicenters of the 1966 and 2004 M_6 earthquakes that motivated much of the research. The HRSN has recorded exceptionally high-quality data, owing to its 13 closely-spaced three-component borehole sensors (generally emplaced in the extremely low attenuation and background noise environment at 200 to 300 m depth (Table 4.4.2), its high-frequency, wide bandwidth recordings (0–100 Hz; 250 sps), and its sensitivity to very low amplitude seismic signals (e.g., recording signals from micro-earthquakes and non-volcanic tremors with equivalent magnitudes below 0.0 M_L).

Several aspects of the Parkfield region make it ideal for the study of small earthquakes and nonvolcanic tremors and their relationship to tectonic processes and large earthquakes. These include the fact that the network spans the SAFOD (San Andreas Fault Observatory at Depth) experimental zone, the nucleation region of earlier repeating magnitude 6 events, and a significant portion of the transition from locked to creeping behavior on the San Andreas fault; the availability of three-dimensional P and S velocity models (*Michelini and McEvilly, 1991; Thurber et al., 2006*); a long-term HRSN repeating seismicity catalog (complete to very low magnitudes and that includes over half of the M_6 seismic cycle); a well-defined and relatively simple fault segment; the existence of deep nonvolcanic tremor (NVT) activity; and a relatively homogeneous mode of seismic energy release as indicated by the earthquake source mechanisms (over 90% right-lateral strike-slip).

In recent years, these features have also spurred additional investment in seismic instrumentation in the area that greatly enhances the HRSN's utility, including the ongoing installation of the TremorScope array (funded by the Moore Foundation) and the NSF's EarthScope SAFOD and PBO stations.

In a series of journal articles and Ph.D. theses, the cumulative, often unexpected, results of research by UC Berkeley and others using HRSN data trace the evolution of a new and exciting picture of the San Andreas fault zone, and they are forcing new thinking on the dynamic processes and conditions both within the seismogenic (upper ~15 km) and sub-seismogenic depths (~15–35 km), where recently discovered nonvolcanic tremors are occurring.

Parkfield has also become the focus of a major component of

the NSF's EarthScope project known as the San Andreas Fault Observatory at Depth (<http://www.earthscope.org/observatories/safod>). The SAFOD project is a comprehensive effort whose objectives include drilling into the hypocentral zone of repeating ~ M_2 earthquakes on the San Andreas Fault at a depth of about 3 km and establishing a multi-stage geophysical observatory in the immediate proximity of these events. The purpose of such an observatory is to carry out a comprehensive suite of down-hole measurements in order to study the physical and chemical conditions under which earthquakes nucleate and rupture (*Hickman et al., 2004*). In these efforts, the HRSN plays a vital support role by recording seismic data used to directly constrain seismic signals recorded in the SAFOD main hole and by recording seismic events in the surrounding region to provide information on the larger scale fault zone processes that give rise to any changes observed in the main hole.

HRSN Overview

Installation of the HRSN deep (200–300 m) borehole sensors initiated in late 1986, and recording of triggered 500 sps earthquake data began in 1987. The HRSN sensors are three-component geophones in a mutually orthogonal gimbaled package. This ensures that the sensor corresponding to channel DP1 is aligned vertically and that the others are aligned horizontally. The sensors are also cemented permanently in place, ensuring maximum repeatability of the sensors' responses to identical sources, and allowing for precise relative measurements with minimal need for corrections and assumptions associated with moving the sensors. Originally a 10-station network, fully operational by January 1988, the HRSN was expanded to 13 borehole stations in late July 2001, and the original recording systems (see previous Berkeley Seismological Laboratory Annual Reports) were upgraded to 24-bit acquisition (Quanterra 730s) and 56K frame relay telemetry to UCB. As part of funding from the American Recovery and Reinvestment Act (ARRA), an additional replacement/upgrade of the Quanterra 730 acquisition systems to 24-bit BASALT acquisition systems was accomplished in 2010–2011 and allows for local site storage and later retrieval of data during periods of sporadic telemetry failures. Properties of the sensors are summarized in Table 4.4.3.

The three newest borehole stations (CCRB, LCCB, and SCYB) were added, with NSF support, at the northwest end of the network as part of the SAFOD project to improve resolution of the structure, kinematics, and monitoring capabilities in the SAFOD drill-path and target zones. Figure 4.4.1 illustrates the location of the drill site and the new borehole sites, as well as locations of repeating earthquakes and nonvolcanic tremors recorded by the HRSN.

The three new stations have a similar configuration to the original upgraded 10 station network and include an additional channel for electrical signals. Station descriptions and instrument properties are summarized in Tables 4.4.2 and 4.4.3. All the HRSN data loggers employ FIR filters and

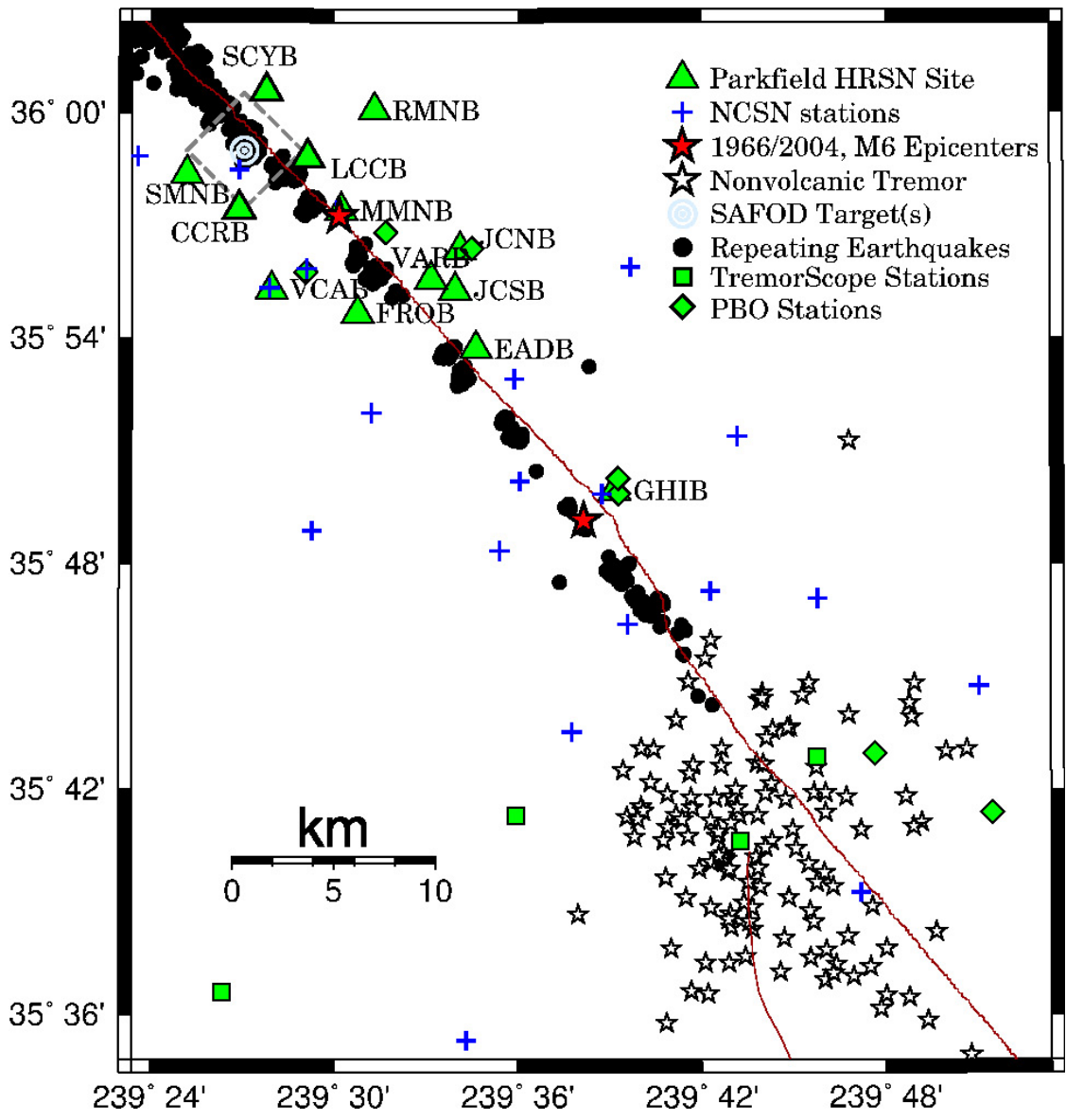


Figure 4.4.1: Map showing the San Andreas Fault trace and locations of the 13 Parkfield HRSN stations, the repeating earthquakes including the 3, ~ M_2 SAFOD targets (a 4 km by 4 km dashed box surrounds the SAFOD target zone), and the epicenters of the 1966 and 2004 M_6 Parkfield mainshocks. Also shown are locations (stars) of nonvolcanic tremors in the Cholame, CA area and routine locations of clusters of repeating earthquakes processed by the integrated HRSN and NCSN networks. Recently installed or planned (Moore Foundation funded) TremorScope and borehole PBO stations (squares and diamonds, respectively) also complement the HRSN borehole coverage and are particularly useful for the study of the tremor. There are an additional five TremorScope stations and one PBO station outside the map bounds.

extract data at 250 Hz (causal) and 20 Hz (acausal) (see Table 4.4.1).

The remoteness of the SAFOD drill site and supporting HRSN stations required an installation of an intermediate data collection point at Gastro Peak, with a microwave link to our CDF (California Department of Forestry) facility. There was also one station, RMNB, that was located on Gastro Peak that transmitted directly to the CDF and served as a repeater for station LCCB. Prior to June 2008, eight of the HRSN sites transmitted either directly to or through repeaters directly to the CDF. This included stations RMNB and LCCB. The other five sites transmitted to a router at Gastro Peak, where the data was aggregated and transmitted to the CDF. However, due to dis-

proportionately increasing landowner fees for access to the Gastro Peak site, we reduced our dependence on it in the summer and fall of 2008 (in cooperation with the USGS) by re-routing telemetry of five of the sites from Gastro Peak to an alternative site at Hogs Canyon (HOGS). This eliminated the Gastro Peak microwave link, but left station RMNB and its repeater for LCCB at the mercy/good-graces of the Gastro Peak landowner. Subsequent negotiations with the landowner stalled and it was decided that RMNB was to be closed. An alternative repeater path for LCCB was also identified and made operational.

Continuous 20 and 250 Hz data from all HRSN channels are recorded and telemetered to the USGS site at Carr Hill for automatic picking and inclusion into Northern California Seismic

System (NCSS) processing. The waveform data are also telemetered over a dedicated T1 circuit to the USGS and the Northern California Earthquake Data Center (NCEDC) at UC Berkeley for archiving and for online access by the community. The HRSN system also generates autonomous station triggers and event associations that are also archived at the NCEDC.

Sensor	Channel	Rate	Mode	FIR
Geophone	DP?	250.0	C	Ca
Geophone	BP?	20.0	C	Ac

Table 4.4.1: Data streams currently being acquired at operational HRSN sites. Sensor type, channel name, sampling rate, sampling mode, and type of FIR filter are given. C indicates continuous; Ac acausal; Ca causal. The “?” indicates orthogonal, vertical, and two horizontal components.

The HRSN’s telemetry system provides remote access to the local site data acquisition systems for state of health monitoring and control, and the recent upgrade to BASALT acquisition systems allows for local storage and retrieval of the data during telemetry outages.

Another feature of the HRSN system that has been particularly useful both for routine maintenance and for pathology identification has been the Internet connectivity of the central site processing computer and the individual stations’ data acquisition systems. Through this connectivity, locally generated warning messages from the central site processor are sent directly to the BSL for evaluation by project personnel. If, upon these evaluations, more detailed information on the HRSN’s performance is required, additional information can also be remotely accessed from the central site processing computer and generally from the individual site data loggers as well. Analysis of this remotely acquired information has been useful for trouble shooting by allowing field personnel to schedule and plan the details of maintenance visits to Parkfield. The connectivity also allows for local site acquisition shutdowns and restarts and for remote implementation of data acquisition parameter changes when needed.

The network connectivity and seamless data flow to UC Berkeley also provide near-real-time monitoring capabilities that are useful for rapid evaluation of significant events as well as the network’s general state of health.

For example, shown in Figure 4.4.2 are surface wave seismograms of the distant region M_w 8.3 earthquake in the Sea of Okhotsk (Lat.: 54.874N; Lon.: 153.281E; depth 609 km) occurring on May 24, 2013 05:44:49 (UTC) recorded on the SP1 (vertical) channels of the 12 HRSN borehole stations in operation at the time. The seismic data from the quake was telemetered to Berkeley and available for analysis by the Northern California Seismic System (NCSS) real-time/automated processing stream within a few seconds of being recorded by the HRSN.

This is also a good signal source for examining the relative responses of the BP borehole network station/components to seismic ground motion. In this case, the vertical channels for 9 of the 12 stations appeared to be working well and with prop-

er polarities. However, vertical channels for JCNB and JCSB show anomalously large noise superposed contaminating the earthquake signal, and it is unclear whether or not MMNB has recorded any signal from the earthquake. Follow-up field investigation of these problems revealed that the JCNB noise is likely the result of greater noise levels from the shallow post-hole depth of sensor installation at this site. The noise problem at JCSB appears to be related to a failed data-logger, and the MMNB problem was caused by thermal cycling of pre-amp components at that site requiring cleaning and reseating of the pre-amp’s circuit boards.

By rapidly generating such plots following large teleseismic events, quick assessment of the HRSN seismometer responses to real events is easily done and corrective measures implemented with relatively little delay.

Data Flow

Initial Processing Scheme

Continuous data streams on all HRSN components are recorded at 20 and 250 sps locally on the BASALT data logger systems and transmitted in near-real-time over the T1 circuit to the USGS at Menlo Park, CA, where they are integrated into the NCSS real-time/automated processing stream. The data are also transmitted to the BSL for archiving at the NCEDC.

This integration of HRSN data into the NCSS data flow has significantly increased the sensitivity of the NCSN catalog at lower magnitudes, effectively doubling the number of small earthquake detections in the Parkfield area and SAFOD zone.

Shortly after being collected and recorded to disk on the central site HRSN computer at the USGS Carr Hill facility, event triggers for the individual stations are determined, and a multi-station trigger association routine then processes the station triggers and generates a list of HRSN-specific potential earthquakes.

For each potential earthquake association, a unique event identification number (compatible with the NCEDC classification scheme) is also assigned. Prior to the San Simeon earthquake of December 22, 2003, 30 second waveform segments were then collected for all stations and components and saved to local disk as an event gather, and event gathers were then periodically telemetered to BSL and included directly into the NCEDC earthquake database (DBMS) for analysis and processing.

Because of its mandate to record very low amplitude seismic signals and microearthquakes in the Parkfield area, the HRSN was designed to operate at very high-gain levels to enhance signal sensitivity. This comes at the expense of dynamic range for the larger events (above $\sim M3.0$). The sensitivity to low amplitude signals is also enhanced by the placement of sensors in the low noise borehole environment (200-300 m depth) and by exhaustive efforts at knocking down extraneous noise sources that arise in each station’s electronics, grounding, power, and telemetry systems and from interference from anthropogenic noise near the stations. As a consequence of the network’s high sensitivity, the HRSN also records numerous outside signals from regional events and relatively distant and small amplitude nonvolcanic tremor events. For example, spot checks of after-

Site	Net	Latitude	Longitude	Surf. (m)	Depth (m)	Date	Location
EADB	BP	35.89525	-120.42286	466	245	01/1987 -	Eade Ranch
FROB	BP	35.91078	-120.48722	509	284	01/1987 -	Froelich Ranch
GHIB	BP	35.83236	-120.34774	400	63	01/1987 -	Gold Hill
JCNB	BP	35.93911	-120.43083	527	224	01/1987 - 02/18/2008	Joaquin Canyon North
JCNB*	BP	35.93911	-120.43083	527	4	07/2011 -	Joaquin Canyon North
JCSB	BP	35.9212	-120.43408	455	155	01/1987 -	Joaquin Canyon South
MMNB	BP	35.95654	-120.49586	698	221	01/1987 -	Middle Mountain
RMNB*	BP	36.00086	-120.47772	1165	73	01/1987 - 07/20/2011	Gastro Peak
SMNB	BP	35.97292	-120.58009	699	282	01/1987 -	Stockdale Mountain
VARB	BP	35.92614	-120.44707	478	572	01/1987 - 08/19/2003	Varian Well
VARB*	BP	35.92614	-120.44707	478	298	08/25/2003 -	Varian Well
VCAB	BP	35.92177	-120.53424	758	200	01/1987 -	Vineyard Canyon
CCRB	BP	35.95718	-120.55158	595	251	05/2001 -	Cholame Creek
LCCB	BP	35.98005	-120.51424	640	252	08/2001 -	Little Cholame Creek
SCYB	BP	36.00938	-120.5366	945	252	08/2001 -	Stone Canyon

Table 4.4.2: Stations of the Parkfield HRSN. Each HRSN station is listed with its station code, network id, location, operation period, and site description. The latitude and longitude (in degrees) are given in the WGS84 reference frame. The surface elevation (in meters) is relative to mean sea level, and the depth to the sensor (in meters) below the surface is also given. Coordinates and station names for the three new SAFOD sites are given at the bottom. Notes, denoted with “*”: There are 2 entries for JCNB, which failed in February of 2008 and has been replaced with a post-hole installation with ARRA funds. There are 2 entries for VARB, whose recording from a deep failed sensor (failure in August, 2003) was changed to a shallower sensor. Recording of data from station RMNB ended in July of 2011, due to landowner issues.

Site	Sensor	Z	H1	H2	RefTek 24	Quanterra 730	BASALT
EADB	Mark Products L22	-90	170	260	01/1987 - 06/1998	03/2001 - 07/2011	07/2011 -
FROB	Mark Products L22	-90	338	248	01/1987 - 06/1998	03/2001 - 11/2010	11/2010 -
GHIB	Mark Products L22	90	failed	unk	01/1987 - 06/1998	03/2001 - 07/2011	07/2011 -
JCNB	Mark Products L22	-90	0	270	01/1987 - 06/1998	03/2001 - 02/2008	-
JCNB*	Oyo GeoSpace GS-20DX	90	0	90	-	-	09/2011 -
JCSB	Geospace HS1	90	300	210	01/1987 - 06/1998	03/2001 - 04/2011	04/2011 -
MMNB	Mark Products L22	-90	175	265	01/1987 - 06/1998	03/2001 - 12/2010	12/2010 -
RMNB*	Mark Products L22	-90	310	40	01/1987 - 06/1998	03/2001 - 07/2011	-
SMNB	Mark Products L22	-90	120	210	01/1987 - 06/1998	03/2001 - 04/2011	04/2011 -
VARB	Litton 1023	90	15	285	01/1987 - 06/1998	03/2001 - 04/2011	-
VARB*	Litton 1023	90	358	88	01/1987 - 06/1998	03/2001 - 04/2011	04/2011 -
VCAB	Mark Products L22	-90	200	290	01/1987 - 06/1998	03/2001 - 04/2011	04/2011 -
CCRB	Mark Products L22	-90	258	348	-	05/2001 - 08/2011	08/2011 -
LCCB	Mark Products L22	-90	50	140	-	08/2001 - 09/2011	09/2011 -
SCYB	Mark Products L22	-90	342	72	-	08/2001 - 08/2011	08/2011 -

Table 4.4.3: Instrumentation of the Parkfield HRSN. Most HRSN sites have L22 sensors and were originally digitized with a RefTek 24 system. The WESCOMP recording system failed in mid-1998, and after an approximate three year hiatus the network was upgraded and recording was replaced with a new 4-channel system. The new system, recording since July 27, 2001, uses a Quanterra 730 4-channel acquisition. Three new stations were also added during the network upgrade period (bottom) In 2010-2011, with ARRA funding, additional replacement/upgrade to 24-bit BASALT acquisition with station-local data storage took place. Notes, denoted with “*”: There are 2 entries for JCNB, which failed in February of 2008 and has replaced with a post-hole installation with ARRA funds. There are 2 entries for VARB, whose recording from a deep failed sensor (failure in August, 2003) was changed to a shallower sensor. Recording of data from station RMNB ended in July of 2011, due to landowner issues.

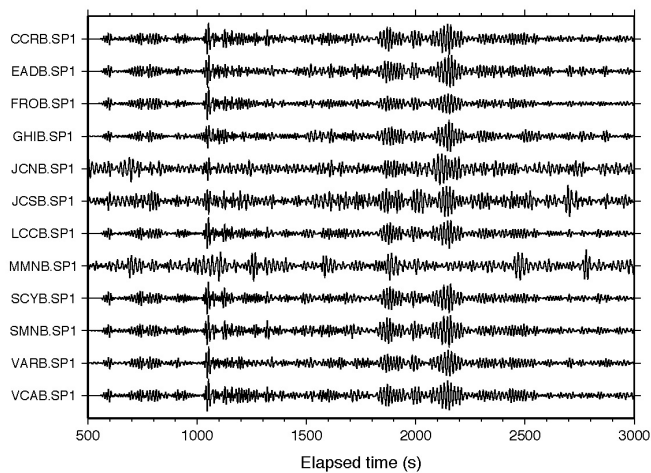


Figure 4.4.2: Plot of surface wave seismograms of the teleseismic M_w 8.3 deep earthquake in the Sea of Okhotsk (Lat.: 54.874N; Lon.: 153.281E; depth 609 km) occurring on May 24, 2013 05:44:49 (UTC) recorded on the SP1 (vertical) channels of the 12 HRSN borehole stations in operation at the time. Station RMNB no longer records data due to landowner issues. Here, vertical component geophone (velocity) data have been 0.05-0.10 Hz bandpass filtered and normalized by the maximum amplitude for each trace.

shocks following the $M6.5$ San Simeon earthquake of December 22, 2003 using continuous data and HRSN event detection listings revealed that the overwhelming majority of HRSN-generated detections following San Simeon resulted from seismic signals generated by San Simeon's aftershocks, despite the HRSN's ~ 50 km distance from the events. Data from the California Integrated Seismic Network (CISN) show that there were $\sim 1,150$ San Simeon aftershocks with magnitudes >1.8 in the week following San Simeon, and during this same period, the number of HRSN event detections was $\sim 10,500$ (compared to an average weekly rate before San Simeon of 115 HRSN detections). This suggests that the HRSN was detecting San Simeon aftershocks well below magnitude 1 at distance of ~ 50 km or more.

Current Processing

Since the beginning of the network's data collection in 1987, and up until 2002, local and regional events were discriminated based on analyst assessment of S-P times, and only local events with S-P times less than ~ 2.5 s at the first arriving station were picked and located as part of the HRSN routine catalog. However, because of the network's extreme sensitivity to the large swarm of aftershocks from the 2003 San Simeon and 2004 Parkfield $M6$ earthquakes (e.g., in the first five months following the San Simeon mainshock, over 70,000 event detections were made by the HRSN system, compared to an average five month detection rate of 2500 prior to San Simeon) and because of ever declining funding levels, analyst review of individual micro-earthquakes was abandoned.

In addition, the dramatic increase in event detections following the San Simeon and Parkfield earthquakes vastly exceeded the HRSN's capacity to process and telemeter both continuous and triggered event waveform data. To prevent the loss of seismic waveform coverage, processing of the triggered waveform

data was discontinued to allow the telemetry and archival of the 20 and 250 sps continuous data to proceed uninterrupted. Subsequent funding limitations have since precluded reactivation of the triggered event processing. Cataloging of associated event triggers from the modified REDI real-time system algorithm continues, however, and both the continuous waveform data and trigger times are telemetered to and archived at the NCEDC, for access by the research community.

Because funding to generate catalogs of local micro-events from the tens of thousands of San Simeon and Parkfield aftershocks was not forthcoming, major changes in our approach to cataloging events had to be implemented. For example, HRSN data flow has now been integrated into the NCSS automated event detection, picking, and catalog processing. In addition, we have implemented a high resolution cross-correlation (pattern matching) based procedure to automatically detect, pick, locate, double-difference relocate, and determine magnitudes for select similar and repeating earthquake families down to very low magnitudes (i.e., below $-0.0M_L$). These new schemes are discussed in more detail in the activities section below.

2012-2013 Activities

In addition to routine operations and maintenance, project activities this year include: a) Further development and implementation of state of health (SOH) monitoring using repeating events; b) routine monitoring of non-volcanic tremor activity in the Parkfield-Cholame area and the implementation of a routinely updated web-page of tremor activity in support of the TremorScope project, and c) supporting and SAFOD activities with the repeating and similar event seismicity catalogs.

Routine Operations and Maintenance

Routine maintenance tasks to keep the HRSN in operation include cleaning and replacing corroded electrical connections; grounding adjustments; cleaning solar panels; testing and replacing failing batteries; ventilating battery and data logger housings to address problems with low power during hot weather, and repairing and realigning repeater sites and antennas.

Remote monitoring of the network's health using the Berkeley Seismological Laboratory's internally developed SeisNet-Watch software is also performed to identify both problems that can be resolved over the Internet (e.g., rebooting of data acquisition systems due to clock lockups) and more serious problems requiring field visits. Over the years, such efforts have paid off handsomely by providing exceptionally low noise recordings of low amplitude seismic signals produced by microearthquakes (below $0.0M_L$) and nonvolcanic tremors.

The network connectivity over the T1 circuit also allows remote monitoring of various measures of the state of health (SOH) of the network in near-real-time using waveforms directly. For example, background noise levels can be rapidly evaluated. We have developed and implemented an automated estimation of the power spectral density (PSD) distributions of background noise for all recorded HRSN channels and have developed summary PSD plots of these estimations to promote rapid evaluation of the noise levels through time.

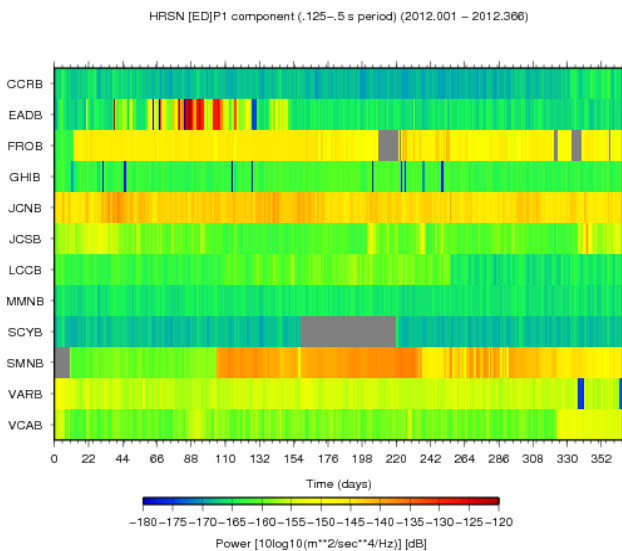


Figure 4.4.3: One-year summary plots of 250 sps vertical component (i.e., DP1 channel) background noise Power Spectral Density (PSD) levels for the 12 operating HRSN borehole stations in the strong tremor frequency band (2 -8 Hz or period 0.125 - 5 s). Year is 2012. The mean PSD (dB) ranking (lowest to highest) at 3 Hz obtained from all available 2012 data on these channels are:

SCYB.BP.DP1 -162.932
 CCRB.BP.DP1 -162.266
 MMNB.BP.DP1 -159.813
 LCCB.BP.DP1 -155.841
 GHIB.BP.DP1 -154.641
 JCSB.BP.DP1 -152.542
 VCAB.BP.DP1 -150.762
 EADB.BP.DP1 -150.390
 VARB.BP.DP1 -149.114
 SMNB.BP.DP1 -143.171
 FROB.BP.DP1 -142.076
 JCNB.BP.DP1 -137.057

Note that station RMNB is now closed due to landowner issues and failed station JCNB (failure in late 2007) has been reopened as a post-hole installation.

Shown in Figure 4.4.3 are power spectral density (PSD) plots of background noise for the 12 vertical HRSN channels in operation during 2012 for the 2-8 Hz frequency band where strong tremor signals are typically recorded. By continuously updating such plots in a variety of bands, we can rapidly evaluate changes in the network's station response to seismic signals across the wide band high-frequency spectrum of the borehole HRSN sensors. Changes in the responses often indicate problems with the power, telemetry, or acquisition systems, or with changing conditions in the vicinity of station installations that are adversely affecting the quality of the recorded seismograms. Once state of health issues are identified with these evaluations further remote tests can be made to more specifically determine possible causes for the problem, and corrective measures can then be planned in advance of field deployment within a relatively short period of time.

SOH using Similar and Repeating Events

New thinking on how to detect and catalog microearthquakes recorded by the HRSN has been prompted by the increased microseismicity (thousands of events) resulting from the San Simeon $M6.5$ (SS) and Parkfield $M6$ (PF) events, the lack of funds available to process and catalog the increased number of microearthquakes, and the increased interest in using the microquakes in repeating earthquake and SAFOD research.

One action taken to help address this problem has been to integrate HRSN data streams into the NCSN event detection and automated cataloging process. This approach has been successful at detecting and locating a significantly greater number of microearthquakes over the previous NCSN detection and location rate (essentially doubling the number of events processed by the NCSN). However, the HRSN-sensitized NCSN catalog is still only catching about half the number of local events previously cataloged by the HRSN using the old, HRSN-centric processing approach. Furthermore, triggered waveforms for the additional small NCSN-processed events are often not reviewed by an analyst, nor do these smaller events generally have NCSN magnitude determinations associated with them.

These limitations can severely hamper research efforts relying on the more numerous similar and characteristically repeating micro-events (e.g., earthquake scaling studies, SAFOD-related research, deep fault slip rate estimation, and the compilation of recurrence interval statistics for time-dependent earthquake forecast models). They also reduce the efficacy of using frequently recurring micro-events as a tool for monitoring the network state-of-health.

To help overcome these limitations, we continued this year to implement our semi-automated similar event cataloging scheme based on pattern matching (match filter) scans using cross-correlation of the continuous HRSN data. The method uses a library of reference event (pattern) waveforms, picks, locations, and magnitudes that have been accurately determined, to automatically detect, pick, locate, and determine magnitudes for events similar to the reference event with a level of accuracy and precision that only relative event analysis can bring.

The similar event detection is also remarkably insensitive to the magnitude of the reference event used, allowing similar micro-events ranging over about 3 magnitude units to be fully cataloged using a single reference event, and it does a remarkably good job at discriminating and fully processing multiple superposed events.

Once a cluster of similar events has been processed, an additional level of resolution can then be achieved through the identification and classification of the subset of characteristically repeating microearthquakes (i.e., near identical earthquakes) occurring within the similar event family (see Figure 4.4.4). The pattern scanning approach also ensures optimal completeness of repeating sequences owing to scans of the matching pattern through "all" available continuous data, which is critical for applications relying on recurrence interval information. For example, only about half of the magnitude 0.26 events shown in Figure 4.4.4 were picked up by the NCSN-HRSN integrated network.

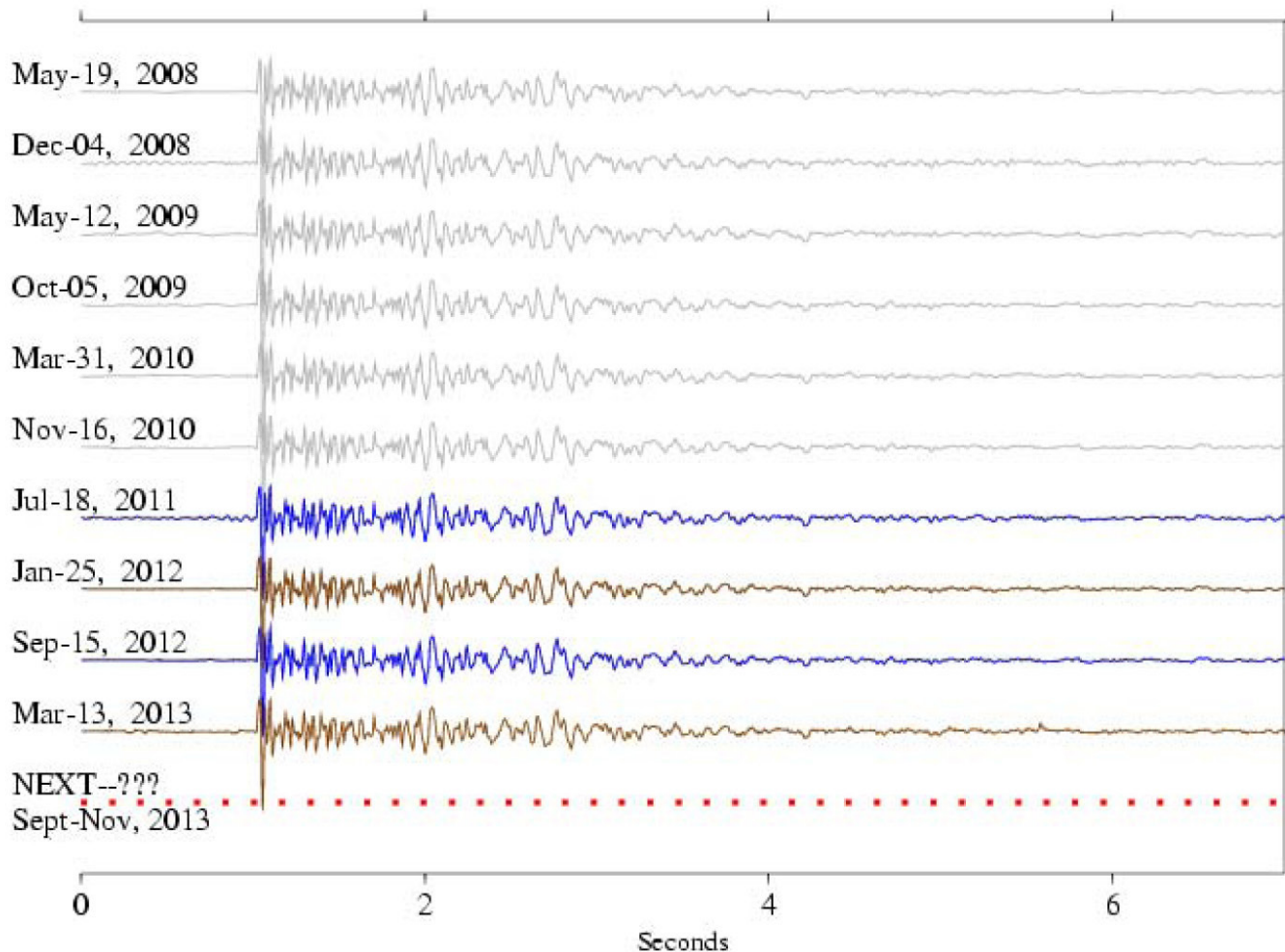


Figure 4.4.4: The ten most recent repeats of a characteristic sequence of repeating magnitude 0.26 (Mp, USGS preferred magnitude) microearthquakes recorded by vertical (DP1) channel of HRSN station VCAB. This sequence has repeated 49 times since the initiation of HRSN recording in 1987. Characteristically repeating micro-events are extremely similar in waveform (typically 0.95 cross-correlation or better). High-precision location and magnitude estimates of these events show they are also nearly collocated (to within 5-10 m) and have essentially the same magnitude (± 0.13 Mp units, among all sequences studied). Immediately following the Parkfield *M*6 mainshock on Sept. 28, 2004, the frequency of repetition was greatly accelerated due to post-seismic loading from the main-shock (e.g., 7 repeats in the 3 months following the mainshock). As time passes, however, the post-seismic effects from the mainshock have gradually diminished, repeating about 2 times a year.

In the BSL annual reports for 2010-2011 and 2011-2012 we noted that the recurrence intervals (i.e., times between events in the repeating sequence) for events in this sequence were on the order of 6 to 8 months. Based on this we predicted in the 2010-2011 report that the next repeat of the sequence would take place sometime in May through July of 2011. The occurrence of the July 18, 2011 event (blue/black) proved our prediction to be correct, and a subsequent repeat on January 25, 2012 (brown/dark-gray) also followed the 6 to 8 month recurrence pattern. Another prediction was made in the following 2011-2012 annual report where we predicted at least one and possibly two additional repeats within the next year, with the next repeat expected in July through September of 2012. These predictions were also fulfilled with the occurrence of the September 15, 2012 (blue/black) and March 13, 2013 (brown/dark-gray) events. The dashed line labeled “NEXT” serves to illustrate our expectation that events in this sequences will continue the repeat pattern. Because the recent recurrence intervals continue to range between about six to eight months, we again predict at least one and possibly two additional repeats within the next year, with the next repeat expected to occur sometime in September through November of 2013.

For network operational purposes, the repeating behavior of this and other sequences in the Parkfield area allows us to use repeating sequences to monitor changes in channel response relative to past performance and to rapidly identify and correct state-of-health issues with real, naturally occurring signals. Making future predictions for such frequently repeating events and testing the prediction using real earthquakes could also be a useful motivating tool for teaching about earthquakes in an educational setting.

Figure 4.4.4 also shows how stable the performance of the borehole VCAB.BP.DP1 channel has remained over the ~4.5 year period shown. Due to station malfunctions or human error during field maintenance, this would not necessarily be the case. Because repeating events can generally be identified using any combination of four of the HRSN's 35 channels, assessment of the channel responses for channels not in the 4 channel combination can be carried out. This can be carried out repeatedly through time as additional repeats are identified with time resolutions depending on the number of repeating sequences used and the frequency of their repeats. Repeating sequences of this magnitude typically repeat every 1 to 2 years, and we are in the process of expanding our similar event monitoring capability to 61 of these sequences. Hence, on average, evaluations of this type can be possible approximately every 10 days on an automated basis. However, there are on the order of 200 such sequences known in the Parkfield area, and if one is willing to include even more frequently occurring similar but non-identical events into the equation, near-daily automated SOH analyses are a possibility.

Armed with this type of information, technicians and field engineers can quickly identify and address major problems. In addition to a visual assessment, the high similarity of the events lends itself to the application of differencing techniques in the time and frequency domains to automatically identify even subtle SOH issues. For other networks recording continuously in the Parkfield area (e.g., NCSN, BDSN) it is also a relatively simple process to extend the SOH analysis using characteristic repeating event signals recorded at their stations (See the BDSN station RAMR example in Figure 4.4.5 of last year's (2011-2012) annual report). Furthermore, numerous repeating and similar event sequences are also known to exist in the San Francisco Bay, San Juan Bautista and Mendocino Triple Junction areas, where continuous recording takes place. Hence, application of the repeating event SOH technique to these zones should also be feasible.

This year we have finished adapting our cataloging codes to take advantage of faster computing now available on LINUX based machines. We have expanded the library of reference event patterns and retroactively scanned these patterns through previously recorded and ongoing data to capture and catalog an ever growing body of similar and repeating earthquakes for research purposes, in support of SAFOD, and for SOH monitoring (including the use of repeaters to identify and correct problems associated with the recently activated TremorScope stations). We have also continued to revise and automate our SOH waveform displays for rapid evaluation of HRSN performance based on repeater waveforms and have begun development of additional automated processing and display schemes to include visualization of spectral characteristics to the repeating event SOH analyses.

Tremor Monitoring and TremorScope

The HRSN played an essential role in the initial discovery of nonvolcanic tremors (NVT) and associated Low Frequency Events (LFE) along the San Andreas Fault (SAF) below Cholame, CA (Nadeau and Dolenc, 2005; Shelly et al., 2009), and

continues to play a vital role in ongoing NVT and LFE research. The Cholame tremors occupy a critical location between the smaller Parkfield (~M6) rupture zone and the adjacent and much larger Ft. Tejon (~M8) rupture zone along the SAF to the southeast (Figure 4.4.1). Because the time-varying nature of tremor activity is believed to reflect time-varying deep deformation and presumably episodes of accelerated stressing of faults (Guilhem and Nadeau, 2012), and because anomalous changes in Cholame area NVT activity preceded the 2004 Parkfield M6 earthquake (Nadeau and Guilhem, 2009; Shelly, 2009), and because tremor activity appears to be an ongoing process in the area (Guilhem and Nadeau, 2012) we are continuing to monitor the tremor activity observable by the HRSN to look for additional anomalous behavior that may signal an increased likelihood of another large SAF event in the region.

To date, over 3300 NVT bursts have been identified and cataloged, and regular updates of the NVT catalog continue on a ~biweekly basis. Over the last year we have also developed and posted a website where a map and section of recent 90-day tremor activity can be viewed and a complete list of detected Parkfield-Cholame area tremor starting in July of 2001 can be downloaded by researchers and the public (http://seismo.berkeley.edu/research/recent_tremor.html).

Efforts in Support of SAFOD

An intensive and ongoing effort is underway to drill through, sample, and monitor the active San Andreas Fault at seismogenic depths and in very close proximity (within a few tens of kilometers or less) to a repeating magnitude 2 earthquake site. The HRSN data plays a key role in these efforts by providing azimuthal coverage of low noise and high sensitivity seismic waveforms from active and passive sources in the SAFOD region, by providing a backbone catalog of very small similar and repeating earthquakes detections, and by recording and archiving continuous waveform data.

As of early September 2007, SAFOD drilling had penetrated the fault near the Hawaii (HI) repeating target sequence and collected core samples in the fault region that presumably creeps and surrounds the repeatedly rupturing HI patch. Unfortunately, due to complications during drilling, penetration and sampling of the fault patch involved in repeating rupture was not possible, though core sampling and installation of seismic instrumentation in the region adjacent to the repeating patch was achieved. Current efforts are focused on analysis of collected core samples and long-term monitoring of the ongoing chemical, physical, seismological, and deformational properties in the zone (in particular any signals associated with subsequent repeats of the SAFOD target sequences).

HRSN activities this year have contributed in three principal ways to these and longer-term SAFOD monitoring efforts:

- 1) Processing of integrated HRSN and USGS data streams in the Parkfield area continues, effectively doubling the number of small events available for monitoring seismicity in the SAFOD target zone and for constraining relative locations of the ongoing seismic activity.

- 2) Telemetry of all HRSN channels (both 20 and 250 sps data streams) continues to flow directly from Parkfield, through the

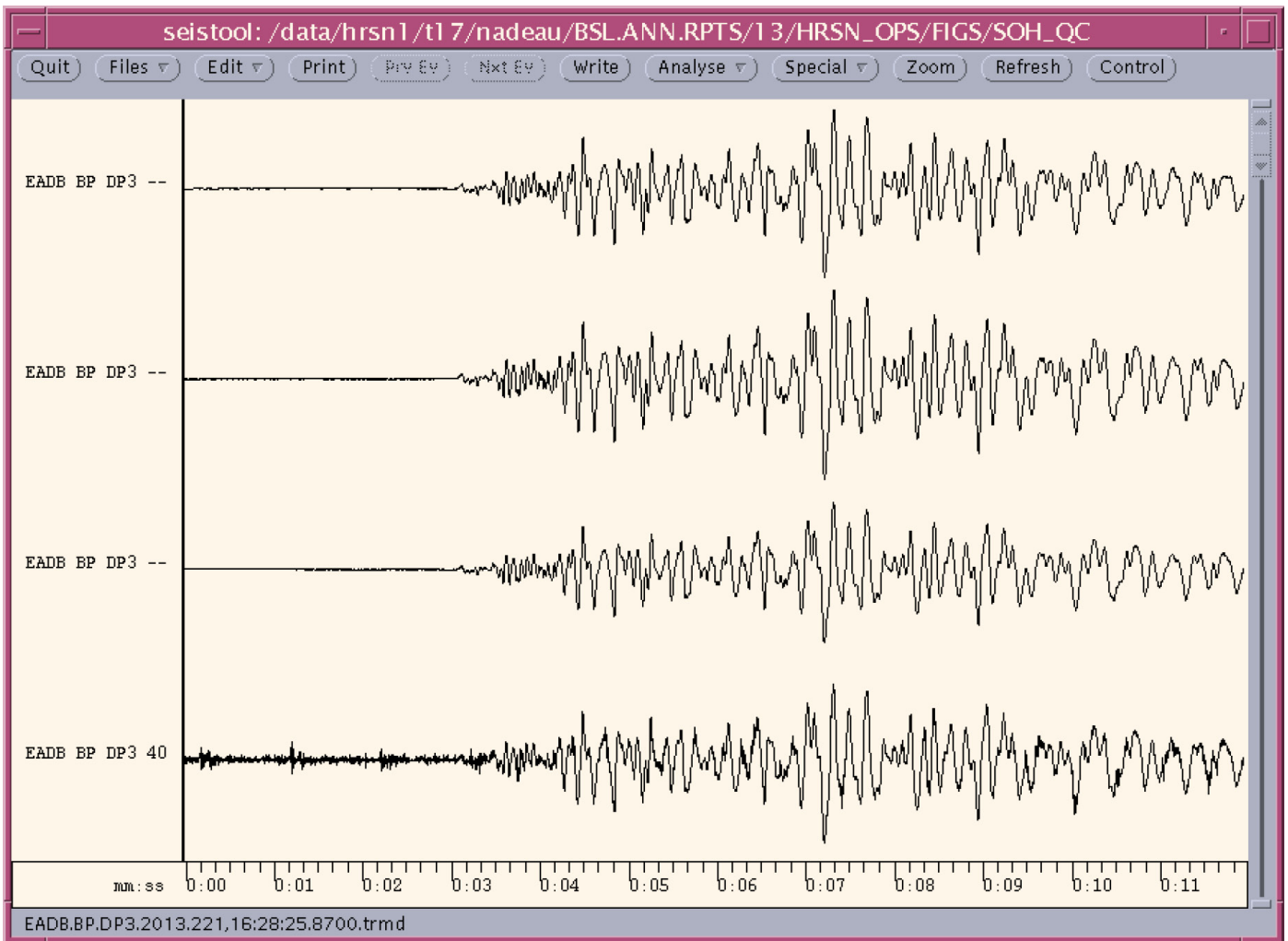


Figure 4.4.5: Repeating earthquake data illustrating their utility for identifying problematic channel responses. Here a repeat of EarthScope's SAFOD SF sequence ($\sim M2.1$) occurring on August 9, 2013 was identified using HRSN stations. The event and its previous repeats was used to evaluate the performance of stations from the HRSN and other networks out to distances greater than 50 km from the HRSN. Shown are the last four SF sequence events recorded on the DP3 horizontal channel of Berkeley's HRSN station EADB with no filtering. EADB is 16 km from the repeating events. From top to bottom, the events occurred on 11/02/2006, 12/20/2008, 11/23/2010, 05/30/2007, and 08/09/2013, respectively. Waveforms for the first three events are well recorded and consistent, indicating healthy station response. However, for the most recent event a significant degradation in response is seen. Signal from the 2013 event is contaminated with spiking about every second (indicative of solar charger issues) and a background noise buzz with an \sim white spectrum is superposed on the earthquake signal. Corrective action taken was to ensure proper grounding of the electronic components at the installation and to replace the datalogger.

USGS Parkfield T1 and the Northern California Earthquake Management Center (NCEMC) T1, to the USGS and the BSL for near-real-time processing, catalog processing, and data archiving at the Web-accessible NCEDC portal. This also provides near-real-time access to the HRSN data for the SAFOD community, without the week, or month long delay associated with the previous procedure of having to transport DLT tapes to Berkeley to upload and quality check the data.

3) Continued monitoring and expansion of our repeating (characteristic and similar event sequences) earthquake catalog, with particular focus on expansion and refinement of repeating event data within the 1.5 cubic km volume centered on the SAFOD target zone. Last year, we expanded the number of repeating sequence reference patterns in this zone from 3 to 18 and cataloged (detected, double difference relocated, and determined magnitudes for) this year we have expanded the

number of earthquakes within this small volume to nearly 1300 micro-quakes. The pattern matching approach to detection is prone to identifying the same event from more than one reference earthquake, so a procedure was also developed to remove redundant events from the over-all catalog. A procedure was also developed to integrate arrival time information from the redundant pattern matches to improve connectivity of events from different similar event sequences in the double-difference relocations. Continued monitoring of the 18 sequence in the immediate SAFOD zone this year has led to the identification of the next repeats of the SAFOD SF and LA sequences which both occurred on August 9, 2013. The apparent triggering within less than a day of the repeat of the LA sequence by the repeat of the SF sequence reflects the first evidence of a return of this triggering relationship since its disruption at the time of the 2004 Parkfield $M6$ mainshock.

Figure 4.4.5 shows recordings of the horizontal (DP3) channel from HRSN station EADB for the most recent (bottom) and three previous repeats of the SAFOD SF sequence. While the repeated nature of these events is apparent, it is clear that the quality of the recording of the most recent event is below standard, and actions have been taken to rectify the problem. Waveforms recorded on most other HRSN channels do not show the high frequency lower amplitude buzz and spiking apparent on the EADB DP3 channel. While degradation of the signal is apparent visually, such degradation is not generally apparent from automated quality control checks of station performance. This illustrates, then, the additional benefit of visual inspection and comparison of repeating events in SOH evaluations.

Acknowledgments

Under Peggy Hellweg's and Robert Nadeau's general supervision, Doug Neuhauser, Taka'aki Taira, and the engineering team (Joshua Miller, Sarah Snyder and John Friday) all contribute to the operation of the HRSN. Robert Nadeau prepared this section with help from Taka'aki Taira. During this reporting period, operation, maintenance, and data processing for the HRSN project was supported by the USGS, through grant G10AC00093.

References

- Bakun, W. H., and A. G. Lindh, The Parkfield, California, prediction experiment, *Earthq. Predict. Res.*, 3, 285-304, 1985.
- Guilhem, A. and R.M. Nadeau, Episodic tremors and deep slow-slip events in Central California, *Earth Planet. Sci. Lett.*, 357-358, 1-10, doi:10.1016/j.epsl.2012.09.028 2012.
- Hickman, S., M.D. Zoback and W. Ellsworth, Introduction to special section: Preparing for the San Andreas Fault Observatory at Depth, *Geophys. Res. Lett.*, 31, L12S01, doi:10.1029/2004GL020688, 2004.
- Michelini, A. and T.V. McEvelly, Seismological studies at Parkfield: I. Simultaneous inversion for velocity structure and hypocenters using B-splines parameterization, *Bull. Seismol. Soc. Am.*, 81, 524-552, 1991.
- Nadeau, R.M. and A. Guilhem, Nonvolcanic tremor evolution and the San Simeon and Parkfield, California earthquakes, *Science*, 325, 191-193, doi:10.1126/science.1174155, 2009.
- Nadeau, R.M. and D. Dolenc, Nonvolcanic Tremors Deep Beneath the San Andreas Fault, *Science*, 307, 389, 2005.
- Shelly, D.R., Possible deep fault slip preceding the 2004 Parkfield earthquake, inferred from detailed observations of tectonic tremor, *Geophys. Res. Lett.*, 36, L17318, doi:10.1029/2009GL039589, 2009.
- Shelly, D.R., W.L. Ellsworth, T. Ryberg, C. Haberland, G.S. Fuis, J. Murphy, R.M. Nadeau and R. Bürgmann, Precise location of San Andreas Fault Tremors near Cholame, California using seismometer clusters: Slip on the deep extension of the fault?, *Geophys. Res. Lett.*, 36, L01303, doi:10.1029/2008GL036367, 2009.
- Thurber, C., H. Zhang, F. Waldhauser, J. Hardebeck and A. Michael, Three-dimensional compressional wavespeed model, earthquake relocations, and focal mechanisms for the Parkfield, California region, *Bull. Seismol. Soc. Am.*, 96, S38-S49, doi:10.1785/0120050825, 2006.
- Uhrhammer, R.A., D. Dreger, and B. Romanowicz, Best Practice in Earthquake Location Using Broadband Three-component Seismic Waveform Data, *Pure and Applied Geophys.*, 158, 259-276, 2001.
- Zhang, H., R.M. Nadeau, R.N. Toksoz, C.H. Thurber and M. Fehler, Nonvolcanic Tremors in Localized Low Shear Wave Velocity Zones Beneath the San Andreas Fault, *J. Geophys. Res.*, (in revision), 2012.

5 Bay Area Regional Deformation Network

Introduction

The Bay Area Regional Deformation (BARD) network is a collection of permanent, continuously operating GPS receivers that monitor crustal deformation in the San Francisco Bay Area (SFBA) and Northern California. Started in 1991 with two stations spanning the Hayward Fault, BARD has been a collaborative effort of the Berkeley Seismological Laboratory (BSL), the USGS at Menlo Park (USGS/MP), and several other academic, commercial, and governmental institutions. The BARD network is designed to study the distribution of deformation in Northern California across the Pacific-North America plate boundary and interseismic strain accumulation along the San Andreas fault system in the Bay Area for seismic hazard assessment, and to monitor hazardous faults and volcanoes for emergency response management. It also provides data in real time for use in Earthquake Early Warning (EEW) and rapid response applications. The BSL maintains and/or has direct continuous telemetry from 31 stations comprising the BARD Backbone, while additional stations operated by the USGS, US Coast Guard and others fill out the extended BARD network.

Since the completion of major construction on the Plate Boundary Observatory (PBO) portion of EarthScope in 2004,

the number of GPS stations in Northern California has expanded to over 250 (Figure 4.5.1). Together, PBO and BARD stations provide valuable information on the spatial complexity of deformation in the SFBA and Northern California, while the BARD network has the infrastructure and flexibility to additionally provide information on its temporal complexity over a wide range of time scales as well as in real-time. All BARD Backbone stations collect data at 1 Hz sampling frequency and stream their data in real time to the BSL, and in turn is provided in real time to the public. Furthermore, seventeen BARD Backbone sites are collocated with broadband seismic stations of the BDSN, with which they share continuous telemetry to UC Berkeley. As geodetic and seismic data become more closely integrated, these collocated stations are already available to provide combined data products.

Station configuration

The BARD networks include two models of receiver: Trimble NetRS and Topcon Net-G3A. All BARD stations use a radome-equipped, low-multipath choke-ring antenna, designed to provide security and protection from weather and other natural phenomena, and to minimize differential radio prop-

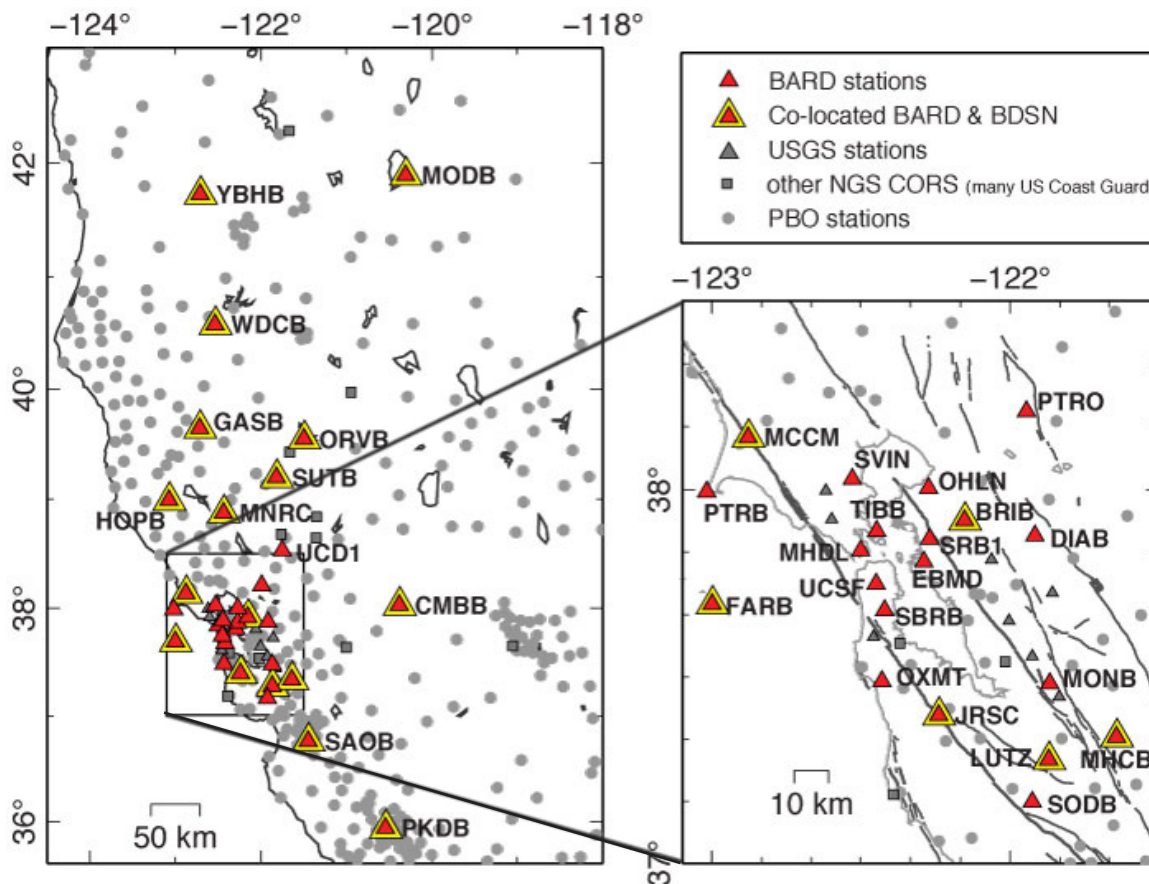


Figure 4.5.1: Map of the BARD Backbone network and surrounding PBO sites in Northern California. The right figure is an enlarged view of the box on the left figure.

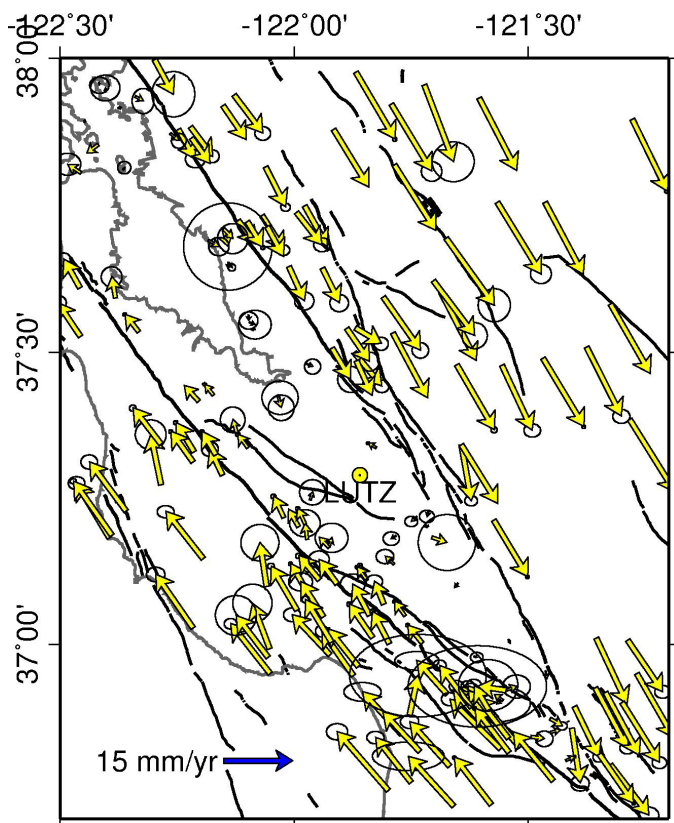


Figure 4.5.2: Velocities from BAVU3 β , including BARD stations, as well as campaign, and PBO stations. Yearly velocities are relative to station LUTZ, marked by a yellow circle.

agation delays. A low-loss antenna cable is used to minimize signal degradation on the longer cable setups that normally would require signal amplification. Low-voltage cutoff devices are installed to improve receiver performance following power outages.

All BARD stations are continuously telemetered to the BSL. Many use frame relay technology, either alone or in combination with radio telemetry. Other methods include direct radio link to Berkeley and satellite telemetry. At MODB, MCCM, and MNRC we are able to telemeter 1 Hz data using the USGS VSAT system that collects seismic broadband data as part of the National Seismic Network (NSN). We have also changed our data strategy by allowing some data to be transferred by web-based telemetry (ADSL lines). This will reduce our communication operational costs and, we hope, will not affect our ability to react to a large event.

BARD station monumentations broadly fall into three types. Most are anchored into bedrock, either directly or via a steel-reinforced concrete cylinder. The five “mini-PBO” (mPBO) stations that are still operated by the BSL are collocated with USGS strainmeters, and their GPS antennas are bolted onto the borehole casing using an experimental mount developed at the BSL, which has since been adopted by PBO for their strainmeter sites. Four sites (UCD1, SRB1, UCSF, SBRB) are located on the roofs of buildings. Most of the last type have been installed in the past four years, and their stability over long periods of time is yet to be evaluated. Six stations installed under the American

Recovery and Reinvestment Act (ARRA) have PBO style short-brace monuments cemented into bedrock.

Data handling

Archival

Raw and RINEX data files from the 31 BARD Backbone stations and several other stations run by BARD collaborators, such as the USGS and LBNL, are archived at the Northern California Earthquake Data Center (NCEDC). The data are checked to verify their integrity, quality, completeness, and conformance to the RINEX standard, and are then made accessible, usually within 1 hour of the end of the UTC day, to all participants and other members of the GPS community through the Internet, both by anonymous FTP and through the World Wide Web (<http://ncedc.org/>). BARD data are also available to the community through the GPS Seamless Archive Centers (GSAC), such as that hosted by the Scripps Orbit and Permanent Array Center (SOPAC, <http://gsac.ucsd.edu>). High-rate raw data are also decimated to create 15 s RINEX data files. 1 Hz RINEX files are available for all BARD Backbone sites after May 2010.

As part of the activities funded by the USGS through the BARD network, the NCEDC has established an archive of the 10,000+ survey-mode occupations collected by the USGS since 1992 and the NCEDC is the principal archive for this dataset. These and other survey-mode data are used together with data from BARD and PBO stations to produce BAVU (Bay Area Velocity Unification), a united set of continuous and survey data from the wider San Francisco Bay Area, processed under identical conditions using GAMIT (*d'Alessio et al., 2005*).

Data from five of our sites (HOPB, MCHB, CMBB, OHLN, and YBHB) are sent to the National Geodetic Survey (NGS) in the framework of the CORS (Continuous Operating Reference Stations) project (<http://www.ngs.noaa.gov/CORS/>). The data from these five sites are also distributed to the public through the CORS FTP site.

Real-time streaming

All BARD stations are currently available in real time with 1 Hz data sampling; a step toward our goal of integrating GPS with the Northern California Seismic System (NCSS) for use in hazard assessment and emergency response and for Earthquake Early Warning applications. Data streams are received from the stations in BINEX format. They are received at the BSL and converted into RTCM using Sharc software package (maintained by USGS, Pasadena). Both the original BINEX and RTCM streams are then made available to the public from an Ntrip-caster operated by the BSL (<http://seismo.berkeley.edu/bard/realtime>). The BSL also acts as a conduit for real-time streams for seven continuous GPS stations operated by the USGS, Menlo Park and five stations installed by the Lawrence Berkeley National Lab (LBNL), in order to make those data easily accessible to the GPS community.

Site	Lat. (deg)	Lon. (deg)	Receiver	Telem.	Samp. Rate	Colloc. Net.	Location
BRIB	37.92	-122.15	NETRS	FR	1 Hz	BDSN	Briones Reservation, Contra Costa County
CMBB	38.03	-120.39	NET-G3A	FR	1 Hz	BDSN	Columbia College, Tuolumne County
DIAB	37.88	-121.92	NETRS	FR	1 Hz		Mt. Diablo , Contra Costa County
EBMD	37.82	-122.28	LEICA	R	1 Hz		East Bay MUD Headquarters, Alameda County
FARB	37.70	-123.00	NETRS	R-FR	1 Hz	BDSN	Farallon Island , San Francisco County
GASB	39.65	-122.72	NET-G3A	R-FR	1 Hz	BDSN	Alder Springs, Glenn County
HOPB	39.00	-123.07	NET-G3A	R-FR	1 Hz	BDSN	Hopland Field Station, Mendocino County
JRSC	37.41	-122.23	NET-G3A	Int	1 Hz	BDSN	Jasper Ridge Biol. Preserve, San Mateo County
LUTZ	37.29	-121.87	NET-G3A	FR	1 Hz	BDSN	SCC Communications , Santa Clara County
MCCM	38.14	-122.88	NET-G3A	VSAT	1 Hz	BDSN	Marconi Conference Center, Marin County
MHCB	37.34	-121.64	NETRS	FR	1 Hz	BDSN	Lick Observatory, Santa Clara County
MHDL	37.84	-122.49	NETRS	R-FR	1 Hz	mPBO	Marin Headlands, Marin County
MNRC	38.88	-122.44	NET-G3A	VSAT	1 Hz	BDSN	McLaughlin Mine, Lake County
MODB	41.90	-120.30	NETRS	VSAT	1 Hz	BDSN	Modoc Plateau , Modoc County
MONB	37.50	-121.87	NET-G3A	FR	1 Hz		Monument Peak, Santa Clara County
OHLN	38.01	-122.27	NET-G3A	FR	1 Hz	mPBO	Ohlone Park, Contra Costa County
ORVB	39.55	-121.50	NET-G3A	FR	1 Hz	BDSN	Oroville , Butte County
OXMT	37.50	-122.42	NET-G3A	FR	1 Hz	mPBO	Ox Mountain , San Mateo County
PKDB	35.95	-120.54	NETRS	R-T1	1 Hz	BDSN	Bear Valley Ranch, Monterey County
PTRB	38.00	-123.01	NETRS	R-FR	1 Hz		Point Reyes Lighthouse , Marin County
PTRO	38.21	-121.94	NET-G3A	FR	1 Hz	BDSN	Potrero Hills, Solano County
SAOB	36.77	-121.45	NETRS	FR	1 Hz	BDSN	San Andreas Observatory, San Benito County
SBRB	37.69	-122.41	NET-G3A	FR	1 Hz	mPBO	San Bruno Replacement, San Mateo County
SODB	37.17	-121.93	NET-G3A	R-FR	1 Hz		Soda Springs, Santa Clara County
SRB1	37.87	-122.27	NET-G3A	Fiber	1 Hz		Seismic Replacement Building, Alameda County
SUTB	39.21	-121.82	NETRS	R-FR	1 Hz	BDSN	Sutter Buttes , Sutter County
SVIN	38.03	-122.53	NET-G3A	R-FR	1 Hz	mPBO	St Vincents , Marin County
TIBB	37.89	-122.45	NET-G3A	R-Int	1 Hz		Tiburon , Marin County
UCD1	38.54	-121.75	NETRS	Int	1 Hz		UC Davis , Yolo County (operated by UC Davis)
UCSF	37.76	-122.46	NET-G3A	FR	1 Hz		UC San Francisco , San Francisco County
WDCB	40.58	-122.54	NET-G3A	FR	1 Hz	BDSN	Whiskeytown Dam, Shasta County
YBHB	41.73	-122.71	NETRS	FR	1 Hz	BDSN	Yreka Blue Horn Mine, Siskiyou County

Table 4.5.1: List of BARD stations maintained by the BSL. The receivers operating now are: Trimble NETRS, (NETRS) and Topcon Net-G3A (Net-G3A). Site EBMD, operated by the East Bay Municipal Utility District, has a Leica GX1230 receiver and Leica AR10 antenna. The telemetry types listed are FR = Frame Relay, R = Radio, Int = Internet, VSAT = Satellite, T1 = Private T1 line. mPBO are the remaining “mini-PBO” sites operated by the BSL. Telemetry often includes a radio hop from the GPS site to the seismic vault, indicated by an initial R. All (except EBMD) are equipped with Ashtech or Topcon choke ring antennas.

Interseismic Velocities and Daily Time Series

Average station coordinates are estimated from 24 hours of observations for BARD stations and other nearby continuous GPS sites using the GAMIT/GLOBK software developed at MIT and SIO (Herring *et al.*, 2010a & b). GAMIT uses double-difference phase observations to determine baseline distances and orientations between ground-based GPS receivers. Ambiguities are fixed using the widelane combination followed by the narrowlane, with the final position based on the ionospheric free linear combination (LC). Baseline solutions are loosely constrained until they are combined together. GAMIT produces solutions as “H-files”, which include the covariance parameters describing the geometry of the network for a given day and summarize information about the sites. We combine daily, ambiguity-fixed, loosely constrained H-files using the Kalman filter approach implemented by GLOBK (Herring, 2010b). They are combined with solutions from the IGS global network and PBO and stabilized in an ITRF2005 reference frame. The estimated relative baseline determinations typically

have 2-4 mm long-term scatter in the horizontal components and 10-20 mm scatter in the vertical.

BARD data are an important component of the Bay Area Velocity Unification (BAVU) project (*d’Alessio et al.*, 2005). BAVU contains all available campaign data in Northern California and processes them in a consistent manner to produce a comprehensive and high-density velocity map. It relies on a network of CGPS stations to provide a framework on which these data can be combined. With data going back to 1992, BARD stations can provide such a framework (Figure 4.5.2). Average linear velocities for each station are estimated from monthly combinations of the campaign, BARD, PBO and IGS solutions and are shown in Figure 4.5.2.

Time series of station positions are produced with daily, automated updates. BARD data are processed within 24 hours using IGS rapid orbit information and the time series are updated immediately. When rapid PBO and IGS global station solutions become available (usually within 2-3 days), they are combined with the rapid BARD solutions using GLOBK and the time se-

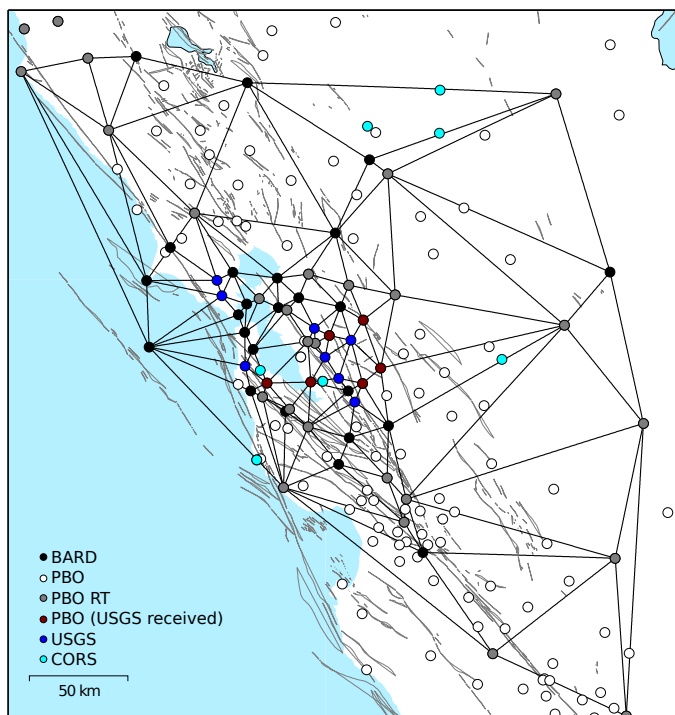


Figure 4.5.3: Map showing triangulated real-time processing network. Each black line represents an independent processing instance of trackRT.

ries is again updated. Final processing with both GAMIT and GLOBK occurs when IGS final orbits and final PBO solutions become available (1-2 weeks); the time series is then updated for the last time with the final positions.

After each update, the time series are cleaned by removing outliers and common mode noise. Common mode noise is estimated by stacking the difference between observations and modeled motion for all stations. The model is derived from *a priori* values for station velocity, coseismic offsets and post-seismic decay. The cleaned data is then used to re-estimate the *a priori* model parameters in an iterative process. Outliers are identified as points whose misfit to a linear trend is greater than 4σ on any single component of motion (North, East, or Up). Overall time series scatter is low; with average RMS values across the BARD network of 1.8 mm, 2.9 mm, and 5.8 mm for the North, East and Up directions respectively. Plots of station time series are posted daily on the BARD website (<http://seismo.berkeley.edu/bard/timeseries>).

Earthquake Early Warning

With support from the Gordon and Betty Moore Foundation, we have been working on integrating information from GPS into Earthquake Early Warning (EEW) algorithms in a module we call G-larms. Our goals for this project include establishing a robust system for processing GPS data streams into displacement time series and designing and implementing methods to use these results to supplement seismic Earthquake Early Warning systems during large earthquakes. More details on G-larms are available in Research Sections 2.32 and 2.33.

The BSL is now using data from 62 GPS stations in the greater

San Francisco Bay Area to generate real-time position estimates on a routine basis. This includes 26 stations that are operated by the BSL and 8 that are operated by the USGS, Menlo Park. We also process 29 stations operated by the Plate Boundary Observatory (PBO), who collect real-time data for a subset of their stations and make these available to the public.

Additionally, we use trackRT, together with predicted orbits from the International GPS service (IGS) to produce high sample rate displacement time series with 2-3 second latency. TrackRT was developed at MIT and is based on GAMIT/GLOBK, which we use for daily processing. TrackRT follows a network processing approach, with displacements generated with respect to a reference station. The benefits of this approach are that common noise sources, such as local atmosphere, are canceled out, leading to more precise relative displacements.

We employ a fully triangulated network scheme in which neighboring station pairs are processed individually, such that no station serves as the universal reference site (Figure 4.5.3). This makes our network resilient against an outage or telemetry loss at any individual station. The low processing overhead of trackRT makes it possible for us to run separate instances of the program to produce displacement time series for all ~160 baselines in our network.

The scatter in the displacement time series for each baseline depends on distance and increases during days with changeable weather conditions. However, it is often within 2 cm over the course of 24 hours, which is considered a stable result. Simulations of a $M6.9$ Hayward fault earthquake show that relative motions of over 20 cm would be expected between many of the station pairs near the fault and would be easily resolved by well-behaved data (see Research Section 2.33).

Earthquake Rapid Response

While real-time processing of GPS data is capable of providing measurements of displacement within seconds of its occurrence, post-processing provides results with lower noise levels, leading to better precision. We have developed a strategy to use real-time GPS data access with rapid post-processing (RPP) techniques to estimate static offsets from moderate to large earthquakes and use them to constrain a non-linear search for fault plane parameters. Rapid post-processing requires waiting 1-2 minutes after the earthquake for data to accumulate, but displacement time series can then be generated within 5 minutes using the software Track, developed at MIT. From these, full fault plane determination can be performed within another 5 minutes. While real-time processing techniques are critical for using GPS data for Earthquake Early Warning, rapid post-processing provides higher precision in the static offset measurement. This allows GPS data to be used for smaller earthquakes and still finishes within a time frame appropriate for ShakeMap.

Using data from the 2007 $M5.6$ Alum Rock and 2004 $M6.0$ Parkfield earthquakes, we find that RPP with Track allows more robust static offset determination from these smaller earthquakes than real-time processing (as it exists today). For both earthquakes, sub-cm offsets can be resolved and match post-event analyses well. We perform our search for the best-fitting

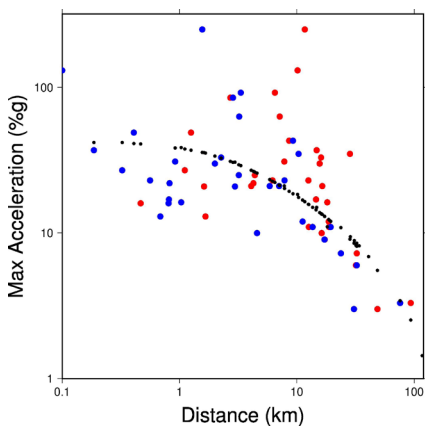
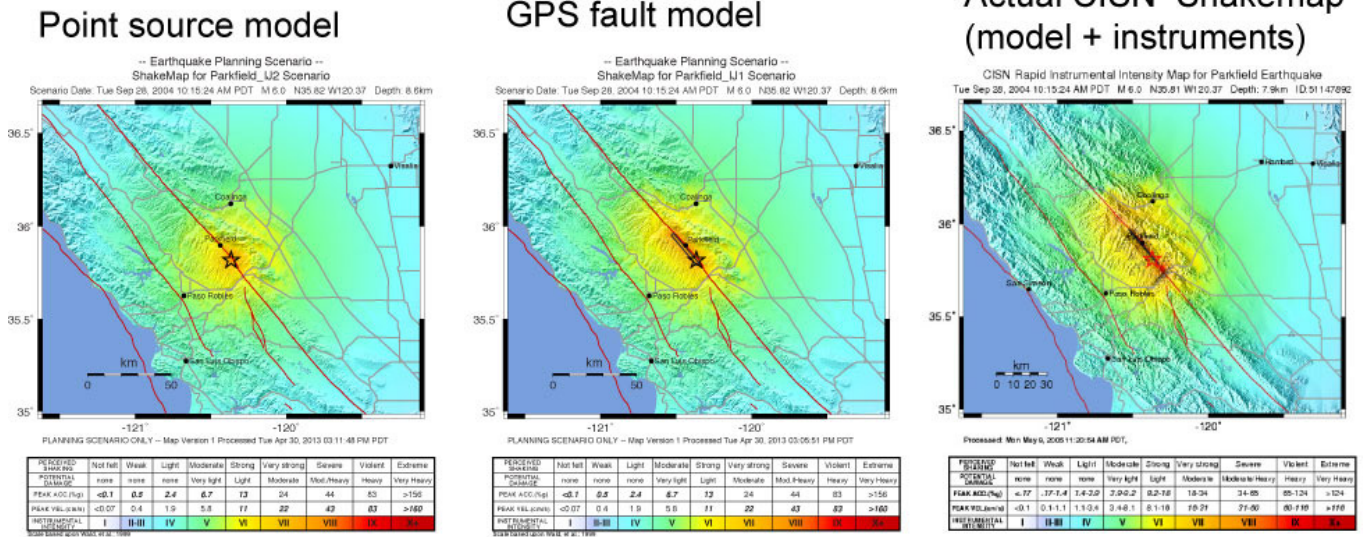


Figure 4.5.4 (Above): Three ShakeMaps for the 2004 Parkfield earthquake. The left and middle ShakeMaps are scenarios that contain only information from a distance/attenuation model. The right-most figure is the official CISM ShakeMap using both a model and instrumental data. Distance in the left-most figure is calculated to the earthquake epicenter only; in the middle plot, it is the closest distance to the fault plane.

Figure 4.5.5 (At left): Distance vs. maximum acceleration for stations given the point source (red points) and the finite fault (blue points). The black points show the modeled relationship. The difference between the red and blue points is in how the distance from the station to the earthquake is calculated.

fault plane parameters using no *a priori* information. That is, we attempt to simulate a situation where the type and location of faulting for these earthquakes is not known. While low station density makes this difficult for the $M_{5.6}$ Alum Rock earthquake, the fault plane for the $M_{6.0}$ Parkfield earthquake can be quickly and robustly determined. We therefore expect this strategy to be successful for earthquakes of at least $M_{6.0}$ and could be used for smaller events in areas with good station coverage.

Figure 4.5.4 shows how including the fault plane affects the ShakeMap calculations for the Parkfield earthquake; including the RPP determined plane produces a ShakeMap that matches the final CISM ShakeMap well. However, while the finite plane used for the official ShakeMap matches the GPS determined plane, it was determined manually based on the aftershock distribution. As such, it was several hours before this information was incorporated into the ShakeMap. By contrast the same information can be obtained from GPS within 15 minutes.

Acknowledgements

The BARD program is overseen by Ingrid Johanson and Richard Allen. Joshua Miller, Sarah Snyder, John Friday, Aaron Enright, Doug Neuhauser, Mario Aranha and Jennifer Taggart

contributed to the operation of the BARD network in 2012–2013. Operation of the BARD network is partially supported by funding from the USGS/NEHRP program grant #G10AC00141. Real-time data processing is supported by a grant from the Moore Foundation.

References

d'Alessio, M. A., I. A. Johanson, R. Bürgmann, D. A. Schmidt, and M. H. Murray, Slicing up the San Francisco Bay Area: block kinematics and fault slip rates from GPS-derived surface velocities, *J. Geophys. Res.*, 110(B06403), doi:10.1029/2004JB003496, 2005.

Herring, T. A., R. W. King, and S. C. McClusky, *GAMIT: GPS Analysis at MIT—Release 10.4*, MIT, 2005. [online] Available from: http://www-gpsg.mit.edu/~simon/gtgk/GAMIT_Ref.pdf.

Herring, T. A., R. W. King, and S. C. McClusky, *GLOBK: Global Kalman filter VLBI and GPS analysis program—Version 10.4*, MIT, 2010. [online] Available from: http://www-gpsg.mit.edu/~simon/gtgk/GLOBK_Ref.pdf.

6 Data Acquisition and Quality Control

Introduction

Stations from the networks operated by the BSL transmit data continuously to the BSL facilities on the UC Berkeley campus for analysis and archival. In this section, we describe activities and facilities which pertain to the individual networks described in Operational Sections 4.1, 4.3, and 4.4, including procedures for data acquisition and quality control, and sensor testing capabilities and procedures. Some of these activities are continuous from year to year and have been described in prior BSL annual reports. In this section, we describe changes and activities which are specific to 2012–2013.

Data Acquisition Facilities

The data acquisition computers and associated telemetry equipment are located in the campus computer facility in Warren Hall at 2195 Hearst Avenue. This building was constructed to current “emergency grade” seismic codes and is expected to be operational even after a $M7$ earthquake on the nearby Hayward Fault. The hardened campus computer facility within was designed with special attention for post-earthquake operations. The computer center contains state-of-the-art seismic bracing, UPS power and air conditioning with generator backup, and extensive security and equipment monitoring.

Data Acquisition

Central-site data acquisition for data from the BDSN/HRSN/NHFN/mPBO networks is performed by two computer systems in the Warren Hall data center (Figure 4.6.1). These acquisition systems also collect data from the Parkfield-Hollister electromagnetic array and the BARD network. A third system is used primarily for data exchange. This system transmits data to the U.S. National Seismograph Network (USNSN) from HOPS, CMB, SAO, WDC, HUMO, JCC, MOD, MCCM, ORV and YBH. Data from various subsets of stations also go to the Pacific and Alaska Tsunami Warning Centers, to the University of Washington and to the University of Reno, Nevada. In addition, the Southern California Earthquake Management Center has access to our wavepools for retrieving waveform data for inclusion in its event gathers. Data for all channels of the HRSN are now telemetered continuously from Parkfield to the BSL over the USGS T1 from Parkfield to Menlo Park, and over the NCEMC T1 from Menlo Park to Warren Hall.

The BSL uses the programs *qmaserv*, *seedlink*, *scream* and for some legacy data loggers, *comserv*. These programs receive data from remote Quanterra, Basalt and Guralp data loggers and redistribute it to one or more client programs. The clients include *datalog*, which writes the data to disk files for archival purposes; *wdafill*, which writes the data to the shared memory region for processing with the network services routines that provide parameters to AQMS, the earthquake monitoring software system; and to other programs such as the DAC480 system feeding our helicorder and the feed for the Memento Mori Web page.

The two computers performing data acquisition are also “network services” computers that reduce waveforms for processing with the AQMS software (Figure 4.6.2). To facilitate processing, each system maintains a shared memory region containing the most recent 30 minutes of data for each channel.

Currently, BDSN data loggers from sites which use frame relay telemetry are configured to enable data transmission over a single frame relay T1 circuit to UCB, a possible point of failure. The second T1 circuit, to which we subscribed in the past, was discontinued due to the decrease in funding from the State. For Quanterra data loggers, the *qmaserv/comserv* client program *cs2m* receives data and multicasts it over a private ethernet. The program *mcast*, a modified version of Quanterra’s *comserv* program, receives the multicast data from *cs2m*, and provides a *comserv*-like interface to local *comserv* clients. Thus, each network services computer has a *comserv/qmaserv* server for all stations, and each of the two systems has a complete copy of all waveform data.

The multicasting approach now handles data received from other types of data loggers and from other networks like the NCSN and UNR (University of Nevada, Reno). Data from partner networks are received by Earthworm data exchange programs, are converted to MiniSEED and are also multicast. On both network services computers *mserv* receives multicast data and handles just as it does BSL MiniSEED data.

In 2006, the BSL established a real-time data feed of all BSL waveforms between the BSL acquisition systems and the NCEDC computers using the open source Freeorb software. This allows the NCEDC to provide near-real-time access to all BSL waveform data through the NCEDC DART (Data Available in Real Time) system.

We monitor seismic stations and telemetry using the program *seisnetwatch*. This program extracts current information such as time quality, mass positions, and battery voltage and allows it to be displayed. If the parameter departs from the nominal range, the station is marked with yellow or red to indicate a possible problem.

Seismic Noise Analysis

BSL seismic data are routinely monitored for state of health. An automated analysis is computed regularly to characterize the seismic noise level recorded by each broadband seismometer. In addition, this year we took advantage of the April 11, 2012, $M 8.6$ earthquake off the coast of northern Sumatra to check noise levels at our STS1 stations in the frequency band from 0.2 mHz to 2 mHz, by looking at the normal mode spectra (see Operational Section 4.1).

In 2000–2001, the BSL began to routinely monitor the Power Spectral Density (PSD) of ground motion recorded at its seismic stations (see past Annual Reports, http://earthquakes.berkeley.edu/annual_report/). The PSD provides an objective measure of background seismic noise characteristics

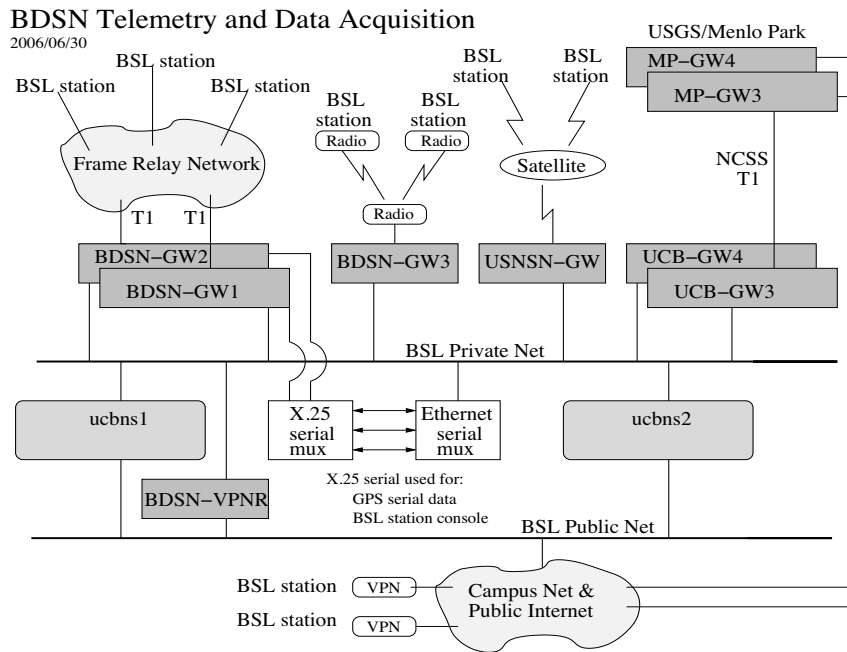


Figure 4.6.1: Data flow from the BDSN, NHFN, mPBO, HRSN, nad BARD networks into the BSL central processing facility.

over a wide range of frequencies. Observing it throughout the year also provides an objective measure of seasonal variation in noise characteristics and supports early diagnoses of instrumental problems. The PSD estimation algorithm was developed at the BSL by Bob Uhrhammer in the early 1990s, for both characterizing the background seismic noise and as a tool for quality control. That algorithm generates a bar graph output in which all the BDSN broadband stations can be compared by component. Cumulative PSD plots were generated for each station which showed the noise level in five frequency bands for the broadband channels. In addition to the station-based plots, a summary plot was produced for each channel. Although we have moved to new noise monitoring procedures, these figures remain available on the web at <http://earthquakes.berkeley.edu/seismo/bdsn/psd/>, as they provide a record of equipment performance for the years 2000–2005.

Our main tool for monitoring seismic noise is now the Ambient Noise Probability Density Function (PDF) analysis system developed by *McNamara and Buland* (2004). This system performs its noise analysis over all the data of a given time period (week or year). The data processed includes earthquakes, calibration pulses, and cultural noise. This is in contrast to Bob Uhrhammer's PSD analysis, which looked at only the quietest portion of data within a day or week. Pete Lombard of the BSL extended the McNamara code to cover a larger frequency range and support the many different types of sensors employed by the BSL. Besides the originally supported broadband sensors, our PDF analysis now includes surface and borehole geophones and accelerometers, strainmeters, and electric and magnetic field sensors. The enhancements to the PDF code, plus a number of bug fixes, were provided back to the McNamara team for incorporation in their work. The results of the PDF analysis are presented on our webpage at <http://www.ncedc.org/>

[ncedc/PDF/](http://www.ncedc.org/ncedc/PDF/). The entry page now provides summary figures of the noise at each station for the BDSN and for other networks and stations we archive at the NCEDC, so they can be reviewed quickly. To provide an overview, we have developed summary figures for all components in two spectral bands, 32 - 128 s and 0.125 - 0.25 s for broadband sensors, and only in the short period band for other short period sensors. The figures are also available on the web at <http://www.ncedc.org/ncedc/PDF/>. The entry web page also provides access to the PDF plots for all stations, by network, component and year.

Sensor Testing and Calibration

The BSL has an Instrumentation Test Facility in the Byerly Seismographic Vault where the characteristics of sensors can be systematically determined and compared. The test equipment consists of an eight-channel Quanterra Q4120 high-resolution data logger and a custom interconnect panel. The panel provides isolated power and preamplification, when required, to facilitate the connection and routing of signals from the sensors to the data logger with shielded signal lines. The vault also has a GPS rebroadcaster, so that all data loggers in the Byerly vault operate on the same time base. Upon acquisition of data at up to 200 sps from the instruments under test, PSD analysis, coherence analysis, and other analysis algorithms are used to characterize and compare the sensor performance. Tilt tests and seismic signals with a sufficient signal level above the background seismic noise are also used to verify the absolute calibration of the sensors. A simple vertical shake table is used to assess the linearity of a seismic sensor. The BSL's sensor testing facility is described in detail in the 2001 2002 Annual Report (http://earthquakes.berkeley.edu/annual_report).

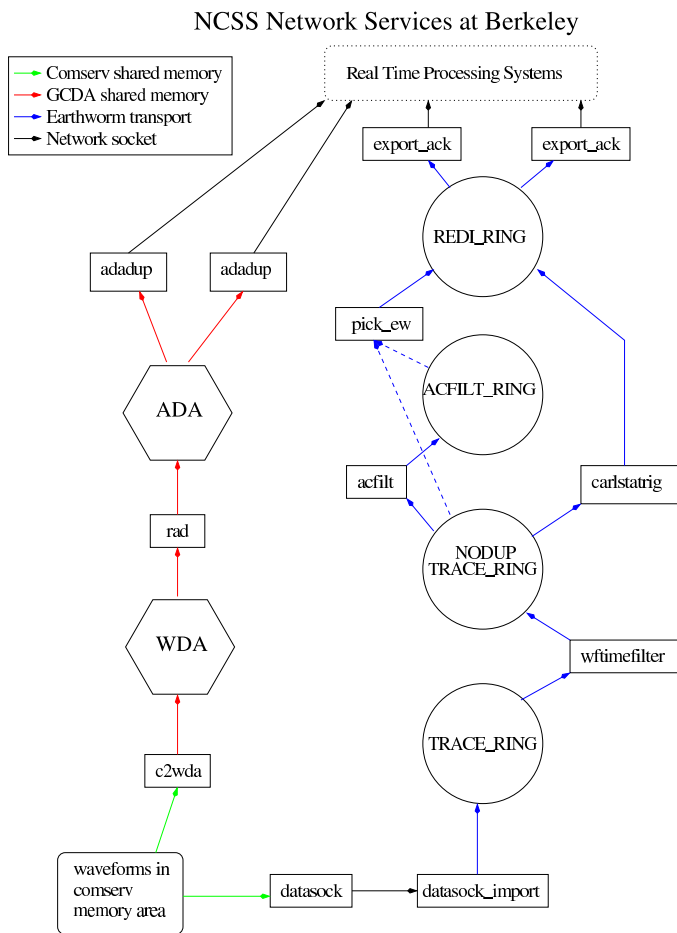


Figure 4.6.2: Flow of data from *comserv/qmaserv* areas through network services processing. One stream of the network services provides picks (and currently still provides codas) determined using the programs shown in the right flow path. Every five seconds, ground motion parameters are also determined, including PGA, PGV, PGD, and ML100 (left flow column). Parameters from the network services are available to the AQMS software for event detection and characterization. Data are also logged to disk (via *datalog*), distributed to other computers (*mserv*), and spooled into a trace ring for export.

Evaluating Tiltmeter Waveforms for Earthquake Source and Earth Structure Studies

Tiltmeters monitor angular changes of ground deformation in microradian with high fidelity across a broad range of frequencies over time scales from hours to years. In principle, they are also capable of recording high frequency deformation signals such as Earth's free oscillation (~ 1000 s period). Tilt is typically sampled at ultra low sampling rates (1 minute or longer). The monitoring capability from tiltmeters is therefore not fully exhausted in the field.

In collaboration with the U.S. Geological Survey (USGS), we conducted a prototype experiment in the Bay Area, to collect continuous data sampled at 40 sps from borehole tiltmeters from two HFN sites, BK.OXMT and BK.MHDL, over a six-month interval starting in the summer of 2012. At the same time, STS-2 broadband sensors were temporary installed at these sites.

During the experiment, a number of signals from teleseismic and local events were recorded. A comparison of tilt records and seismic data from the co-located STS-2 sensors (Figure 4.6.3a) shows that both waveforms are nearly identical in the broad frequency range from 0.001 Hz to 5 Hz.

Additionally, we analyzed six months of continuous noise data to explore Green's function or noise cross-correlation functions (NCFs) between the two sensors. The noise signals recorded from tiltmeter and STS-2 for non-overlapping one hour windows were first rotated into the radial and transverse components that are relative to the azimuthal direction of the station pair. The waveforms were whitened in a frequency range from 0.1 to 0.9 Hz, and NCFs were computed between the two stations. We estimated the average of the NCFs for the entire six months interval.

Three different sets of NCFs were obtained through our analysis: 1) STS-2-STS-2 NCF, 2) Tilt-Tilt NCF, and 3) STS-2-Tilt NCF. The average NCFs from all three sets are in good agreement with each other (Figure 4.6.3b), and they show Rayleigh and Love phases on radial and transverse components (not shown), respectively. These results demonstrate an expanded observational capability that tiltmeter waveform at high sampling rates can be used as broadband seismic data to investigate earthquake source and Earth structure.

Testing Strong Motion Sensors

Self-noise and performance of seismic sensors is an important consideration for developing and maintaining high quality seismic networks. We are characterizing the performance of 4 accelerometers, as a complementary study to *Ringler and Hutt's* (2010, SRL) work on weak-motion sensors. We installed a Kinemetrics EpiSensor ES-T, Guralp CMG-5TC, Metrozet TSA-100S, and Nanometrics Titan (all sensors are accelerometers) at the Berkeley Seismological Laboratory Instrumentation Test Facility in the Byerly Vault (BKS). Analog outputs from all 4 sensors were recorded on Quanterra Q330 data loggers at 200 samples per second. This site has relatively low ambient background noise. In addition to the test equipment, as a BDSN site, BKS is permanently equipped with a set of Streckeisen STS-1 broadband seismometers and an EpiSensor ES-T recorded on a Quanterra Q330-HR data logger. They provide reference ground motion recordings. The noise test was performed for several weeks to ensure the sensors had settled and to obtain seismic signals from local and teleseismic earthquakes. The recording interval included the 2013 M_w 7.5 Alaska earthquake. Seismic recordings from both local and teleseismic earthquakes allow the characterization of the sensors in a broad frequency range; tilt tests were conducted to confirm their absolute calibration. The sensors in the test were separated by about 10 cm (Figure 4.6.4a), located near the BKS sensors (about 1 m separation).

We have done preliminary validation of the waveforms (Figure 4.6.4b), as well as initial evaluation of relative orientation, orthogonality and channel coherences. We intend to pursue these investigations in more detail, as well as evaluating manufacturers' instrument response specifications through tilt test data, and assessing sensors' responses at very long periods

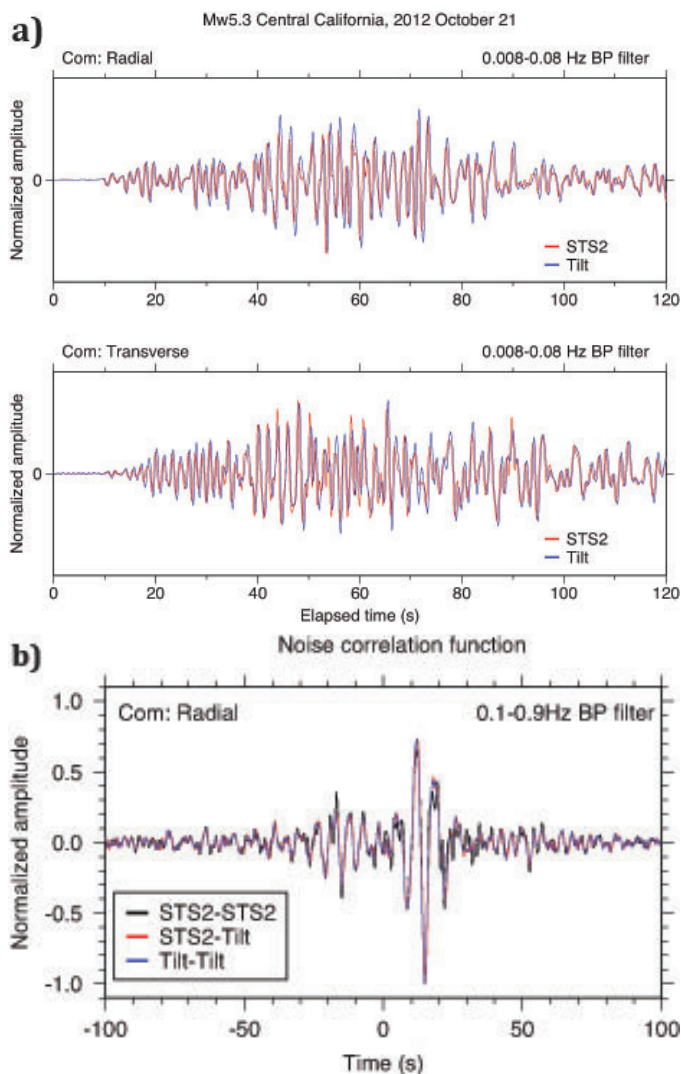


Figure 4.6.3: (a) Observed STS-2 (red) and tilt (blue) waveforms recorded at BK.OXMT for the October 21, 2012 M_w 5.3 Central California earthquake. A 0.008-0.08 Hz bandpass filter was applied to the waveforms. The amplitudes were normalized by their maximum amplitudes. (b) Average noise correlation functions between BK.OXMT and BK.MHDL in the radial component from STS-2-STS-2 (black), STS-2-tilt (red), and tilt-tilt (blue) ambient noise wavefields. Strong Rayleigh pulses are observed at both -20 s and 20 s.

(20 s–100 s), using the recordings of a large teleseism, and at high frequencies (>30–40 Hz) using recordings of nearby small earthquakes.

Monitoring Temporal Stability of Instrument Response

The BSL has implemented software to monitor sensor response as a function of time, by analyzing and comparing waveform data collected from multiple sensors with the same orientation installed at a single station. For BDSN sites, broadband and strong-motion waveforms are compared. The software extracts waveforms from local earthquakes ($M > 3.0$) that occurred within 100 km of the stations and obtains absolute ground acceleration waveforms by removing the instruments'

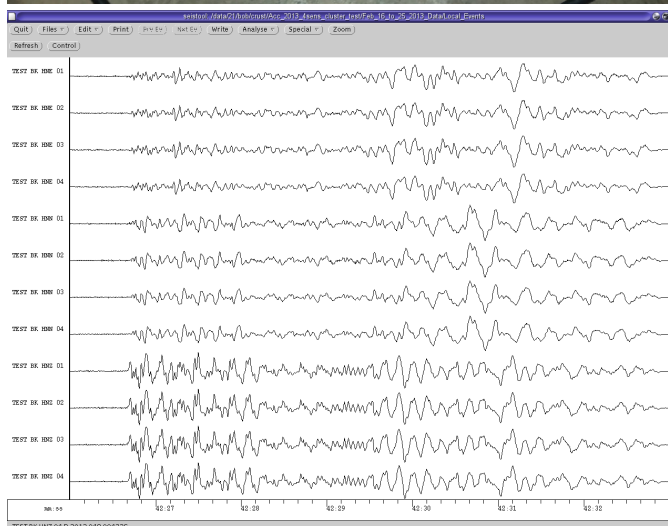


Figure 4.6.4: (a) Strong motion accelerometers for the test on the pier at BKS. (b) Waveform validation showing absolute scaled ground accelerations inferred from the four accelerometers using the factory calibration data, with components grouped together. The order of the traces is Guralp, Episensor, Metrozet, Titan. The plot shows a $M2.58$ local earthquake which occurred 16.7 km SSE of BKS.

response. The waveforms are then filtered with a 1–8 Hz bandpass filter. Spectral amplitude and phase are computed for about five minutes of data including the direct P-waves. We primarily focus on the amplitude ratio between waveforms from two sensors to address the temporal stability of sensor response and estimate the median amplitude ratio in the frequency range used.

Calibration of QEP Temperature, Humidity, and Pressure Sensors

The BSL staff have calibrated the Quanterra Environmental Package (QEP) temperature (T), relative humidity (RH), and pressures (P) sensors which will be deployed at our seismic stations with STS-1s. For the calibration, we compared T, P and HR recordings from the QEP collected on the roof of McCone Hall with meteorological data collected by NOAA at the Oakland Airport and Half Moon Bay (Figure 4.6.6). The data from a set of ten QEPs were analyzed.

Using NOAA data as reference, we performed linear least squares fitting to determine the coefficients for individual QEPs. The following three equations best represent the instrument responses:

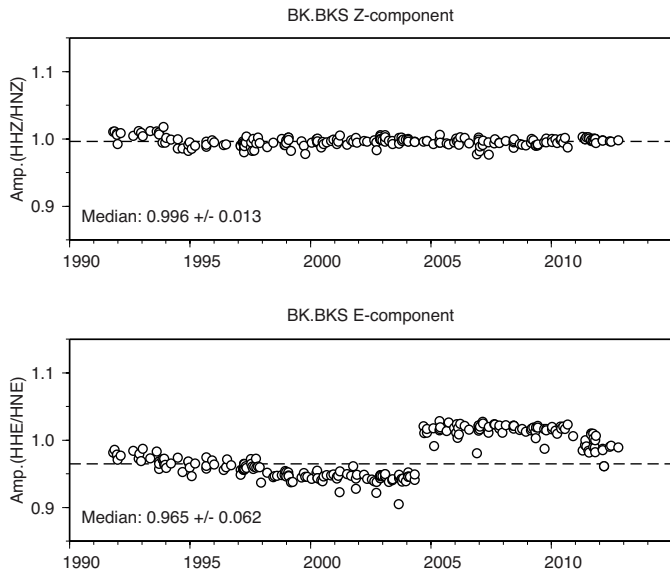


Figure 4.6.5: The temporal evolution of the amplitude ratio between the STS-1 broadband and strong-motion data at BK.BKS in the vertical and East-West components for a 20-year period. There were a number of upgrades of the equipment during this interval. The spectral amplitude ratio for the vertical component is stable over time, which indicates that the sensors' responses are stable and well described by the instrument response functions stored in the database. For the BKS East-West component, the median amplitude ratio has gradually decreased. This temporal reduction of the amplitude ratio is most likely due to a change in the characteristics of the STS-1E sensor induced by high humidity in the vault.

$$RH(\%) = r_0 + r_1 \times counts$$

$$P(\bar{\mu}) = p_0 + p_1 \times du$$

$$T(^{\circ}C) = t_0 + t_1 \times du + t_2 \times du^2 + t_3 \times du^3$$

where T , P , and RH are the temperature, pressure, and percent relative humidity, respectively, and du is the digital counts from the data logger and the parameters t_i , p_i and r_i are available from the instrument response information in our database.

Monitoring Instrument Response of the STS-1/E300 Systems in the BDSN

After the data logger for the CTBT STS-2 was reinstalled at YBH, we noticed that the response of the STS-1/E300 at that site had changed. As a result, we decided to regularly calibrate the STS-1/E 300 combinations installed in the BDSN. We have experienced problems calibrating using the E300 at two sites. Since its installation at KCC, the E300 has not responded to remote commands. Under the assumption that this was due to moisture that entered the cables at splices, we replaced those cables with a factory prepared set (see Operations Section BDSN). There, the E300 serial port still needs to be reconnected to the FRAD, however, but access has been closed due to a nearby forest fire. The second station is SAO. There it appears that the STS-1 calibration circuits have been modified, so that the amplitude of the calibration signal emanated by the E300 clips the

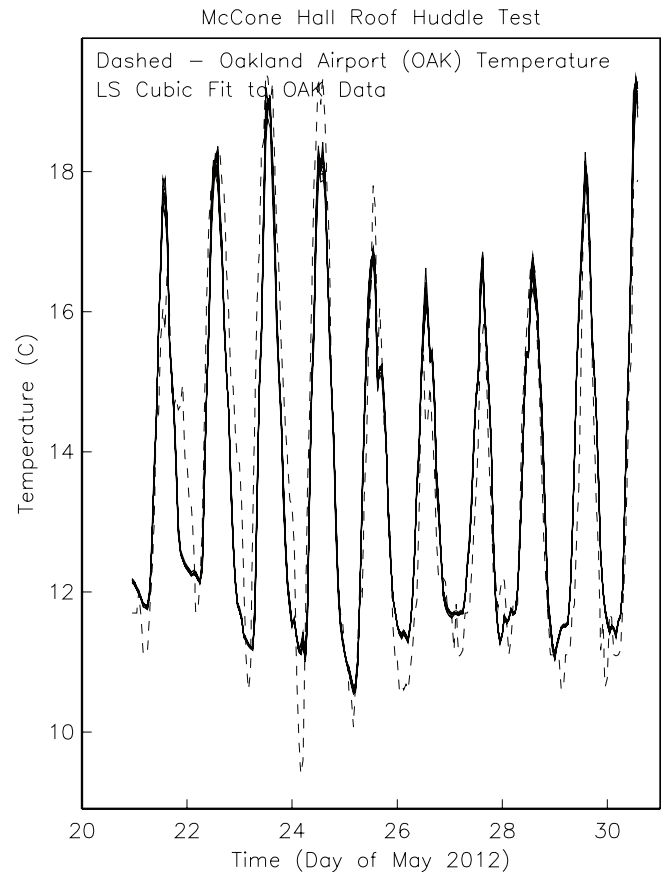


Figure 4.6.6: QEP temperature data (solid lines) from the ten QEPs from our experiment. The dashed line is air temperature data collected at the Oakland airport by NOAA.

sensors. Table 4.6.1 shows results from STS-1/E300 calibrations over time, and a recent calibration manually performed at MHC, where there is no E300. Note that the E-component at YBH continues to change over time.

Acknowledgements

Doug Neuhauser, Bob Uhrhammer, Taka Taira, Peggy Hellweg, Pete Lombard, Jennifer Taggart and Clay Miller are involved in the data acquisition and quality control of BDSN/HRSN/NHFN/mBPO data. Development of the sensor test facility and analysis system was a collaborative effort of Bob Uhrhammer, Tom McEvelly, John Friday, and Bill Karavas. IRIS (Incorporated Research Institutions for Seismology) and DTRA (Defense Threat Reduction Agency) provided, in part, funding for and/or incentive to set up and operate the facility, and we thank them for their support.

Bob Uhrhammer, Taka Taira, Peggy Hellweg, Pete Lombard and Doug Neuhauser contributed to the preparation of this section.

References

McNamara, D. and R. Buland, Ambient Noise Levels in the Continental United States *Bull. Seism. Soc. Am.*, 94, 4, 2004.

Rodgers, P.W., A.J. Martin, M.C. Robertson, M.M. Hsu and D.B. Harris, Signal-coil calibration of electromagnetic seismometers, *Bull. Seism. Soc. Am.*, 85, 845-850, 1995.

Calibration Date	Stn	Cmp	Ts	hs	fg	hg	Calibration Date	Stn	Cmp	Ts	hs	fg	hg
2011.235	BKS	Z	359.8	0.715	12.38	0.437	2010.117	HOPS	Z	391.6	0.732	14.98	0.350
			-3.8%	-3.6%	0.5%	4.6%				-0.6%	0%	6.1%	3.1%
2012.040	BKS	Z	346.2	0.689	12.44	0.457	2012.039	HOPS	Z	389.1	0.732	15.89	0.361
			0.6%	0.3%	0%	0.9%				-0.4%	-0.7%	-0.1%	0%
2012.122	BKS	Z	348.2	0.691	12.44	0.461	2012.128	HOPS	Z	387.5	0.727	15.88	0.361
			0.10%	0.10%	-2.80%	-1.30%				0.80%	0.80%	-0.30%	-1.10%
2012.256	BKS	Z	348.4	0.692	12.09	0.455	2012.254	HOPS	Z	390.6	0.733	15.83	0.357
2011.235	BKS	N	360.7	0.716	17.10	0.336	2010.117	HOPS	N	391.9	0.740	16.17	0.326
			-3.8%	-2.5%	-0.8%	0%				1.2%	3.5%	3.9%	7.1%
2012.040	BKS	N	347.1	0.698	16.96	0.336	2012.039	HOPS	N	396.5	0.766	16.80	0.349
			0.7%	0.9%	0.9%	0%				-0.4%	-0.4%	1.8%	-4.3%
2012.122	BKS	N	349.4	0.704	17.11	0.336	2012.128	HOPS	N	394.8	0.763	17.11	0.334
			0%	-1.00%	-0.40%	0.30%				0.90%	1.30%	-0.40%	0%
2012.256	BKS	N	349.3	0.697	17.05	0.337	2012.254	HOPS	N	398.4	0.773	17.05	0.334
2011.235	BKS	E	360.5	0.722	13.19	0.400	2010.117	HOPS	E	392.4	0.731	15.85	0.339
			-4%	-4.3%	0.8%	5.2%				-1.4%	-1.6%	6%	2.9%
2012.040	BKS	E	346.1	0.691	13.30	0.421	2012.039	HOPS	E	387.1	0.719	16.80	0.349
			0.5%	-0.3%	-0.1%	0.2%				-0.5%	-0.7%	-0.1%	-1.7%
2012.122	BKS	E	347.9	0.689	13.29	0.422	2012.128	HOPS	E	385.3	0.714	16.79	0.343
			0.20%	1.00%	0%	-1.90%				0.60%	0.80%	-0.50%	1.20%
2012.256	BKS	E	348.5	0.696	13.29	0.414	2012.254	HOPS	E	387.7	0.72	16.7	0.347
2011.012	CMB	Z	365.7	0.731	12.91	0.461	2011.160	YBH	Z	371.5	0.731	11.94	0.465
			-0.1%	1.6%	2%	1.1%				-2%	-3.6%	1.9%	1.7%
2012.041	CMB	Z	365.4	0.743	13.17	0.466	2012.038	YBH	Z	364.0	0.705	12.17	0.473
			-0.3%	-0.3%	0.3%	0.2%				0%	-0.1%	-0.1%	-0.2%
2012.123	CMB	Z	364.4	0.741	13.21	0.467	2012.124	YBH	Z	364.1	0.704	12.16	0.472
			0.10%	-3.90%	0.70%	-1.90%				0.20%	0.10%	0%	-0.20%
2012.255	CMB	Z	364.9	0.712	13.12	0.458	2012.255	YBH	Z	365	0.705	12.16	0.471
2011.012	CMB	N	365.4	0.714	17.11	0.335	2011.160	YBH	N	370.2	0.736	13.12	0.418
			-0.3%	-1%	1.9%	-7.8%				-1.5%	-1.5%	-0.8%	5.7%
2012.041	CMB	N	364.3	0.707	17.43	0.309	2012.038	YBH	N	364.6	0.725	13.01	0.442
			0.2%	0.4%	-0.1%	4.2%				0.1%	-0.1%	-0.5%	-3.6%
2012.123	CMB	N	365.1	0.710	17.42	0.322	2012.124	YBH	N	365.0	0.724	12.95	0.426
			0.20%	3.20%	-0.50%	1.20%				0.10%	1.10%	0.30%	2.60%
2012.255	CMB	N	366	0.733	17.33	0.326	2012.255	YBH	N	365.2	0.732	12.99	0.437
2011.012	CMB	E	365.0	0.718	13.31	0.425	2011.160	YBH	E	389.0	1.019	12.76	0.430
			-0.4%	-2.8%	1.7%	9.4%				11.7%	28.9%	4.8%	-4.4%
2012.041	CMB	E	363.5	0.698	13.53	0.465	2012.038	YBH	E	434.6	1.313	13.37	0.411
			0.4%	1.4%	-1.3%	-29%				1.8%	5.6%	0%	1.9%
2012.123	CMB	E	365.1	0.708	13.35	0.330	2012.124	YBH	E	442.3	1.386	13.37	0.419
			0.40%	0.10%	2.90%	33.30%				10.90%	0.20%	-0.10%	-9.10%
2012.255	CMB	E	366.4	0.709	13.74	0.44	2012.255	YBH	E	490.7	1.389	13.36	0.381

Table 4.6.1: Results from STS-1/E300 calibrations over time

7 Northern California Earthquake Monitoring

Introduction

Earthquake information production and routine analysis in Northern California have been improving over the past two decades. Since June 2009, the BSL and the USGS in Menlo Park have been operating mirrored software systems (see the 2010 Annual Report). For this system, processing begins as the waveforms arrive at the computers operating the real-time, or AQMS, software, and ranges from automatic preparation of earthquake information for response to analyst review of earthquakes for catalogs and quality control.

This is the most recent step in a development at the BSL that began in the mid-1990s with the automated earthquake notification system called Rapid Earthquake Data Integration (REDI, *Gee et al.*, 1996; 2003a). That system determined earthquake parameters rapidly, producing near real-time locations and magnitudes for earthquakes in Northern and Central California, estimated rupture characteristics and the distribution of ground shaking following significant earthquakes, and provided tools for the rapid assessment of damage and estimation of loss.

A short time later, in 1996, the BSL and the USGS began collaborating to produce information for Northern and Central California earthquakes. Software operating in Menlo Park and Berkeley were merged to form a single, improved earthquake notification system using data from both the NCSN and the BDSN (see past annual reports). Since 2000, the USGS and the BSL operate as the Northern California Earthquake Management Center (NCEMC) of the California Integrated Seismic Network (Operational Section 4.2).

With support from the USGS and the Gordon and Betty Moore Foundation, the BSL is now also participating in the development and assessment of a statewide prototype Earthquake Early Warning system. A full-fledged system will provide warning of imminent ground shaking in the seconds after an earthquake has initiated but before strong motion begins at sites that may be damaged. This Annual Report has several Research Studies describing the project (see Research Sections 2.28, 2.29, 2.30, 2.31, 2.32, 2.33, 2.34).

Northern California Earthquake Management Center

In this section, we describe how the Northern California Earthquake Management Center fits within the CISN system. Figure 4.2.3 in Operational Section 4.2) illustrates the NCEMC as part of the CISN communications ring. The NCEMC is a distributed center, with elements in Berkeley and in Menlo Park. The 35 mile separation between these two centers is in sharp contrast to the Southern California Earthquake Management Center, where the USGS Pasadena is located across the street from the Caltech Seismological Laboratory.

As described in Operational Section 4.2, the CISN partners are now connected by an Internet-based communications link. The BSL has maintained two T1 communication links

with the USGS Menlo Park, to have robust and reliable links for shipping waveform data and other information between the two processing systems.

Figure 4.7.1 provides more detail on the system operating at the NCEMC since mid-June 2009. Now, complete earthquake information processing systems operate in parallel in Menlo Park and Berkeley. Incoming data from each network are processed locally at each of the two data centers in network services computers. The continuously reduced data, which include picks, codas, ground motion amplitudes, and ML100, are exchanged between the data centers and fed into both processing streams. Real time analysis is coordinated using up-to-date information from the local real-time database, which is replicated to the local data center database. Event review and automatic downstream processes such as computation of fault plane solutions access the internal data center databases. To maintain redundancy, robustness, and completeness, these two databases replicate with each other across the San Francisco Bay. They also replicate with the public database from which information is made available to the public. The system includes the production of location and origin time as well as estimates of M_d , M_L , and M_w . For events with $M \geq 3.5$, ShakeMaps are also calculated on two systems, one in Menlo Park and one in Berkeley. Finite fault calculation is not yet integrated into the new processing system. It is only calculated at the BSL at this time.

This system combines the advantages of the NCSN with those of the BDSN. The dense network of the NCSN contributes to rapid and accurate earthquake locations, low magnitude detection thresholds, and first-motion mechanisms. The high dynamic range data loggers, digital telemetry, and broadband and strong-motion sensors of the BDSN provide reliable magnitude determination, moment tensor estimation, calculation of peak ground motions, and estimation of source rupture characteristics. Robust preliminary hypocenters, or "Quick Looks" are published within a few tens of seconds of the origin time. Event information is updated when preliminary coda magnitudes are available, within 2-4 minutes of the origin time. Estimates of local magnitude are generally available less than 30 seconds later, and other parameters, such as the peak ground acceleration and moment magnitude, follow within 1-4 minutes (Figure 4.7.2).

Earthquake information is now distributed to the web through EIDS (Earthquake Information Distribution System) and PDL (Product Distribution Layer), and is available through the USGS Earthquake Notification Service (<http://sslearthquake.usgs.gov/ens>). We are working with the USGS in Golden, CO, to complete the implementation of PDL. This will allow larger packages of more complete event information in XML format to pass from our analysis systems to the National Earthquake Information Center. We are also developing readers and writers for QuakeML. For organizations which need very rapid access to earthquake information, CISN Display is a useful tool (<http://www.cisn.org/software/cisndisplay>).

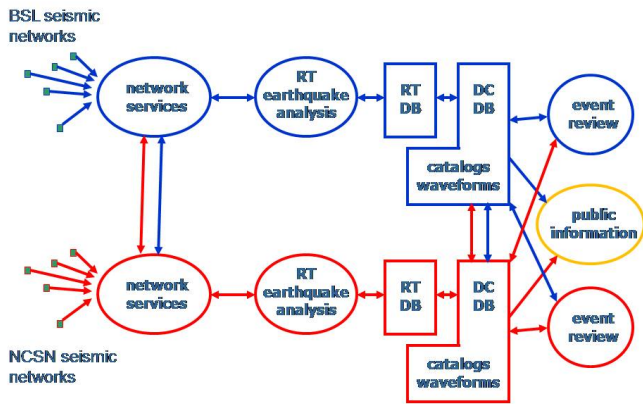


Figure 4.7.1: Details of the Northern California earthquake information processing system. Network services processing, that is, production of picks, ground motion amplitudes, and other reduced information, occurs at both datacenters, and the information is exchanged. Complete earthquake information processing systems exist on both sides of the San Francisco Bay, and up-to-date information is exchanged by database replication.

htm). The USGS has upgraded its earthquake information site (<http://earthquake.usgs.gov/earthquakes/map/>), as has the BSL (<http://earthquakes.berkeley.edu>). These web sites provide valuable resources for information which are useful not only in the seconds immediately after an earthquake, but in the following hours and days as well.

Earthquake Information Processing

In June 2009, we began operating the ANSS Quake Monitoring System (AQMS) software, formerly CISM Software, as the production system in the Northern California Seismic System (NCSS) for monitoring and reporting on Northern California earthquakes. This came as the result of a long effort to adapt and test software developed for the TriNet system operating in Southern California.

Data flow in the Northern California system (Figure 4.7.3) allows for our diverse forms of data acquisition and variability in network distribution. In addition, the BSL and the USGS have minimized the use of proprietary software in the system.

One exception is the database program, Oracle. The NCEDC Oracle database hosts all earthquake information and parameters associated with the real time monitoring system. It is the centerpoint of the new system, providing up-to-date information to all processing modules. Reliability and robustness are achieved by continuously replicating the databases. The public, read-only, database provides event and parametric information to catalog users and to the public.

During the last few years, BSL staff members, particularly Pete Lombard, have become extremely familiar with elements of the TriNet software. The software is now adapted for Northern California, with many adjustments and modifications completed along the way. For example, Pete Lombard adapted the

TriNet magnitude module to Northern California. Pete made a number of suggestions on how to improve the performance of the magnitude module and has worked closely with Caltech and the USGS/Pasadena on modifications.

The BSL and the USGS Menlo Park are exchanging “reduced amplitude time series”. One of the important innovations of the TriNet software development is the concept of continuous processing (Kanamori *et al.*, 1999). Waveform data are constantly processed to produce Wood Anderson synthetic amplitudes and peak ground motions. A program called *rad* produces a reduced time series, sampled every 5 seconds, and stores it in a memory area called an “Amplitude Data Area” or ADA. Other modules can access the ADA to retrieve amplitudes to calculate magnitude and ShakeMaps as needed. The BSL and the USGS Menlo Park have collaborated to establish tools for ADA-based exchange. The next step in improving reliability and robustness is to implement ADA exchange with Southern California as well.

2012-2013 Activities

Moment Tensor Solutions with *tmts* and Finite Fault Analysis

The BSL continues to focus on the unique contributions that can be made from the broadband network, including moment tensor solutions and finite fault analysis. *tmts* is a Java and web-based moment tensor processing system and review interface based on the complete waveform modeling technique of Dreger and Romanowicz (1994). The improved, web-based review interface has been operating in Northern California since July 2007. The automatically running version for real-time analysis was extensively tested and updated by Pete Lombard, and has been running since June 2009. Reporting rules now allow automatically produced solutions of high quality to be published to the web. From July 2012 through June 2013, BSL analysts reviewed many earthquakes in Northern California and adjoining areas of magnitude 2.9 and higher. Reviewed moment tensor solutions were obtained for 76 of these events (through 6/30/2013). Figure 4.7.4 and Table 4.7.1 display the locations of earthquakes in the BSL moment tensor catalog and their mechanisms. During this year, no finite fault inversions were produced for Northern California earthquakes.

The version of *tmts* currently operating in Northern California allows full inversions that include an isotropic element of the source, i.e. explosions or collapses. With the advent of the new code, we reviewed “old” events in the Geysers events from before 2007 with the new interface to produce and store deviatoric solutions for them in the database. Past events have now been reanalyzed events and “full” solutions have been produced and archived for those few which exhibit robust isotropic components.

We are currently developing a new version of the moment tensor system which will permit the use of records from strong motion sensors.

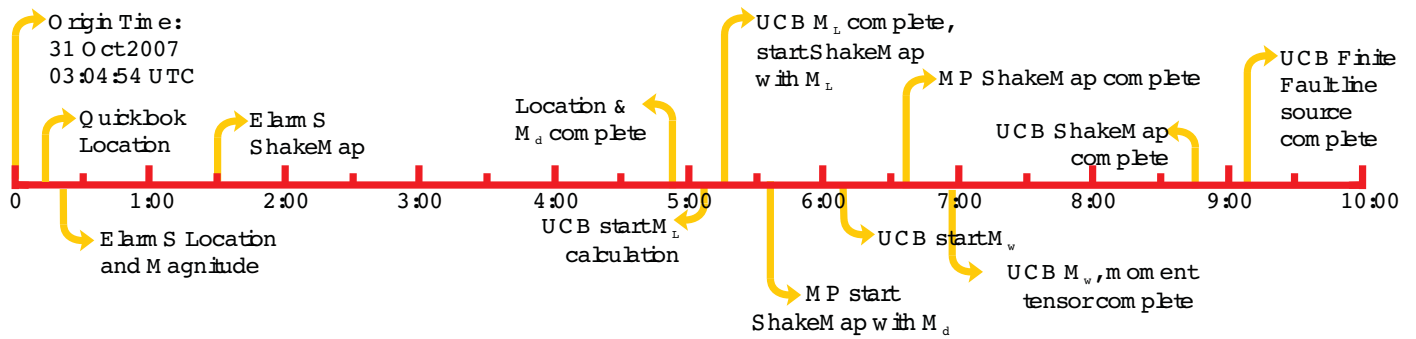


Figure 4.7.2: Illustration of the earthquake products timeline for the M_w 5.4 Alum Rock earthquake of October 30, 2007. Note that all processing was complete within 10 minutes of the origin time.

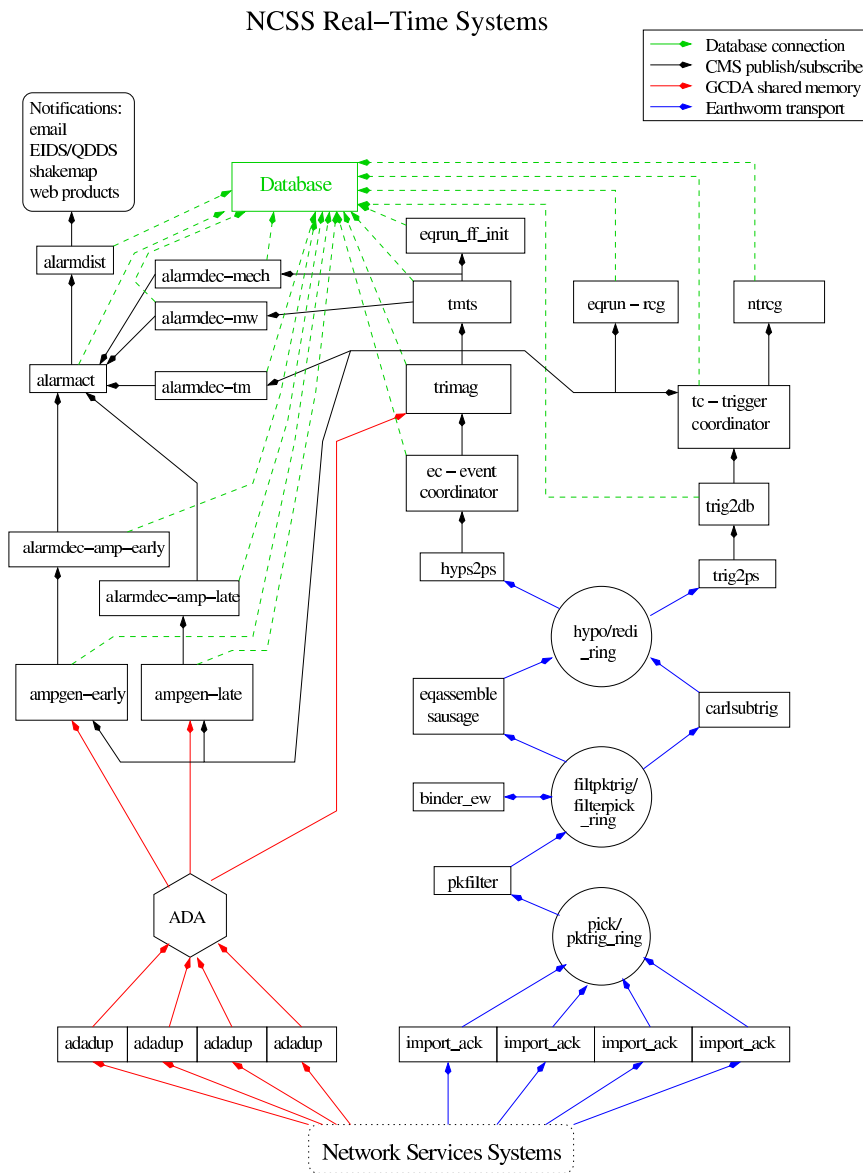


Figure 4.7.3: Schematic diagram of processing in the NCSS system. The design combines elements of the Earthworm, TriNet, and REDI systems.

Station Metadata, Reversals and *fpfit*

In a review of the fault plane solution for a recent event near the Geysers, we discovered that the orientation information for many of the seismic stations there was inconsistent. The fault plane solution program, *fpfit*, uses a file listing the stations with “reversed” polarity from the standard orientation. In the past, this file has been generated by hand and updated only occasionally. We reviewed the orientations of the borehole sensors contributing data to NCEMC operations, at Parkfield, in the San Francisco Bay Area and at the Geysers, using regional or teleseismic earthquakes. This information has been fed into the instrument response data. In a final step, we developed a procedure to compile the reversals file for *fpfit* from the database.

Routine Earthquake Analysis

In fiscal year 2012-2013, more than 32,000 earthquakes were detected and located by the automatic systems in Northern California. This compares with more than 27,000 in 2011-2012 and over 25,000 in 2010-2011. Of these events, 142 had preliminary magnitudes of three or greater. Twenty-two events had M_L or M_w greater than 4. The four largest events (on May 24, 2013, October 21, 2012, and two on July 21, 2012) had magnitudes greater than 5. The first two were located near Canyon Dam, CA, and New Idria, CA, respectively, and the latter two were offshore of Petrolia, CA (see Table 4.7.1 for more details).

Although BSL staff no longer read BDSN records for local and regional earthquakes (see *Annual Report of 2003-2004*), they now participate in timing and reviewing earthquakes with *Jiggle*, mainly working on events from past sequences that have not yet been timed. This work contributes to improving the earthquake catalog for Northern California, but also ensures robust response capabilities, should the Menlo Park campus be disabled for some reason.

Acknowledgements

Peggy Hellweg oversees our earthquake monitoring system and directs the routine analysis. Peter Lombard and Doug Neuhauser contribute to the development of software. Taka'aki Taira, Ingrid Johanson, Doug Dreger, Sierra Boyd, Holly Brown, Sanne Cottaar, Andrea Chiang, Shan Dou, Scott French, Aurelie Guilhem, Mong-Han Huang, Rob Porritt, Jennifer Taggart, Amanda Thomas, Kelly Wiseman, and Zhou (Allen) Zheng contribute to the routine analysis of moment tensors. Peggy Hellweg, Doug Neuhauser, and Taka'aki Taira contributed to the writing of this section. Partial support for the development, implementation and maintenance of the AQMS software, as well as for the production of earthquake information, is provided by the USGS under Cooperative Agreement G10AC00093, and from the California Office of Emergency Services.

References

Dreger, D., and B. Romanowicz, Source characteristics of events in the San Francisco Bay region, *USGS Open File Report 94-176*, 301-309, 1994.

Gee, L., J. Polet, R. Uhrhammer, and K. Hutton, Earthquake Mag-

nitudes in California, *Seism. Res. Lett.*, 75(2), 272, 2004.

Gee, L., D. Neuhauser, D. Dreger, M. Pasyanos, R. Uhrhammer, and B. Romanowicz, The Rapid Earthquake Data Integration Project, *Handbook of Earthquake and Engineering Seismology*, IAS-PEI, 1261-1273, 2003a.

Gee, L., D. Dreger, G. Wurman, Y. Gung, B. Uhrhammer, and B. Romanowicz, A Decade of Regional Moment Tensor Analysis at UC Berkeley, *Eos Trans. AGU*, 84(46), Fall Meet. Suppl., Abstract S52C-0148, 2003b.

Gee, L., D. Neuhauser, D. Dreger, M. Pasyanos, B. Romanowicz, and R. Uhrhammer, The Rapid Earthquake Data Integration System, *Bull. Seis. Soc. Am.*, 86, 936-945, 1996.

Pasyanos, M., D. Dreger, and B. Romanowicz, Toward real-time estimation of regional moment tensors, *Bull. Seis. Soc. Am.*, 86, 1255-1269, 1996.

Romanowicz, B., D. Dreger, M. Pasyanos, and R. Uhrhammer, Monitoring of strain release in central and northern California using broadband data, *Geophys. Res. Lett.*, 20 1643-1646, 1993.

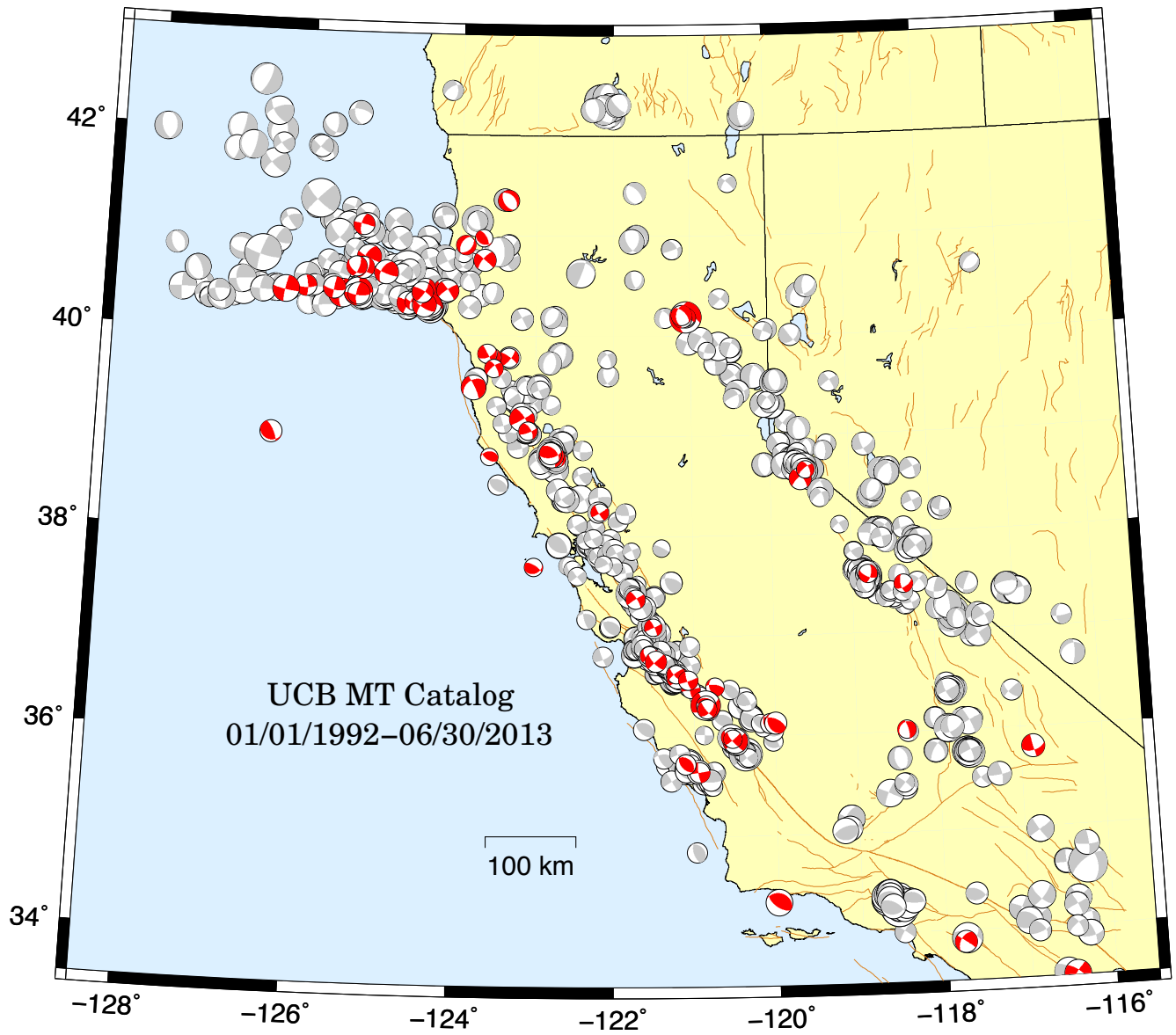


Figure 4.7.3: Map comparing reviewed moment tensor solutions determined by the BSL from past years (gray) with those from the fiscal year 2012-2013 (red/dark).

Location	Date	UTC Time	Lat.	Lon.	MT Depth	M _L	M _w	M _o	Str.	Dip	Rake
Covelo, CA	7/1/2012	10:05:53 AM	39.78	-123.35	10.76	3.22	3.56	2.74E+21	305	80	164
Fort Bragg, CA	7/8/2012	12:05:49 PM	39.48	-123.8	8.08	4.14	4.42	5.38E+22	334	81	-130
The Geysers, CA	7/9/2012	12:01:18 AM	38.82	-122.8	3.91	3.52	3.83	6.85E+21	25	66	-79
Willow Creek, CA	7/12/2012	10:39:08 AM	40.75	-123.68	30.44	3.68	3.99	1.18E+22	310	88	-162
New Idria, CA	7/19/2012	7:59:00 AM	36.49	-120.74	10.82	3.32	3.32	1.20E+21	279	68	57
Petrolia, CA	7/21/2012	1:52:02 AM	40.39	-125.53	25.01	4.58	5.1	5.60E+23	94	86	160
Petrolia, CA	7/21/2012	6:04:21 AM	40.41	-125.33	6.12	4.48	5.19	7.60E+23	184	89	8
Petrolia, CA	7/23/2012	8:57:45 AM	40.39	-125.38	26.87	3.22	3.49	2.11E+21	274	88	170
Anderson Springs, CA	8/3/2012	06:30:01 PM	38.78	-122.72	2.09	3.08	3.25	9.28E+20	199	60	-65
Parkfield, CA	8/6/2012	7:35:49 AM	35.95	-120.5	11.63	4.58	4.45	5.94E+22	231	90	12
Ferndale, CA	8/9/2012	03:24:27 PM	40.76	-125.2	24.8	4.1	4.38	4.69E+22	117	82	153
Parkfield, CA	8/31/2012	09:44:08 PM	35.99	-120.56	4.37	3.22	3.32	1.20E+21	47	84	-20
Huron, CA	9/7/2012	01:22:10 PM	36.12	-120.06	14.84	3.82	3.68	4.06E+21	309	57	81
Kettleman City, CA	9/7/2012	01:23:48 PM	36.12	-120	10.5	4.16	4.06	1.55E+22	297	59	72
Point Arena, CA	9/11/2012	04:44:33 PM	38.79	-123.58	10.54	2.95	3.12	6.04E+20	120	58	110
Rio Dell, CA	9/14/2012	11:53:18 AM	40.44	-124.19	27.23	4.14	4.43	5.44E+22	50	83	-10
Rio Dell, CA	9/14/2012	06:19:51 PM	40.44	-124.16	26.79	3.47	3.96	1.08E+22	325	84	-170
The Geysers, CA	9/16/2012	06:53:03 PM	38.79	-122.77	3.34	3.14	3.43	1.74E+21	128	65	-149
The Geysers, CA	9/16/2012	06:54:00 PM	38.81	-122.81	0.71	0	2.88	2.63E+20	334	71	-148
Petrolia, CA	9/22/2012	2:55:25 AM	40.46	-124.45	26.08	3.29	3.51	2.30E+21	114	87	-174
Talmage, CA	9/25/2012	03:15:010 PM	39.17	-123.17	11.46	3.96	4.51	7.36E+22	60	87	20
Trinidad, CA	9/26/2012	5:53:34 AM	41.08	-125.28	25.65	3.44	3.84	7.08E+21	283	87	-157
Green Valley, CA	10/8/2012	04:09:32 PM	38.24	-122.17	9.47	3.03	3.25	9.36E+20	59	86	-10
Ferndale, CA	10/14/2012	04:53:07 PM	40.65	-125.27	23.43	3.57	4	1.26E+22	125	73	-144
Pinnacles, CA	10/19/2012	05:44:46 PM	36.47	-121.04	8.46	3.65	3.41	1.63E+21	78	89	-10
New Idria, CA	10/21/2012	6:55:010 AM	36.31	-120.86	9.18	5.28	5.29	1.08E+24	332	90	159
New Idria, CA	10/21/2012	7:37:47 AM	36.31	-120.85	10.16	3.65	3.58	2.91E+21	112	61	87
Blue Lake, CA	10/21/2012	08:40:08 PM	40.9	-123.93	21.9	3.24	3.55	2.67E+21	211	48	-99
Petrolia, CA	10/23/2012	7:45:52 AM	40.3	-124.53	8.71	3.25	3.69	4.32E+21	97	87	-173
Pinnacles, CA	10/29/2012	4:25:16 AM	36.59	-121.2	9.02	4.18	3.94	1.01E+22	136	84	-168
San Martin, CA	10/31/2012	9:52:58 AM	37.09	-121.5	8.07	3.29	3.22	8.34E+20	65	89	10
Willow Creek, CA	10/31/2012	03:29:53 PM	40.97	-123.7	12.64	3.18	3.21	8.02E+20	330	62	108
San Juan Bautista, CA	11/1/2012	02:34:18 PM	36.81	-121.55	6	3.41	3.33	1.24E+21	47	84	-33
Talmage, CA	11/13/2012	01:40:05 PM	39.05	-123.09	3	3.1	3.32	1.18E+21	68	77	28
Ferndale, CA	11/18/2012	6:53:04 AM	40.66	-125.36	23.07	3.37	3.72	4.69E+21	19	68	-47
The Geysers, CA	11/24/2012	8:10:19 AM	38.81	-122.79	3.97	3	3.28	1.05E+21	39	50	-64
Pinnacles, CA	11/24/2012	03:44:35 PM	36.62	-121.22	6.24	3.35	3.33	1.24E+21	232	76	17
Petrolia, CA	12/12/2012	03:49:50 PM	40.29	-124.5	20.01	3.2	3.52	2.37E+21	191	79	39
The Geysers, CA	12/13/2012	5:17:23 AM	38.82	-122.8	4.33	3.36	3.7	4.43E+21	18	72	-108
The Geysers, CA	12/17/2012	12:03:27 AM	38.79	-122.76	2.29	2.99	3.09	5.33E+20	150	83	-165
Petrolia, CA	12/19/2012	12:02:24 PM	40.28	-124.36	19.4	3.43	3.79	6.02E+21	193	84	6
Lake Nacimiento, CA	12/23/2012	10:02:45 AM	35.64	-120.94	5.49	3.86	3.74	5.01E+21	82	89	-12

Parkfield, CA	12/26/2012	11:32:32 AM	35.97	-120.53	12.01	3.42	3.3	1.13E+21	51	83	-15
Pinnacles, CA	1/3/2013	09:04:25 PM	36.56	-121.07	8.77	3.46	3.4	1.57E+21	348	85	175
Laytonville, CA	1/11/2013	10:46:03 AM	39.78	-123.57	9.27	3.17	3.31	1.16E+21	128	83	-147
Petrolia, CA	1/13/2013	10:28:18 AM	40.39	-125.32	16.12	3.45	4.02	1.32E+22	94	75	161
Pinnacles, CA	1/15/2013	03:14:31 PM	36.56	-121.07	8.56	3.67	3.52	2.41E+21	71	84	-11
Markleeville, CA	1/24/2013	8:21:48 AM	38.56	-119.62	5.95	4.02	3.67	3.95E+21	232	89	-19
Petrolia, CA	1/24/2013	11:22:57 AM	40.44	-125.64	17.85	3.64	4.02	1.32E+22	190	88	19
Markleeville, CA	1/24/2013	011:25:51 PM	38.56	-119.62	6.71	4.4	4	1.23E+22	228	75	-19
Rockport, CA	1/26/2013	01:10:39 PM	39.82	-123.63	6.33	3.16	3.45	1.86E+21	331	87	148
San Lucas, CA	1/26/2013	05:49:43 PM	36.27	-120.84	7.63	3.18	3.44	1.80E+21	141	79	-146
Petrolia, CA	2/5/2013	010:03:45 PM	40.45	-126.01	15.33	3.68	3.81	6.49E+21	356	77	-17
Laytonville, CA	2/15/2013	09:18:21 PM	39.67	-123.54	6.11	3.03	3.36	1.36E+21	230	69	-23
Petrolia, CA	3/3/2013	05:46:51 PM	40.31	-124.67	14.36	3.79	4.18	2.34E+22	27	89	7
Point Reyes, CA	3/9/2013	10:13:010 AM	37.69	-123	7.02	3.41	3.31	1.14E+21	301	70	115
The Geysers, CA	3/14/2013	9:09:23 AM	38.81	-122.79	2.2	4.23	4.44	5.66E+22	340	84	-158
The Geysers, CA	3/14/2013	9:10:09 AM	38.83	-122.8	3.55	3.85	3.95	1.05E+22	79	57	54
Markleeville, CA	3/15/2013	3:05:02 AM	38.65	-119.55	0.2	3.26	3.14	6.29E+20	232	73	-37
Ferndale, CA	3/24/2013	05:25:41 PM	40.61	-124.97	14	3.72	4.29	3.43E+22	111	80	143
San Simeon, CA	3/29/2013	1:22:39 AM	35.72	-121.11	6.98	3.74	3.62	3.39E+21	138	53	95
Toms Place, CA	3/30/2013	3:19:31 AM	37.59	-118.8	9.19	3.52	3.37	1.40E+21	12	65	-29
Bishop, CA	4/14/2013	12:02:30 PM	37.48	-118.36	8.73	3.4	3.39	1.51E+21	168	63	-144
Petrolia, CA	5/1/2013	09:03:23 PM	40.3	-124.38	8.78	3.5	3.86	7.70E+21	190	86	-16
Alum Rock, CA	5/10/2013	5:12:25 AM	37.37	-121.72	8.34	3.3	3.5	2.21E+21	237	86	-13
Petrolia, CA	5/11/2013	6:11:00 AM	40.33	-124.59	20.19	3.17	3.57	2.86E+21	109	71	151
Petrolia, CA	5/18/2013	01:46:09 PM	40.29	-124.46	23.62	3.72	4.28	3.29E+22	122	71	159
Petrolia, CA	5/18/2013	03:54:05 PM	40.42	-124.49	25.08	3.52	3.78	5.84E+21	300	77	165
Canyondam, CA	5/24/2013	3:47:08 AM	40.19	-121.06	9.69	5.87	5.69	4.28E+24	292	70	-145
Canyondam, CA	5/25/2013	06:43:03 PM	40.18	-121.05	7.86	3.56	3.47	1.98E+21	180	65	-47
Canyondam, CA	5/25/2013	010:27:40 PM	40.19	-121.05	11.49	3.28	3.37	1.41E+21	301	85	-161
Isla Vista, CA	5/29/2013	02:38:01 PM	34.33	-120	18.07	4.82	4.78	1.87E+23	126	61	98
Canyondam, CA	5/30/2013	09:08:35 PM	40.18	-121.1	4.76	3.62	3.54	2.56E+21	185	79	-28
Prattville, CA	6/7/2013	3:56:35 AM	40.21	-121.11	9.48	3.71	3.73	4.82E+21	315	58	-124
Somes Bar, CA	6/10/2013	010:16:58 PM	41.35	-123.38	34.56	3.6	3.78	6.07E+21	150	50	-79
San Juan Bautista, CA	6/28/2013	3:52:39 AM	36.75	-121.47	6.88	4.03	3.87	7.81E+21	47	90	-17

Table 4.7.1: Moment tensor solutions for significant events from July 1, 2012 through June 30, 2013 using a complete waveform fitting inversion. Epicentral information is from the UC Berkeley/USGS Northern California Earthquake Management Center. Moment is in dyne-cm and depth is in km.

8 Northern California Earthquake Data Center

Introduction

The Northern California Earthquake Data Center (NCEDC) is a permanent archive and distribution center primarily for multiple types of digital data relating to earthquakes in central and Northern California. The NCEDC is located at the Berkeley Seismological Laboratory, and has been accessible to users via the Internet since mid-1992. The NCEDC was formed as a joint project of the Berkeley Seismological Laboratory (BSL) and the U.S. Geological Survey (USGS) at Menlo Park in 1991, and current USGS funding is provided under a cooperative agreement for seismic network operations.

Time series data come from broadband, short period, and strong motion seismic sensors, and geophysical sensors such as electromagnetic sensors, strain meters, creep meters, pore pressure, water level, and wind speed sensors. Earthquake catalogs can include time, hypocenter, magnitude, moment tensor, mechanisms, phase arrivals, codas, and amplitude data. GPS data are available in both raw observables and RINEX formatted data.

The NCEDC also provides support for earthquake processing and archiving activities of the Northern California Earthquake Management Center (NCEMC), a component of the California Integrated Seismic Network (CISN). The CISN is the California regional organization of the Advanced National Seismic System (ANSS).

2012-2013 Activities

By its nature, data archiving is an ongoing activity. In 2012-2013, the NCEDC continued to expand its data holdings and enhance access to the data. Projects and activities of particular note include:

- *Purchased and installed an 8 Gbit SAN (Storage Area Network) fibre channel switches to upgrade and expand the NCEDC data storage and archive systems.*
- *Installed production Web services for the distribution of station metadata using Station XML, waveform inventory, and MiniSEED data at <http://service.ncedc.org>.*
- *Began receiving, archiving, and distributing event information (hypocenter, magnitude, phase, and amplitude data) and waveforms for the DOE Enhanced Geothermal Systems (EGS) monitoring project.*
- *Finished process of reading and archiving continuous NCSN seismograms from tapes for 1993-1995.*
- *Continued to support the NCEMC earthquake analysis by providing real-time access to earthquake parameters and waveforms from the NCEDC for the CISN*
- *Completed work with the NCSN and USGS National Strong*

Motion Program (NSMP) to import the metadata and build dataless SEED volumes for all NSMP dialup stations.

- *Began continuous data archiving from the LBNL Geysers Network, a dense network of 32 3-component stations acquiring data at 500 samples/second to be used in studies of transient stress changes in the Geysers Geothermal Field.*

Data Types and Contributors

Table 4.8.1 and Figure 4.8.1 provide a breakdown of the NCEDC data by data type. Figure 4.8.2 shows the total data volume by year as itemized in Table 4.8.1.

BDSN/NHFN/mPBO Seismic Data

The BDSN (Operations Section 4.1), NHFN (Operations Section 4.3), and Mini-PBO (Operations Section 4.5) stations (all with the network code of BK) send real-time data from 50 seismic data loggers to the BSL. These data are written to disk files, used by the CISN AQMS software for real-time earthquake processing and by the prototype CISN ShakeAlert earthquake early warning (EEW) system, and delivered to the DART (Data Available in Real Time) system at the NCEDC, where they are immediately available to anyone on the Internet. Continuous high-rate data (200–500 samples/second) are now available for most of the NHFN borehole seismic data channels. All timeseries data from the Berkeley networks continue to be processed and archived by an NCEDC analyst using *calqc* quality control procedures in order to provide the highest quality and most complete data stream for the NCEDC archive. The recent upgrade to the BDSN stations increased the onsite storage at each site, which allows us to recover data from the station after telemetry outages and improve the completeness of the BDSN data archive.

NCSN Seismic Data

NCSN continuous waveform data are transmitted from USGS/Menlo Park in real time to the NCEDC via the internet, converted to MiniSEED, and made available to users immediately through the NCEDC DART. NCSN event waveform data, as well as data from all other real-time BSL and collaborating networks, are automatically collected by the NCEMC waveform archiver and stored at the NCEDC for event review and analysis and for distribution to users. All NCSN and NCEMC data are archived in MiniSEED format.

Improvements in the acquisition of NCSN data, described in the 2005-2006 BSL Annual report, enabled the NCEDC to start archiving continuous NCSN waveforms in early 2006. We then started the process of reading and archiving continuous NCSN waveforms from previous years that had been saved on tapes. We finished the first phase of the NCSN tape continuous waveform archiving for the data from 1996 to early 2006, and have continued the project this year by processing and archiving NCSN tape data from 1993 through 1995.

Data at the NCEDC Archive by Network

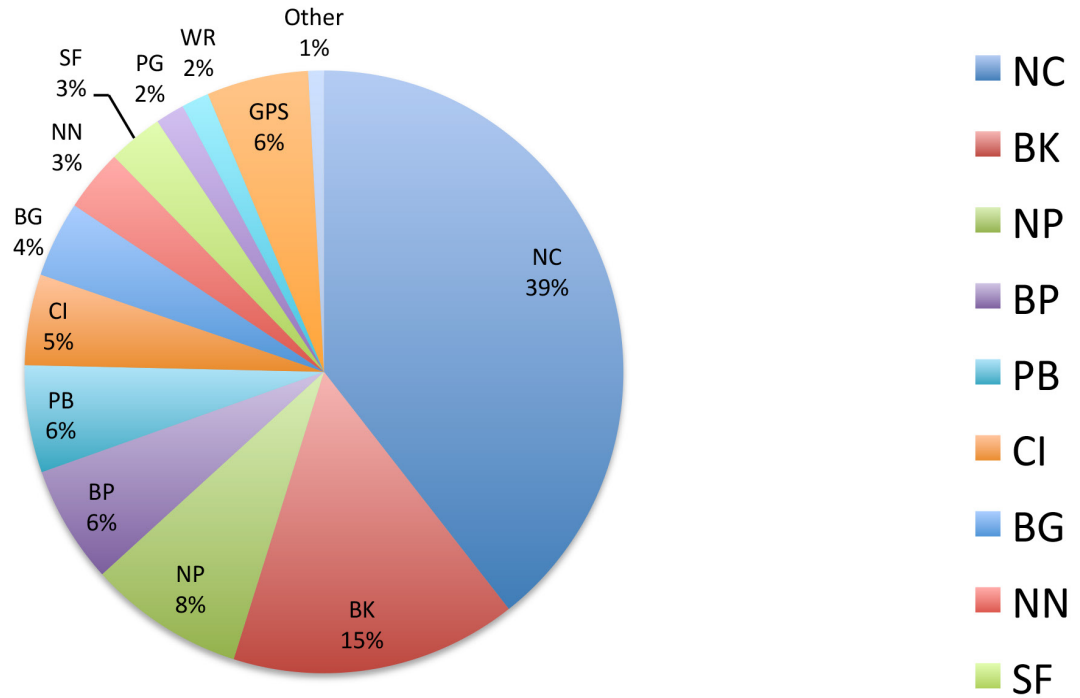


Figure 4.8.1: Chart showing the relative proportion of each data set at the NCEDC. BK - Berkeley Digital Seismic Network; BP - Berkeley High-resolution Seismic Network in Parkfield; NCSN - Northern California Seismic Network and collaborators; CI - Southern California Seismic Network; NN - University of Nevada, Reno Seismic Network; GPS - various GPS datasets, including BARD; EarthScope - data from various EarthScope activities; Other - various small data sets.

Network Code	Size (GB)	Percent of archive
NC	28,849.52	39.41%
BK	11,325.47	15.47%
NP	6,149.66	8.40%
BP	4,623.87	6.32%
PB	4,214.10	5.76%
CI	3,569.83	4.88%
BG	2,989.97	4.08%
NN	2,439.03	3.33%
SF	2,170.43	2.96%
PG	1,145.37	1.56%
WR	1,086.99	1.48%
GPS	4,020.68	5.49%
Other	619.00	0.85%
Total	73,203.93	100.00%

Table 4.8.1: Volume of data archived at the NCEDC by network code.

Data in NCEDC Archive by Year

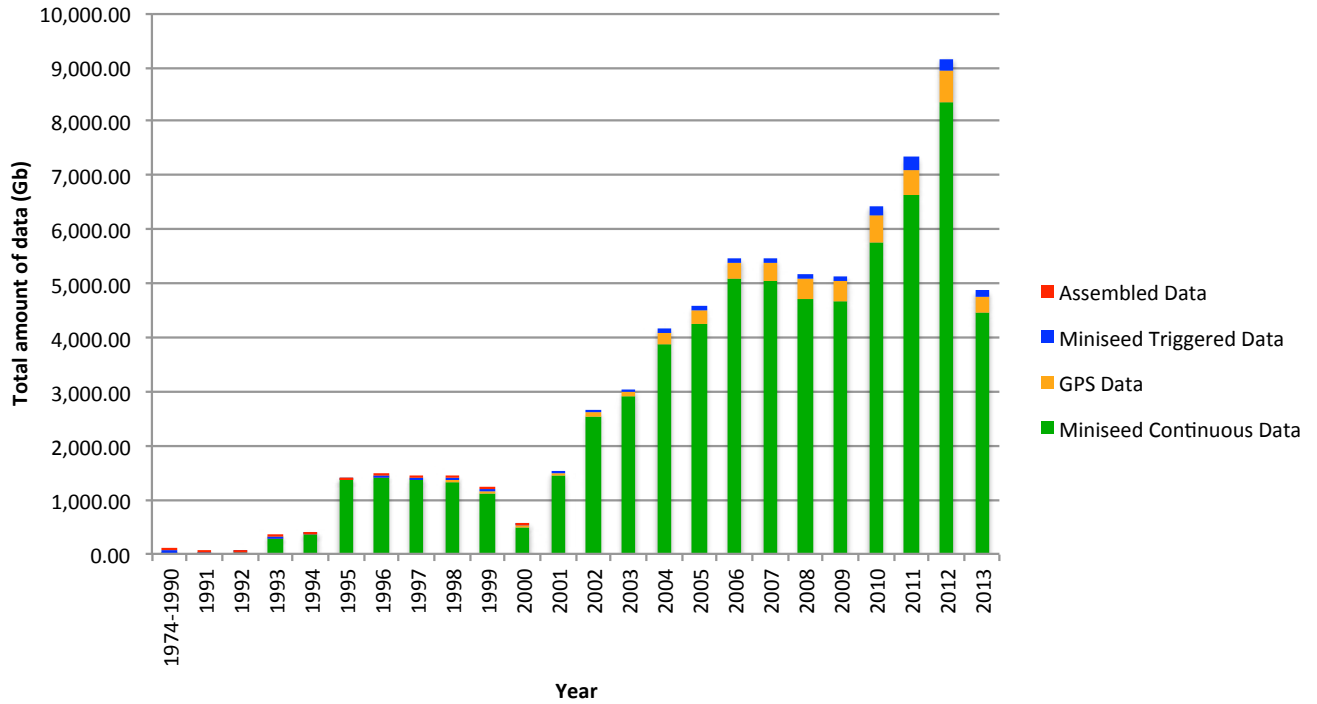


Figure 4.8.2: Figure showing the total volume of data archived at the NCEDC, broken down by data year.

Data in NCEDC Archive by Type

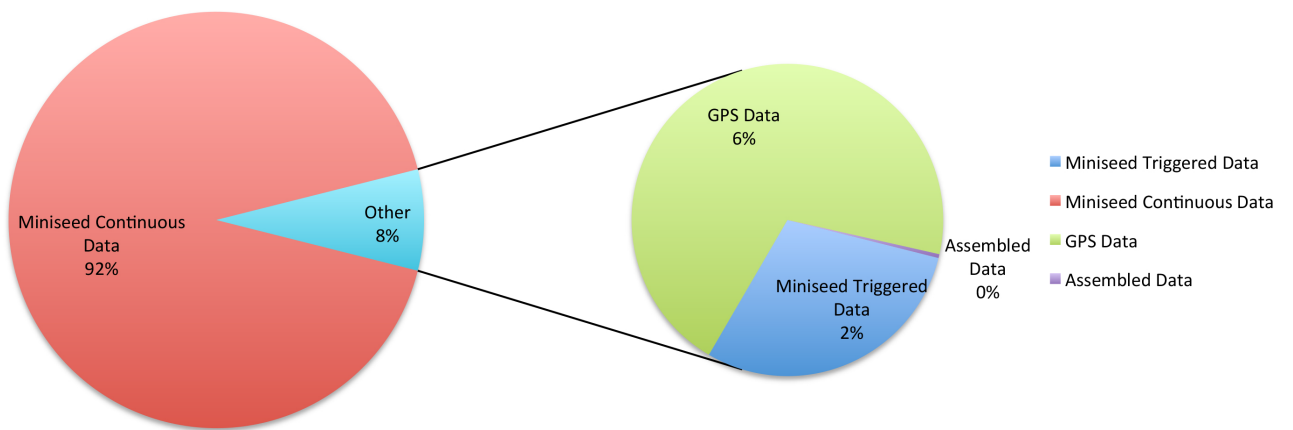


Figure 4.8.3: Percent of data in NCEDC archive by data type.

Network	Size (GB)
NC	2050.45
BK	1657.22
BG	1640.52
PB	1195.66
NP	527.32
BP	409.59
NN	395.7
CI	304.87
PG	229.32
WR	203.88
TA	120.44
SF	70.59
CE	17.99
UL	0.001
GPS	575.09
TOTAL	9398.66

Table 4.8.2a: Continuous data gathered for the 2013 Fiscal Year by network.

NCSS Catalog Fiscal Year 2013			
Size (GB)	Num. WFID	Num. Event SNCLs	Num. Events
184.82	6689707	6294428	43281

Table 4.8.2b: Event data metrics for Fiscal Year 2013. The columns show the size for the Fiscal Year, the number of waveform IDs (WFID), the number of SNCLs and the number of events.

Parkfield High Resolution Seismic Network Data

The history of upgrades to the acquisition and archival of HRSN data can be found in the 2010-2011 BSL Annual Report. We continue to archive continuous 250 and 20 sample-per-second data from the HRSN stations. The most recent HRSN station upgrade added 16GB of local storage at each site, which allows us to recover data from the station after telemetry outages, and greatly improves the completeness of the HRSN data archive.

Earthscope Plate Boundary Observatory (PBO) Strain Data

The NCEDC is one of two funded archives for PBO EarthScope borehole and laser strain data. Strain data are collected from all of the PBO strain sites and are processed by UNAVCO. MiniSEED data are delivered to the NCEDC using SeedLink, and raw and XML processed data are delivered to the NCEDC using Unidata's Local Data Manager (LDM).

The MiniSEED data are inserted into the NCEDC DART and are subsequently archived from the DART. UNAVCO provides EarthScope funding to the NCEDC to help cover the processing, archiving, and distribution costs for these data. In early 2010, the NCEDC began receiving and archiving all of the continuous seismic waveform data from the PBO network to complement the PBO strain data. The seismic data are received from an Antelope ORB server at UNAVCO and converted from their native format to MiniSEED on a data import computer. The data are then transferred via the SEEDLink protocol to the NCEDC, inserted into the NCEDC DART for immediate internet access, and subsequently archived from the DART.

EarthScope SAFOD

The NCEDC is an archive center for the San Andreas Fault Observatory at Depth (SAFOD) event data and has also processed the continuous SAFOD data. Starting with the initial data in July 2002 from the SAFOD Pilot Hole, and, later, data from the SAFOD Main Hole, the NCEDC converted data from the original SEG-2 format data files to MiniSEED, and developed the SEED instrument responses for this data set. Continuous 4KHz data from SAFOD written to tape at SAFOD were periodically sent to the BSL to be converted, archived, and forwarded to the IRIS DMC (IRIS Data Management Center). SAFOD EarthScope funding to the NCEDC is for covering the processing, archiving, and distribution costs for these data. A small subset of the continuous SAFOD data channels are also incorporated into the NCSN, are available in real-time from the NCEDC DART, are archived at the NCEDC, and are forwarded to the IRIS DMC. After the failure of the SAFOD permanent instrument in September 2008, the USGS deployed a temporary network in the Main Hole, and the NCEDC continued to process and archive these data. Both the permanent and temporary seismic instruments were removed in mid-2010 in order to analyze the failure of the permanent SAFOD instrument packet, but the temporary seismic instruments were reinstalled in late 2010 and continue to send data for distribution and archiving to the NCEDC.

Through a UNAVCO EarthScope contract, the NCEDC developed software to convert raw data from the SAFOD vertical laser strainmeter operated by UCSD to MiniSEED format for long-term archiving and distribution.

UNR Broadband Data

The University of Nevada at Reno (UNR) operates several broadband stations in western Nevada and eastern California that are important for Northern California earthquake processing and analysis. Starting in August 2000, the NCEDC has been receiving and archiving continuous broadband data from selected UNR stations. The data are transmitted in real time from UNR to UC Berkeley, where they are made available for CISM real-time earthquake processing and for archiving. Initially, some of the stations were sampled at 20Hz, but all stations are now sampled and archived continuously at 100Hz.

The NCEDC installed Simple Wave Server (SWS) software at UNR, which provides an interface to UNR's recent collection of waveforms. The SWS is used by the NCEDC to retrieve waveforms from UNR that were missing at the NCEDC due to real-time telemetry outages between UNR and UC Berkeley.

In early 2006, the NCEDC started to archive continuous data from the UNR short-period stations that are contributed to the NCSN. Both the broadband and short-period UNR stations contributed to the CISN are available in real-time through the NCEDC DART.

Electro-Magnetic Data

The NCEDC continues to archive and process electric and magnetic field data acquired at several UC Berkeley sites. The BSL operates both magnetic and electric field sensors at SAO. However, most of these channels have been down for repair during the 2010-2011 year. Through a collaboration with Dr. Simon Klemperer at Stanford University, we acquire magnetic and electric field channels at BSL sites JRSC and BRIB, and magnetic field channels at site MHDL. The three magnetic field channels and either two or four electric field channels are digitized at 40 Hz, 1 Hz, and 0.1 Hz, and are telemetered in real-time along with seismic data to the Berkeley Seismological Laboratory, where they are processed and archived at the NCEDC in a similar fashion to the seismic data.

GPS Data

The NCEDC continues to archive GPS data through the BARD (BayArea Regional Deformation) network of continuously monitored GPS receivers in Northern California (Operations Section 4.5). The NCEDC GPS daily archive now includes 80 continuous sites in Northern California. Of these, there are ~32 core BARD sites owned and operated by UC Berkeley, USGS (Menlo Park and Cascade Volcano Observatory), LLNL, UC Davis, UC Santa Cruz, Trimble Navigation, and Stanford. Data are also archived from sites operated by other agencies, including the East Bay Municipal Utilities District, the City of Modesto, the National Geodetic Survey, and the Jet Propulsion Laboratory (JPL).

In addition to the standard 15 second continuous GPS data files, the NCEDC is now archiving and distributing high-rate 1 Hz continuous GPS data from all of the BSL-operated BARD stations. In collaboration with UC San Diego/Scripps Institution of Oceanography (UCSD/SIO), USGS/Pasadena and USGS/MP, the BSL is now streaming real-time 1 Hz continuous data from 42 sites, including all BSL sites and the 13 PBO stations in Parkfield, to the BSL, where it makes the data available to researchers in real time through an Ntripcaster.

The NCEDC also archives non-continuous survey GPS data. The initial dataset archived is the survey GPS data collected by the USGS Menlo Park for Northern California and other locations. The NCEDC is the principal archive for this dataset. Significant quality control efforts were implemented by the NCEDC to ensure that the raw data, scanned site log sheets, and RINEX data are archived for each survey.

Geysers Seismic Data

The Calpine Corporation operated a micro-seismic monitoring network in the Geysers region of Northern California. Prior to 1999, this network was operated by Unocal. Through various agreements, both Unocal and Calpine have released triggered event waveform data from 1989 through 2000 along with preliminary event catalogs for the same time period for archiving and distribution through the NCEDC. This dataset represents over 296,000 events that were recorded by the Calpine/Unocal Geysers network and are available via research accounts at the NCEDC.

The Lawrence Berkeley National Laboratory (LBNL), with funding from the California Energy Commission, currently operates a 32 station network in the Geysers region with an emphasis on monitoring seismicity related to well water injection. The earthquake locations and waveforms from this network are sent to the NCEDC, and the locations are forwarded to the NCSN so that they can be merged into the NCSN earthquake catalog. In August 2007, the NCSN installed an Earthworm system at the Geysers to receive continuous LBNL Geysers data, and this system provides event waveforms for events detected by the NCEMC real-time earthquake monitoring and processing system and the corresponding event data archive at the NCEDC. In March 2012, the NCEDC began to receive continuous data from the stations in near real-time, and began archiving these continuous data.

DOE Enhanced Geothermal Monitoring (EGS) Data

Starting in 2010-2011, BSL was funded through LBNL to archive and disseminate seismic event parameters and corresponding waveform timeseries from monitoring networks operated under the auspices of the US Department of Energy Geothermal Monitoring Program. We have collected and verified the station metadata for these networks, and populated the data into the database. This year we began to receive and archive the event data and waveforms from these networks. The timeseries data are available via our suite of data delivery methods, and the event and parametric information are available via a new web catalog search page. The Geysers event waveform from this data set from April 2003 to August 2007 will also be associated with events from the NCSN catalog and will be included with the existing waveforms for these events.

USGS Low Frequency Data

Since 1974, the USGS at Menlo Park, in collaboration with other principal investigators, has collected an extensive low-frequency geophysical data set that contains over 1300 channels of tilt, tensor strain, dilatational strain, creep, magnetic field, and water level as well as auxiliary channels such as temperature, pore pressure, rain and snow accumulation, and wind speed. In collaboration with the USGS, we assembled the requisite information for the hardware representation of the stations and the instrument responses for many

channels of this diverse dataset, and developed the required programs to populate and update the hardware database and generate the instrument responses. We developed the programs and procedures to automate the process of importing the raw waveform data and converting it to MiniSEED format. Since these data are delivered to the NCEDC on a daily basis and immediately archived, these data are not inserted into the NCEDC DART.

We have currently archived timeseries data from 887 data channels from 167 sites, and have instrument response information for 542 channels at 139 sites. The waveform archive is updated on a daily basis with data from 350 currently operating data channels.

The USGS is reducing support for these stations, and the network is being slowly retired. The NCEDC continues to receive and archive the data channels that are being provided by the USGS.

SCSN/Statewide Seismic Data

In 2004, the NCEDC started to archive broadband and strong motion data from 15 SCSN (network code CI) stations that are telemetered to the Northern California Earthquake Management Center (NCEMC) of the California Integrated Seismic Network (CISN). These data are used in the prototype real-time state-wide earthquake processing system and also provide increased coverage for Northern California events. Since the data are telemetered directly from the stations in real time to both the SCSN and to the NCEMC, the NCEDC archives the NCEMC's copy of the data to ensure that at least one copy of the data will be preserved. Due to reduced state funding, the SCSN has gradually reduced the number of telemetered stations to seven.

In early 2006, the NCEDC started to continuously archive all of the selected SCSN short-period stations that are contributed to the NCSN. All of these data are also available in real time from the NCEDC DART. In 2009, the NCEMC started incorporating data from ~25 additional SCSN stations near the southern border of the NCEMC monitoring area in its event waveform collection to provide better azimuthal coverage of events in that area. In 2009-2010, the NCEMC also started retrieving event waveform data from the SCSN for other SCSN stations that are expected to receive signals from Northern California earthquakes. All of these event waveforms are also archived at the NCEDC.

Earthquake Catalogs

The NCEDC hosts multiple earthquake catalogs.

Northern California catalog: The NCEDC provides searchable access to both the USGS and BSL earthquake catalogs for northern and central California. The "official" UC Berkeley earthquake catalog begins in 1910 and runs through 2003, and the "official" USGS catalog begins in 1966. Both of these catalogs are archived and available through the NCEDC, but the existence of two catalogs has caused confusion among both researchers and the public.

In late 2006, the NCEMC began archiving and distribut-

ing a single unified Northern California earthquake catalog in real time to the NCEDC through database replication from the NCEMC's real-time systems. The NCEDC developed and tested the required programs used to enter all previous NCSN catalog data into the NCEDC database. In 2008, we migrated all of the historic NCSN catalog, phase, and amplitude data from 1967 through 2006 into the NCEMC catalog. In addition, we spent considerable effort addressing the mapping of phase data in the BSL catalog to SEED channel names. We plan to merge the BSL catalog with the NCEMC catalog to form a single unified Northern California catalog from 1910 to the present. The BSL and the USGS have spent considerable effort over the past years to define procedures for merging the data from the two catalogs into a single northern and central California earthquake catalog in order to present a unified view of Northern California seismicity. The differences in time period, variations in data availability, and mismatches in regions of coverage all complicate the task.

Enhanced Geothermal Systems (EGS) catalog: US Department of Energy Geothermal Monitoring Program is operating a number of seismic networks that monitor earthquakes in the regions of enhanced geothermal systems. The event catalogs and parametric information are available via a new EGS catalog search page.

Worldwide catalog: The NCEDC, in conjunction with the Council of the National Seismic System (CNSS) in the 1990s, produced and distributed a world-wide composite catalog of earthquakes based on the catalogs of the national and various U.S. regional networks. Each network updates their earthquake catalog on a daily basis at the NCEDC, and the NCEDC constructs a composite world-wide earthquake catalog by combining the data, removing duplicate entries that may occur from multiple networks recording an event, and giving priority to the data from each network's authoritative region. The catalog, which includes data from 14 regional and national networks, is searchable using a web interface at the NCEDC. The catalog is also freely available for bulk download by anyone on the internet.

With the disbanding of the CNSS and the development of the Advanced National Seismic System (ANSS), the NCEDC was asked to update its web pages to present the composite catalog as a product of the ANSS. This conversion was completed in the fall of 2002. The NCEDC continues to create, house, distribute, and provide a searchable web interface to this ANSS composite catalog, and to aid the regional networks in submitting data to the catalog. The ANSS is currently developing a new ANSS Combined Catalog (ComCat) which, when fully populated with historical events, may replace the current NCEDC's ANSS composite catalog.

The BSL made significant progress on data submission to the new ANSS ComCat using the new Product Distribution Layer (PDL), and provided timely feedback to the USGS Earthquake Hazards (EHZ) development team on both PDL and QuakeML issues. We developed a flexible XML writer for AQMS systems that can generate QuakeML for any or all of

the following PDL products:

1. Origin products (hypocenter and magnitudes)
2. Phase products (hypocenter, magnitudes, phase, and amplitudes readings)
3. Mechanism products (mechanism information with related gif images)
4. Moment tensor products (moment tensor information with related gif images).

The NCSS has provided the AQMS QuakeML writer to all ANSS AQMS operators, and is currently using it to submit real-time and reviewed Mechanism and Moment Tensor products as well as Shakemap products to the production ComCat system. We are not yet submitting origin or phase products to the production Comcat since we have not had sufficient access to the ComCat development system in order to adequately test how ComCat handles these products.

The NCSS progress in adopting PDL for all earthquake data distribution has been impeded by the following issues:

1. Delays in USGS providing access through firewalls to the development ComCat system and to the redundant NCSS PDL hubs located in Menlo Park.
2. No defined QuakeML definition for the deletion of Moment Tensor products or Mechanism products.

NCEDC Operations

The current NCEDC facilities consist of a mass storage environment hosted by a 8-core Sun X4150 computer, a 100 slot LTO3 tape library with two tape drives and a 20 TByte capacity, and 180+ TBytes of RAID storage, all managed with the SAM-FS hierarchical storage management (HSM) software. Four additional 8-core Sun computers host the DART data import, data archiving, computing Probability Density Function (PDF) plots for the bulk of the NCEMC waveforms, data quality control procedures, and Internet distribution. Two 64-bit Linux systems host redundant Oracle databases.

In 2005, the NCEDC relocated its archive and distribution system from McCone Hall to a new state-of-the-art computer facility in a new seismically braced building on the Berkeley campus. The facility provides seismically braced equipment racks, gigabit Ethernet network, air conditioning, and power conditioning. The entire facility is powered by a UPS with generator backup.

In 2008-2009, the tape library was upgraded from LTO2 to LTO3 drives, and all online tape data was re-archived on LTO3 tapes. DLT tape libraries are used to read NCSN continuous data tapes.

In 2011-2012, the NCEDC data archive grew to exceed the NCEDC online disk capacity. We acquired a new SAN disk storage system that provides the NCEDC with ~90 TB of primary online storage and ~90 TB of SAMFS cache to improve filesystem performance. We migrated all of the waveform and GPS archive data to the new SAN storage. In addition, we upgraded the fiber channel switches to support the 8 Gbit/

second interfaces of the new SAN disk system and computer interfaces.

The SAMFS hierarchical storage management software used by the NCEDC is configured to automatically create multiple copies of each data file in the archive. The NCEDC creates one copy of each file on an online RAID, a second copy on LTO3 tape (of which the most recent data are stored online in the tape library), and a third copy on LTO2 tape which is stored offline and offsite. In addition, all SAMFS data are stored in an online disk cache which provides instant access to these data. In 2011-2012 we renewed our SAMFS license, which now allows us to manage an unlimited amount of storage.

The NCEDC operates two instances of its Oracle database, one for internal operations and one for external use for user data queries and data distribution programs, and communicates with a third identical database operated offsite by the USGS in Menlo Park. These three databases are synchronized using multi-master replication.

DART (Data Available in Real Time)

The DART provides a network-accessible structured filesystem to support real-time access to current and recent timeseries data from all networks, stations, and channels. All real-time timeseries data streams delivered to the NCEDC are placed in MiniSEED files in a web-accessible directory structure. The DART currently contains the most recent 40 days of data. The DART waveforms can be accessed by users from web browsers or command-line programs such as *wget*, or through NCEDC data services described in the data distribution section of this document.

We use the IRIS ringserver software as the primary method for delivering real-time data to the DART. The ringserver packages implement an object ring buffer (ORB) and server which provides a reliable storage ring buffer and an interface for client programs to read, write, and query the orbserver. Clients running at the NCEDC computer connect to remote servers at the BSL, USGS/Menlo Park, and UNAVCO, retrieve the MiniSEED timeseries data records, and write them to daily channel files in the NCEDC DART. Strain data from the EarthScope PBO network are delivered to the NCEDC using SeedLink and are inserted into the DART using a similar SeedLink client program.

The NCEDC developed an automated data archiving system to archive data from the DART on a daily basis. It allows us to specify which stations should be automatically archived, and which stations should be handled by the NCEDC's Quality Control program *calqc*. The majority of non-BSL data channels are currently archived automatically from the DART.

Data Quality Control

The NCEDC developed a GUI-based state-driven system *calqc* to facilitate the quality control processing that is applied to the BSL stations continuously archived data sets at the NCEDC. The quality control procedures for these datasets include the following tasks:

- data extraction of a full day of data
- quickcheck program to summarize the quality and stability of the stations' clocks
- determination if there is missing data for any data channel
- provided procedures to retrieve missing data from the stations and incorporate it into the day's data
- optional creation of multi-day timeseries plots for state-of-health data channels
- optional timing corrections for data
- optional extraction of event-based waveforms from continuous data channels
- optional repacking of MiniSEED data
- creating waveform inventory entries in the NCEDC database,
- publishing the data for remote access on the NCEDC

calqc is used to process all data from the BDSN and HRSN network, and all continuous broadband data from the NCSN, UNR, and SCSN networks that are archived by the NCEDC. The remainder of the continuously archived data are automatically archived without any analyst interaction.

Database Activity

The NCEDC continues to support the Northern California Earthquake Management Center (NCEMC) by providing information and resources vital to the NCEMC's role of rapid earthquake analysis and data dissemination. The NCEDC receives earthquake parametric data in real time from the NCEMC real-time systems and provides real-time access to the NCEDC database for *jiggle*, the CISN event analysis tool. The NCEMC continues to support the maintenance and distribution of the hardware configurations and instrument responses of the UCB, USGS/MP NCSN, and other seismic stations used by the NCEMC. BSL staff currently chair the CISN Schema Change working group, which coordinates all database schema changes and enhancements within the CISN.

The NCEDC instrument response schema represents full multi-stage instrument responses (including filter coefficients) for the broadband data loggers. The hardware tracking schema represents the interconnection of instruments, amplifiers, filters, and data loggers over time, and is used to describe all of the UC Berkeley and USGS stations and channels archived at the NCEDC.

Database developments in the 2012-2013 year include support for the EGS catalog and waveforms, and the ability to separately request EGS waveform as well as provide all EGS waveforms through standard NCEDC waveform requests by channel and time selection.

Full details on the database schema used at the NCEDC may be found at <http://www.ncedc.org/db>.

Data Distribution

The NCEDC continues to use the internet as the interface for users to request, search for, and receive data from the NCEDC. In fall 2005, the NCEDC acquired the domain name *ncedc.org*.

Information about the NCEDC, it's data sets and networks, and catalog search forms can be found at <http://www.ncedc.org>. The NCEDC Web Services are available at the new web site <http://service.ncedc.org>.

Earthquake Catalogs

The NCEDC provides users with searchable access to Northern California earthquake catalogs, the DOE EGS catalogs, and the ANSS world-wide catalog via the Web. Users can search the catalogs by time, magnitude, and geographic region, and can retrieve either hypocenter and magnitude information or a full set of earthquake parameters including phase readings, amplitudes, and codas. Moment tensor and first motion mechanisms have been added to the NCEMC California earthquake catalog and are searchable from the NCEDC Web catalog search page.

Station Metadata

In addition to the metadata returned through the various data request methods, the NCEDC provides dataless SEED volumes and SEED RESP files for all data channels archived at the NCEDC. The NCEDC currently has full SEED instrument responses for 20,891 data channels from 2,315 stations in 23 networks. This includes stations from the California Geological Survey (CGS) strong motion network that will contribute seismic waveform data for significant earthquakes to the NCEDC and SCEDC. In collaboration with the USGS NCSN and the NSMP (National Strong Motion Program), the NCEDC constructed the metadata and dataless SEED volumes for over 700 stations and 4700 data channels of the NSMP dialup stations. Station metadata can be acquired by downloading pre-assembled dataless SEED files, using NetDC to request metadata by station, channel and time, or by new NCEDC Web services.

Web Services

The NCEDC developed and deployed five web services for distributing both time series and related channel metadata. Web services use standard web HTTP protocol for sending requests and receiving data. Web services can be used interactively from a web browser, or can be easily called from scripts and user programs. These web services are compatible with the corresponding IRIS DMC web services. These new data services are:

- *ws-station*—provides station and channel metadata in StationXML format.
- *ws-resp*—provides channel instrument response in RESP format.
- *ws-availability*—returns information about what time

series data is available at the NCEDC archive.

- *ws-dataselect*—returns a single channel of time series data in miniSEED format from the NCEDC archive.
- *ws-bulkdataselect*—returns multiple channels of time series data in miniSEED format for specified time ranges.

In order to encourage standards for data delivery from data centers, the International Federation of Digital Seismograph Networks (FDSN) defined in 2012 specification for three web services that could provide earthquake catalog information, station and channel metadata, and time series data. In 2012-2013, the NCEDC developed and deployed beta test services for each of the FDSN-defined web services.

- *fdsnws-station*—provides station and channel metadata and optional time series availability in StationXML format.
- *fdsnws-event*—provides earthquake catalog information in QuakeML format.
- *fdsn-dataselect*—returns one or more channel of time series data in miniSEED format for specified time ranges.

StationXML is an XML (Extensible Markup Language) schema for representing station and channel metadata. StationXML was originally designed at the SCEDC and adopted by the FDSN. RESP format is the ascii channel response format created by the IRIS rdseed program, and supported by programs such as evalresp. Documentation on Station XML is available at <http://www.fdsn.org/xml/station/>.

SeismiQuery

The NCEDC ported and installed the IRIS *SeismiQuery* program at the NCEDC, which provides a web interface to query network, station, and channel attributes and query the availability of archived timeseries data.

NetDC

In a collaborative project with the IRIS DMC and other worldwide datacenters, the NCEDC helped develop and implement *NetDC*, a protocol which will provide a seamless user interface to multiple datacenters for geophysical network and station inventory, instrument responses, and data retrieval requests. *NetDC* builds upon the foundation and concepts of the IRIS *BREQ_FAST* data request system. The *NetDC* system was put into production in January 2000 and operated at several datacenters worldwide, including NCEDC, IRIS DMC, ORFEUS, Geoscope, and SCEDC. The *NetDC* system receives user requests via email, automatically routes the appropriate portion of the requests to the appropriate datacenter, optionally aggregates the responses from the various datacenters, and delivers the data (or FTP pointers to the data) to the users via email.

The IRIS DMC deprecated *NetDC* in 2012, but the NCEDC continues to support *NetDC* data, inventory, and metadata requests.

STP

In 2002, the NCEDC wrote a collaborative proposal with the SCEDC to the Southern California Earthquake Center, with the goal of unifying data access between the two data centers. As part of this project, the NCEDC and SCEDC are working to support a common set of three tools for accessing waveform and parametric data: *SeismiQuery*, *NetDC*, and *STP*.

The *Seismogram Transfer Program* or *STP* is a simple client-server program, developed at the SCEDC. Access to *STP* is either through a simple direct interface that is available for Sun or Linux platforms, or through a GUI web interface. With the direct interface, the data are placed directly on a user's computer in several possible formats, with the byte-swap conversion performed automatically. With the web interface, the selected and converted data are retrieved with a single FTP command. The *STP* interface also allows rapid access to parametric data such as hypocenters and phases.

The NCEDC continued work on *STP*, working with the SCEDC on extensions and needed additions. We added support for the full SEED channel name (Station, Network, Channel, and Location), and are now able to return event-associated waveforms from the NCSN waveform archive.

EVT_FAST

In order to provide Web access to the NCSN waveforms before the SEED conversion and instrument response for the NCSN has been completed, the NCEDC implemented *EVT_FAST*, an interim email-based waveform request system similar to the *BREQ_FAST* email request system. Users email *EVT_FAST* requests to the NCEDC and request NCSN waveform data based on the NCSN event ID. *EVT_FAST* event waveforms can be delivered in either MiniSEED or SAC format, and are now named with their SEED channel names.

FISSURES

The *FISSURES* project developed from an initiative by IRIS to improve earth scientists' efficiency by developing a unified environment that can provide interactive or programmatic access to waveform data and the corresponding metadata for instrument response, as well as station and channel inventory information. *FISSURES* was developed using CORBA (Common Object Request Broker Architecture) as the architecture to implement a system-independent method for the exchange of this binary data. The IRIS DMC developed a series of services, referred to as the *Data Handling Interface (DHI)*, using the *FISSURES* architecture to provide waveform and metadata from the IRIS DMC.

The NCEDC has implemented the *FISSURES Data Handling Interface (DHI)* services at the NCEDC, which involves interfacing the DHI servers with the NCEDC database schema. These services interact with the NCEDC database and data storage system and can deliver NCEDC channel metadata as well as waveforms using the *FISSURES* interfaces. We have separate *FISSURES DHI* waveform servers to serve ar-

chived and DART data streams. Our *FISSURES* servers are registered with the IRIS *FISSURES naming services*, which ensures that all *FISSURES* users have transparent access to data from the NCEDC.

The IRIS DMC deprecated its support for *FISSURES* in 2012-2013, but the NCEDC continues to support all of its *FISSURES* servers and assumed responsibility for the *FIS-SURES* name service.

SWC and SWS

UC Berkeley developed the Simple Wave Server (*sws*) and Simple Wave Client (*swc*) programs to provide access to its MiniSEED data from the DART and the NCEDC archive. It currently operates a separate server for each of the above services. The *swc* program is a command-line client program written in perl that runs under Linux, Unix, and MacOS and allows users to easily retrieve waveform data in MiniSEED format by channel and time window or by NCEMC event gathers. The program is packaged for easy user installation and can be downloaded from the NCEDC web site.

The NCEDC operates two distinct SWS services. The *ncedc_archive* service provides access to data that has been formally archived at the NCEDC, and the *dart* service provides access to real-time data from the DART.

GPS

GPS data (raw data, RINEX data at 15 second interval, and high-rate 1 Hz RINEX data) are all available via HTTP or FTP over the Internet in a well-defined directory structure organized by data type, year, and day-of-year.

Metrics for 2012-2013

- NCEDC uptime for data delivery was over 99.5% for the year.
- Table ??? shows the amount and type of data distributed by the NCEDC during this fiscal year.
- Tables 4.8.3 and 4.8.4 show the percentage of data archived as a percentage of the station operational time for BSL stations based on the highest rate vertical data channel for each station. If channels were renamed during the year due to equipment upgrades, or we operated multiple data loggers at the site, there may be multiple entries for that site.

Data Format	GigaBytes
Assembled Datasets	691
Catalog data	3797
GPS data	418
MiniSEED Time Series	7866
Total Data Distributed	12773

Table 4.8.2: Data distributed for 2012-2013 by data format.

Net	Station	Chan	Loc	% Archived
BP	CCRB	DP1	40	100.00
BP	EADB	DP1	40	100.00
BP	FROB	DP1	40	99.33
BP	GHIB	DP1	40	100.00
BP	JCNB	DP1	40	99.97
BP	JCSB	DP1	40	99.97
BP	LCCB	DP1	40	99.92
BP	MMNB	DP1	40	99.99
BP	SCYB	DP1	40	99.99
BP	SMNB	DP1	40	99.95
BP	VARB	DP1	40	100.00
BP	VCAB	DP1	40	99.99

Table 4.8.3: Percentage of Continuous Data Archived for BP stations based on station operation time for the year.

Net	Station	Chan	Loc	% Archived
BK	BDM	HHZ	00	100.00
BK	BKS	HHZ	00	100.00
BK	BL67	HHZ	00	98.52
BK	BL88	HNZ	00	100.00
BK	BRIB	HHZ	00	90.57
BK	BRIB	CN3	40	78.41
BK	BRIB	BQ2	10	100.00
BK	BRIB	BT1	20	100.00
BK	BRK	HHZ	00	100.00
BK	CMAB	CN1	40	99.65
BK	CMB	HHZ	00	99.99
BK	CVS	HHZ	00	99.74
BK	FARB	HHZ	00	99.45
BK	GASB	HHZ	00	100.00
BK	HAST	HHZ	00	99.52
BK	HATC	HHZ	00	99.72
BK	HELL	HHZ	00	100.00
BK	HERB	CN1	40	99.85
BK	HOPS	HHZ	00	99.97
BK	HUMO	HHZ	00	99.82
BK	JCC	HHZ	00	100.00
BK	JRSC	HHZ	00	100.00
BK	JRSC	BQ2	10	100.00
BK	JRSC	BT1	20	100.00
BK	KCC	HHZ	00	34.71
BK	MCCM	HHZ	00	100.00
BK	MHC	HHZ	00	100.00
BK	MHDL	HHZ	00	99.38
BK	MHDL	HS1	40	99.21
BK	MHDL	BT1	20	98.98
BK	MNRC	HHZ	00	100.00
BK	MOBB	BHZ	00	99.03
BK	MOBB	VFP	10	99.01
BK	MOD	HHZ	00	100.00
BK	ORV	HHZ	00	100.00
BK	OXMT	HHZ	00	99.97
BK	OXMT	HS1	40	99.72
BK	PACP	HHZ	00	99.99
BK	PETB	HN1	40	100.00
BK	PKD	HHZ	00	99.67
BK	RAMR	HHZ	00	96.07
BK	RB2B	DP1	--	99.95
BK	RFSB	CN1	40	99.93
BK	RFSB	HNZ	00	100.00
BK	SAO	BQ2	--	100.00
BK	SAO	HHZ	00	100.00
BK	SBRN	HS1	40	96.14
BK	SCCB	HNZ	00	67.20
BK	SCZ	HHZ	00	99.99
BK	SCZ	HHZ	50	99.99
BK	SM2B	CN1	40	90.97
BK	SUTB	HHZ	00	97.28
BK	SVIN	HS1	40	99.82
BK	TCHL	HHZ	00	99.98
BK	THIS	HHZ	00	85.14
BK	TRAM	HHZ	00	99.59
BK	TSCN	HHZ	00	85.31
BK	VAK	HHZ	00	100.00
BK	VALB	HN1	40	99.97
BK	WDC	HHZ	00	100.00
BK	WENL	HHZ	00	99.94
BK	YBH	HHZ	00	100.00
BK	YBH	HHZ	50	99.96

Table 4.8.4: Percentage of continuous data archived for BK sta-

tions based on station operation time for the year.

Acknowledgements

The NCEDC is a joint project of the BSL and the USGS Menlo Park and is funded primarily by BSL and USGS Cooperative Agreements G10AC00141 and G10AC00093. Additional funding for the processing and archiving of the EarthScope PBO and SAFOD data were provided by EarthScope subawards EAR0732947-07 through UNAVCO. Archival of geothermal monitoring data are provided through LBNL project number 6948613.

Douglas Neuhauser is the manager of the NCEDC. Stephane Zuzlewski, Mario Aranha, Ingrid Johanson, Ta-ka'aki Taira, Jennifer Taggart, Clay Miller, and Peggy Hellweg of the BSL contribute to the operation of the NCEDC. Doug Neuhauser, Peggy Hellweg, and Clay Miller contributed to the preparation of this section.

Glossary of Common Acronyms

Acronym	Definition
ADA	Amplitude Data Area
ANSS	Advanced National Seismic System
ANSS NIC	ANSS National Implementation Committee
AQMS	ANSS Quake Monitoring System
ARRA	American Recovery and Reinvestment Act
BARD	Bay Area Regional Deformation
BAVU	Bay Area Velocity Unification
BDSN	Berkeley Digital Seismic Network
BSL	Berkeley Seismological Laboratory
CalEMA	California Emergency Management Agency
Caltrans	California Department of Transportation
CDF	California Department of Forestry
CGS	California Geological Survey
CISN	California Integrated Seismic Network
DART	Data Available in Real Time
EEW	Earthquake Early Warning
ElarmS	Earthquake Alarm Systems
EM	Electromagnetic
FACES	FlexArray along Cascadia Experiment for Segmentation
FEMA	Federal Emergency Management Agency
HFN	Hayward Fault Network
HRSN	High Resolution Seismic Network
InSAR	Interferometric Synthetic Aperture Radar
IRIS	Incorporated Research Institutions in Seismology
IRIS DMC	IRIS Data Management Center
LBNL	Lawrence Berkeley National Laboratory
LFE	Low Frequency Event
LLNL	Lawrence Livermore National Laboratory
MARS	Monterey Accelerated Research System
MBARI	Monterey Bay Aquarium Research Institute
MOBB	Monterey Ocean Bottom Broadband Observatory
mPBO	Mini-Plate Boundary Observatory
MT	Magnetotelluric
MT	Moment Tensor
MTJ	Mendocino Triple Junction
NCEDC	Northern California Earthquake Data Center
NCEMC	Northern California Earthquake Management Center
NCSN	Northern California Seismic Network
NCSS	Northern California Seismic System
NHFN	Northern Hayward Fault Network

Continued on next page

NVT	Non-volcanic Tremor
PBO	Plate Boundary Observatory
PDF	Probability Density Function
PGV	Peak Ground Velocity
PSD	Power Spectral Density
QDDS/EIDS	Quake Data Distribution System/Earthquake Information Distribution System
REDI	Rapid Earthquake Data Integration
RES	Repeating Earthquake Sequence
SAF	San Andreas Fault
SAFOD	San Andreas Fault Observatory at Depth
SCSN	Southern California Seismic Network
SEED	Standard for Exchange of Earthquake Data
SEM	Spectral Element Method
SHFN	Southern Hayward Fault Network
SOH	State of Health
SSE	Slow Slip Event
UNACO	University NAVSTAR Consortium
USGS/MP	United States Geological Survey/ Menlo Park
USNSN	United States National Seismic Network

Appendix I: Publications, Presentations, Awards and Panels

Publications

- Bodin, T., M Salmon, B Kennett, M Sambridge, Probabilistic Surface Reconstruction from Multiple Data-sets—An Example for the Australian Moho, *Journal of Geophysical Research—Solid Earth*, 117, B02301, 2012.
- Bodin, T., H. Yuan and B. Romanowicz. Inversion of Receiver Functions without Deconvolution—Application to the Indian Craton, *GJI, in revision*.
- Böse, M., Allen, R., Brown, H., Cua, G., Fischer, M., Hauksson, E., Heaton, T., Hellweg, M., Liukis, M., Neuhauser, D., Maechling, P. & CISN EEW Group, “CISN ShakeAlert: An Earthquake Early Warning Demonstration System for California”, in *Early Warning for Geological Disasters—Scientific Methods and Current Practice*, edited by F. Wenzel and J. Zschau, Springer Berlin Heidelberg, New York, 2013, ISBN 978-3-642-12232-3.
- Boyd, O.S., D. S. Dreger, V. H. Lai, and R. Gritto, Full Moment Tensor Analysis Using first Motion Data at The Geysers Geothermal Field, *Proceedings, Thirty-Eighth Workshop on Geothermal Reservoir Engineering*, Stanford University, SGP-TR-198.
- Chen, K. H., R. Bürgmann, and R. M. Nadeau, Do earthquakes talk to each other? Triggering and interaction of repeating sequences at Parkfield, *Journal of Geophysical Research*, 118, doi:10.1029/2012JB009486, 2013.
- CISN Earthquake Early Warning Team, “Prototype Development of the new CISN Earthquake Alert System (‘CISN ShakeAlert’): Collaborative Research with California Institute of Technology, University of California at Berkeley, University of Southern California, and Swiss Federal Institute of Technology, Zürich”, *USGS EEW Report*, 2012.
- Cottaar, S., and B. Romanowicz, Observations of changing anisotropy across the southern margin of the African LLSVP, *Geophys. J. Int.*, *in revision*.
- Cottaar S. and B. Romanowicz, An unusually large ULVZ at the base of the mantle near Hawaii, *Earth Planet. Sci. Lett.*, 355-356, 213-222, 2012.
- Daley, T., Freifeld, B., Ajo-Franklin, J., Dou, S., Pevzner, R., Shulakova, V., Kashikar, S., Miller, D., Goetz, J., Henningses, J., and Lueth, S., Field testing of fiber-optic distributed acoustic sensing (DAS) for subsurface seismic monitoring, *The Leading Edge*, 32(6), 699–706, 2013.
- Fielding, E. J., A. Sladen, Z. Li, J.-P. Avouac, R. Bürgmann, and I. Ryder, Kinematic fault slip evolution source models of the 2008 M7.9 Wenchuan earthquake in China from SAR interferometry, GPS and teleseismic analysis and implications for Longmen Shan tectonics, *Geophysical Journal International*, 194(2), doi:10.1093/gji/ggt1155, 2013.
- Foster, K.A., K. Dueker, B. Schmandt, and H. Yuan, Sharp cratonic lithosphere-asthenosphere boundary beneath the American Midwest and its relation to mantle flow, *EPSL, in revision*.
- Grapenthin, R., CrusDe: A plug-in based simulation framework for composable CRUstal DEformation studies using Green’s functions, *Computers and Geosciences, in press*, doi:10.1016/j.cageo.2013.07.005, 2013.
- Goktepe, F., Kuyuk H.S., Celebi, E., “Efficiency of Wave Impeding Barrier in Pipeline Construction under Earthquake Excitation using Non-Linear Finite Element Analysis”, *Sadhana—Academy Proceedings in Engineering Science, accepted*.
- Guilhem A., D. S. Dreger, H. Tsuruoka, and H. Kawakatsu, Moment tensors for rapid characterization of megathrust earthquakes: the example of the 2011 M9 Tohoku-oki, Japan earthquake, *Geophys. Journ. Int.*, doi:10.1093/gji/ggs045, 2012.
- Guilhem, A. and R.M. Nadeau, Episodic tremors and deep slow-slip events in Central California, *Earth Planet. Sci. Lett.*, 357-358, 1-10, doi:10.1016/j.epsl.2012.09.028, 2012.
- Huang, M.-H., D. Dreger, R. Bürgmann, S.-H. Yoo, and M. Hashimoto, Joint inversion of seismic and geodetic data for the source of the 2010 March 4, Mw 6.3 Jia-Shian, SW Taiwan, earthquake, *Geophys. J. Int.*, 193, 1608-1626, doi:10.1093/gji/ggt058, 2013.
- Iaffaldano, G., T Bodin, M Sambridge, Reconstructing plate-motion changes in the presence of finite rotations noise, *Nature Communications*, 3, 1048, 2012.

- Iaffaldano, G., T Bodin, M Sambridge, Slow-downs and speed-ups of India Eurasia convergence since ~20Ma: Data-noise, uncertainties and dynamic implications, *Earth and Planetary Science Letters*, 367, 146-156, 2013.
- Kelly, C.M., A. Rietbrock, D.R. Faulkner and R.M. Nadeau, Temporal Changes in Attenuation associated with the 2004 M6.0 Parkfield Earthquake, *J. Geophys. Res.*, 118, 630–645, doi:10.1002/jgrb.50088, 2013.
- Knecht, A., R. Hong, DW. Zumwalt, B. Delbridge, et. al, Precision Measurement of the He-6 Half-Life and the Weak Axial Current in Nuclei, *Phys. Rev. Lett*, v. 108, 2012.
- Knecht, A., R. Hong, DW. Zumwalt, B. Delbridge, et. al., Precision Measurement of the He-6 Half-Life and the Weak Axial Current in Nuclei, *Phys. Rev. C.*, 2012.
- Kuyuk H.S., R.M. Allen, Optimal seismic network density for earthquake early warning: A case study from California, *Seismological Research Letters*, in press, 2013.
- Kuyuk, H.S. Brown H., Henson I., Allen R.M., Hellweg M., Neuhauser D., Designing a network-based earthquake early warning system for California: ElarmS-2, *Bulletin of Seismological Society of America*, accepted.
- Kuyuk H.S., Yildirim E., Dogan E., Horasan G., Application of k-means and Gaussian mixture model for classification of seismic activities in Istanbul, *Nonlinear Processes in Geophysics*, 19 (4), pp. 401-419, 2012.
- Kuyuk H.S., Yildirim E., Dogan E., Horasan G., Clustering Seismic Activities using Linear and Nonlinear Discriminant Analysis, *Journal of Earth Science*, in press, 2013.
- Lekic, V., S. Cottaar, A. Dziewonski, and B. Romanowicz, Cluster analysis of global lower mantle tomography: a new class of structure and implications for chemical heterogeneity, *Earth Planet. Sci. Lett.*, 357-358, 68-77, 2012.
- McLaskey, G.C., A.M. Thomas, S.D. Glaser and R.M. Nadeau, Fault healing promotes high-frequency earthquakes in laboratory experiments and on natural faults, *Nature*, 491, 101-105, doi:10.1038/nature11512, 2012.
- Montagner, JP, C. Larmat, Y. Capdeville, M. Fink, H. Phung, B. Romanowicz, E. Clévéde and H. Kawakatsu, Time-reversal method and cross-correlation techniques by normal mode theory: a three-point problem, *Geophys. J. Int.*, 191, 637-652, 2012.
- Pollitz, F., R. Bürgmann, and W. Thatcher, Illumination of rheological mantle heterogeneity by the M7.2 2010 El Mayor-Cucapah earthquake, *Geochem. Geophys. Geosystems*, 13(Q06002), doi:10.1029/2012GC004139, 2012.
- Pollitz, F., R. S. Stein, V. Sevilgen, and R. Bürgmann, The 11 April 2012 M=8.6 East Indian Ocean earthquake triggered large aftershocks worldwide, *Nature*, doi: 10.1038/nature11504, 2012.
- Pollitz, F. F., A. G. Wech, H. Kao, and R. Bürgmann, Annual modulation of non-volcanic tremor in northern Cascadia, *J. Geophys. Res.*, 118, doi:10.1002/jgrb.50181, 2013.
- Reddy, C. D., P. S. Sunil, R. Bürgmann, D. V. Chandrasekhar, and T. Kato, Postseismic relaxation due to Bhuj earthquake on January 26, 2001: possible mechanisms and processes, *Natural Hazards*, 65(2), doi: 10.1007/s11069-11012-10184-11067, 2013.
- Reiter, D., M. Leidig, S.-H. Yoo, and K. Mayeda, Source characteristics of seismicity associated with underground wastewater disposal: A case study from the 2008 Dallas-Fort Worth earthquake sequence, *The Leading Edge*, 31(12), 1454-1460, 10.1190/tle31121454.1, 2012.
- Ryder, I., R. Bürgmann, and E. Fielding, Static stress interactions in extensional earthquake sequences: an example from the South Lunggar Rift, Tibet, *J. Geophys. Res.*, 117(B09405), doi:10.1029/2012JB009365, 2012.
- Sambridge, M., T Bodin, K Gallagher, H Tkalčić, Transdimensional inference in the geosciences, *Phil. Trans. R. Soc. A*, 371, 20110547, doi:10.1098/rsta.2011.0547, 2012.
- Shirzaei, M., and R. Bürgmann, Time-dependent model of creep on the Hayward fault from joint inversion of 18 years of InSAR and surface creep data, *J. Geophys. Res.*, 118, doi:10.1002/jgrb.50149, 2013.
- Shirzaei, M., T. Taira, and R. Bürgmann, Implications of recent asperity failures and aseismic creep for time-dependent earthquake hazard on the Hayward fault, *Earth and Planetary Science Letters*, 371-372, doi:10.1016/j.epsl.2013.1004.1024, 2013.
- Taira, T., Z. Zheng, and B. Romanowicz, On the systematic long period noise reduction on ocean floor broadband seismic sensors collocated with differential pressure gauges, *Bull. Seism. Soc. Am.*, accepted, 2013.
- Tesauro, M., P. Audet, M. Kaban, R. Bürgmann, and S. Cloetingh, The effective elastic thickness of the continental lithosphere: Comparison between rheological and inverse approaches, *Geochem. Geophys. Geosystems*, 13(9), doi:10.1029/2012GC004162, 2012.
- Tkalčić, H., M Young, T Bodin, S Ngo, M Sambridge, The Shuffling rotation of the Earth's inner core revealed by earthquake

doublets, *Nature Geoscience*, 6, 497-502, 2013.

Thomas, A. M., R. Burgmann, and D. S. Dreger, Incipient faulting near Lake Pillsbury, California, and the role of accessory faults in plate boundary evolution, *Geology*, doi:10.1130/G34588.1, 2013.

Turner, R., R. M. Nadeau, and R. Bürgmann, Aseismic Slip and Fault Interaction from Repeating Earthquakes in the Loma Prieta Aftershock Zone, *Geophys. Res. Lett.*, 40(1-5), doi:10.1029/2012GL054252, 2013.

Wen, Y., Z. Li, C. Xu, I. Ryder, and R. Bürgmann, Postseismic motion after the 2001 Mw 7.8 Kokoxili earthquake in Tibet observed by InSAR time series, *Journal of Geophysical Research*, 117(B8), doi:10.1029/2011JB008514, 2012.

Wiseman, K., P. Banerjee, R. Bürgmann, K. Sieh, D. S. Dreger, and I. Hermawan, Source model of the 2009 Mw 7.6 Padang intra-slab earthquake and its effect on the Sunda megathrust, *Geophys. J. Int.*, 190, doi: 10.1111/j.1365-1246X.2012.05600.x, 2012.

Wiseman, K., and R. Bürgmann, Stress triggering of the great Indian Ocean strike-slip earthquakes in a diffuse plate boundary zone, *Geophys. Res. Lett.*, 39(L22304), doi:10.1029/2012GL053954, 2012.

Yoo, S.-H. and K. Mayeda, Validation of Non-Self-Similar Source Scaling Using Ground Motions from the 2008 Wells, Nevada, Earthquake Sequence, *Bull. Seismol. Soc. Am.*, 103, 2520-2533, doi:10.1785/0120120327, 2013.

Young, M., N Rawlinson, T Bodin, Transdimensional Inversion of ambient seismic noise for 3d shear velocity structure of the Tasmanian crust, *Geophysics*, 78(3), WB46-WB62, 2013.

Zechar, J.D. and R.M. Nadeau, Predictability of repeating earthquakes near Parkfield, California, *Geophys. J. Int.*, 190, 457-462, doi:10.1111/j.1365-246X.2012.05481.x, 2012.

Zheng Z. and B. Romanowicz, Do double “SS precursors” mean double discontinuities?, *Geophys. J. Int.*, 191, 1361-1373, 2012.

Presentations

SEG Annual Meeting, Houston, TX

A Ray, K Key, T Bodin. Hierarchical Bayesian inversion of marine CSEM data over the Scarborough gas filed lesson in correlated noise.

SCEC 2012 Annual Meeting, Palm Springs, CA, September 9–12, 2012

Nomura, S, Y. Ogata and R.M. Nadeau, Space-Time Model and Analysis of Repeating Earthquakes in Parkfield Segment.

Taira T., Spatiotemporal Behaviors in Earthquake Multiplets at the Geysers Geothermal Field, CA, Poster 201.

Monitoring Research Review, Albuquerque, NM, September 18–20, 2012

Dreger, D.S., Chiang, A., Ford, S.R., and Walter, W. R., Refinement of regional distance seismic moment tensor and uncertainty analysis for source-type identification, Abstract 3-04.

Society of Exploration Geophysicists, Annual Meeting, Las Vegas, Nevada, November 4–8, 2012

Dou, S. and Ajo-Franklin, J., Potentials of applying surface-wave methods for imaging subsurface properties in permafrost soils, SEG Technical Program Expanded Abstracts 2012: pp. 1-9. doi: 10.1190/segam2012-1586.1.

American Geophysical Union, 2012 Fall Meeting, San Francisco, CA, December 3–7, 2012

Arroucau, P., J. A. Davies, T. Bodin, M. Sambridge, G Vlahovic, A Bayesian transdimensional algorithm for earthquake location and 1D velocity model determination, Abstract S53F-02.

Barron, J., V. Lekic, S. French and B. Romanowicz Towards a global 3D upper mantle attenuation model using SEM, Abstract S41A-2377.

Bodin, T., Capdeville, Y. Romanowicz, B., The inverse homogenization, Incorporating Discontinuities in Smooth Full Waveform Inversion Models (Invited), Abstract S31C-02.

Bodin, T., H. Yuan and B. Romanowicz, Inversion of Receiver functions without deconvolution, Abstract S53F-01.

Boyd, O.S., Dreger, D.S., Lai, V.H., and Gritto, R., Full Moment Tensor Analysis Using First Motion Data at The Geysers Geo-

- thermal Field, Abstract S43E-2513.
- Cheng, C., Allen, R., Porritt, R., 3-D Seismic Velocity Structure of the Hawaii Hotspot from Joint Inversion of Body Wave and Surface Wave data, Abstract DI53A-2355.
- Chiang, A., Dreger, D.S., Ford, S.R., and Walter, W. R., Source-type identification analysis using regional moment tensors, Abstract S23A-2537.
- Cottaar, S., Li, M., Miyagi, L M., McNamara, A.K., Romanowicz, B. A., Wenk, H.-R., Forward modeling the perovskite-postperovskite transition in seismically anisotropy models beneath a slab, Abstract DI13A-2418.
- Cottaar, S. and B. Romanowicz, Observations on rotation of flow near LLSVP boundaries (DI001 session)
- Delbridge, B., R. Bürgmann, E. Fielding, S. Hensley, W. Schulz., The Slumgullion Natural Laboratory: Landslide-wide kinematics revealed by combining satellite and airborne interferometric synthetic aperture radar with continuous GPS observations, Abstract IN13C-1510.
- Dou, S., Ajo-Franklin, J., and Dreger, D., Mapping deep low-velocity zones in Alaskan Arctic coastal permafrost using seismic surface waves, Abstract C22B-07.
- French, S.W., Lekic, V., and Romanowicz, B., Spectral-element global waveform tomography: A second-generation upper-mantle model, Abstract S34B-07.
- Godoladze, T., N Tumanova , R. Gök , D. Dreger, Crustal Structure study of the Caucasus, Abstract S44C-06.
- Grapenthin, R., J.T. Freymueller, Volcanic plumes monitored with GPS: The eruptions of Okmok 2008, and Redoubt 2009, Alaska, Abstract NH14A-04.
- Gritto, R., and S.-H. Yoo, Three-Dimensional Velocity Structure of The Geysers Geothermal Field, CA, USA, Abstract S43D-2499.
- Guinois M., Z. Zheng, T. Taira and B. Romanowicz, Near real-time noise removal for the Monterey Ocean Bottom Broadband (MOBB) seismic station data, Abstract S53C-2522.
- Hellweg, M., M. Vinci, R.M. Allen, M. Boese, I.H. Henson and C. Felizardo, CISM ShakeAlert: Beta Test Users Receive Earthquake Early Warning Alerts and Provide Feedback for Improving Alert Delivery, Abstract S52B-03.
- Huang, M.-H. and R. Bürgmann, Probing the Deep Rheology of Tibet: Constraints from the 2008 Mw 7.9 Wenchuan, China Earthquake, Abstract T33K-08.
- Iaffaldano, G., Bodin, T., Sambridge, M., Slow-downs and speed-ups of India-Eurasia convergence since ~20 Ma: Data-noise, uncertainties and dynamic implications, Abstract T54B-04.
- Joannes-Boyau, R., Bodin T., Scheffers, A., Sambridge, M., Statistical Detection of Anthropogenic Temporal Changes in the Distribution of Tropical Cyclones, Abstract A21D-0095.
- Johanson, I., D. Dreger, Real-time GPS Strategies for Rapid Response Applications, Abstract G52A-03.
- Kong, Q., Allen, R.M., Using Smartphones to Detect Earthquakes, Abstract S23B-04.
- Kuyuk, H.S., H. Brown, R.M. Allen, D.S. Neuhauser, I.H. Henson and M. Hellweg, CISM ShakeAlert: Next Generation ElarmS, Abstract S52B-02.
- Kuyuk, H.S. Brown H., Henson I., Allen R.M., Hellweg M., Neuhauser D., ElarmS-2: Designing a network-based earthquake early warning system for California?
- Mayeda, K., and S.-H. Yoo, Validation of Source Scaling using Ground Motions from the 2008 Wells, Nevada Earthquake Sequence, Abstract S53A-2489.
- Meschede, M. and B. Romanowicz On the discrepancy in measurement of Q using surface waves and normal modes, Abstract S43A-2454.
- Munafò, I., S.-H. Yoo, L. Malagnini, K. Mayeda, D. Dreger, and R. M. Nadeau, Comprehensive Assessments of Parkfield Earthquake Source Estimates: A Look into Model Variability, Abstract S51B-2416.
- Nadeau, R.M. and A. Guilhem, Episodic Tremor as Indicators of Slow-slip Events (SSE) at Parkfield, California, Abstract S33B-2535.
- Porritt, R. W., Allen, R. M., Pollitz, F. F., Hung, S-H., Imaging the complex Farallon subduction system with USArray derived joint inversion of body waves and surface waves, Abstract DI23A-2370

- Reiter, D., M. Leidig, S.-H. Yoo, and K. Mayeda, The Use of Seismic Coda to Characterize the Source Mechanisms of Induced Earthquakes, Abstract S43B-2477.
- Romanowicz, B.A., Cottaar S. Observations of anisotropy in the vicinity of LLSVP boundaries in the deep mantle, Abstract DI52A-06.
- Romanowicz, B., S. French and V. Lekic, Low velocities in the oceanic upper mantle and their relations to plumes: new insights from SEM-based waveform tomography, invited, Abstract DI44A-06.
- Sambridge, M., Iaffaldano, G., Bodin, T., Plate motions: Simpler than they look, Abstract T42B-04.
- Schmalze, G., G. Khazaradze, R. McCaffrey, K. Creager, A. Wech, B. Delbridge, Along Strike Variations in Episodic Tremor and Slip Rate, Abstract S33B-2546.
- Taira, T., R. Bürgmann, R.M. Nadeau and D.S. Dreger, Investigating Fault Slip and Rheology Along the San Andreas Fault in the San Juan Bautista Region, Abstract S11A-04.
- Tkalčić, H., Sambridge, M., Young, M., Bodin, T., Pachhai, S., What Really Lies Beneath? Defying Conventional Geophysical Inversion and new Observations From the Crust to the Core, Abstract S31C-01.
- Turner, R.C., R.M. Nadeau and R. Bürgmann, Creep Transients and Fault Interaction from Repeating Earthquakes Near San Juan Bautista, California, Abstract S33B-2536.
- Ventosa, S. and B. Romanowicz, On improving the measurement of differential travel times and amplitudes of phases sensitive to the deep mantle, Abstract DI13A-2415.
- Vidale, J.E., P.E. Bodin, R.M. Allen, M. Hellweg, T. Thomas, I.H. Henson, and D.S. Neuhauser, Early Warning of Cascadian Megaquakes for Pacific Northwestern cities, Abstract S52B-01.
- Yoo, S.-H., K. Mayeda, Source spectral variation and yield estimation for small, near-source explosions, Abstract S23A-2526.
- Young, M., Tkalčić, H., Bodin, T., Sambridge, M., Tanaka, S., Rawlinson, N., New P-wave Velocity Images of the Lowermost Mantle from a Bayesian Inversion of PKP, PcP, and P4KP Differential Travel Times, Abstract DI13A-2419.
- Yuan, H. and B. Romanowicz, Azimuthal anisotropy layering and plate motion in the Pacific Ocean, Abstract DI21B-2353.
- Zheng, Z. and B. Romanowicz, Detection of the Lehmann discontinuity across the Pacific by SS precursors recorded at USArray, Abstract DI11A-2378.

International Science and Technology Conference, Dubai, UAE, December 13–15, 2012.

- Goktepe F., Kuyuk H.S., Celebi E., Effect of Wave Impeding Barrier Depth on Buried Pipeline.

SEG-AGU Joint Workshop (Cryosphere Geophysics: Understanding a Changing Climate with Subsurface Imaging), Boise, ID, January 6–8, 2013

- Dou, S. and Ajo-Franklin, J., Seismic surface wave investigations of “deep” low-velocity zones in Arctic coastal permafrost near Barrow, Alaska.

9th Annual Northern California Earthquake Hazards Workshop, USGS, Menlo Park, CA, January 22–23, 2013

- Johanson, I., D. Dreger, Rapid finite-fault earthquakes and afterslip information from seismic and real-time GPS observations.
- Johanson, I., R. Grapenthin, R. Bürgmann, R. Allen, The BARD Continuous GPS Network: Monitoring Earthquake Hazards in Northern California and the San Francisco Bay Area.
- Taira, T., R. Bürgmann, M. Shirzaei, R.M. Nadeau, and I.A. Johanson, Characteristically Repeating Earthquake Activity Along the Hayward Fault.

38th Workshop on Geothermal Reservoir Engineering, Stanford University, Stanford, CA, February 11–13, 2013

- Boyd, O.S., D. S. Dreger, V. H. Lai, and R. Gritto, Full Moment Tensor Analysis Using first Motion Data at The Geysers Geothermal Field, SGP-TR-198.

Lunar and Planetary Science Conference, Houston, Texas, March 18–22, 2013

M. Manga, A. Patel, B. Delbridge, E. Knappe, S. Birch, J. Dufek, Constraints on surface conditions and atmospheric density inferred from the bomb sag at Home Plate, Mars.

EGU General Assembly, Vienna, Austria, April 7–12, 2013

Choblet, G. Husson, L., Bodin, T., Capdeville Y., Confronting GIA models to a probabilistic surface reconstruction of relative sea-level rise.

Choblet, G. Husson, L., Bodin, T., Capdeville Y., Probabilistic surface reconstruction of relative sea-level rise.

Gallagher, K., Sambridge, K., Bodin, T., Reading, A., The inference of abrupt changes and noise levels in multivariate datasets.

Plonka, A., Cottaar, S., Romanowicz, B., Study of the eastern edge of the Pacific Large Low Shear Velocity Province, Abstract 15, 234.

Masson, Y. and B. Romanowicz, A hybrid method for the computation of quasi-3D seismograms.

Schmalze, G., G. Khazaradze, R. McCaffrey, K. Creager, A. Wech, B. Delbridge, Along strike variations of Episodic Tremor and Slip in the Cascadia Subduction Zone.

Annual Meeting of the Seismological Society of America, Salt Lake City, Utah, April 17–19, 2013

Evans, J.R., R. Allen, A. Chung, E. Cochran, R. Guy, M. Hellweg and J. Lawrence, Class-C Accelerographs in Monitoring and Research: Performance Evaluation Results. *Seismol. Res. Lett.*, 84, 315, 2013.

Godoladze, T., D. Dreger, 3D Wave propagation studies in the Caucasus

Grapenthin, R., I. Johanson, R. Allen, Integrating Real-Time GPS into Earthquake Early Warning for Northern California, *Seism. Res. Lett.* 84(2), 362, 2013.

Hellweg, M., R.M. Allen, S. Colombelli, R. Grapenthin, I. Henson, I. Johanson, H.S. Kuyuk, D. Neuhauser, Operating and Improving Earthquake Early Warning for Northern California and the US West Coast, *Seism. Res. Lett.* 84(2), 362, 2013.

Hellweg, M., P. Lombard, J. Boatwright, T. MacDoald, R. Dollar, L. Hagos, H. Haddidi and A. Shakal, (2013). ShakeMap Operation in the California Integrated Seismic Network. *Seismol. Res. Lett.*, 84, 356, 2013.

Johanson, I., D. Dreger, R. Grapenthin, P. Lombard, Rapid Fault Determination from Real-Time GPS for ShakeMap, *Seism. Res. Lett.* 84(2), 358, 2013.

Kuyuk H.S., Allen R.M. “Neural Networks based Magnitude Estimation for Earthquake Early Warning”

Massin F., J. Farrell, T. Taira, D.R. Shelly, G.P. Waite, and R.B. Smith, Multiplet Earthquake Relocations and Stress Models of the Yellowstone Volcanic Field and Implications for Volcanic-tectonic Interactions.

Taira, T., M. Hellweg and R. Uhrhammer (2013). Evaluating Accelerometers for Use in the Berkeley Digital Seismic Network. *Seismol. Res. Lett.*, 84, 314, 2013.

T. Taira, Z. Zheng and B. Romanowicz (2013) On the Systematic Long Period Noise Reduction on Ocean Floor Broadband Seismic Sensors Collocated with Differential Pressure Gauges”.

Yoo, S.-H., and K. Mayeda, Local Explosion Monitoring from the Source Physics Experiment (SPE): Detection, Yield, and Discrimination using Network Template Matching, Abstract 13-183.

Zheng, Z., T. Taira, and B.A. Romanowicz, On the Systematic Long Period Noise Reduction on Ocean Floor Broadband Seismic Sensors Collocated with Differential Pressure Gauges

Zheng, Z., S. Ventosa and B. Romanowicz (2013) Application of local adaptive slant-stack transform (LSST) to improve the SS precursor record sections recorded on the USArray.

Earthscope National Meeting, Raleigh, NC, May 13–15, 2013

Grapenthin, R., I. Johanson and R. Allen, Integrating Real-Time GPS into Earthquake Early Warning for Northern California.

Johanson, I., R. Grapenthin, P. Lombard, R. Bürgmann, D. Dreger, R. Allen, The BARD Continuous GPS Network: Monitoring Earthquake Hazards in Northern California.

2013 Japan Geoscience Union Meeting (JpGU), Makuhari Messe, Japan, May 19–24, 2013

Nomura, S., Y. Ogata, R.M. Nadeau and N. Uchida, Spatio-temporal renewal model for repeating earthquakes and analysis of slip rate on plate boundaries, Abstract 01949.

Seventh National Seismic Conference on Bridges & Highways (7NSC), Oakland, CA, May 20–22, 2013

Kuyuk H.S., Allen R.M. Strauss, J., On the use of Earthquake Early Warning System for Transportation.

Gordon Research Seminar, Mount Holyoke, MA, June 1–2, 2013

Cottaar, S. and Romanowicz B.A., Direct waveform evidence for strong heterogeneity in the lowermost mantle, (*invited talk*).

Gordon Research Conference, Mount Holyoke, MA, June 2–7, 2013

Cottaar, S. and Romanowicz B.A., Mapping an unusually large ULVZ near Hawaii through Sdiff waveform complexities.

French, S.W., Lekic, V., and Romanowicz, B., Global full-waveform tomography with the SEM: New results from the oceanic upper mantle.

CIG-QUEST-IRIS Seismic Imaging Workshop, Fairbanks, AK, July 12–14, 2013

Meng, L., R. Allen and J-P Ampuero, Application of Seismic Array Processing to Earthquake Early Warning.

Speaking Engagements

Bodin, T., When one of the things you don't know is the number of things you don't know, Scripps, UC San Diego, La Jolla, CA, February 2013.

Bodin, T., When one of the things you don't know is the number of things you don't know, Universite of Nantes, France, November 2012.

Bodin, T., When one of the things you don't know is the number of things you don't know, Applied Math Seminar, Lawrence Berkeley National Lab., Berkeley, CA, November 2012.

Bodin, T., When one of the things you don't know is the number of things you don't know, Statistics seminar, UC Berkeley, Berkeley, CA, September 2012.

Bodin, T., When one of the things you don't know is the number of things you don't know, Berkeley Seismological Laboratory Seminar, UC Berkeley, Berkeley, CA, August 2012.

Boyd, O.S., D. S. Dreger, V. H. Lai, and R. Gritto, Full Moment Tensor Analysis Using first Motion Data at The Geysers Geothermal Field, *proceedings*, Thirty-Eighth Workshop on Geothermal Reservoir Engineering, Stanford University, Stanford, CA, February 11–13, 2013, SGP-TR-198.

Bürgmann, R., California Earthquakes!, UC Berkeley Lair of the Bear, Pinecrest, CA, July 1 and July 3, 2012.

Bürgmann, R., Resolving Postseismic Relaxation Processes Following the 2011 Tohoku Earthquake, Symposium of Global COE Program for Earth Sciences, Tohoku University, Japan, September 26, 2012.

Bürgmann, R., The Value of Seafloor Geodesy for Subduction Zone Earthquake Cycle Studies, EOS Singapore, Workshop on Seafloor Geodesy, Singapore, October 22, 2012.

Bürgmann, R., Huang, M.-H., Pollitz, F.F., Ryder, I., Wiseman, K., and Hu, Y., Postseismic Deformation Probing of Rheology of the Lower Crust and Upper Mantle, Invited presentation, AGU Fall Meeting, San Francisco, CA, December 4, 2012.

Cottaar, S., Piles and puddles in the deep mantle, Berkeley Seismological Laboratory Seminar, UC Berkeley, Berkeley, CA, May 7th, 2013.

Dreger, D. S., Seismic source-type identification and moment tensors of exotic events, Scripps, April 16, 2012.

Dreger, D. S., Towards the understanding of induced seismicity in enhanced geothermal systems, DOE Geothermal Technologies Office Review, Denver April 23, 2013.

Dreger, D. S., Refinement of regional distance seismic moment tensor and uncertainty analysis for source-type identification,

- AFRL Technical Integration Meeting, September 19, 2013
- Dreger, D. S., Refinement of regional distance seismic moment tensor and uncertainty analysis for source-type identification, AFRL Technical Integration Meeting, September 20, 2012
- Godoladze, T., Seismicity of the Caucasus, University of Utah, April 15, 2013.
- Grapenthin, R., Volcano Deformation and Subdaily GPS Products, University of Oregon, Eugene, OR, April 3, 2013.
- Grapenthin, R., Johanson, I., Allen, R., Integrating Real-Time GPS into California's Earthquake Early Warning System, University of Alaska, Fairbanks, AK, Geophysical Institute, March 22, 2013.
- Grapenthin, R., GPS—A Multi-Tool: Plumbing, Plumes, and Early Warning, Central Washington University, Ellensburg, WA, January 4, 2013.
- Grapenthin, R., Towards Real-time GPS in Earthquake Early Warning and Applications for Volcano Monitoring, Northern California GPS User Group Meeting, Martinez, CA, December 14, 2012.
- Grapenthin, R., Towards Real-time GPS in Earthquake Early Warning, Berkeley Seismological Laboratory, UC Berkeley, Berkeley, CA, November 19, 2012.
- Grapenthin, R., Volcano Deformation and Subdaily GPS Products, USGS Earthquake Science Center Seminar, Menlo Park, CA, August 29, 2012.
- Hellweg, M., ShakeAlert—Building and Earthquake Early Warning System for California, Meeting of the Bay Area Earthquake Alliance, Oakland, CA, September 27, 2012.
- Hellweg, M., Berkeley Seismological Laboratory: 125 Years of Sound Science Serving Society, Guralp Systems Ltd., Aldermaston, UK, October 19, 2012.
- Hellweg, M., Moment Tensor Analysis in Northern California, Bensberg Seismological Observatory, University of Cologne, Germany, October 30, 2012.
- Johanson, I., All Shook Up: The science of earthquakes and hazard in the San Joaquin Delta, Delta Kappa Gamma International Society for Key Women Educators, Alpha Zeta Chapter, Stockton, CA, January 16 2013.
- Johanson, I., Strauss, J., Earthquake Early Warning in California, Corcept Therapeutics, Menlo Park, CA, February 13, 2013.
- Kuyuk H.S., Earthquake Early Warning Systems, Berkeley Seismological Lab, UC Berkeley, Berkeley, CA, January 17, 2012.
- Meng, L., Rapid Earthquake Source Imaging At Regional And Local Distance, UCLA Earth, Space and Planetary Science Colloquium Seminar, Los Angeles, CA, April 30, 2013.
- Romanowicz, B., Seismic tomography based on numerical wavefield computations: inferences on viscous fingering in the oceanic upper mantle, University of Munich, Germany, October 2012.
- Romanowicz, B., Inferences on global dynamics from upper mantle tomography based on numerical seismic wavefield computations, ETH Zurich, Switzerland, October 11, 2012.
- Romanowicz, B., Channeled flow at the base of the oceanic lithosphere: evidence from full waveform tomography, Princeton University, Princeton, NJ, February 24, 2013.
- Romanowicz, B., Imag(in)ing the Earth's Interior, University of California, Berkeley, Berkeley, CA, 100th Martin Meyerson Faculty Research Lecture, April 30, 2013.
- Romanowicz, B., *L'imagerie sismique du manteau terrestre*, Société Française de Physique, Marseille, France, July 2, 2013.
- Strauss, J., Ten Seconds, Corcept Therapeutics, Menlo Park, CA, February 13, 2013.
- Strauss, J. and J. Duchover, Earthquakes: CERT Tri-Annual Training, San Leandro Public Library, San Leandro, CA, March 28, 2013.
- Yuan, Huaiyu, A tale of two continents, Institute of Geology and Geophysics, Chinese Academy of Sciences, Beijing, China, Jan 18, 2013.
- Yuan, Huaiyu, Introduction to Seismic Tomography: Methodology, Institute of Geophysics, China Earthquake Administration, Beijing, China, Jan 14 2013.
- Yuan, Huaiyu, Introduction to Seismic Tomography: Data and Processing – including special notes on the LAB, an anisotropic view, Institute of Geophysics, China Earthquake Administration, Beijing, China, Jan 15 2013.
- Yuan, Huaiyu, Introduction to Seismic Tomography: A Global Survey of Results, 1984 to present, Institute of Geophysics, China

Earthquake Administration, Beijing, China, Jan 16 2013.

Awards

Panels and Professional Service

Richard M. Allen

Member, Cascadia Initiative Expedition Team Chair, International Earthquake Early Warning Advisory Committee, Geological Institute of Israel
Member, Scientific Advisory Board, European Union Framework 6 Project: Strategies and tools for Real Time Earthquake Risk Reduction (REAKT)
Chair, Amphibious Array Steering Committee (for the NSF Cascadia Initiative)
Chair, IRIS PASSCAL Standing Committee

Roland Bürgmann:

Associate Editor, Bulletin of the Seismological Society of America
Editorial Advisory Board, Eos
Editorial Board, Earth and Planetary Science Letters
Member, National Earthquake Prediction Evaluation Council (NEPEC)
Member, Southern California Earthquake Center (SCEC) Board of Directors
Member, Earth Science Subcommittee of NASA Advisory Council
Member, Organizing Committee of Workshop on Advancing Experimental Rock Deformation Research: Scientific and Technical Needs

Douglas S. Dreger

Cosmos Board of Directors

Margaret Hellweg

Commissioner, Alfred E. Alquist Seismic Safety Commission
Member, CISN Program Management Committee
Member, CISN Standards Committee
Member, CISN Steering Committee
Member, CISN Outreach Committee
Member, ANSS Performance Standards Committee
Member, ANSS Comprehensive Catalog Advisory Committee
Chair, ANSS Class C Instrumentation Evaluation Committee
Member, Bay Area Earthquake Alliance Committee
Member, Bay Area Earthquake Alliance Executive Committee
Member, Editorial Board of Journal of Volcanology and Geothermal Research
Member, New Media Committee, Seismological Society of America

Douglas S. Neuhauser

Chair, Standards Group, California Integrated Seismic Network (CISN)
Acting Member, CISN Program Management Committee

Barbara Romanowicz

Member, Conseil d'établissement, Collège de France
Membre, advisory committee, COMPRES program
Geophysics Search Committee, Université de Lyon-1 (April-June 2013)
Member, PhD Thesis committee, Stéphanie Durand, ENS Lyon, 10/26/2013
President, PhD thesis committee, Sanne Cottaar, UC Berkeley, May 2013
Member, Scientific advisory committee, GEOSCOPE program (Paris, France)
Selection committee, Arthur Holmes Medal, European Geophysical Union.
Member, review panel for INSIGHT program (seismometer on Mars), IPGP, May 27 2013.
Chair, 2013 Gordon Conference on the Interior of the Earth, Mt Holyoke College, 2-7 June 2013.

Organisation of an annual CIDER (Cooperative Institute on Dynamic Earth Research) workshop, on December 10, 2012 in Berkeley: "Continental Lithosphere: formation, evolution, destruction".
PI, CIDER program, funded by NSF/ FESD. Member of organizing team, 2013 CIDER Summer Program at UC Berkeley, July 1- Aug 2, 2013.

Taka'aki Taira

Member, California Integrated Seismic Network, Standards Committee
Member, , California Integrated Seismic Network, ShakeMap Working Group
Member, Plate Boundary Observatory, Data Working Group

Appendix II: Seminar Speakers

Thomas Bodin

UC Berkeley

“When one of the things you don’t know is the number of things you don’t know.”

August 21, 2012

Cody Worthman

Stanford University

“Vector Time-Series from Multiple Aperture InSAR.”

August 28, 2012

Mark Hildyard

University of Leeds

“New Insights into Real-time Magnitude Estimation for Earthquake and Tsunami Early Warning.”

September 4, 2012

Corinne Bachmann

Lawrence Berkeley National Laboratory

“New approaches towards understanding and forecasting induced seismicity.”

September 11, 2012

Marine Denolle

Stanford University

“Ground Motion Prediction Using the Virtual Earthquake Approach.”

September 18, 2012

Francisco Ortega

Caltech

“Sensitivity based inversion for the post-seismic deformation of the great 11 March Tohoku-Oki (Mw 9.0) earthquake constrained by geodetic observations.”

September 25, 2012

Jennifer Haase

Purdue University

“Seismic hazard and ground motion modeling in the central US.”

October 2, 2012

Tom Hanks

USGS

“Probabilistic Seismic Hazard Assessment: what it is and what it isn’t.”

October 9, 2012

Aaron Wech

Victoria University of Wellington, NZ

“The tremor tool: probing fault strength and plate boundary dynamics.”

October 16, 2012

Holly Brown

UC Berkeley

“Providing Earlier Earthquake Alerts with Assistance from an Artificial Neural Network.”

October 23, 2012

Jian Zhang

Los Alamos National Laboratory

“Probing low-energy yet correlated seismic signals.”

October 30, 2012

Xiaopeng Tong

University of California, San Diego

“High-resolution interseismic velocity data of the San Andreas Fault from GPS and InSAR.”

November 6, 2012

Zach Duputel

Caltech

“Use of long-period seismic waves for earthquake source studies—the off-Sumatra earthquake sequence of April 2012.”

November 13, 2012

Erica Mitchell

University of California, San Diego

“Temperature dependence of frictional healing of Westerly granite: experimental observations and numerical simulations.”

November 20, 2012

Noel Bartlow
Stanford University
"Time-dependent analysis of subduction zone slow slip events in Cascadia and New-Zealand."
November 27, 2012

Tom Heaton
Caltech
"The statistics of long-period ground motion; is probabilistic design of tall buildings feasible?"
January 22, 2013

Weisen Shen
University of Colorado, Boulder
"Modeling the crust and uppermost mantle of W. US from surface wave and receiver functions."
January 29, 2013

Michael Pasyanos
Lawrence Livermore National Laboratory
"LITHO1.0—An updated crust and lithospheric model of the Earth developed using multiple data constraints."
February 5th, 2013

Jane Kanitpanyacharoen
UC Berkeley
"Exit Seminar: Synchrotron X-ray applications toward an understanding of elastic anisotropy."
February 12, 2013

Brandon Schmandt
Univeristy of New Mexico
"Mantle seismic structure beneath USArray and the origin of the Yellowstone hotspot."
February 19, 2013

Nathan Simmons
Lawrence Livermore National Laboratory
"Global P-wave tomography for prediction of regional and teleseismic travel times."
February 26, 2013

Ru-shan Wu
University of California, Santa Cruz
"Break the border of the Linear Kingdom of waveform inversion."
March 5, 2013

Walter Mooney
USGS
"Understanding Intraplate Earthquakes,"
March 12, 2013

Satoshi Ide
University of Tokyo, ERI
"The mechanism and spatial variation of slow earthquakes."
March 19, 2013

Lars Hansen
Stanford University
"Feeling olivine fabrics: Implications of seismic anisotropy for the mechanical properties of upper mantle."
April 2, 2013

Jainbao Sun
Visiting Scholar, UC Berkeley
"Probabilistic inversion of geodetic data with applications to recent large earthquakes."
April 9, 2013

Lori Dengler
California State University, Humboldt
"Three decades of chasing tsunamis: successes, failures and challenges."
April 16, 2013

Rob Porritt
UC Berkeley
"Exit Seminar: Tracing the Farallon plate through seismic imaging with USArray."
April 22, 2013

Sanne Cottaar
UC Berkeley
"Exit Seminar: Piles and puddles in the deep mantle."
May 7, 2013

